Microscopic evaluation of two-photon activated molecular nanomachines for next generation targeted cancer therapeutics

THOMAS SAMUEL BRADFORD

Microscopic evaluation of two-photon activated molecular nanomachines for next generation targeted cancer therapeutics

Thomas Samuel Bradford

A thesis submitted in fulfilment of the requirements of Durham University, for the award of Doctor of Philosophy

2023

Declaration

The work described herein was undertaken at the Department of Chemistry, Durham University between October 2019, and September 2023. All the work is my own, except where specifically stated otherwise. No part has previously been submitted for the award of any other degree at this or any other university.

Statement of copyright

Abstract

Unidirectional molecular nanomachines are small organic molecules consisting of two distinct halves; a stator, and rotor, connected by a sterically overcrowded carbon-carbon double bond. When excited with specific wavelengths of light, commonly used 355 and 365 nm, a *cis-trans* isomerisation occurs, resulting in a unidirectional 360^{o} rotary mechanism capable of overcoming Brownian motion. This has previously been exploited to mechanically damage the outer membranes of cells, triggering an acceleration of irreversible necrotic cell death.

Herein a series of systematic live-cell fluorescence microscopy studies are reported evaluating the capability of new functionalised molecular nanomachines to induce premature cell death. Specifically, work has been carried out to develop methodology and instrumentation capable of activating these molecules with more biologically favourable NIR wavelengths by way of two-photon activation - utilising pulsed (fs) laser light. In addition, experiments aimed at assessing newly developed families of molecular nanomachines capable of crossing the phospholipid bilayer and activating confined and controlled rotary mechanism from within the cell are presented.

Key findings are presented showing how functionalisation of molecular nanomachines, with diamine moieties of various levels of methyl substitution, is able to induce a bathochromic shift in activation wavelength. Specifically, a greater level of amine substitution by electron donating alkyl chains is shown to increase this effect when attached to the rotor half of the nanomachine. Activation of polyethylene glycol functionalised nanomachines by way of a two-photon process is also illustrated both when in solution and, importantly, from within the cell. This is also extended to

nanomachines functionalised with the mitochondrial targeted triphenylphosphine addend.

These developments are then combined. Using attempts to activate internalised molecular nanomachines functionalised with triphenylphosphine from withinside cells. Specifically using therapeutically favourable, less phototoxic, 710 nm NIR wavelengths to induce more biologically compatible routes towards cell death, such as apoptosis. Miscopy images are presented illustrating that with the combination of these techniques, with short precisely designed windows of laser exposure, it is possible to observe clear morphological features of cell death without the addition of fluorescent signs of necrosis.

These results represent a significant step forward towards the development of next generation targeted cancer therapeutics, but also leave a clear avenue for further work within the field. Suggestions are presented on how to extend this research, specifically on methods to measure the multiphoton cross section of photomechanical compounds, such as molecular nanomachines, more accurately. As well as methods for measuring apoptosis caused by nanomechanical damage, and importantly, how to distinguish this from necrotic processes.

Acknowledgements

I would like to take the time to express the deepest possible gratitude to the following people for making this work possible and for keeping me sane throughout the process:

First and foremost, I cannot find a way to put into words the levels of appreciation for my supervisor Prof. Robert Pal. Thank you for everything, both professionally and personally. For not only the unwavering support and guidance, ridiculously quick feedback on thesis chapters, and always having time for the many questions and discussions required to keep this project on track; but also, for allowing me the space to investigate my own ideas and encouraging me to take ownership and shape this work independently. I would not be the scientist I am today without your support. Thank you as well for all the personal advice given over the years, for helping me furnish my flat when first moving to up to Durham, and most importantly for the supply of food from your hunting and fishing trips.

Additional thanks to Prof. James Tour and his lab at Rice University for their synthetic work, collaboration, and support throughout the project.

Thanks as well to all members of the Pal group, both past and present. Thank you to Dr Lewis MacKenzie for all the assistance when first starting my project, and for being the person through whom I found the advert for this position. Thank you to Dominic for being a constant friend in the office for the last four years and for providing much needed laughter to the workday. Thanks to Dr Patrycja Brooke for helping me understand how little I really know about photophysics, and to Arti for giving me someone to blame when I eat the last of the office snacks. Thank you to past members of the Pal group Kathleen and Davide, and to newer members of the office Paolo and

Connor, for keeping CG78/162 a great place to come into work. Thanks go as well to all master's students who worked on the nanomachine project with me over the years, especially Alex whose collaboration was a massive help.

Special thanks to Brian from Lecia, not only for making the drive down from Scotland countless times to fix the various optics that I broke over the years, but also for also being available over email when attempting to troubleshoot the *many* multiphoton laser problems.

Finally, and most importantly, I must thank my family for supporting me not just throughout this process but for all the years prior. Firstly, to my partner Jenny who without a second thought moved to across the country with me when I started this position, and who has provided me with endless belief, support, and love as we paused aspects of our lives to allow me to undertake this four-year long journey. I must of course thank my parents; to Mum and Andy who installed in me from a young age the skills I needed to succeed – resilience, commitment, and most importantly, a sense of humour. To Dad who I wish was still here to see me get this far and to whom I still want to talk to every day, and to Margaret, who both supported me from my very first steps at university - driving a van halfway up the country (and blowing up the engine in the process). Without all of them, and their support and encouragement throughout every stage of life, I would not have made it this far. Lastly, thank you to Lisa and Arther, whose unyielding support for Jenny and I has been invaluable. Words cannot express my gratitude to all of you.

Abbreviations

2PA	Two photon activation
2PCS	Two photon cross section
2PE	Two photon excitation
ADP	Adenosine diphosphate
AIF	Apoptosis inducing factor
AMM	Artificial molecular machine
APD	Avalanche photo-diode
ATP	Adenosine triphosphate
AV	Annexin V Alexa Fluor 488
BBB	Blood brain barrier
BET	Back energy transfer
CCD	Charge-coupled device
CD	Circular dichroism
Cp	Cyclopentadienyl
CPL	Circularly polarised luminescence
DAPI	4’,6-diamidino-2-phenylindole
DMEM	Dulbecco’s modified eagle medium
DMSO	Dimethylsulfoxide
DP	2,2’-dipyridyl
DPBF	1,3-Diphenylisobenzofuran
EOM	Electro-optic modulator
ET	Energy transfer

FBS	Foetal bovine serum
Fl	Fluorescein
FWHM	Full width half maximum
GFP	Green fluorescence protein
GUI	Graphical user interface
HOMO	Highest occupied molecular orbital
HTI	Hemithioindigo
ICW	Intercellular calcium waves
IHME	Institute for Health Metrics and Evaluation
LED	Light emitting diode
LSCM	Laser scanning confocal microscopy
LUMO	Lowest unoccupied molecular orbital
MM	Molecular motor
MP	Multiphoton
MPE	Multiphoton excitation
MPLSCM	Multiphoton laser scanning confocal microscopy
NA	Numerical aperture
NAC	N-acetyl-cysteine
NAD(P)H	Nicotinamide adenine (pyridine) dinucleotide
ND	Neutral density
NIR	Near infrared
NMM	Natural molecular machine
PBS	Phosphate buffered saline
PCD	Programmed cell death

PDT	Photodynamic therapy
PdTPP	Palladium tetraphenylporphyrin
PEG	Polyethylene glycol
Pi	Phosphate
PI	Propidium iodide
PMT	Photon multiplier tube
PS	Photosensitiser
PSF	Point spread function
PTT	Photothermal therapy
Rh	Rhodamine B
ROS	Reactive oxygen species
TD-DFT	Time-dependent density-functional theory
TPP+	Triphenylphosphonium
TTN	Time to necrosis onset

Table of contents

List of figures

List of tables

Chapter 1: Introduction and relevant literature

Summary: *This chapter aims to provide a general introduction to the main scientific concepts underpinning this project, as well as the general rationale for the importance of the work. It will cover the history of the field of molecular machinery and provide a comprehensive overview of the basics of optical microscopy and the fluorescent imaging of biological samples. The photophysics underpinning multiphoton excitation will also be described to present a stable foundation for the work presented herein. Followed by a brief overview of the project specification and objectives.*

1.1 Project context and outlook

The World Health Organization (WHO) Global Cancer Observatory's most recent data, compiled in 2020, determined that there were over nineteen million new reported cases of cancer worldwide within one calendar year.[1] Leading to an estimated 9,958,133 deaths *per annum*; making cancer the second leading cause of death globally as estimated by the Institute for Heath Metrics and Evaluation's (IHME) Global Burden of Disease and Global Terrorism Database.[2] A more comprehensive breakdown of this data is shown in **Figure 1.1**.

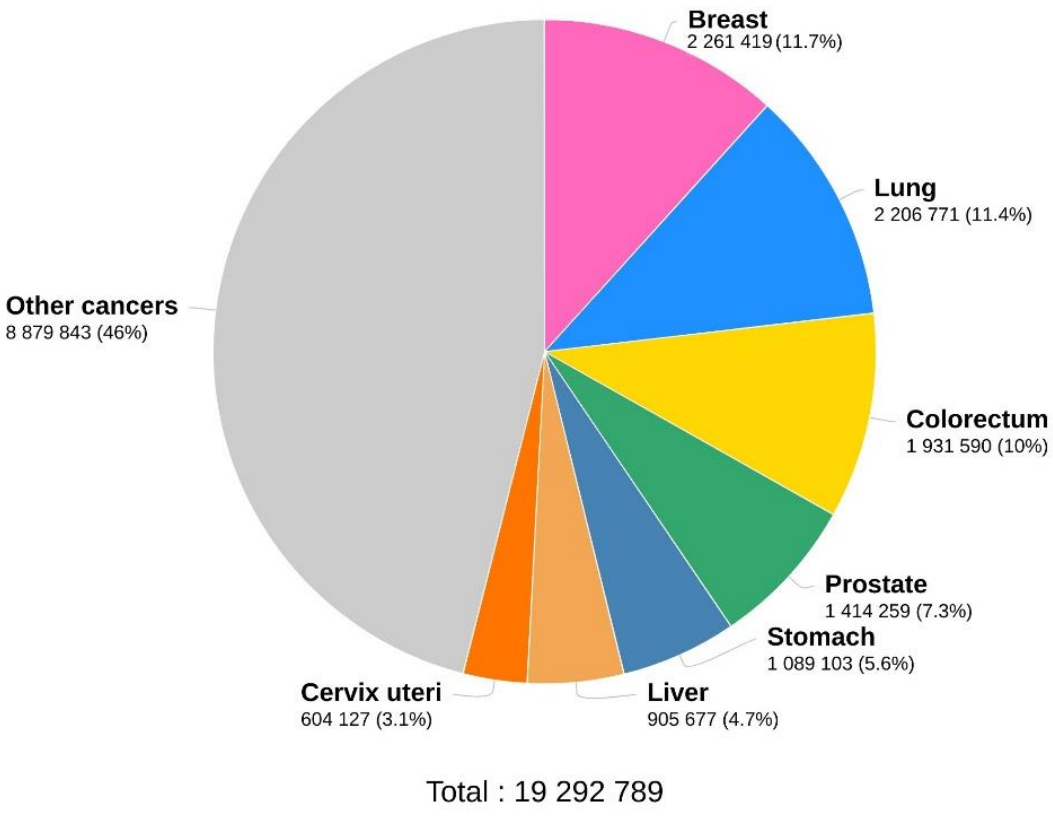

Figure 1.1 Global prevalence of newly reported cases of cancer worldwide between 2019-2020; compiled by the WHO.[1]

It is increasingly obvious that there is a growing global need for a greater number of more effective cancer treatments. Current commonly available, and widely used, therapeutic agents such as the chemotherapy agent cisplatin, and other platinum based intercalators, are the cornerstone for a wide number of combination therapies used to treat a large variety of cancers.[3] While broadly effective at the treatment of cancerous cells, these methods are far from ideal due to a large number of damaging side effects; including both neuro and renal toxicity.[4] The suppression of the production of white blood cells however can pose more complex problems due to a greatly reduced immune system in patients undergoing these treatments; causing a wide range of less predictable issues such as unknown infections and susceptibility to secondary disease.[5] The adverse effects of chemotherapy predominantly arise from the lack of cell specificity

found in the majority of these modern day treatment methods, leading to an inability to treat malignancies without simultaneously targeting healthy tissue.[6]

Owing to the clear need for treatment methods with reduced side effects to non-cancerous tissue there has been an increased global focus on the development of more effective targeting, imaging, cargo delivery, and destruction of specifically selected cell types. This is being realised in emergence of recent work on a number of strategies utilising physical energy modalities for cell specific treatment and targeted drug delivery methods.[7] Various examples within recent literature show the use of this rationale, utilising electric fields (electroporation)[8], magnetic fields (magnetoporation)[9], ultrasound (sonoporation)[10], temperature (thermoporation)[11], and light (optoporation)[12] to aid in the targeted penetration of cellular membranes. This work helps pave the way towards true personalised therapeutics, allowing progression beyond the traditional chemical delivery systems and allowing precise control over the targeting of cells, down to single cell precision.[13]

Photodynamic therapy (PDT) is one of the emerging fields benefiting from this technology, representing one of the first therapeutic uses of a physical energy system being utilised for cell targeting, having been used for cancer treatment since the 1970s.[14] By exploiting the non-invasive and relatively deep penetration of light when compared with other previously discussed methods of poration, alongside a photosensitiser (PS), single cell penetration *via* reactive oxygen species (ROS) can be achieved and utilised in various cancer therapies.[15] In brief, the excitation of a ground state electron (HOMO) from the PS molecule - such as the clinically approved porphyrin based Photofrin®[16] (shown in **Figure 1.2**) – to a short lived excited state (LUMO) allows for reversal of spin (intersystem crossing) to its triplet state.

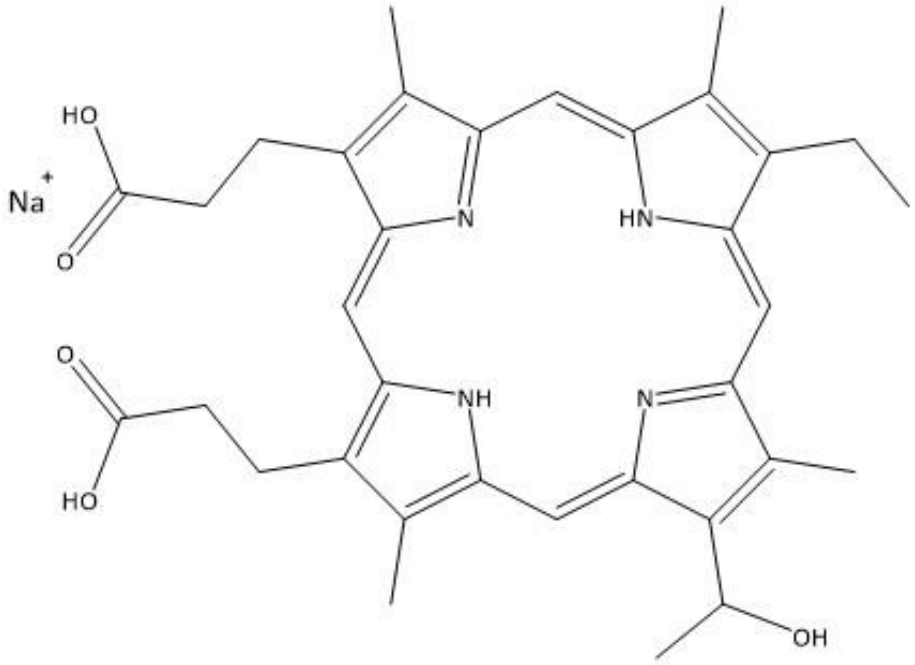

Figure 1.2 Chemical structure of the commonly used photosensitiser Photofrin®.

In this long-lived state several previously impossible photochemical reactions can occur. These reactions can generally be split into two different pathways; type I mechanisms involve an electron transfer reaction from the PS to O_2 resulting in $O_2^{\bullet -}$ that can undergo further transformation to a variety of ROS (H_2O_2, $^{\bullet}OH$) *via* the Fenton reaction.[17] While type II consist of energy transfer directly to molecular oxygen. These processes are summarised in the Jablonski diagram in **Figure 1.3**.

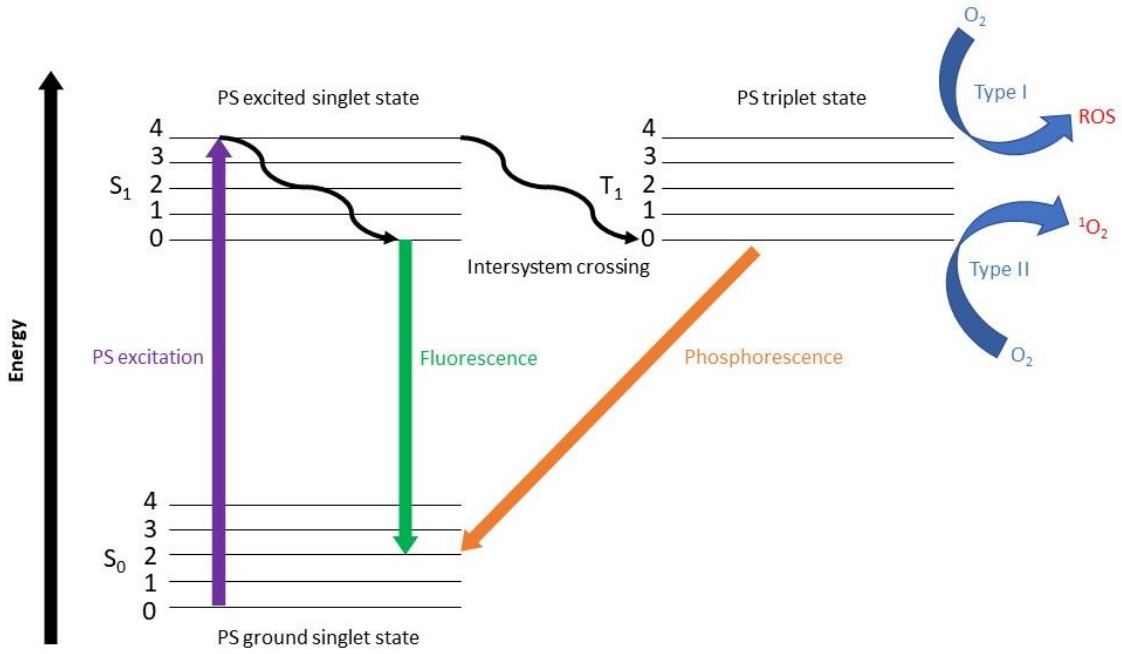

Figure 1.3 Schematic Jablonski diagram depicting the principles of PDT

While these methods offer clear benefits over traditional chemotherapy due to a significantly higher level of presicion, they cannot be said to be truly cell specfifc due to the uncontroled nature of the ROS cascade reaction as well as the difficulty in targeting the localisation of the PS molecule. In addition to this, high PS concentrations as well as the high intensity of light required can lead to inflammatory responses and exacerbation of pain.18 Due to this several other methods have been under investiogation for ways to utilise non-invasive physical stimuli to both image cells and selectively induce either apoptosis or nercrosis.19–21 Of perticular importance to this work is a recent focus on using molecular machines, a preveously underutilised area of chemistry22, as a novel approach towards targeted cancer theraputics.

1.2 Molecular machinery

1.2.1 History and overview

Molecular machines are most commonly defined as the assembly of a discrete number of molecular components specifically designed in such as a way as to perform a range of mechanical-like movements upon exposure to an appropriate external stimulus.[23] It is important to note however that while certain chemical moieties are capable of undergoing specific movements, such as the *cis/trans* isomerisation of various double bonds, it is commonly accepted that the term molecular machine will only apply to species where the induced movement is of a sufficient magnitude – *i.e* capable of overcoming Brownian motion.

The overarching idea of machinery at the molecular level is a relatively aged concept; many systems found within nature, and indeed the human body, can be viewed through this lens as ensembles of individual molecular components performing mechanical work under various external stimuli. The earliest example of these, myosin II, is a dimeric protein containing two motor domains which move along an actin filament from the negative to positive ends responsible for muscle contraction which was first isolated as early as 1864[24]. However, it was not considered a molecular machine until the crystal structure (shown in **Figure 1.4**) of the motor domain was solved in 1993.[25]

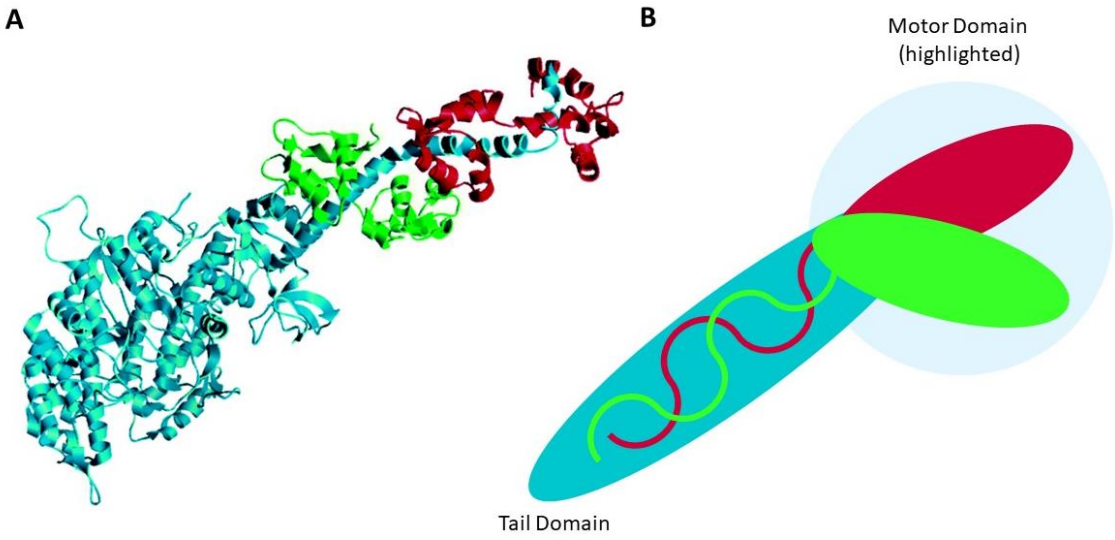

Figure 1.4 A - Crystal struture of Myosin II subfragment S1 **B** - Simplified schematic struture. Blue segments representing a heavy chain, green and red segments representing light chains. Adapted from Kinbara *et al*.[26]

It is now widely accepted that conventional myosin's ability to cause muscle contraction is generated by a so-called "swinging lever arm" mechanism *via* a four-step catalytic ATPase cycle. Whereby myosin II is initially bound to the actin filament before the binding of adenosine triphosphate (ATP) to the motor domain lowers its affinity towards the actin filament. This also triggers a conformational change, resulting in the pivotal motion of the motor. ATP-myosin II is then hydrolysed to produce the adenosine diphosphate (ADP) and phosphate (Pi) conjugate ADP•Pi-myosin II. The subsequential release of ADP and Pi results in another conformation change of almost 90^{o} back to the original structure, the motion of which leads to the contraction of the muscle.[26] This is summarised schematically in **Figure 1.5**.

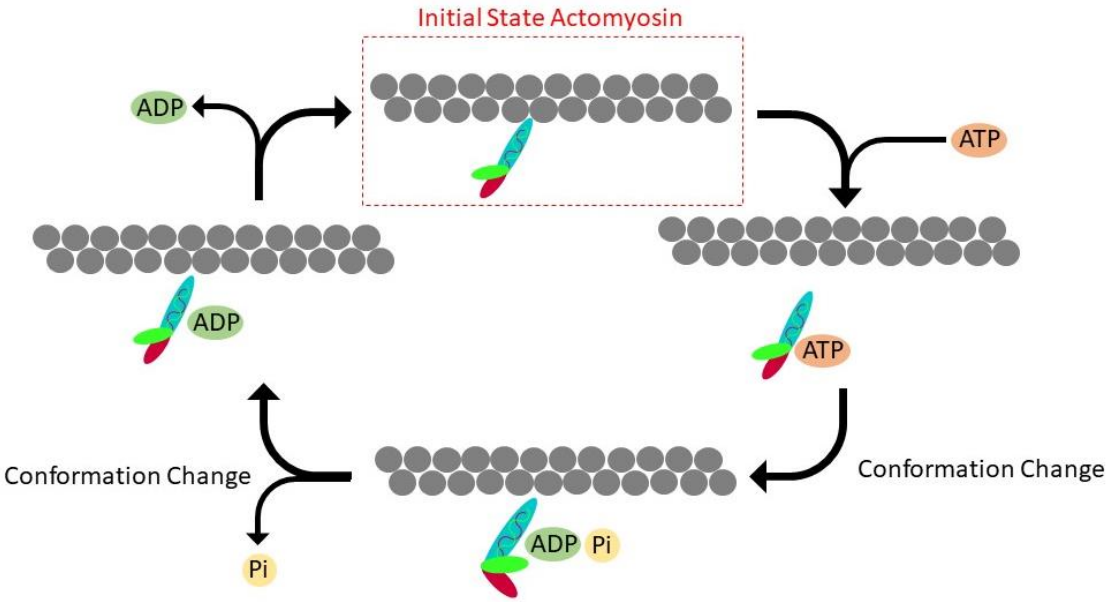

Figure 1.5 Schematic representation of the ATPase catalised myosin II cycle responcible for muscle contraction. Adapted from Kinara *et al*.[26]

The concept of synthesising simplified interpretations of these constructions to create artificial molecular machines is more recent; first proposed by Richard Feynman in his historic 1959 address to the American Physical Society "There is Plenty of Room at the Bottom".[27] This led to what is now considered the first example of a synthetic molecular-level machine in 1984, based upon the photoisomerization of azobenzene.[28] By 1990 this technology had been further utilised to create a water soluble, photo responsive macrocycle based upon two azobenzene units connected *via* two ammonium units with the ability to change its cavity shape upon the previously studied *cis/trans* isomerisation (**Figure 1.6**).[29]

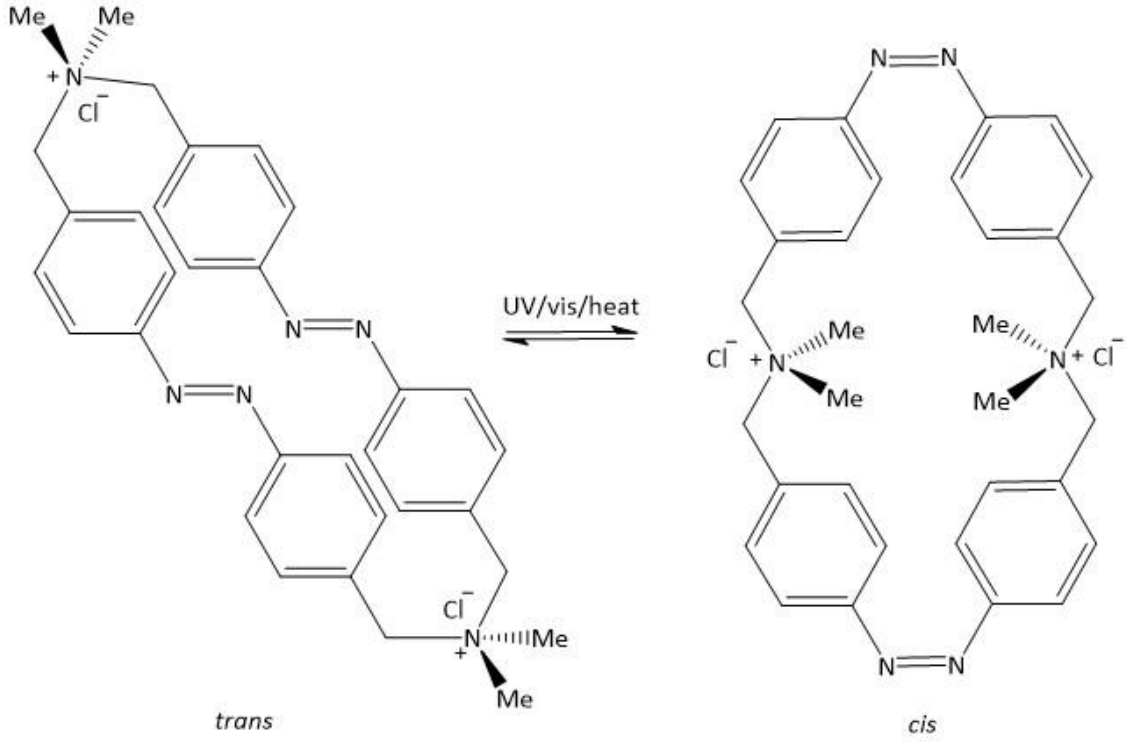

Figure 1.6 Schematic pore opening via *cis/trans* isomerisation of a azobenzene based macrocycle.

The rapid development in the field after the 1980s is often attributed to a small number of major breakthroughs and developments in both chemistry and physics. Firstly, the developments in probe microscopies following the 1986 Nobel prize in physics to Binnig and Rohrer[30]; the increase of research in supramolecular chemistry after the 1987 Nobel prize in chemistry was awarded to Pedersen, Cram, and Lehn[31]; the continued work in obtaining the working mechanisms for several important natural molecular machines such as those involved in ATP synthesis, which led the 1988 Nobel prize in chemistry to Boyer, Skou, and Walker[32]; and in more general terms, a shift away from the top-down Feynman method of thinking about molecular devises that requires solid-state physicists and electronic engineers to fabricate progressively smaller components, to a bottom-up, chemical synthesis based, approach. Resulting in new methodologies starting from single molecules with distinct shapes and unique properties.

These developments culminated in the 2016 Nobel prize for chemistry being awarded for "the design and synthesis of molecular machines" to Sauvage, Stoddart, and Feringa.[33] Recognising their work on chemically interlocked systems as a platform for future molecular machines (Sauvage and Stoddart)[34,35], and the development of synthetic molecular motors (MM) based on naturally occurring photo-switches (Feringa)[36].

1.2.2 Natural molecular machines

Before considering the development of artificial molecular machines it is important to discuss their natural inspirations as the first class of molecular construction to be widely considered as nano-scale machinery. Biological molecular machines, which are usually complex constructions of numerous protein structures (but can be simpler single molecule switches), convert energy from one form, or location, to another within biological systems.[37] While the previously discussed myosin II was the first system to be isolated, it wasn't until much later that its mechanism of action, and thus its classification as a molecular machine, was deduced. The development of single molecule observation techniques, particularly fluorescence spectroscopy and microscopy[38], was instrumental in allowing for the elucidation of these systems.

One of the most widely understood examples of biological rotary motor construction is F_1F_0-ATPase, an enzyme consisting of two subdomains (shown in **Figure 1.7**) responsible for the manufacture of ATP utilising the free energy stored within a cells transmembrane ion gradient.[39,40]

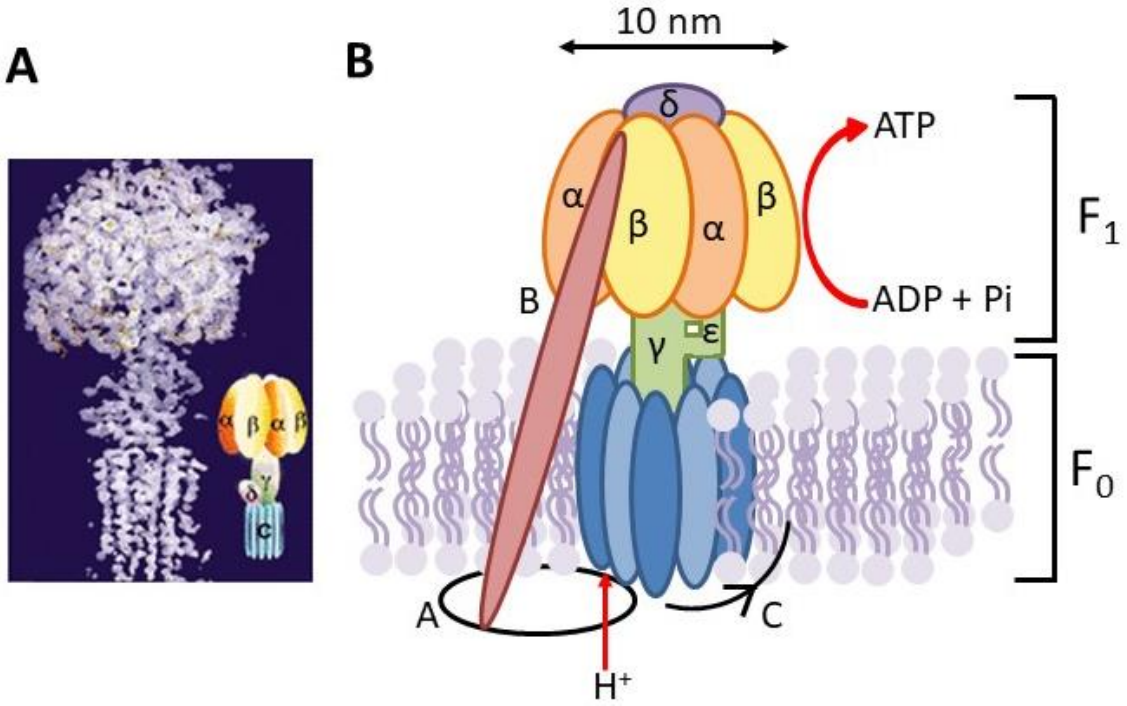

Figure 1.7 *A* - Electron density map of the yeast mitochondrial F_1-C_{10} subcomplex with labbeled subunits in the insert.[41] **B** - Schemetic representation for the rotary model of how F_1F_0 ATP synthase catalyses the synthesis of ATP. Adapted from Cross *at al*.[40] The catalytic region is represented by subunits α-ε, with the proton channel sitting between subsections A and C. As the protons flow through the channel torque is created between these subsections, which is then transmittied to subdomain F1 via the γ shaft; where it is utilised to release ATP from the catalytic site.

The free energy difference produced is sufficient to allow for the synthesis of three ATP units per twelve protons crossing the channel. The importance of understanding molecular machines of this nature, as it relates to the advancement of engineering and medicine, became clear when it was reported that F_0F_1-ATPase is able to convert chemical energy into mechanical 120^o rotations with near 100% efficentcy.[42]

While these constructions are obviously far too complex (although there has been recent work in utilising the biological synthesis of protein tubes and rings to work

towards the assembly of simple man-made natural molecular machines)[43] to be effectively recreated in the chemistry lab, they offer both inspiration and proof-of-concept for the ideas behind using discrete chemical moieties, working together, to produce predictable mechanical effects at the nanoscale. The foundation of which would be pioneered by supramolecular chemists working towards the creation of organised, interlinked, arrangements of molecules.[44] That would later be employed in the creation of molecular-scale devices.

1.2.3 Supramolecular chemistry

Supramolecular chemistry is an important field in the development of molecular machinery, where intermolecular noncovalent bonding is used to assist in the templating of reactions.[45] The foundations of molecular machinery came from the use of supramolecular synthesis for the creation of rotaxanes[46], and supramolecular assistance to molecular synthesis in the development of catenanes.[47] Both spearheaded by the previously discussed Nobel laureates Sauvage and Stoddart.

[2]Rotaxanes are molecules consisting of a macrocyclic component encircled around a linear rod-like section, sterically entrapped by the presence of two bulky stopper-like end groups; forming a dumbbell like structure. This results in a system comprised of two distinct moieties, unable to dissociate from each other despite the lack of covalent bonds locking them together chemically. Providing the possibility of inducing predictable nanoscale motion without destruction of the complex; the first step towards creating an artificial molecular machine. A representative example of this, the first reported example of a “stable complex of a macrocycle and a threaded chain” is shown in **Figure 1.8**.[48]

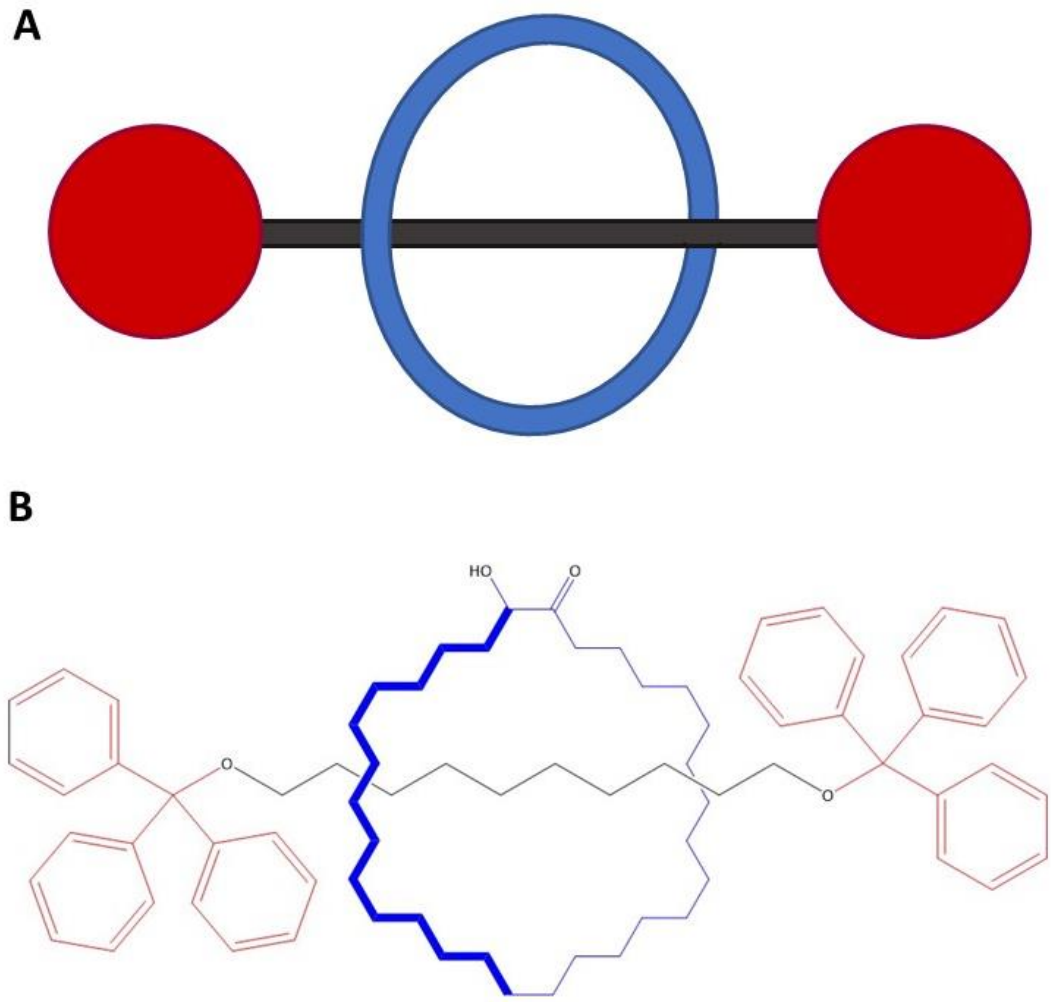

Figure 1.8 A - Schematic representation of a simple [2]rotaxane, **B** – Chemical structure of the first reported rotaxane.[48] Bulky stopper groups illustrated in red, macrocycle illustrated in blue.

This technology was further accelerated towards the synthesis of molecular machines by the addition of two or more coordination sites along the "dumbbell" component, resulting in a degenerate co-conformational equilibrium state where the macrocyclic component can resonate between multiple recognition sites. Complexes with this behaviour are known as molecular shuttles. The first [2]rotaxane system with degenerate molecular shuttle behaviour, as reported by Stoddart[49], is shown in **Figure 1.9**.

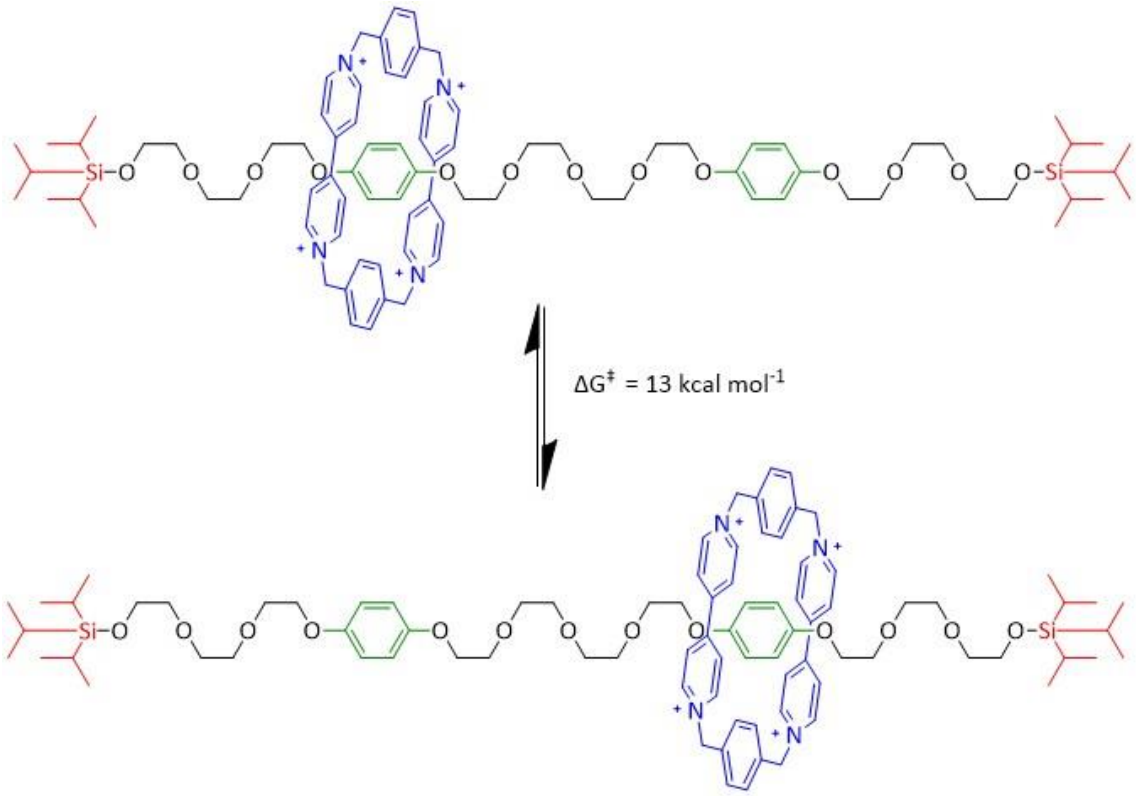

Figure 1.9 Structure and site resonance of the first synthesised degenerate molecular shuttle. The bipyridinium-based cyclophane macrocycle resonates between each 1,4-dioxybenzene site at a rate of about 2000 s^{-1} at ambient temperature [49] Again, bulky stopper groups are illustrated in red and the macrocycle is illustrated in blue, while the coordination sites have been coloured green.

Re-evaluating the definition of a molecular machine - a discrete number of molecular components specifically designed in such as a way as to perform a range of mechanical-like movements upon exposure to an appropriate external stimulus – it is clear these molecular shuttles only meet half the criteria. Mechanical movement had been achieved *via* the macrocycle's oscillation, but a non-degenerative process must be employed to allow for controlled switching between the two coordination sites. The macrocycle must initially bind preferentially at "coordination site A" until a stimulus is applied to switch

off the stronger of the two sites, resulting in an induction of the shuttle like motion as the macrocycle moves to the second weaker binding "coordination site B".

Initially known as smart rotaxanes[50], the first systems to enable controlled switching between recognition sites relied on the exploitation of solvent induced effects.[51] In this example (shown in **Figure 1.10**) the recognition site of the "dumbbell" contains nitrogen atoms which show strong hydrogen bonds to the oxygen present in the crown ether macrocycle. This results in a preferential localisation of the ring about this functional group. Upon switching the solvent system dimethylsulfoxide (DMSO) is able to displace the hydrogen bonding between these atoms, therefore the macrocycle is no longer bound to the NH groups and is instead forced away down the polymer backbone. While not strictly switching between two specific coordination sites, this is the first incident of switchable shuttle behaviour.

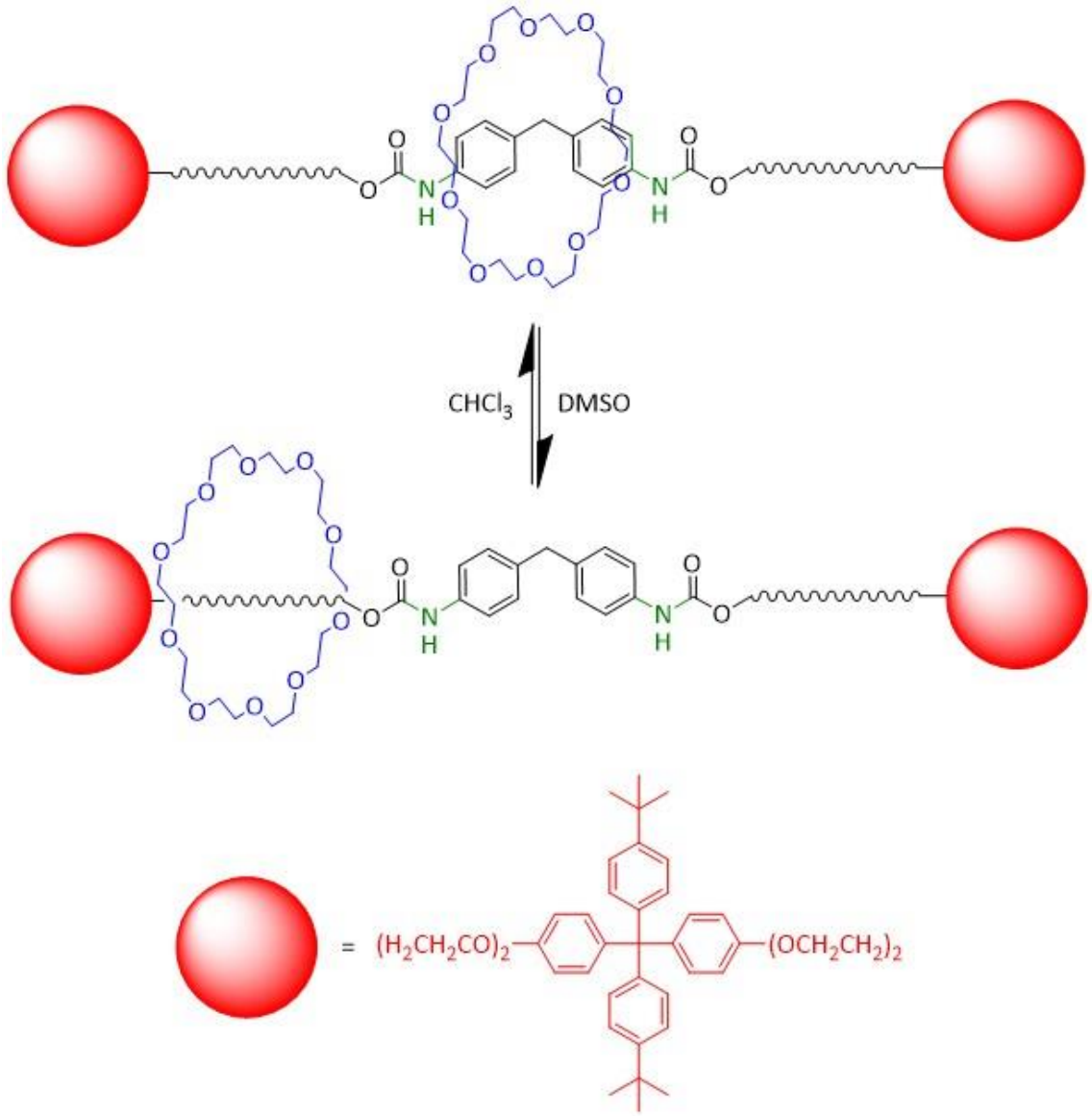

Figure 1.10 Struture of the first class of polymeric molecular shuttles able to exhibit solvent induced localisation of the macrocycle 30C10.[51] Again, bulky stopper groups are illustrated in red and the macrocycle is illustrated in blue, while the coordination sites have been coloured green.

[2]Catenanes are another example of mechanically interlocked complexes created *via* template-directed synthesis. The basic principles of supramolecular chemistry, previously covered in the context of [2]rotaxanes, govern their behaviour in much the same manner. While [2]rotaxanes consist of one macrocyclic component threaded over a dumbbell, [2]catenanes are composed of two interlocked macrocycles. As previously

discussed, these constituents are not covalently bound together, but instead held together by mechanical intramolecular forces, preventing their dissociation. Wasserman's catenane, the earliest successful reported [2]catenane synthesis, is used as an example of this in **Figure 1.11**.[52,53] It is interesting to note that this complex was widely considered a "prophetic compound" – that is, a claimed molecule that was not successfully synthesised – due to the statistical synthesis used to form the interlocked rings in the original 1960 work.[52] However, it has recently been confirmed, *via* modern analytical techniques, that the original methodology indeed results in a [2]catenane formed of a 34-membered cyclic hydrocarbon mechanically linked with a 34-membered cyclic α-hydroxyketone.

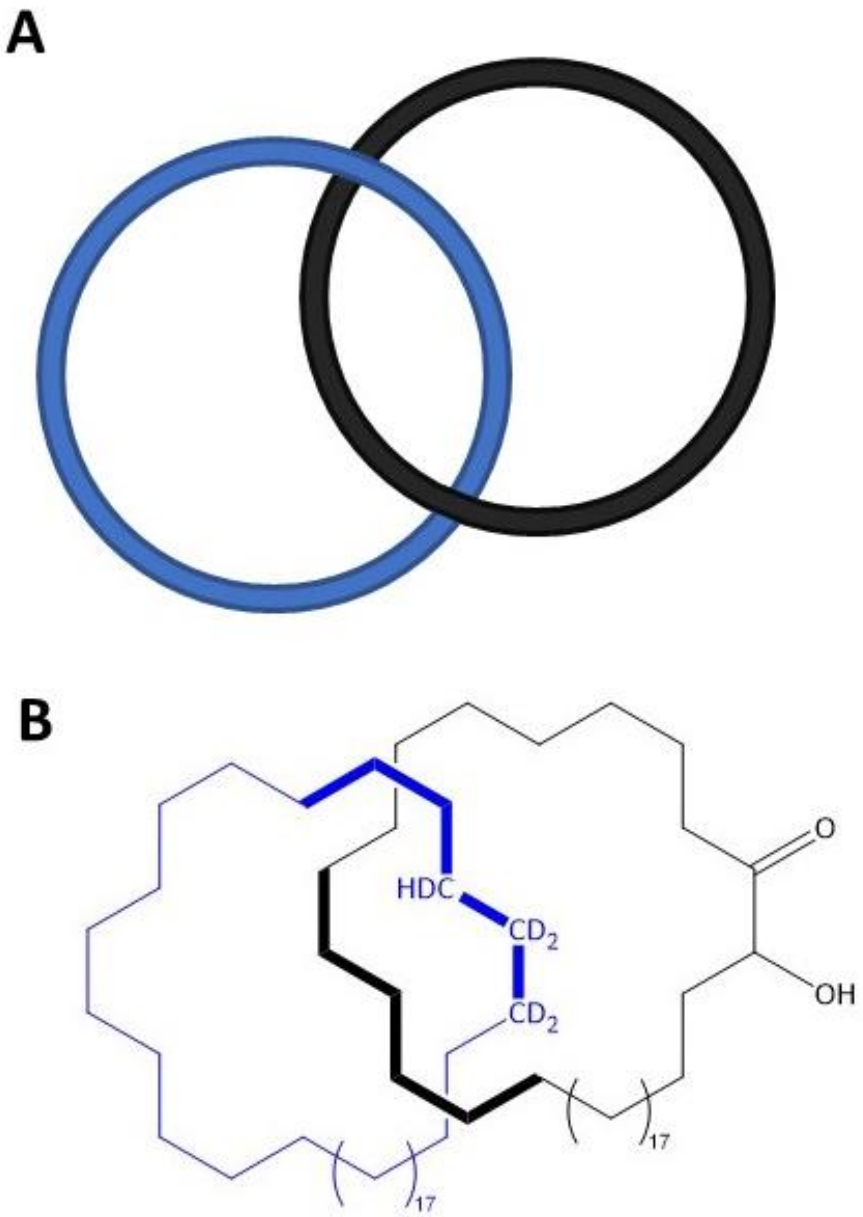

Figure 1.11 A - Schematic representation of a simple [2]catenane, **B** - Structure of Wasserman's catenane, the first recorded synthesis for this class of compound.

In a manner reminicent of the first functionalised molecular shuttles, catenanes that possess two or more identicle coordination sites within the two macrocycles – commonly refered to as “homocircuit” - undergo a rapid degenerate co-conformational change. The additional degrees of freedom present in these supramolecular systems, when compared with traditional covalent structures, allow for both the spinning of one ring about a fixed axis (“pirouetting”) and the repositioning of a ring between the

coordination sites of the other ("shuttling").[54] Resulting in two possible motions for conformational change; i) the pirouetting of ring one, and the shuttling of ring two; ii) the shuttling of ring one, and the pirouetting of ring two . For degenerate homocircuit catenanes both processes are identical. This is shown pictographically in **Figure 1.12**. As with the first prototype molecular shuttles, this represents the initial step towards the realisation of fully synthetic molecular machines.

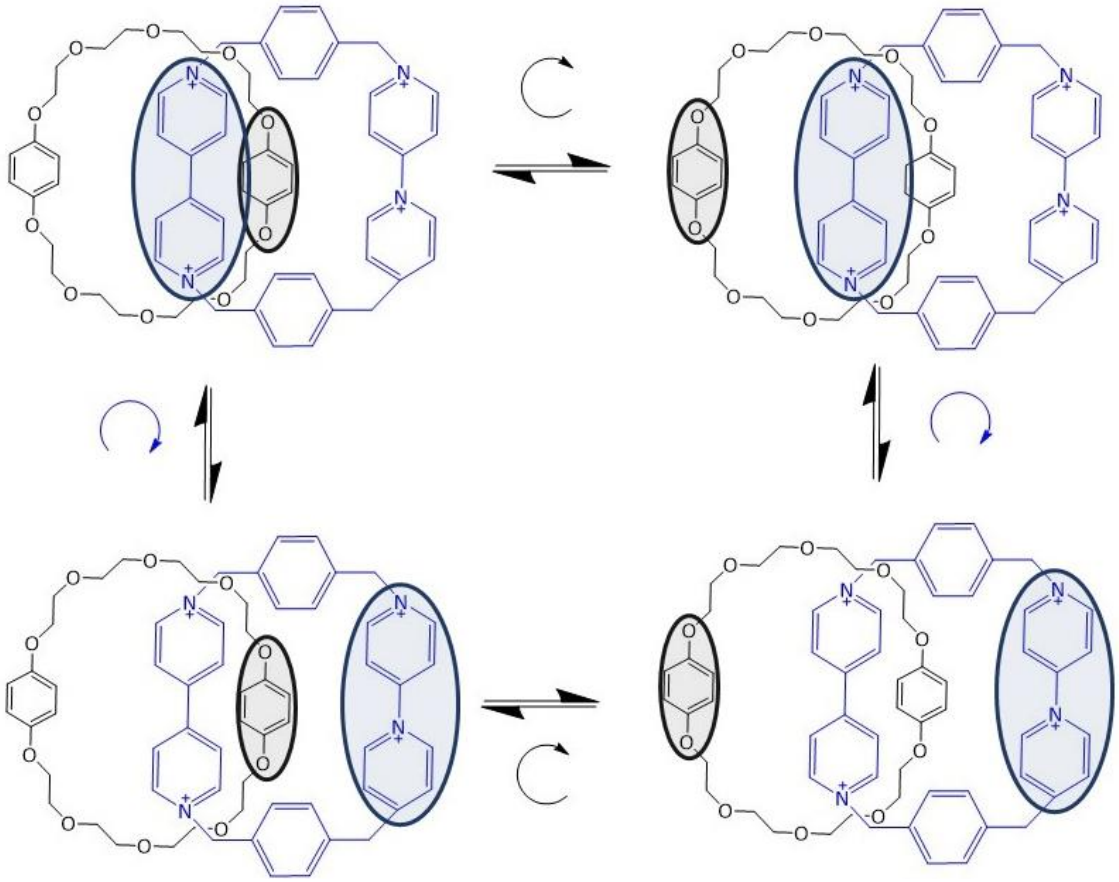

Figure 1.12 Pictorial representation of the dynamic processes involved when the macrocycles of a homocircuit catenane circumrotate through each other.[47]

The development of catenanes formed of "heterocircuit", or "asymmetrical", macrocyclic components led to the possibility of controlled switching between non-degenerate conformations. These co-conformation pairs are stabilised by the presence of noncovalent binding interactions. In solution the equilibrium between these

conformations is governed by the relative magnitudes of the intramolecular bonds locking the macrocycles. By understanding the nature of these binding interactions and switching the recognition sites on or off the relative populations of the two species can be controlled. Mirroring the development of rotaxane technology, the first catenanes designed with this ability were controlled by solvent induced effects.[55] A representative example of this is illustrated in **Figure 1.13**.

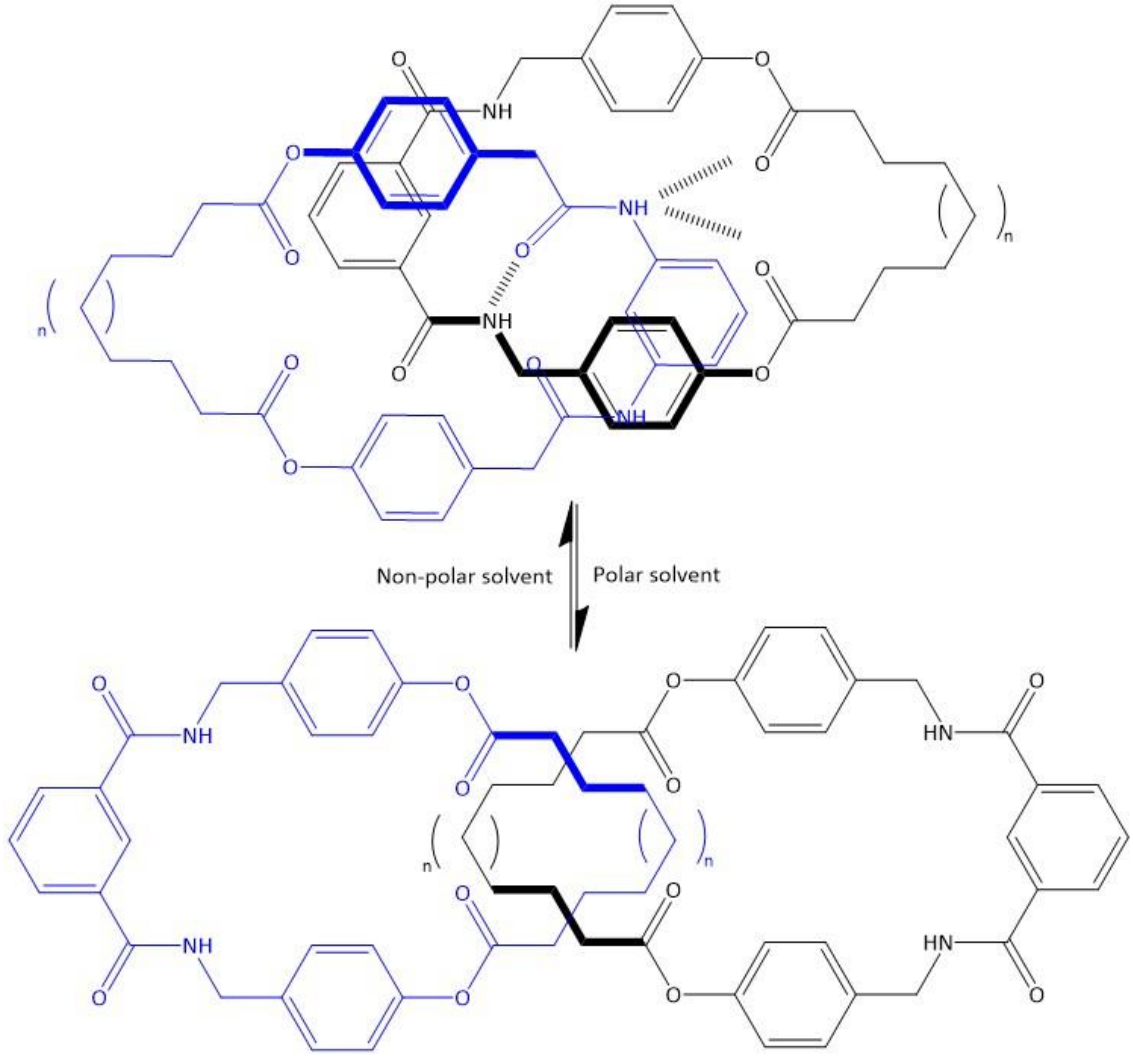

Figure 1.13 Structure of one of the first reported cases of controllable conformation change in a [2]catanene system, with hydrogen bonding represented by dashed lines.

In this instance the polarity of the solvent can be utilised to manipulate the lowest energy state of the interlocked system. When in polar solvents the amphiphilic moieties

of the interlocked units align themselves at the surface of the supramolecular structure where they can form hydrogen bonds with the solvent molecules, whilst the lipophilic carbon chains are oriented in the centre of the system - limiting the number of interactions with the solvent system. Whist in a polar environment this effect is reversed and the catenane inverts, forming internal hydrogen bonds as shown in **Figure 1.13**.[55]

1.2.4 Artificial molecular machines

The developments in supramolecular chemistry clearly paved the way for the first generation of artificial molecular machines. However, it should be noted that not all molecular machines conceived since are based on a supramolecular design philosophy. While hard to classify any area of chemical synthesis it is useful in this discussion to attempt to organise synthetic molecular machines into two overarching families; those where the component molecules undergo topological changes within interlocked systems (*i.e.* those based upon rotaxane and catenane chemistry); and those where the motion involved is produced *via* rotation or other controlled movement about atoms in conventional (non-interlocked) molecules, usually from bond isomerisation. Further distinction may also be made by energy conversion (for example chemical to kinetic) or by comparing these nanoscale devices to their macro-level counterparts: switches, drills, shuttles, motors, *etc*.

Rotaxanes based molecular machines have recently found use within biotechnology as various fluorescence switches.[56] The ability to selectively switch between emission wavelengths, or switch fluorescence off completely, in response to specific stimuli is a desirable trait for molecular tracking and sensing and could find extensive use in medicinal imaging.[57] Spiropyran has been widely used in the construction of logic gates; when irradiated by ultraviolet (UV) light it will switch to a purple merocyanine form with

an absorption band at 568, and emission at 640 nm.[58] A light activated, rotaxane based, molecular machine that can switch the position of the macrocycle between two distinct stations – dipeptide and zwitterionic merocyanine – by utilising this photo-isomerisation of Spiropyran has recently been developed (shown in **Figure 1.14**).[59] The macrocycle preferentially resides on the dipeptide station in its spiropyran form, and will shift to the merocyanine site upon UV excitation. Resulting in a clear absorption output signal.

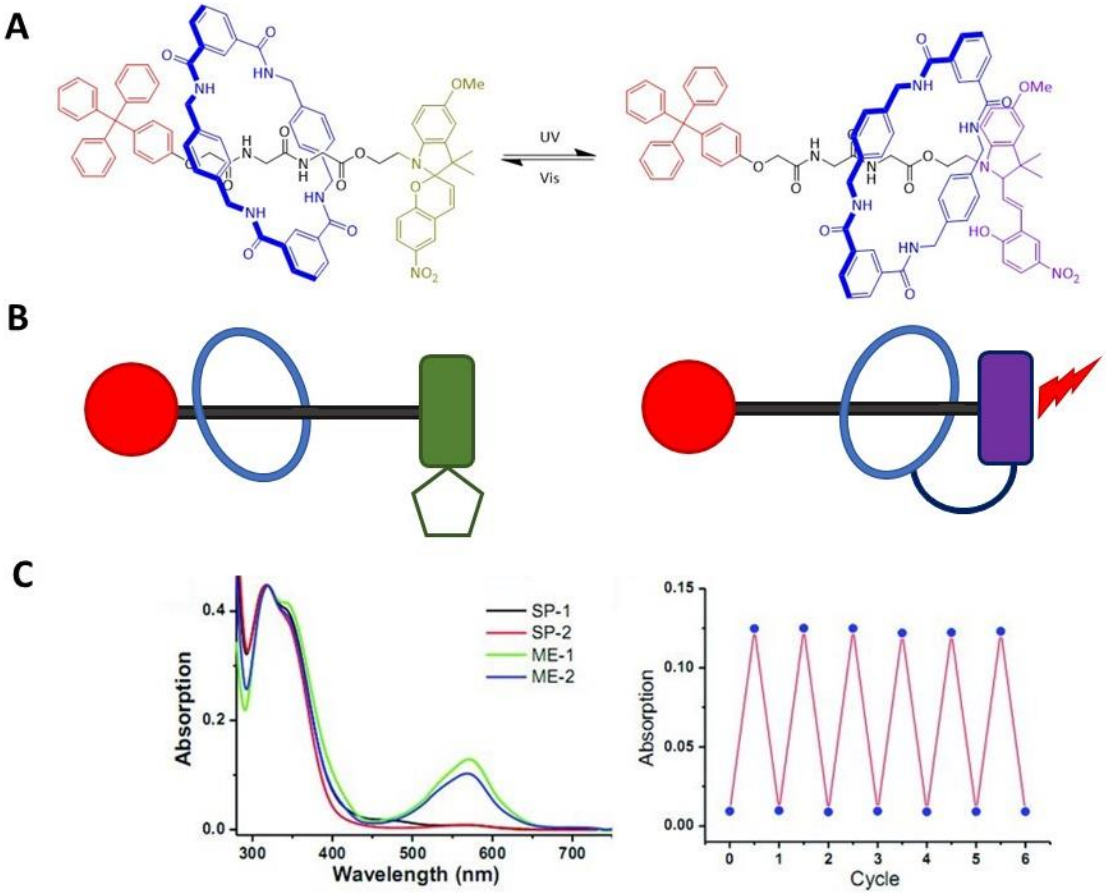

Figure 1.14 A - Molecular struture of a spiropyran/merocycanine based rotaxane molecular machine. **B** - Simplified schematic of molecular shuttle based "switch on" fluoresence. **C** - Absorption spectra of both rotaxane conformations showing "switch on" emission at 568 nm under UV excitation, and absorption spectrum showing the recycling ability of the machine. Adapted from Yang *et al*.[56]

The photo-isomerisation induced shuttle behaviour of the rotaxane shown in **Figure 1.15** shows one of the most dramatic examples of a supramolecular based molecular machine; the ability to utilise its induced nanoscale effects to generate macro-level motion.[60]

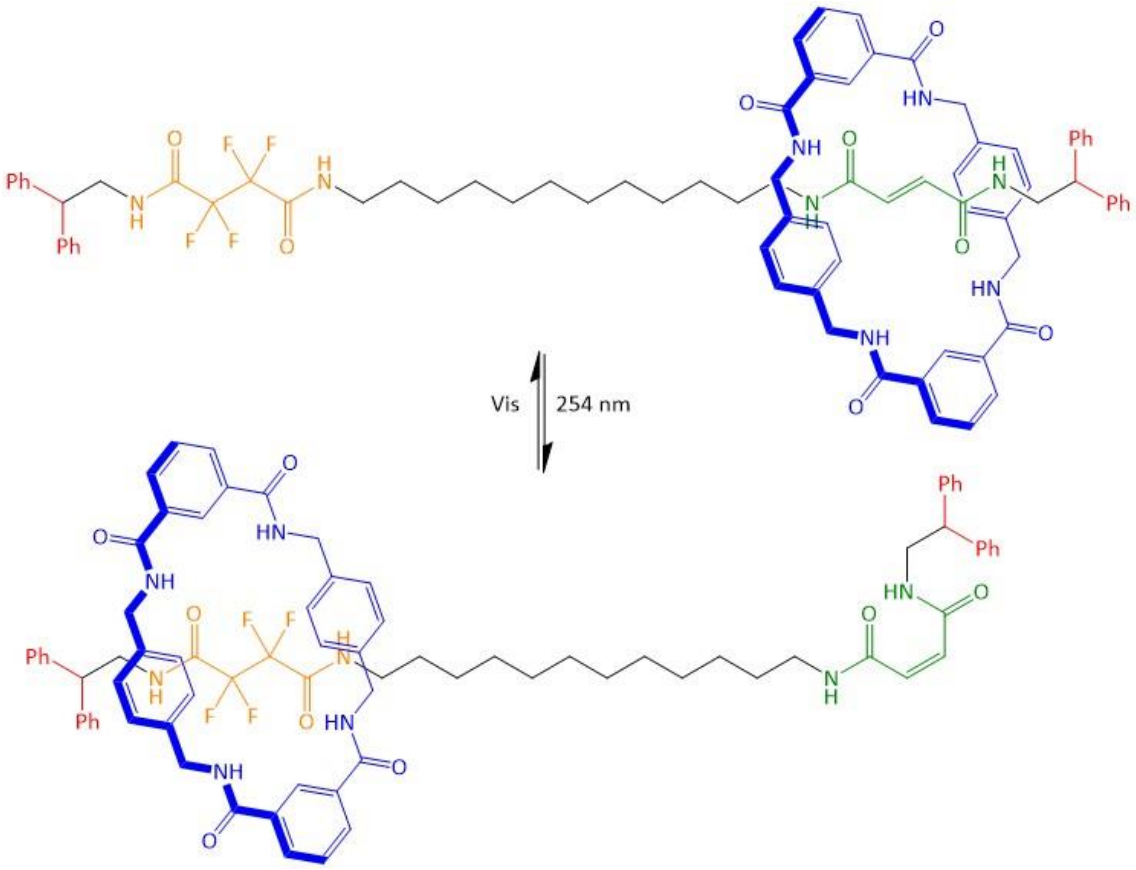

Figure 1.15 Schematic showing the photoisomerisation induced shuttle effect for this rotaxane

When grafted onto well-order self-assembled monolayers of 11-mercaptoundecanoic acid on Au(III) and physiosorbed onto a glass, or silica, surface this rotaxane based shuttle has been shown to demonstrate light-driven directional transport of diiodomethane droplets. In a two-step procedure, the rotaxane "dumbbell" is photoisomerised to *cis* and then asymmetrically irradiated at the rear of the droplet

(*cis*/*trans* isomerisation); selectively altering the layer beneath half the droplet, pushing it forward. Lateral photographs of this process are shown in **Figure 1.16**.

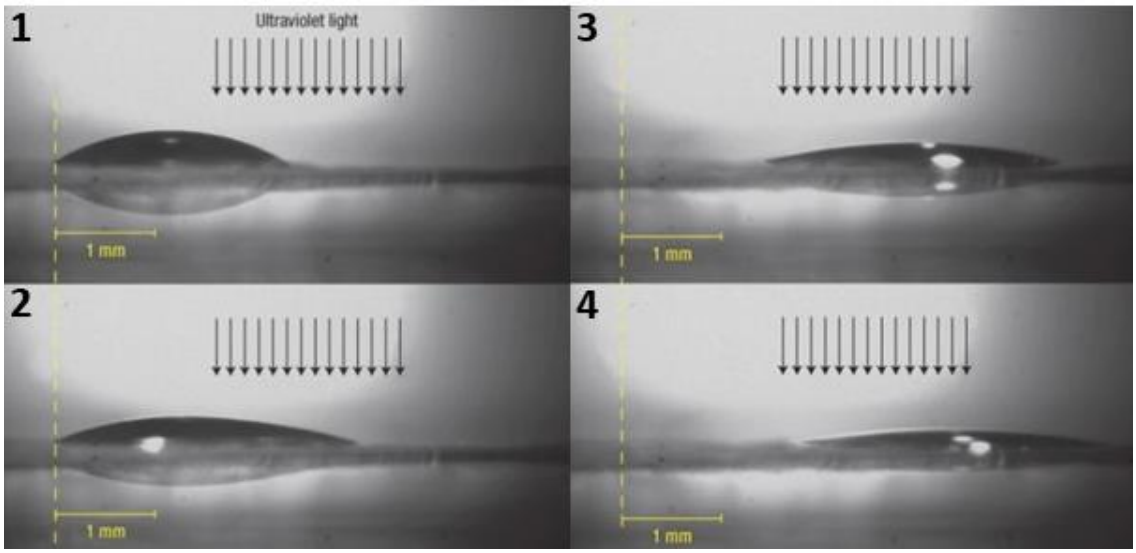

Figure 1.16 Lateral photographs showing the light driven directional transport of a diiodomethane dropplet. Images taken before irradiation, 215 s, 370 s, 580 s.

As previously indicated, several molecular machines based upon more traditional synthesis and not relying on supramolecular techniques – *i.e*., lacking any form of interlocked system – have been developed. Azobenzene can undergo a photoactivated *cis/trans* isomerisation, which has been exploited in a number of rudimentary molecular machines to produce an elongation/contraction motion.[61] When used as a photochromic strap between two cyclopentadienyl (Cp) rings of ferrocene a molecular pivot can be created, due to the ability of the two Fe^{2+} bound Cp rings to rotate freely about each other.[62] This basic concept has been extended to synthesis molecules with the capability to act as molecular scissors, tweezers, and pliers; working towards applications in nano-scale surgery.[63]

Figure 1.17 illustrates an example where the covalent interlocking of the pivotal ferrocene by azobenzene allows for the alteration of the intramolecular distance

between two attached phenol groups *via* exposure to specific wavelengths of light. Resulting in a controlled opening and closing mechanism akin to nanoscale tweezers.

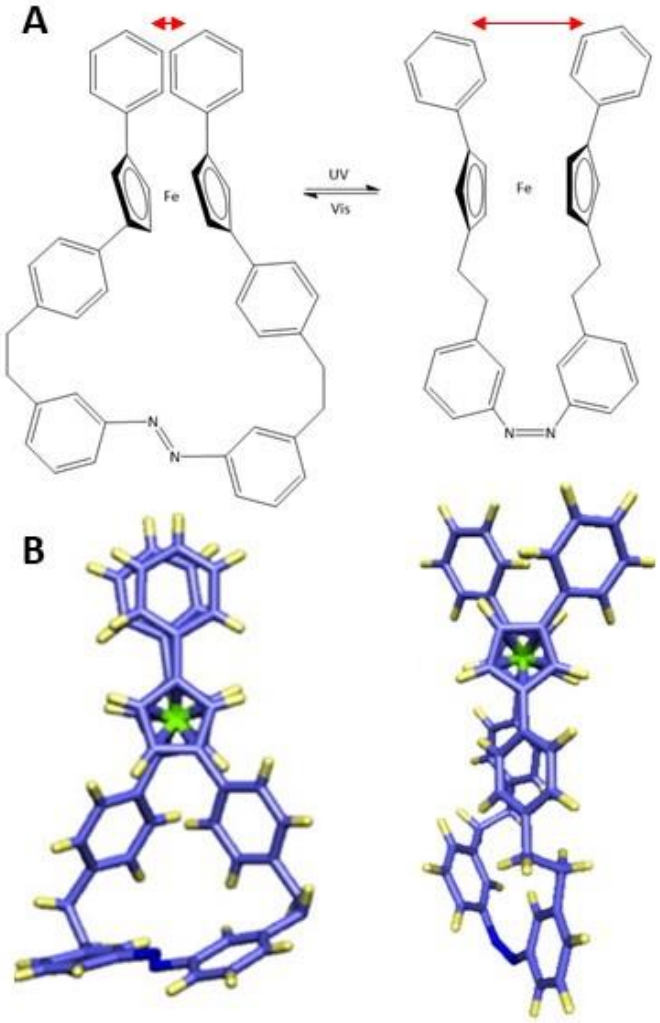

Figure 1.17 A - Schematic illustration of the *trans (left)/cis (right)* photoisomerisation of azobenzene and the Cp pivot. Tweezer distence highlighted in red. **B** - Crystal structure of both isomers adapted from Muraoka *et al*.[63]

This technology has been further utilsied by extending the system to incoroperate non-colvent systems with multiple molecules held together by various coordination bonds, thereby allowing longer range directional transmission of motion.[64]

1.2.5 Molecular motors

There has been considerable work dedicated to molecular motors as a subset of molecular machines. Before discussing the development and theory behind the specific motor-based molecules used within this work, it is important to give a brief overview of the rest of the field. In general, it is useful to separate molecular motor-based machines first based on if they involve interlocked or standard covalent systems, and second by stimulus, *i.e.* chemically fuelled, thermal, magnetic, sonic, or electromagnetic.

Sauvage was the first to demonstrate the possibility of gaining control, albeit non-directional, over the rotary motion of catenanes. Using both electrochemical and photochemical techniques it was possible to switch the relative orientation of the rings within the system, providing the first indication that these interlocked complexes could be utilised as motor-like machines.[65,66]

One of the early examples of sequential and unidirectional rotation being achieved in mechanically interlocked systems is a [3]catenane; two smaller macrocycles move between discrete binding sites upon one larger macrocycle (**Figure 1.18**), driven by either light, heat, or chemical stimuli. Unidirectionality is upheld by the two smaller rings mutually blocking the path of the other, preventing a change in direction caused by the natural Brownian motion of the components.[67]

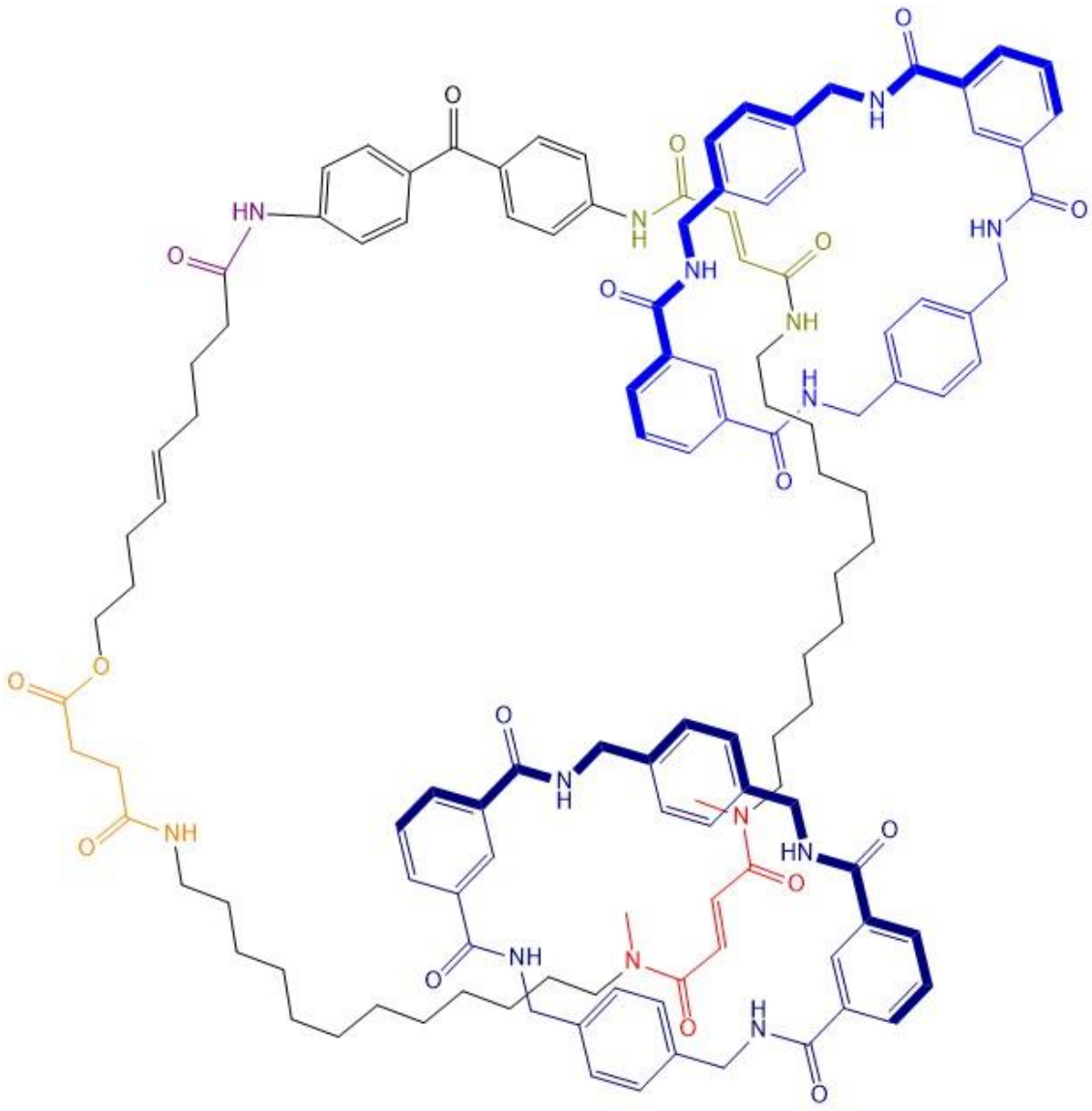

Figure 1.18 Resting state of a [3]catenane molecular motor with four binding sites; fumaramide (1, green), tertiary fumaramide (2, red), succinamide (3, orange), and amide (4, purple). Fumaramide site 1 is located next to a benzophenone unit, allowing for selective photosensitisation over tertiary fumaramide (red).

In the [3]catenane motor's initial state two benzylic amide macrocycles are bound to the two fumaramide units *via* H-bonds between the respective amide groups. Photo-induced isomerisation of site 1 weakens these hydrogen bonds and triggers a macrocycle relocation to the binding site with the next strongest interactions – *i.e.*, the next lowest energy state of the system – site 3. Due to the presence of the second

benzylic amide macrocycle this translocation can only occur in an anti-clockwise direction. An additional photoisomerisation of site 2 cause this ring to shift to site 4, again this can only occur anti-clockwise. Thermal re-isomerisation then occurs without further excitation, regenerating the initial state of the system but critically with the positions of the two benzylic amide rings switched. Allowing for the process to start again, producing the motor-like motion. A summary of this process is shown schematically in **Figure 1.19**.

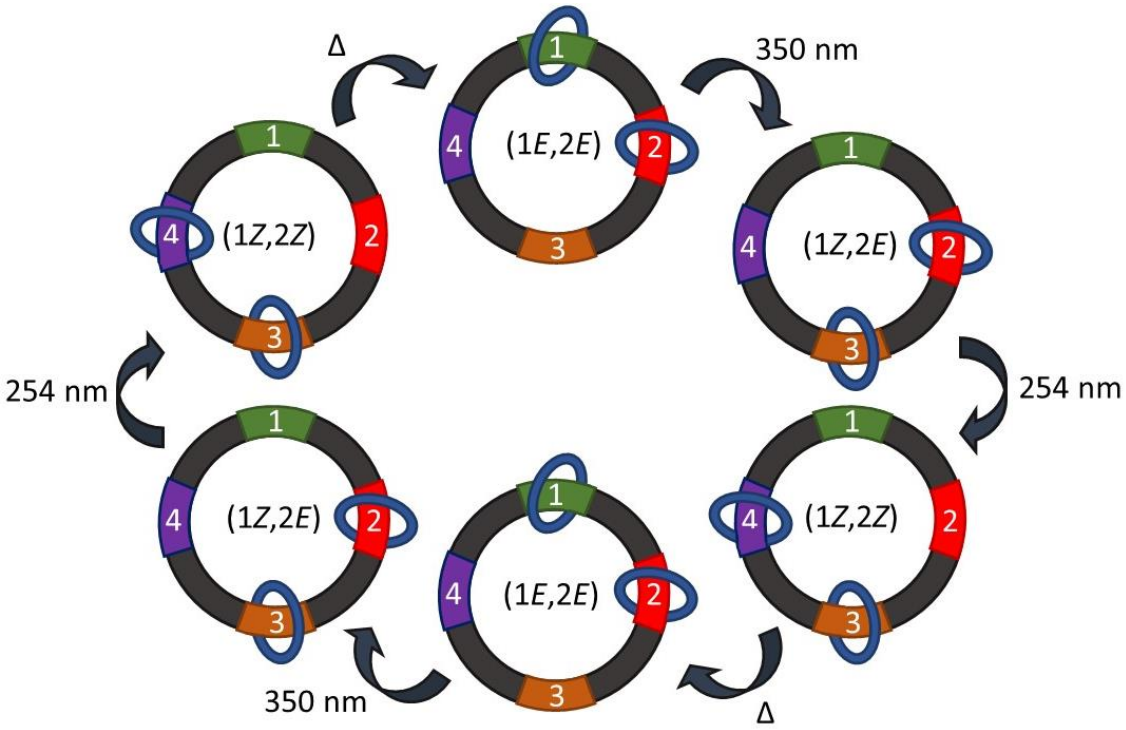

Figure 1.19 Schematioc rotary cycle for a [3]catenane molecular motor. Isomerisations state of the fumaramide sites shown within each ring, isomerisation conditions shown for each step. Adapted from Kassem *et al.*[68]

Molecular motors such as these, while able to find use in engineering and micro-electronics[69], are hard to use for biological / biomedical applications such as those covered in this work. The size of these interlocked systems makes cellular uptake a challenge, with functionalisation being difficult to achieve while maintaining machine-

like function. In addition, much of the modern supramolecular based systems have their motion controlled *via* redox chemistry[70] which is hard to control under physiological conditions.

Due to this much work has been carried out on using other systems to develop molecular motors for use in medicinal applications such as targeted drug delivery[71], cell manipulation[72], and bioimaging[73]. The use of any synthetic motor for *in vivo* applications is limited by their poor biocompatibility, biodegradability, and lack of fine motor control over specific motion. One of the machines that have been shown to allow for such applications is the hydrogen peroxide (H_2O_2) powered Janus micro-motor.[74] Which has been used for the targeted delivery of encapsulated doxorubicin, a well-known chemotherapy drug.[75]

Janus micro-motors generally consist of a hollowed polyelectrolyte capsule, functionalised on one side with the addition of H_2O_2 reducing catalysts, such as platinum based nanoparticles: shown in **Figure 1.20**. Further functionalisation is often carried out on the alternate face; for example, using Fe nanoparticles to allow for magnetic control over the propulsion.

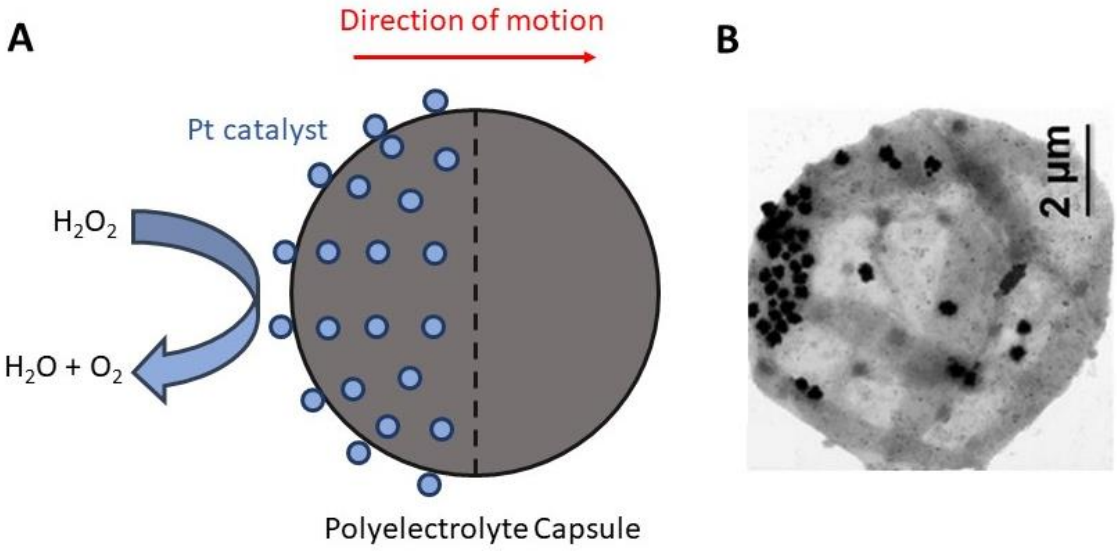

Figure 1.20 A - Schematic reprentation of an exemplar Janus motor. **B** - Transision electron microscopy image of a functionalised capsule.[76]

In the previously mentioned example of doxorubicin delivery, a gold shell functionalised with catalase was utilised instead of a Pt based catalyst due to its lower minimum operational concentration of peroxide fuel (0.1% v/v) at physiological temperature, allowing for use in biomedical applications. The permeable shell was loaded for doxorubicin and magnetically directed to colonies of HeLa cells, before being exposed to 808 nm light. This caused the polyelectrolyte capsule to break down and release the chemotherapy agent to the targeted cellular cluster. This process is illustrated in the microscopy images in **Figure 1.21**.[75]

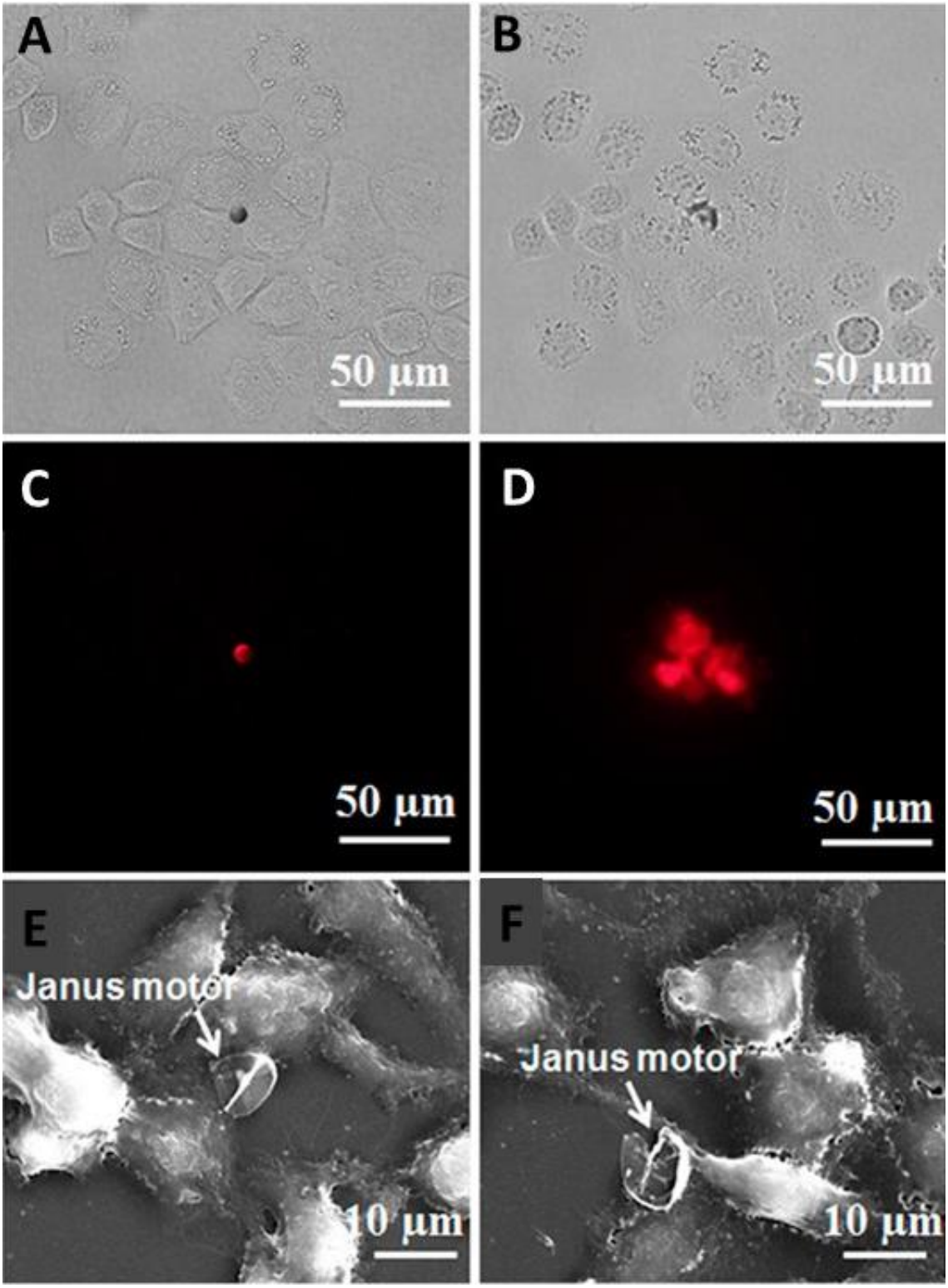

Figure 1.21 Transmission images of Janus motors before (**A**) and after (**B**) NIR exposure, fluorescence images of doxorubicin before (**C**) and after (**D**) shwoing relase

into the HeLa cluster, scanning electron micropy images of Janus motors before (**E**) and after (**F**) showing the breakdown of the capsule. Taken from Wu *et al*.[76]

While it has clearly been shown that this technology can be applied to biological systems, it is still limited due to the chemical fuel required for its motion. Several fuel free molecular motors have been in development using many different stimuli, such as magnetic, electrical, and ultrasonic fields. However, the majority of these are outside of the scope of this project and many reviews have been published covering them in great detail.[77]

1.2.6 Fergina type motors

Feringa was awarded the previously discussed 2016 Nobel prize in chemistry[33], alongside Sauvage and Stoddart, for their pioneering work on light activated molecular motors based not on interlocked systems like their peers but instead on traditional covalent systems; namely overcrowded olefin species. Starting from initial molecular switches and leading to the creation of light activated molecular motors.

The development of this form of the technology follows a similar pattern to that of the previously discussed supramolecular techniques; first taking inspiration from natural sources. The study of the underlying processes of vision found the first case of a natural photo-activated molecular switch. The primary stage of vision involves a light induced *cis/trans* isomerisation of a specific alkene within the protein bound retinal molecule (**Figure 1.22**).[78] This small mechanical change, triggered by a single photon, is responsible for initiating a cascade reaction, starting with a change in protein structure, that is capable of transmitting a visual signal to the brain. From this inspiration came the

first fully covalent artificial optical switches, which would lead to the development of Feringa molecular motors.

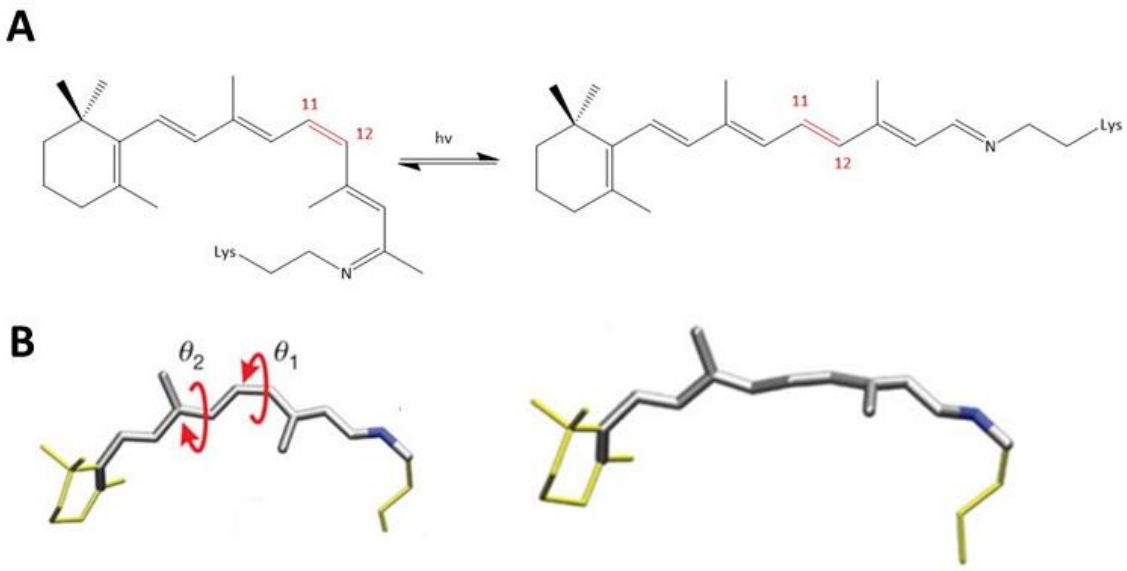

Figure 1.22 A - Structure of the key photoisomerisation stage of rhodopsin in mammalian rod cells. **B** - Crystal structure showing the change in conformation.[79]

The first artificial molecular machines to be synthesised from this discovery were chiroptical molecular switches, constructed from helical shaped overcrowded olefins.[80] The switching principle in these molecules differs from their natural counterparts due to the lack of incorporated protein architecture, the change in states is instead based upon the switching helicity of the species. Using the overcrowded alkenes in

Figure 1.23 A - Switching mechanism of the first reported enantioselective molecular switch. **B** - Illustration of helical chirality using [7]helicene as an example.

as an example, the photo-induced *cis/trans* isomerisation triggers a reversible interconversion between the right-handed (P) and left-handed (M) helical conformations. While hard to represent these helical structures specifically, the P and M forms of [7]helicene are also shown in an effort to illustrate the isomerisation process.

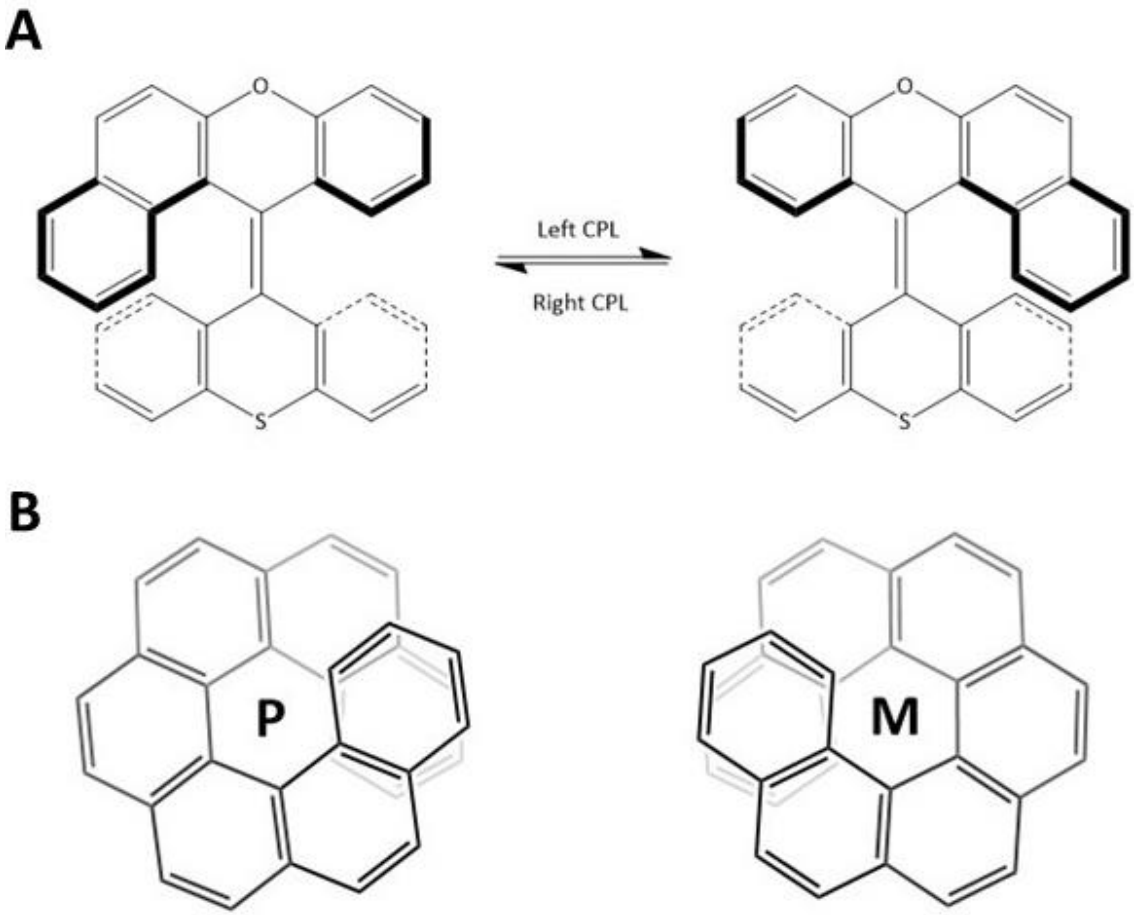

Figure 1.23 A - Switching mechanism of the first reported enantioselective molecular switch. **B** - Illustration of helical chirality using [7]helicene as an example.

This style of molecular switch found practical application in the development of luminescence switching probes. A dual mode fluorescent switching system was designed based on the overcrowded olefin class of compound, in which a single molecule can have differing level of emission based upon stereoselective photoisomerization as well as being switched off entirely *via* protonation.[81] This system is illustrated in **Figure 1.24**.

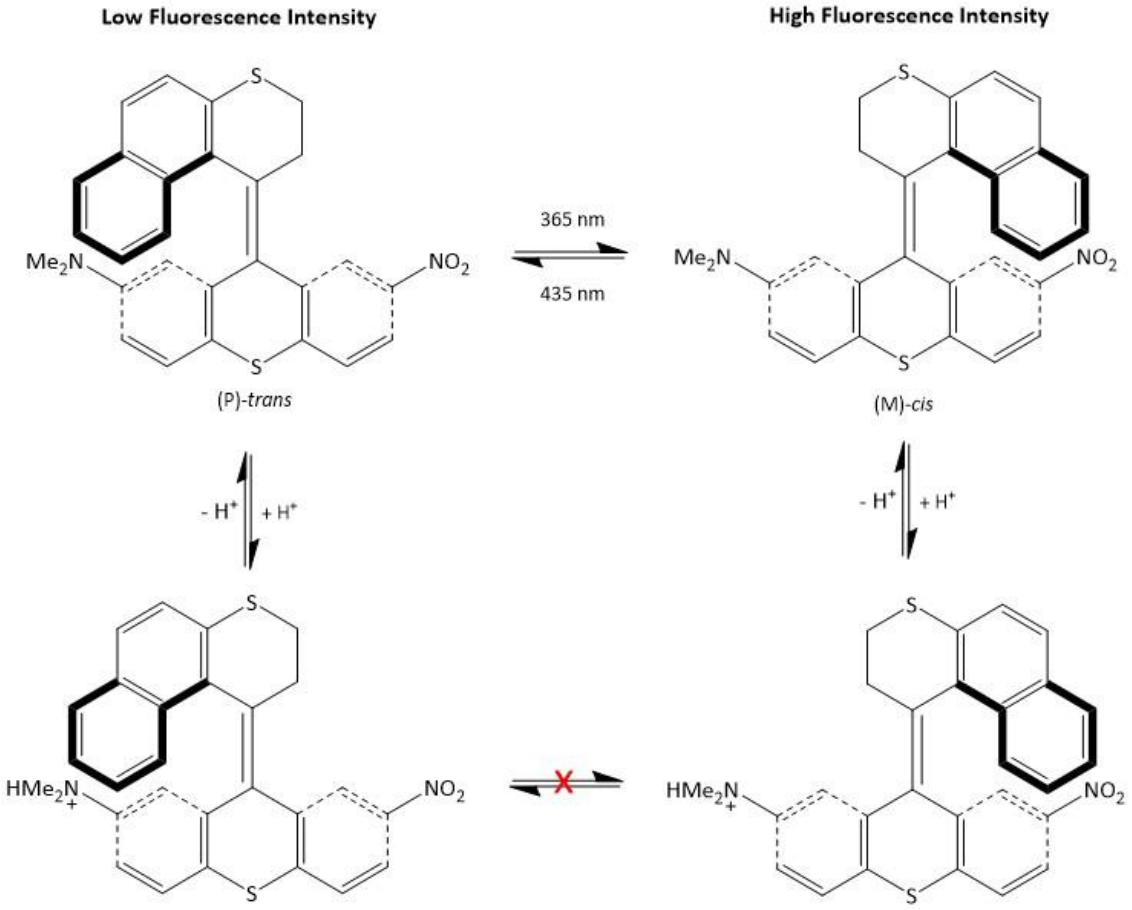

Figure 1.24 Mechanism of dual mode photo-switching fluorescence behaviour of a donor-acceptor molecular switch system. Adapted from Huck *et al*.[81]

First generation Feringa molecular motors were the first time unidirectional rotary motion was induced by light in a molecular system, representing a massive step forward in the field of molecular machines / motors.[82] This was achieved by the addition of an additional stereogenic centre when compared with the previously discussed molecular switches. The joint action of two chiral elements – in this instance the stereogenic centre and the molecular helicity – in one excitation event, due to the diastereomeric nature, causes single handedness in the induced motion. In this system (illustrated in **Figure 1.25**) the helicity is switched *via* photoisomerization by the same mechanism as the previous switches.

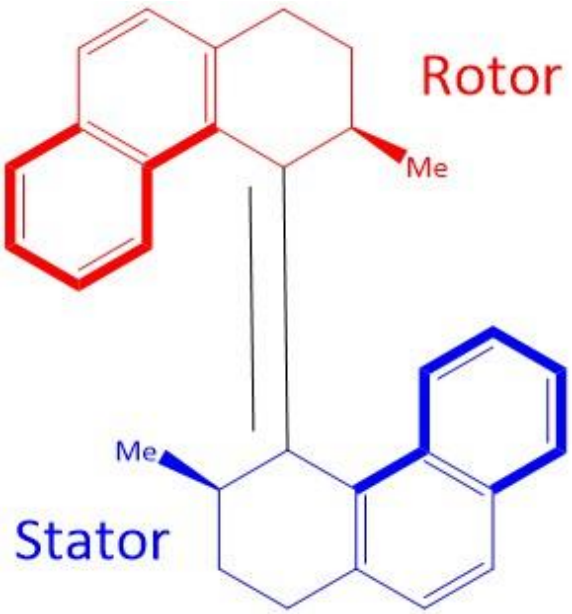

Figure 1.25 General structure of a first generation Feringa molecular motor. Top half (rotor) highlighted in red, bottom half (stator) highlighted in blue. It should be noted that without isoalting each step of the rotary cycle, these labels are purely figurative.

However, the added methyl substituent can now adopt either an axial or equatorial position in both isomers. These have noticeably different stabilities; the difference between unstable (3*R*,3'*R*)-(*M*,*M*)-*cis* with an equatorial methyl substituent (2) and stable (3*R*,3'*R*)-(*P*,*P*)-*cis* with an axial methyl substituent is 46.0 kJ^{-1} mol^{-1}, attributed to the additional steric interference when the methyl group lies equatorially, resulting in the molecule flipping its helix (*M* – *P*) to adopt the more energetically favoured conformation - thermal helix inversion. Similarly the trans isomers on the other side of the rotary cycle, (3*R*,3'*R*)-(*M*,*M*)-*trans* and (3*R*,3'*R*)-(*P*,*P*)-*trans*, possess a difference in stability of 35.9 kJ^{-1} mol^{-1}. By exposing the system to specific wavelength of light, and heat, the unidirectional rotation of the rotor, with respect to the stator, proceeds *via* a four-step process (shown in **Figure 1.26**). Starting with the (3*R*,3'*R*)-(*P*,*P*)-*trans* form an initial reversible photoisomerisation step occurs - in much the same way as the molecular switch - which converts this stable isomer to the unstable (3*R*,3'*R*)-(*M*,*M*)-*cis*

form with equatorial methyl groups. This readily undergoes a thermal helix inversion to release the strain on the system, resulting in the, again stable, (3*R*,3'*R*)-(*P*,*P*)-*cis* form. An additional photon can then be utilised in another photoisomerisation, resulting in a second unstable formation - (3*R*,3'*R*)-(*M*,*M*)-*trans*. Once again the equatorial methyl groups lead to this conformation being energetically unstable, resulting in thermal helix inversion back to the initial (3*R*,3'*R*)-(*P*,*P*)-*trans* form. However, with first generation molecular motors this second inversion required heating at 60 ^{o}C.

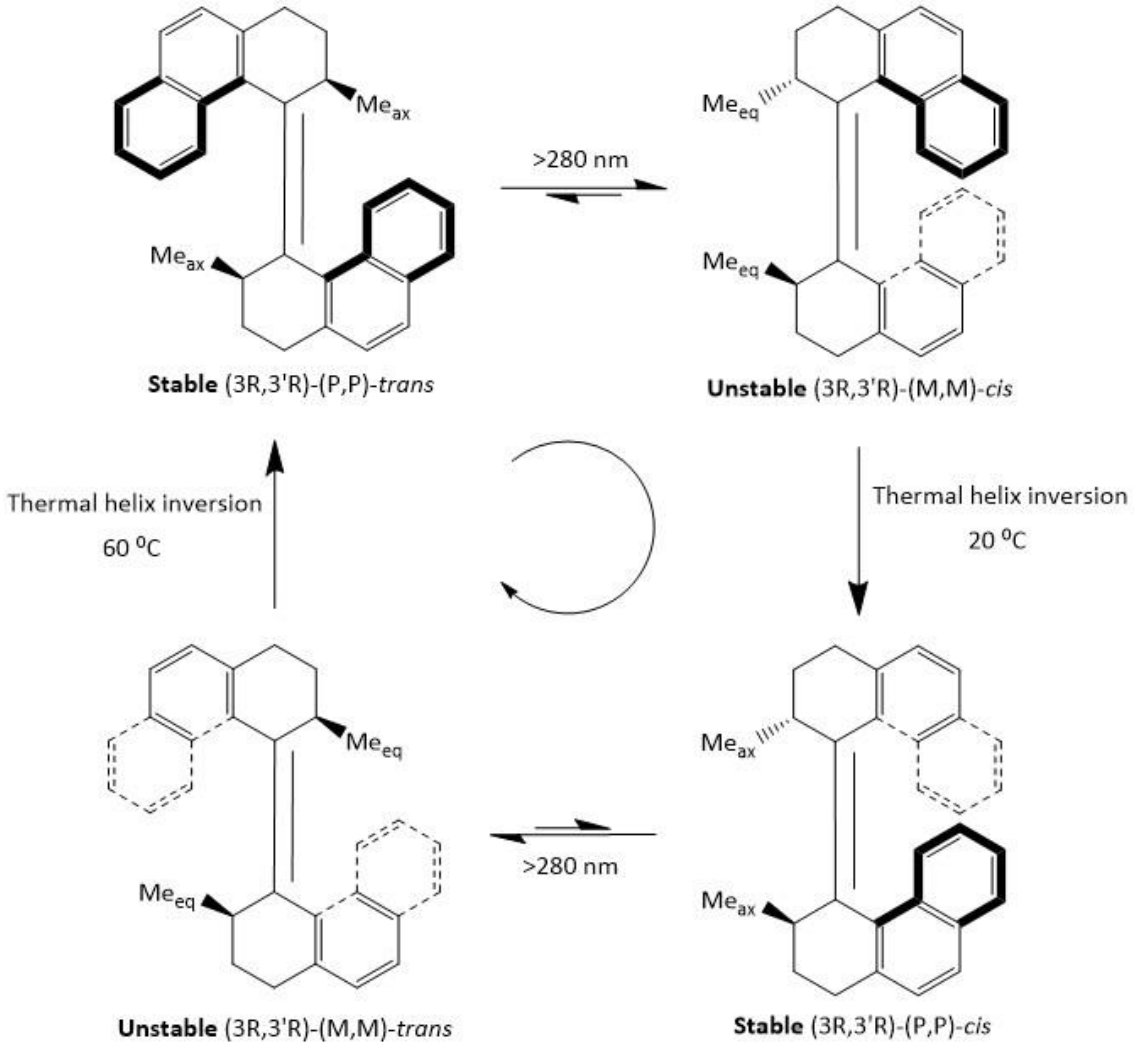

Figure 1.26 Summary of the photochemical and thermal isomerisation processes responcible for unidirectional rotation of a first generation Feringa motor.

Due to the change in helicity taking place within each stage of the rotation cycle, the motors movement can be tracked by circular dichroism (CD) spectroscopy, as shown in **Figure 1.27**.

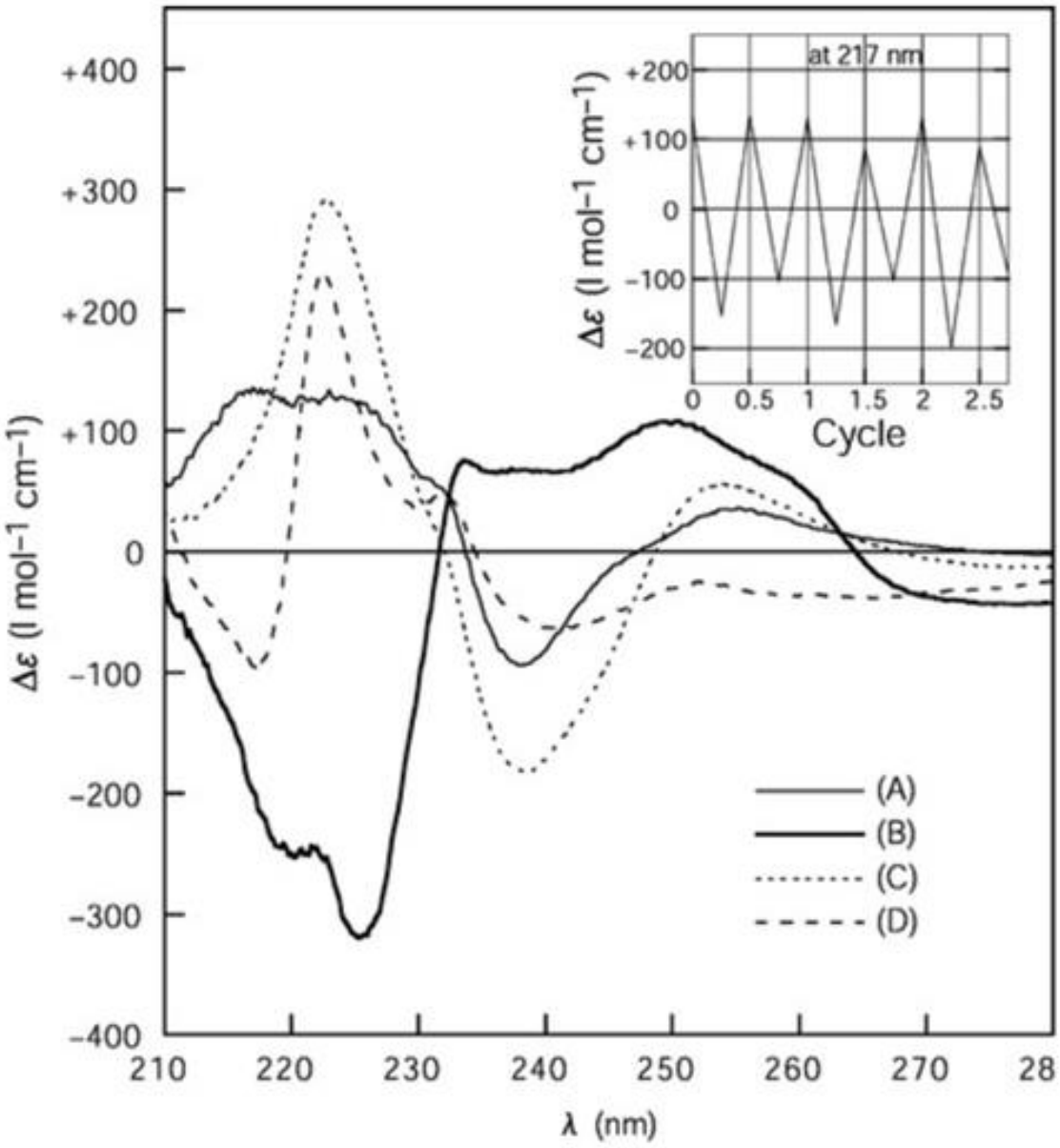

Figure 1.27 CD spectra of each isolated stage of motor rotation. Trace A: *P*,*P-trans*. Trace B: *M*,*M-cis*. Trace C: *P*,*P-cis*. Trace D: *M*,*M*,*trans*.[82]

Further development of light activated molecular motors for use as part of more complex molecular machinery, and for uses such as those carried out in this work, focused on increasing the rotation to an appreciable speed.[83] The alkene isomerisation

is a photochemical process occurring on an extremely fast timescale (<300 ps), as such focus was given to reducing the energy barrier of the rate-limited thermal helix inversion steps without compromising on unidirectionality.[84] Investigations on specifically altering this property of Feringa motors highlighted the importance of the christened "fjord region"; the geometry and conformation about the central double bond axis of rotation – illustrated in **Figure 1.28**. Second generation motors were able to achieve up to a 1.2-million-fold increase[85] in the speed of rotation by altering the position of the methyl substituent into a more favourable axial orientation in the stable form, while also promoting a more crowded equatorial position when in the unstable form (**Figure 1.29**).[86]

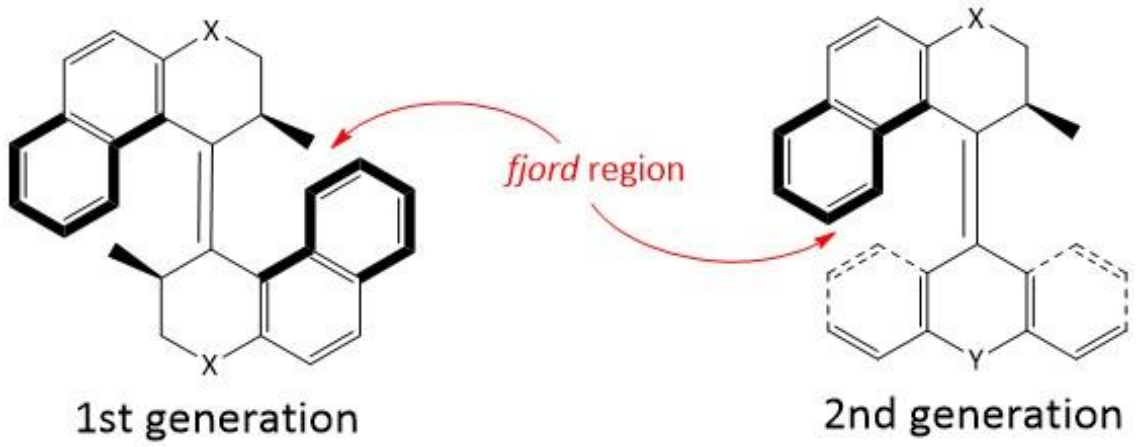

Figure 1.28 Structures of 1st and 2nd generation Feringa motors with the fjord region indicated in red.

Second generation Feringa motors notably are able to induce unidirectional rotation with only a single stereogenic centre, allowing for a non-symmetrical design of the rotor and stator; key to this project's work as this opens up the possibility of functionalisation without altering the rotary properties of the molecule.

The four-step rotary cycle of this new generation of motors (**Figure 1.29**) initially allowed for unidirectional rotations speeds of 80 revolutions per second; approaching the speeds found in naturally occurring molecular machines, such as the previously examined ATPase (135 rotations s^{-1}). Of great implication to this work is the fact that the accompanying thermal helix inversion steps were induced at only 20 ^{o}C, meaning possible biological applications of Feringa motors were possible for the first time.

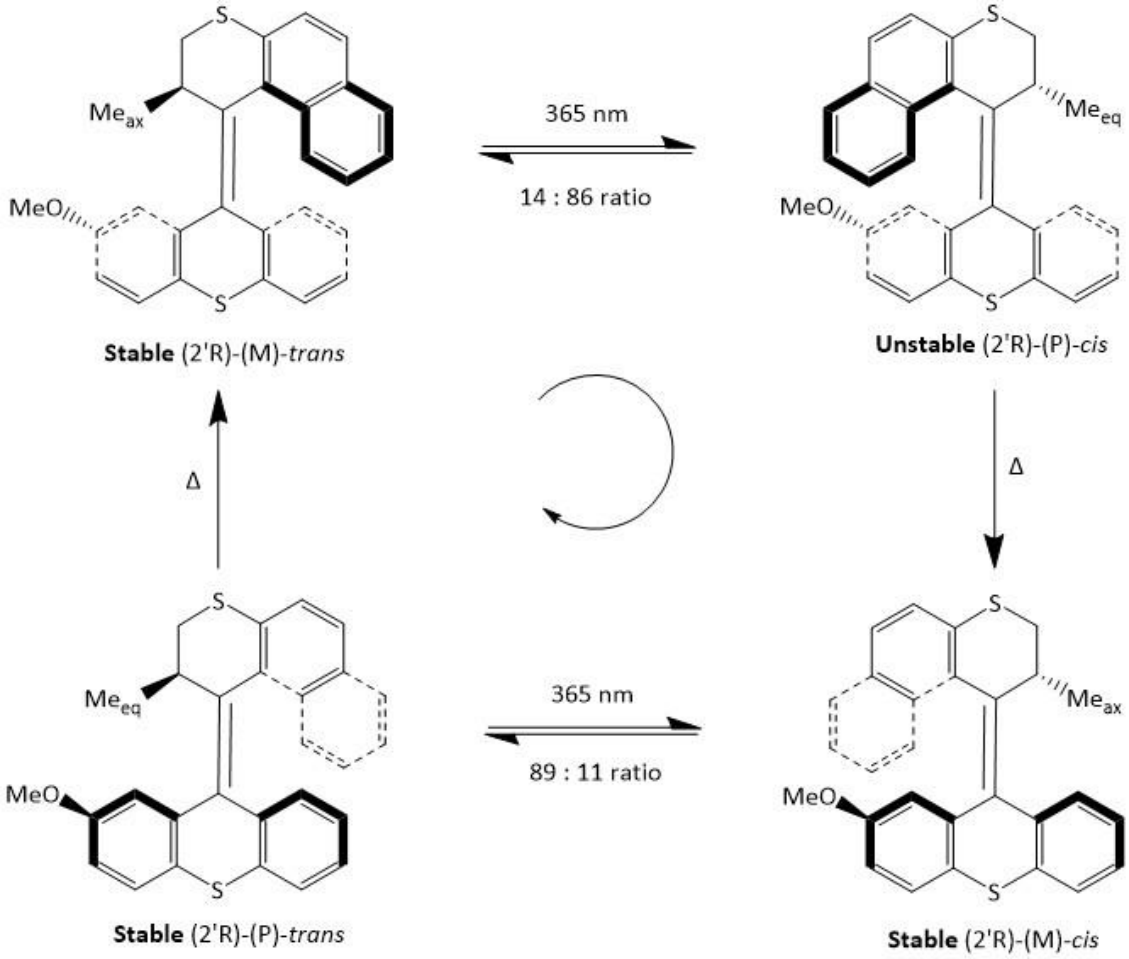

Figure 1.29 Summary of the photochemical and thermal isomerisation processes responible for the unidiretional rotation of a second-generation Feringa motor. Of note is the presence of only a single sterogenic centre.[87]

While the molecules used within this work are based on second generation Feringa motors, it is important to briefly discuss the recent development of achiral molecules

with the ability to undergo unidirectional rotation – so-called third generation molecular motors (**Figure 1.30**).[88]

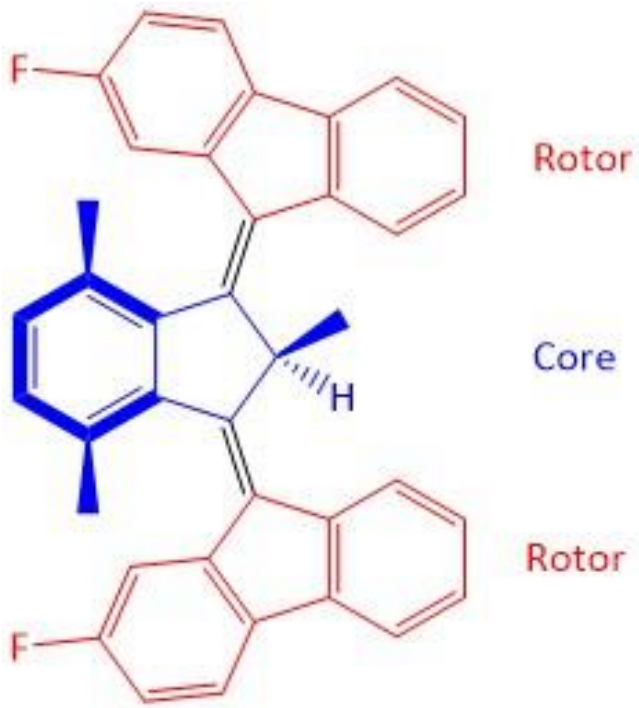

Figure 1.30 Stucture of a third generation Ferigna achiral motor possessing two symmetric overcorwded alkenes and a pseudo-asymmetric carbon atom.

While second generation motors can operate with up to MHz frequencies of rotation[83] and are able to convert light to directional rotation motions – used for this work – the idea of incorporating them into more complex molecular mechanical structures for unidirectional translation resulted in the further development of this third generation. Upon irradiation with light, one rotor isomerises to from a metastable product which, similarly to previous generations, undergoes thermal helix inversion to a stable conformation. This is followed by the same process about the second axle as shown in **Figure 1.31**.

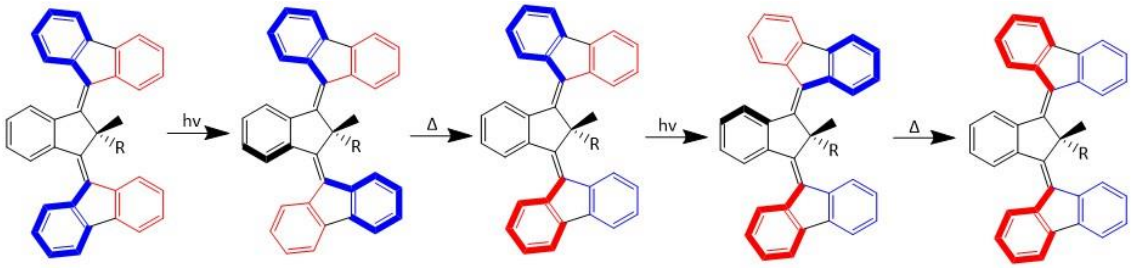

Figure 1.31 Sequential rotation about both axis of a third generation Feringa motor using alternating photochemical and thermal isomerisations. Otherwise symmetrical rotors are coloured to aid in understanding of their rotation. Adapted from Roy *et al*.[89]

Feringa motors have been previously incorporated into basic nano-scale machinery, the most well-known of which being Tour's light powered "nanocar"[90], a light driven motorised molecule where full rotation of the Feringa motor results in propulsion in a circling motion across a glass surface. Developed as an iteration of the first nano-car[91], an unpowered construction consisting of an alkyl unit based "chassis" with four freely rotating fullerene (C_{60}) "wheels", which showed a rolling motion across metallic surfaces. This motorised continuation incorporated a second-generation Feringa motor (3 MHz at 25 ^{o}C) as well BODIPY functionalisation and adamantane wheels, as shown in **Figure 1.32**.

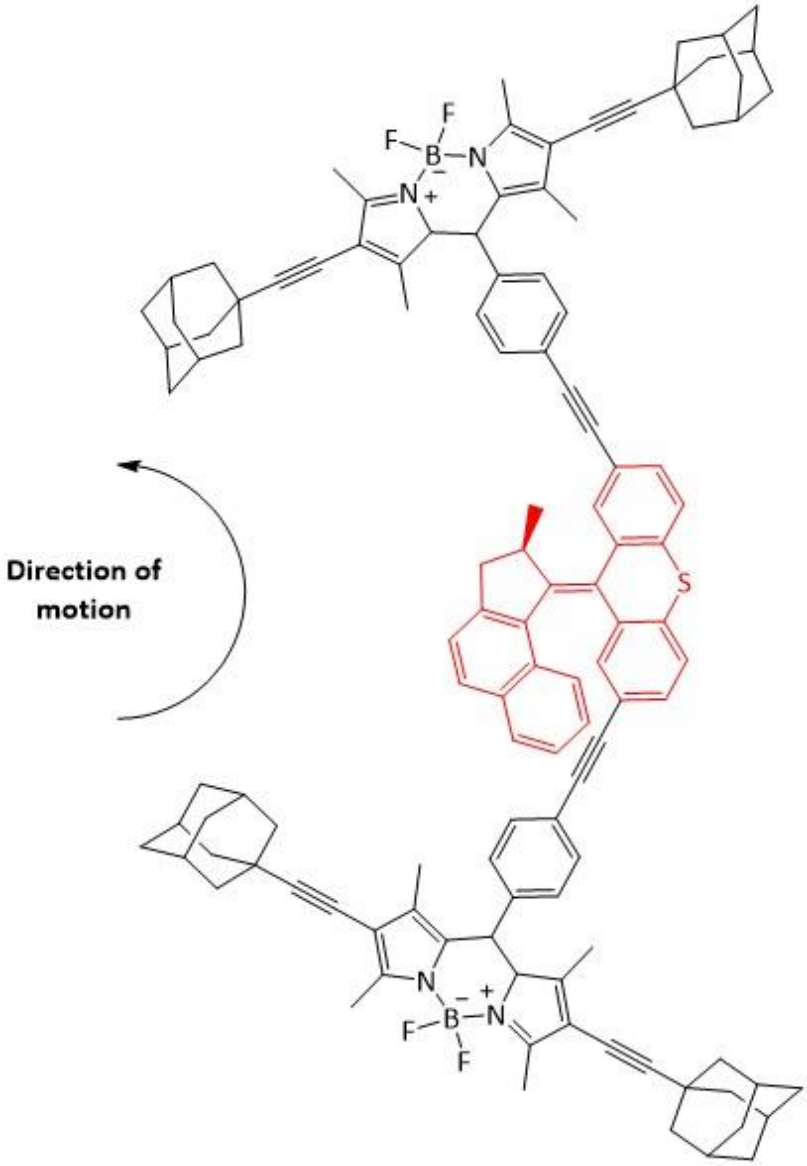

Figure 1.32 Structure of the Tour motorised nanocar. Second generation Feringa motor highlighted in red.

The development of various iterations of nanocars was carried out with the overarching goal of using them as transporters of nano-scale cargo, either material or information, however this is a complex goal and is yet to be realised.

1.3 Microscopy

1.3.1 Principles of optical microscopy

The theory behind the basic compound microscope was initially developed by Hans and Zacharias Janssen in the 16th century[92], and propagated by Hooke's famous "Micrographia" publication in the 17th century.[93] Despite the multitude of developments – covered within this section - the general principle of light microscopy has remained relatively static. Every microscope is based upon the original two fundamental lenses; a powerful objective lens that produces the majority of the magnification, and a tube, or eyepiece lens, that focuses this magnified image into a sensor (be this the retina or an electronic detector).

Figure 1.33 illustrates this with a comparison between ray diagrams for a simple two lens system, like that used in early microscopes (**A**), and a modern iteration (**B**). While modern microscope systems utilise significantly more complex compound objective lens for better image clarity, the basic concept has remained unchanged.

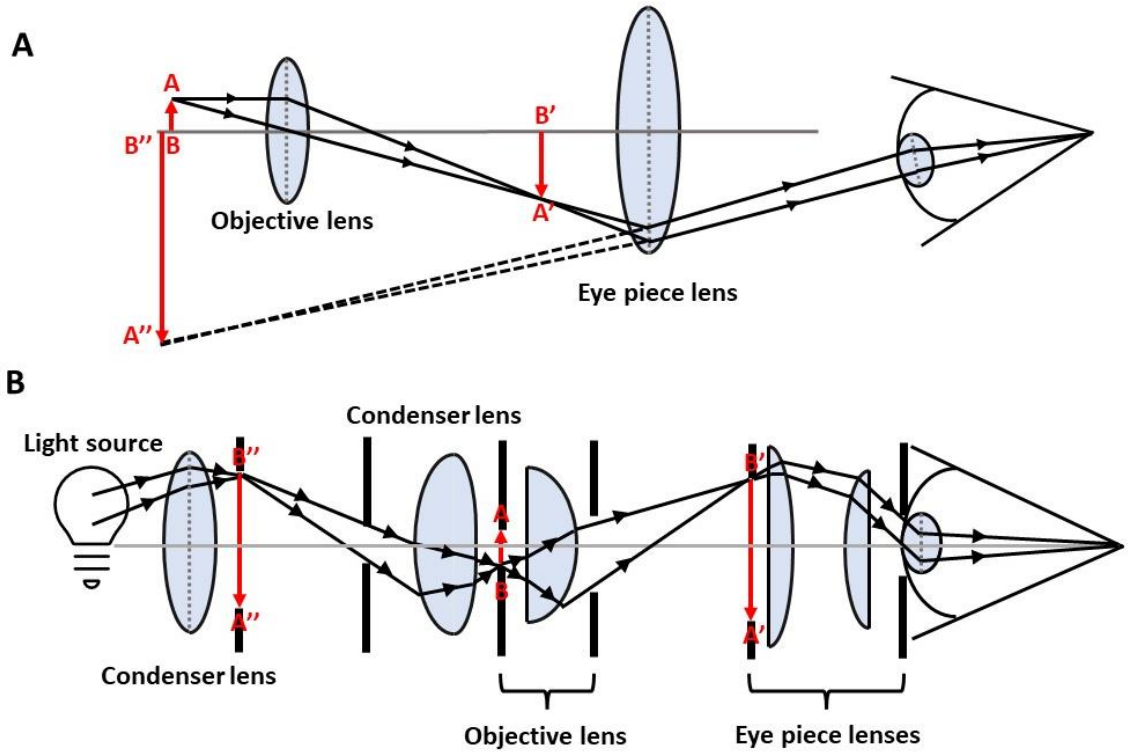

Figure 1.33 A – Two lens microscope ray diagram showing sample AB, real intermediate image A'B', and the apprent location of virtual image A''B''. **B** - Imageing ray path diagram for a modern mult-lens objective microscope showing light source condensation.[94]

As the field has progressed there have of course been remarkable improvements first and foremost to the achievable resolution of the system; that is, the ability of the microscope to distinguish details of a sample, or the minimum distance between two distinct points of a sample where they can be seen as separate entities by the observer. Assuming a circular aperture, there are three widely used formulae for computing resolution: In order of size, the Rayleigh limit[95], Abbe limit[96], and sparrow limit[97].

The diffraction limit arises due to the interaction between the wave nature of light and the optical components it passes through. Specifically, the diffraction, or scattering, of the incoming light as it passes through the entrance to the microscope's objective leading to a loss of information. An example of this is given in **Figure 1.34** where a single

molecule of green fluorescence protein (GFP) is emitting a photon at 510 nm, resulting in an intensity distribution patten on a charge-coupled device (CCD) camera; known as the Airy pattern.

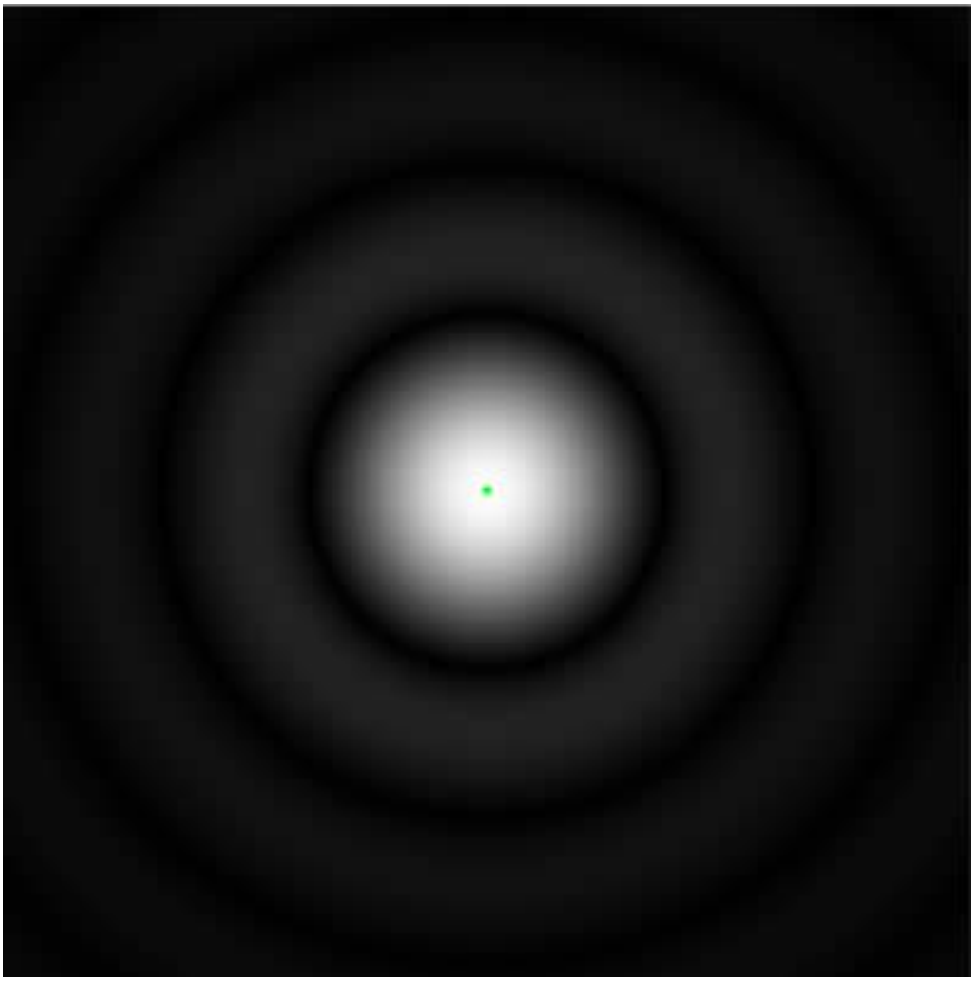

Figure 1.34 Intensity profile of a single molecule of GFP emitting at 510 nm.[98]

It is clearly seen that the Airy pattern for a single emitter is much larger than its actual size, meaning that if multiple molecules were within the radius of this profile, it would not be possible to distinguish between them. This is the concept of the resolution limit; there exists a minimum distance in space between two emitters be such that their individual pattern of emitted light – or their point spread function (PSF) – can be distinguished from each other. This is where the three formulae for resolution are utilised; both Rayleigh and Abbe find use within microscopy – with Abbe being the most

applicable to this work – and will be covered extensively within, while the Sparrow criterion is more conventionally used within astronomy. **Figure 1.35** shows a comparison between these three methods.

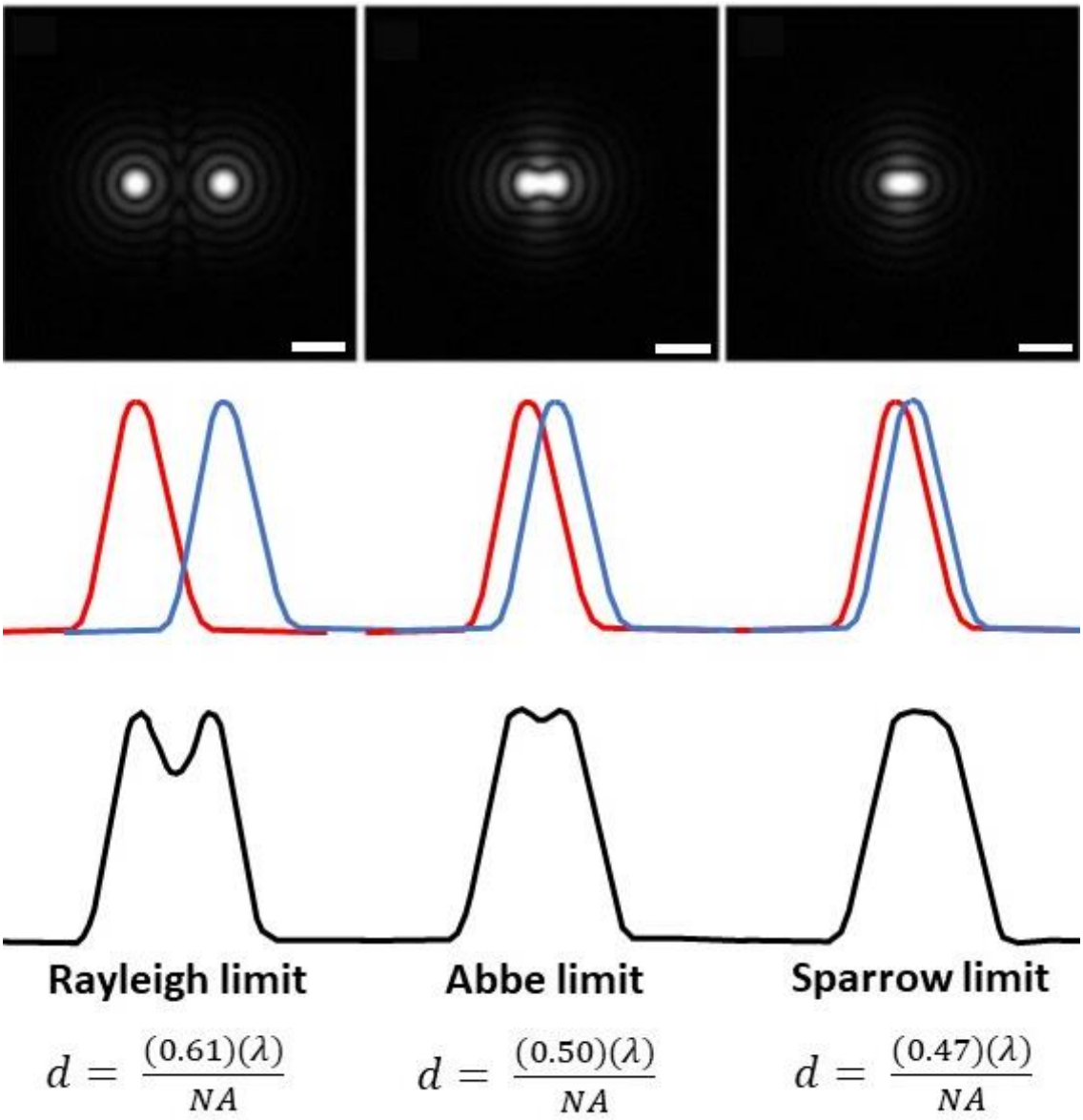

Figure 1.35 A summary of the three widely utilised formulae for resolution computation. Red and blur curves represent the individual Airy profiles of the point emitters, with the black trace shwoing the summation of these functions. Scale bars 800 nm. Adapted from Kaderuppan *et al*.[99]

All formulea for calcualing the resolving power of a system rely on the concept of numerial apperature (NA) of the imaging system; defined by:

$$NA = (n)(\sin\theta)$$

Equation 1.1

Where n is the refractive index of the imaging medium and ϑ is the half-angle of the cone of light presented to the lens (illustrated in **Figure 1.36**).

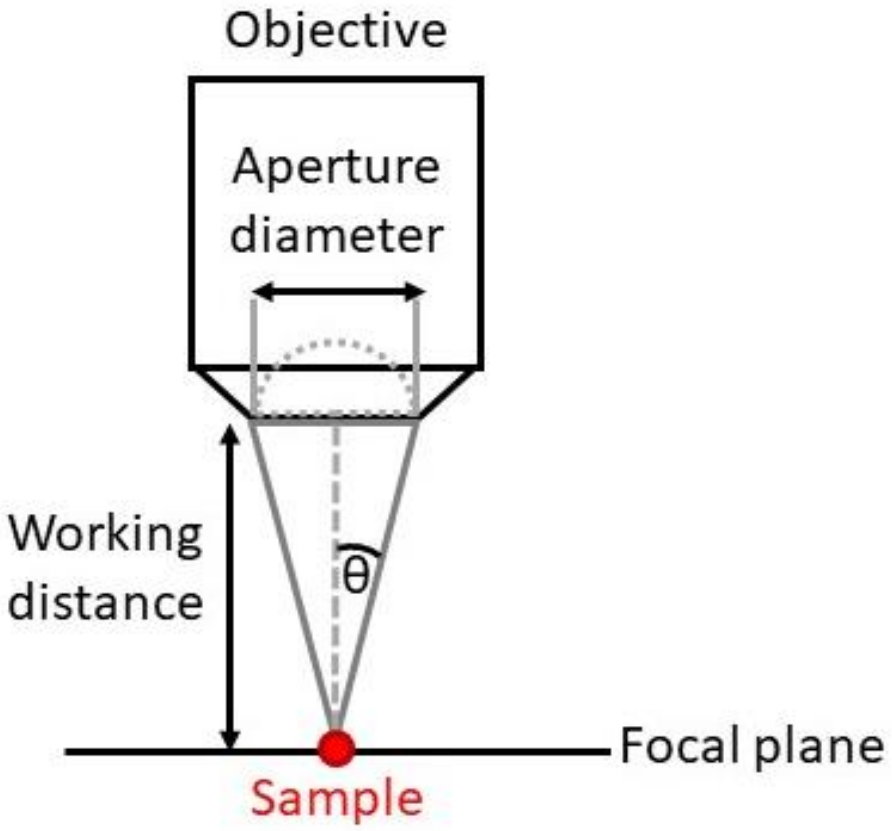

Figure 1.36 Half angle, θ, illustrated for a standard upright objective.

The Rayleigh formula defines the resolution limit of a system as the minimal distance between two point sources before the first minima of one point source overlaps with the maxima of the second. Shown for lateral and axial resolutions respectively in **Equation 1.2** and **Equation 1.3**.

$$d_{x,y} = 0.6\,\frac{\lambda}{NA}$$

Equation 1.2

$$d_z = 2n\frac{\lambda}{NA^2}$$

Equation 1.3

Where λ is the imaged wavelength and n is, again, the refractive index of the imaging medium.

The sparrow formula is the narrowest of the three and defines two points as resolved if there is any intensity variation between the two maxima as previously shown in **Figure 1.35**. Defined for lateral resolution as:

$$d_{x,y} = 0.47\frac{\lambda}{NA}$$

Equation 1.4

While this is narrower than the Rayleigh, and the yet to be discussed Abbe criteria, this formula finds little application within microscopy and is more commonly applied in astronomy where the resolution between of emitters is more important than the ability to distinguish larger structures.

The final, and most widely used within optical microscopy, formula is the Abbe diffraction limit and was the first to be formally defined in 1883.[96] Where species are defined as resolved if there is no overlap between the full width half maxima (FWHM) of the central maximum intensity of the point sources (PSF) (illustrated in **Figure 1.37**).

Equation 1.5 and **Equation 1.6** show the formal definition for lateral and axial resolution respectively.

$$d_{x,y} = 0.5\frac{\lambda}{NA}$$

Equation 1.5

$$d_z = \frac{2\lambda}{NA^2}$$

Equation 1.6

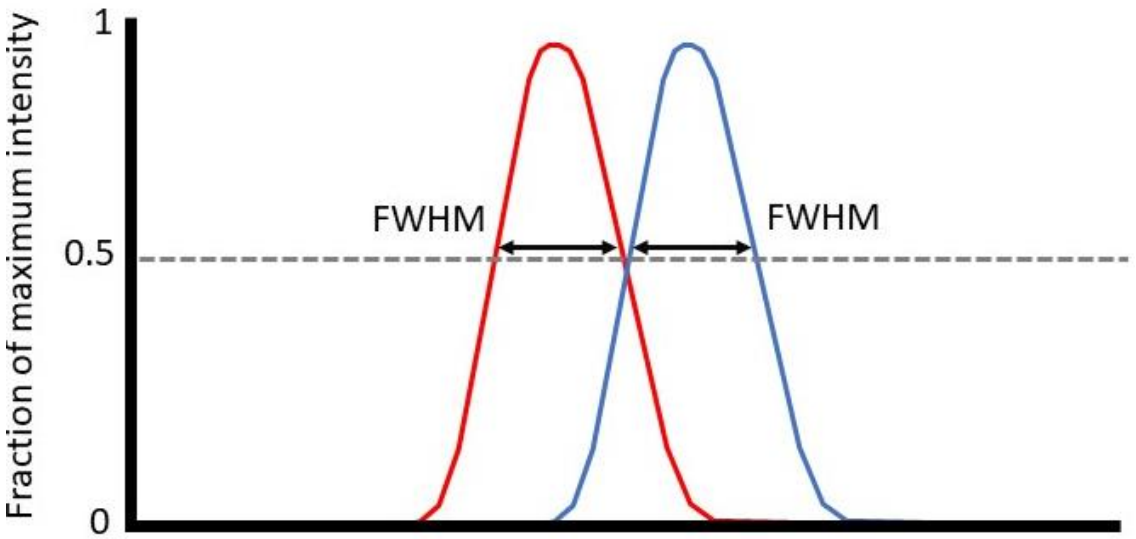

Figure 1.37 Example illustration of two resolved PSFs according to Abbe's diffraction limit, where there is no overlap between FWHM.

It is worth noting, when striving for a comprehensive overview of the field, that recent advances have achieved resolutions that bypass this diffraction limit. However, this work is outside the scope of what is required for this project and numerous detailed reviews have been published offering excellent summaries of the various techniques available.[100]

1.3.2 Fluorescence and fluorescence microscopy

One of the biggest advancements in optical microscopy came with the introduction of fluorescent probes as regular labels in biological imaging. Fluorescence occurs when electrons within a molecules highest occupied molecular orbital (HOMO) are excited into the lowest unoccupied molecular orbital (LUMO) by an electron possessing energy exactly matching that of the HOMO-LUMO energy gap. After losing some of this energy to vibrational relaxation processes, these excited electrons subsequently transition back down to their ground state and the excess energy is emitted as a lower energy photon. This fundamental process is summarised by the Jablonski diagram in **Figure 1.38**.

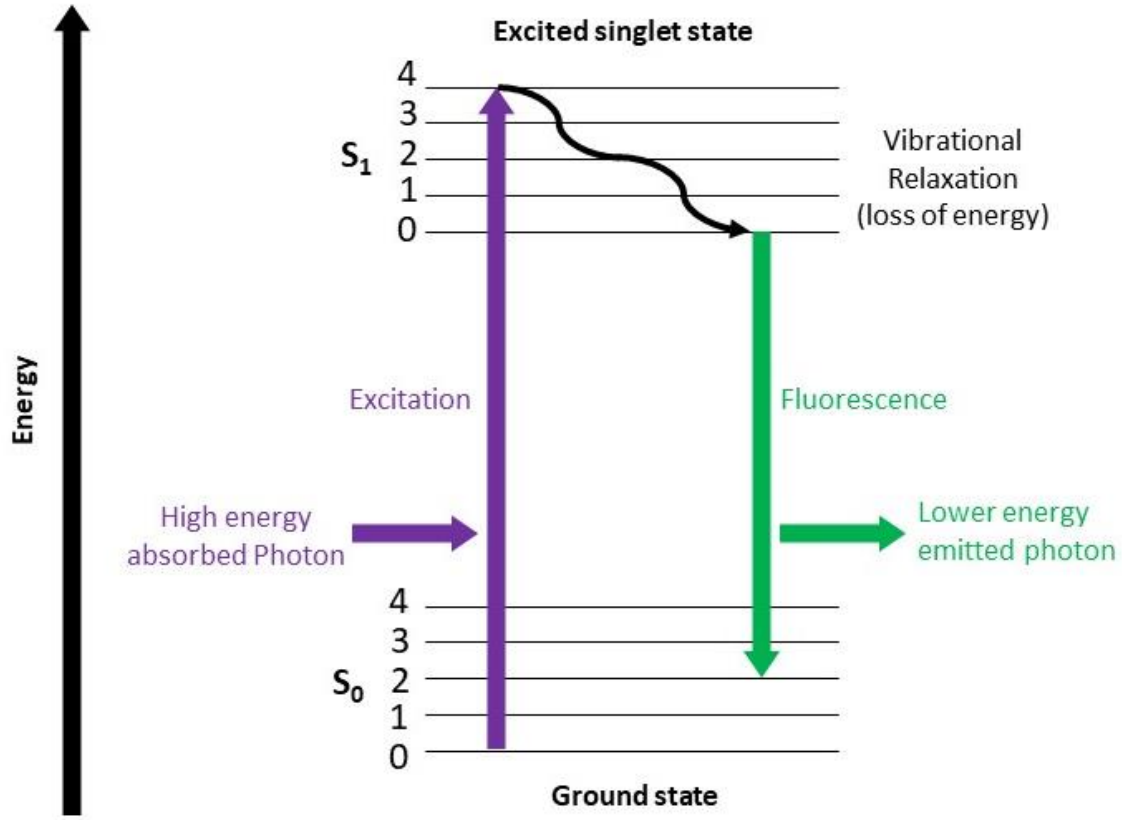

Figure 1.38 Jablonski diagram illustrating the basic processes behind fluorescence.

As previously stated, the emitted light is always lower energy than the absorbed photon due to the kinetic energy lost during the electron's vibrational relaxation. Hence, the emitted light will have a longer wavelength. The difference between the maximum

intensity wavelength of light emitted and absorbed is known as the Stokes shift, illustrated for Rhodamine 6G in **Figure 1.39**. In biological imaging larger Stokes shifts are typically preferred due to the ease of separating the two signals.

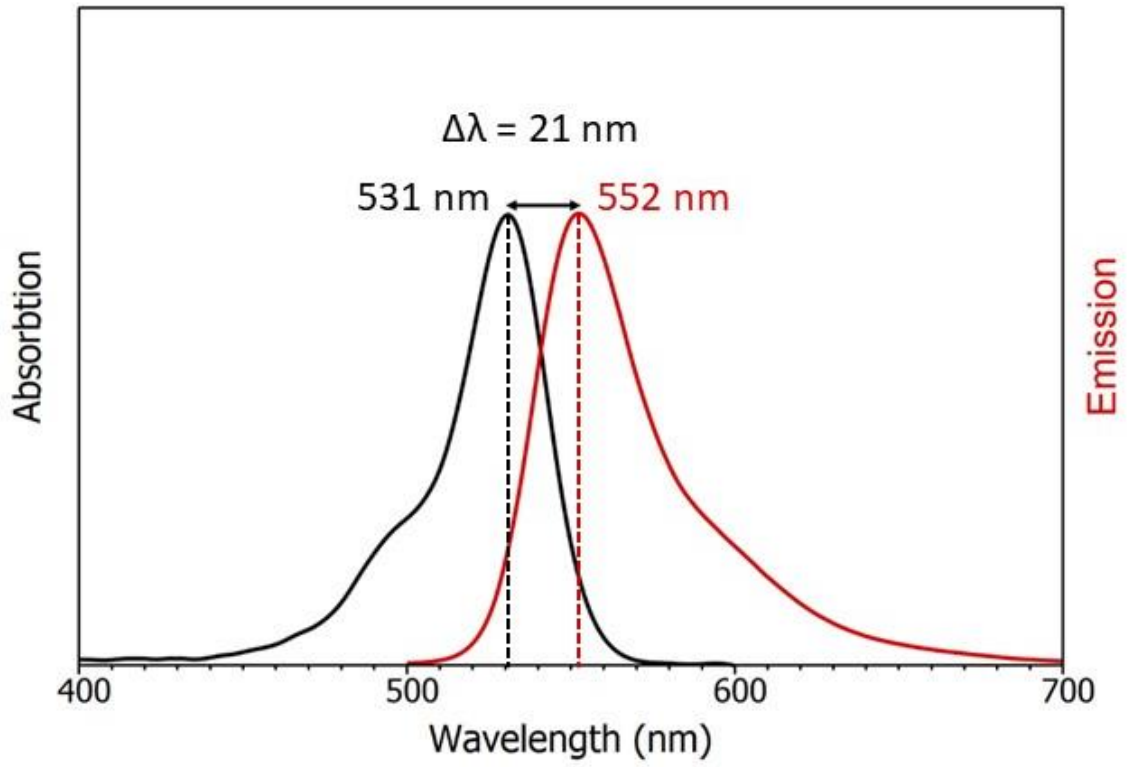

Figure 1.39 Absorption (black) emission (red) spectra for Rhodamine 6G with Stokes shift illustrated. Adapated from Edinburgh Instruments.[101]

Since the majority of biological structures are themselves relatively non-fluorescent using widely available visible excitation sources, other compounds possessing strong excitation and emission properties are often utilised to label specific areas of interest. It has been reported that fluorescent stains for biological structures and tissues began to be used as early as the 1940s.[102] The vast array of stains now available to the microscopist results in a massive increase in the amount of information that can be obtained. An example of this is shown in **Figure 1.40** where co-staining of a cellular sample allows the localisation of a novel compound to be studied.

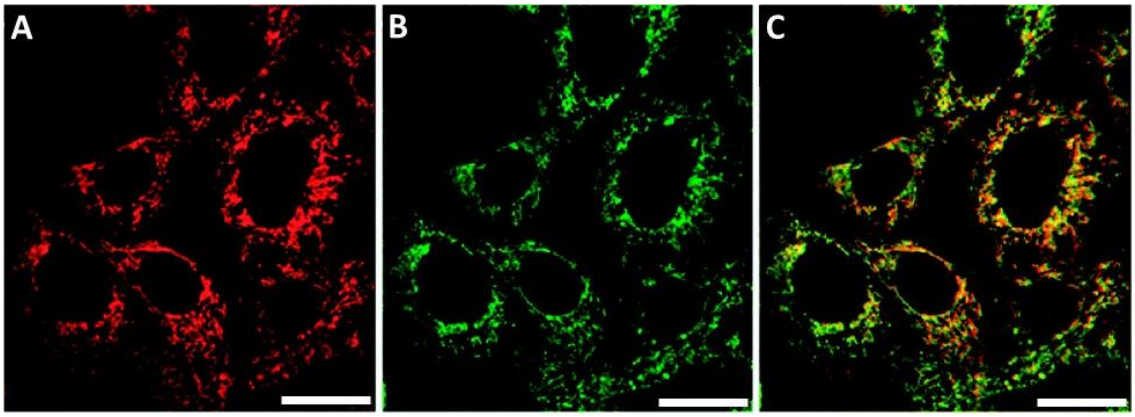

Figure 1.40 Representitive example of multicolour labeling in biological imaging of NIH 3T3 cells. **A** - Novel Eu complex (λ_{ex} 355 nm, λ_{em} 605-720 nm). **B** – MitoTracker green (λ_{ex} 488 nm, λ_{em} 500-530 nm). **C** – RGB colour merged image. Scale bars 30 µm. Images adapted from Butler *et al*.[103]

Without the advent of fluorescence microscopy, it would be impossible to track the localisation of compounds added to biological samples. Here mouse skin fibroblasts were treated with a novel Eu complex with an emission maximum of ~620 nm, by co-staining the sample with a dye known to localise to the mitochondria (Mitotracker green, λ_{max} 512 nm) and overlaying the images the colocalization of the novel compound and the mitochondria specific dye can be determined. More specifically, these developments allowed for quantification of colocalisation by way of Pearson's correlation coefficient – using the formula presented in **Equation 1.7**.[104] Where R_i and G_i refer to the intensity of the red and green channels of given pixel *i* respectively, while R' and G' represent the mean intensities of the red and green channels of the entire field of view. Giving a value between 1 and -1, with 1 showing two channels whose intensities are perfectly linearly corelated and -1 representing two channels perfectly inversely related to each other. Hence, values around zero will show two signals with little to no correlation – i.e. a mitochondrial stain and a lysosome specific probe.

$$PCC = \frac{\sum_i (R_i - R')(G_i - G')}{\sqrt{\sum_i (R_i - R')^2 \times \sum_i (G_i - G')^2}}$$

Equation 1.7

1.3.3 Laser scanning confocal microscopy

The expansion of fluorescence microscopy was accompanied by the development of one of the most important techniques in the history of microscopic imaging; laser scanning confocal microscopy (LSCM). Pioneered by Minsky in 1955, a confocal microscope forms a much sharper image than that of a conventional setup by emitting light from the sample that is not from the microscopes focal plane. Achieved using pinholes for both the illuminating and detected light – a so called "double focusing" system - as shown by Minsky's original technical drawing in **Figure 1.41**.[105]

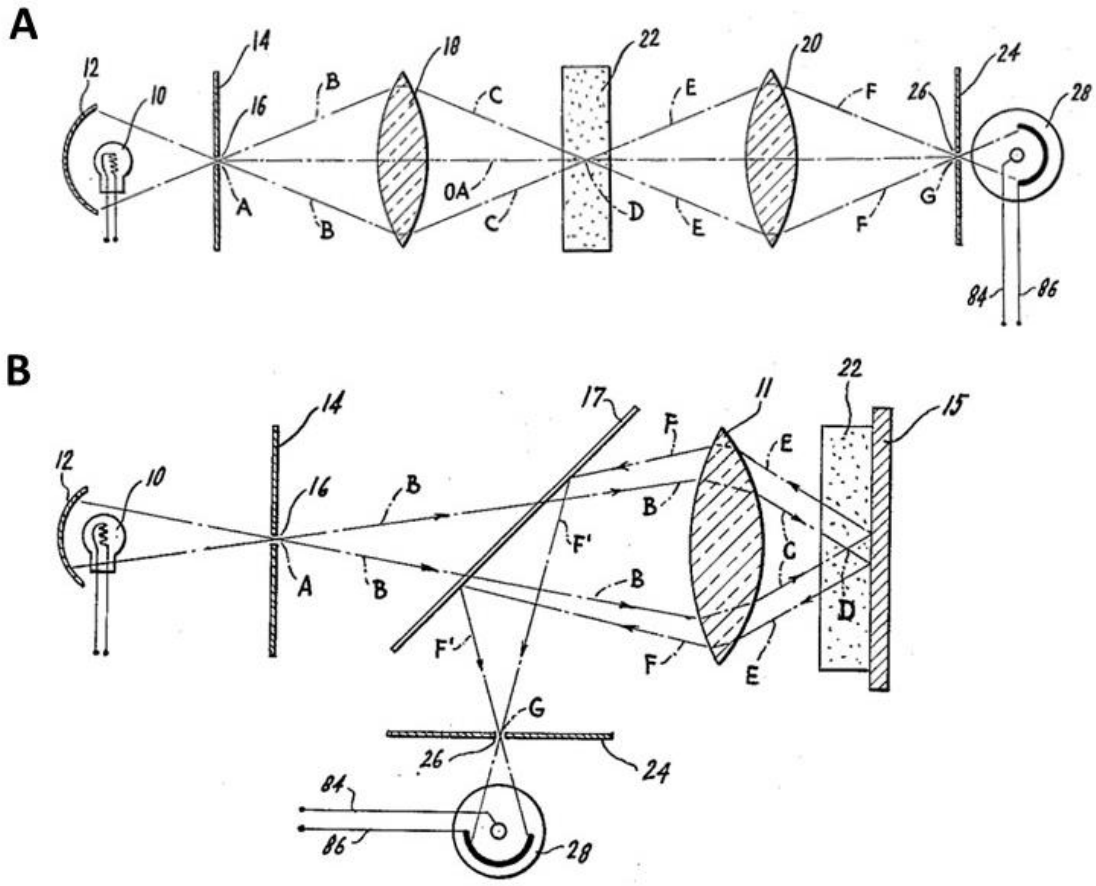

Figure 1.41 Minsky's original patent diagrams showing two embodiments (**A**,**B**) of his confocal optical system. Both utilising two pinholes (16,26) to create a point source of light from the lamp (10) and remove out of focus light from the detector (28) respectively.

LSCM allows point-by-point image construction by focusing a point of light (created *via* the use of the first pinhole) sequentially across the sample and measuring the signal at each position while emitting any light from outside the focal plane (by way of the second pinhole). It is important to note that the image of the sample is collected *via* the movement of the stage rather than the incoming light, thereby avoiding any problems with alignment of the optical components.

Modern LSCM systems have changed little from Minsky's original design; while obvious advances in optics and electronics have led to improvements in both speed of image

acquisition and image quality, most confocal microscopes produce an image by either reflecting light off the sample, or by collecting emitted light from previously discussed fluorophores. In the first confocal systems the pinhole was placed between the sample and an incoherent light source (**Figure 1.41**, 10), such as a mercury vapor lamp. In modern iterations coherent laser light sources are often used to produce narrow excitation bandwidth without the use of filters, allowing for high levels of specificity when exciting molecules of interest. Originally, a photoemissive cell was utilised after the second pinhole for detection of light collected from the focal spot. Here the photons detected would strike a photocathode, knocking electrons from its surface, thereby creating a detectable current as they move towards the anode. Typically, this signal without amplification, was of the order of μA. Making detection, and separation from background noise, a significant problem. Nowadays the pointillistic detectors used are photon multiplier tubes (PMTs) or avalanche photo-diodes (APDs) illustrated in **Figure 1.42** – although hybrid detector systems are becoming increasing utilised, combining aspects from both systems[106] - allowing for amplification of the signal and greater sensitivity.

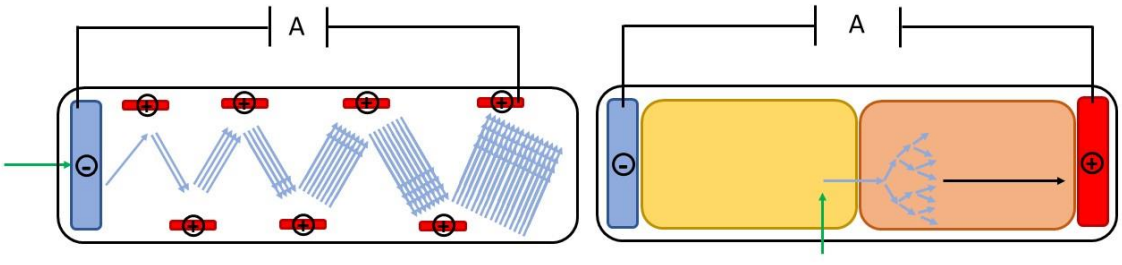

Figure 1.42 Schematic representation of common pointillistic detectors, PMT (left) and APD (right).

PMTs operate by allowing light to hit a photocathode (blue) generating an electron (light blue arrow) which proceeds to be accelerated down the tube *via* the presence of a high

voltage. A series of dynodes (red) bounce this electron down the tube while simultaneously releasing more photo-electrons, amplifying the current to be measured (A). APDs involve light hitting a semi conductive material and generating an electron-hole pair; an electron that was occupying a specific energy level is displaced, leaving behind a "hole" in the energy level which behaves as if it were a positive charge carrier. The electron is accelerated through the avalanche region (orange) creating a cascade of further electron holes, multiplying the signal (A) that is detected when these electrons reach the anode.

1.4 Multiphoton excitation

1.4.1 Principles of multiphoton excitation

First proposed theoretically by Goeppert-Mayer in 1931, multiphoton excitation (MPE) originated with the doctoral dissertation of two-photon quantum transitions in atoms.[107] Constituting part of the work that would lead to the first Nobel prize in theoretical physics awarded to a woman. This photophysical event could not be experimentally observed until the development of laser light sources[108] with the first proposed two photon excitation (2PE) effect being recorded in 1961.[109]

MPE is based upon the proposal that if absorbed simultaneously – within approximately 10^{-18} s – multiple lower energy photons may promote the same electronic excitation, *via* a virtual state, as a single higher energy photon (Illustrated by the Jablonski diagram in **Figure 1.43**).[110] A phenomenon that is, under normal conditions, incredibly unlikely. Illustrated with an analogy by Denk, one of the principal minds behind multiphoton imaging; a single molecule of rhodamine, if exposed to direct sunlight, will absorb a

single photon approximately once per second, while a two photon absorption event will occur once every 10 million years.[111]

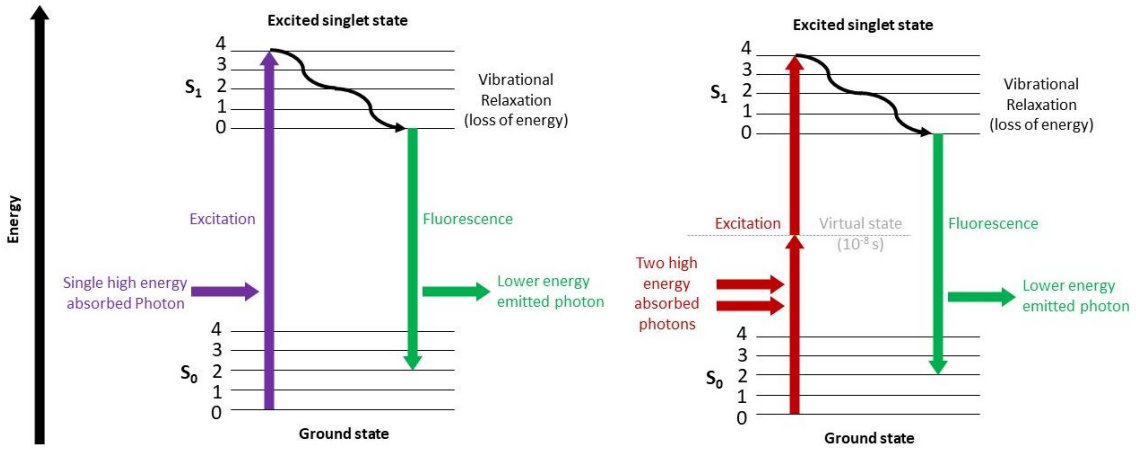

Figure 1.43 A comparison of the Jablonski diagrams for single photon (left) and two photon (right) excitation.

This low probability can be represented as a molecules two-photon cross section (2PCS). Each molecule possesses an innate property known as the absorption cross section; the probability that a photon passing through the molecule will be absorbed multiplied by the average cross-sectional area of the molecule, usually given the symbol **σ**.[112] This can be extended, giving each molecule a 2PCS i.e. a measurement of how likely a two-photon absorption event is to occur. Typically reported in the units of Goeppert-Mayer (**GM**) where one GM is 10^{-50} cm^4 s $photon^{-1}$. This can be used to calculate the total number of absorbed photons per unit time ($\mathbf{N_{abs}}$), which is directly related to the two-photon fluorescence (**F(t)**) shown in **Equation 1.8** and **Equation 1.9**.

$$N_{abs} = \int_V dV\sigma C(r,t)I^2(r,t)$$

Equation 1.8

$$F(t) = \frac{1}{2} \emptyset \eta N_{abs}$$

Equation 1.9

Where **V** is the illuminated sample volume, **C** is fluorophore concentration, **I** is incident light intensity, and **ϕ** and **η** are the fluorescence quantum efficiency of the fluorophore and the fluorescence collection efficiency of the system respectively.[113]

Therefore, to overcome these inherent low 2PCS', large levels of photon flux (**Equation 1.10**) are required. Initially this was achieved with incredibly powerful lasers, preventing this technology from being used on biological systems without sample destruction. It was not until the creation of ultra-short pulsed (femtosecond) laser systems in the 1990s that the possibility of biological 2PE fluorescence was a possibility.[114]

$$\Phi = \frac{number\ of\ photons}{s\ m^2}$$

Equation 1.10

The probability of 2PE occurring is further increased by focusing the incident laser light down to a diffraction limited spot, resulting in a sub-femtolitre volume of excitation as illustrated in **Figure 1.44**. The combination of such a brief photon pulse with such a small volume results in high power lasers only increasing the local temperature of the focal plane by 0.2 K[115], leading to development of biologically non-toxic MPE.

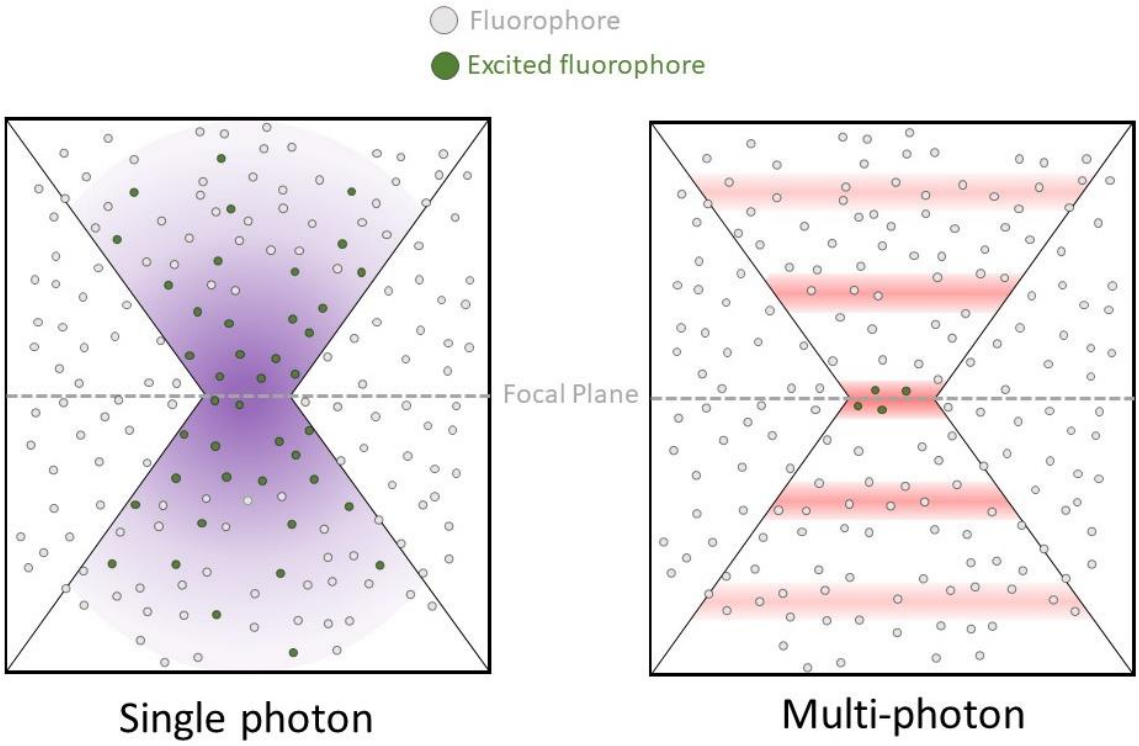

Figure 1.44 Excitation of fluorophores for single (left) and multi (right) photon systems. For single photon excitation a continuous wave of UV light is shone on the sample, exciting fluorophores throughout the whole volume. In MPE highly pulsed infrared light is pulsed so that photon density is only high enough to promote emission at the focal point.

These small excitation volumes result in multi photon excitation being inherently confocal thus providing a method of optical sectioning that pairs well with the previously discussed traditional confocal microscopy.

1.4.2 Multiphoton excitation microscopy

The use of multiphoton activation methods for fluorophores in biological samples during microscopy offers several benefits compared to traditional single photon excitation. Firstly, since the excitation is inherently limited to a sub-micron volume no confocal aperture is required to emit light from outside of the focal plane. This is useful when

imaging large tissue samples, where scattering can result in emitted light being misdirected away from the pinhole of a traditional confocal detector setup, leading to a reduction in sensitivity and contrast. This described axial confocality also allows for the inherent ability to select an isolated z-axis slice from within a sample, shown in the microscopy images in **Figure 1.45** allowing for optical sectioning from deeper within samples when compared with standard confocal imaging.[116]

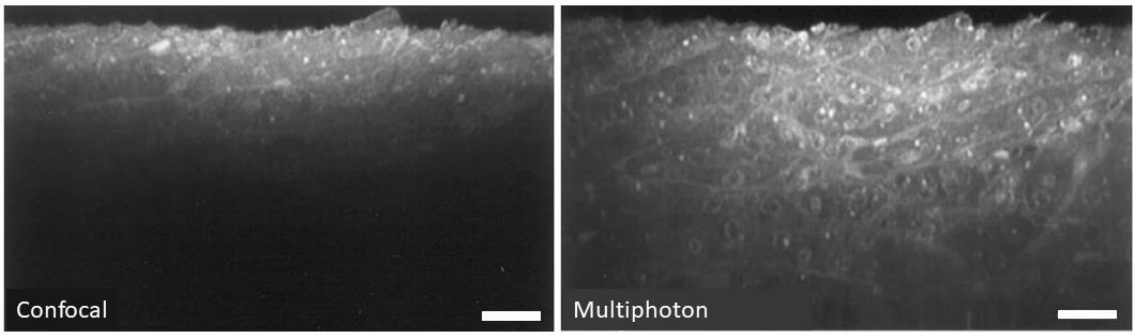

Figure 1.45 Comparison of the optical sectioning of five XZ sections through acid-fuscin stained monkey kidney, imaged by confocal and multiphoton methods. Scale bar 20 µm. Adapted from Centonze *et al*.[116]

The ability of 2PE to selectively excite fluorophores in a submicron focal spot, compared to the excitation outside of the focal plane on standard single photon lasers, is further illustrated in **Figure 1.46**. Here, two lasers (355 nm UV single and 710 nm visible two photon) are focused on the same plane within the centre of a sample of fluorescein.

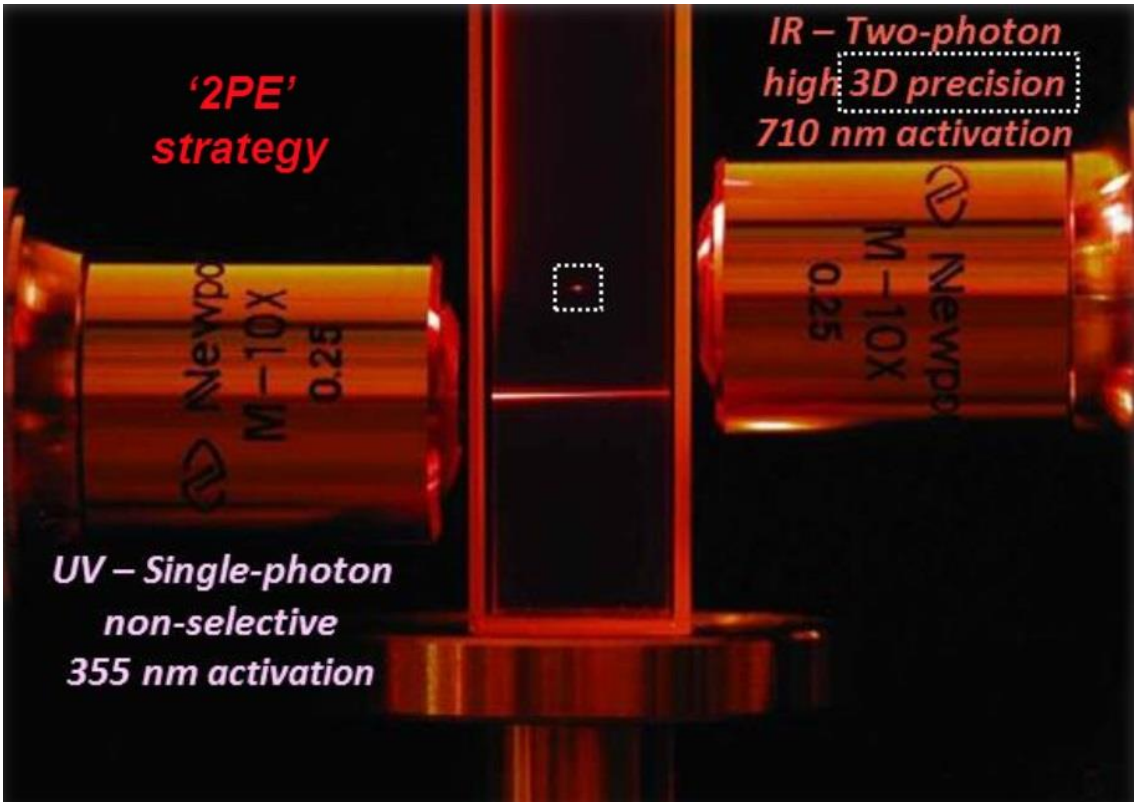

Figure 1.46 Comparison of single and two photon laser induced excitation of fluorescein.[117]

Other benefits result not just from the 2PE process itself but rather from the nature of excitation light used. Most commercial fluorescent stains for biological imaging require activation in either the visible or UV regions of the electromagnetic spectrum. Multiphoton activation results in the activation wavelength being multiplied by the factor of the photon process, i.e., 2PE will double the wavelength required (355 to 710 nm) for emission. This can be explained from fundamental principles when considering that 2PE has no effect on the energy required to promote an electron to its excited state, therefore regardless of the number of photons being used the same amount of energy must be applied to the fluorophore. Recalling the relationship between a photon's energy and wavelength, **Equation 1.11**, it is shown that for two photons to transfer the same energy as one the wavelength must double.

$$E = h\nu = \frac{hc}{\lambda}$$

Equation 1.11

This allows for biologically compatible wavelengths to be used to image previously inaccessible fluorophores. For example, the imaging of serotonin requires excitation in the deep UV (< 300 nm) preventing long term study due to the phototoxicity associated with such high energy wavelengths. However, the use of multiphoton allows for much more tolerable near infrared (NIR) wavelengths to be used resulting in live-cell imaging of previously impossible biological structures.[118]

A fundamental problem with the microscopic imaging of tissue is the penetration depth of the required wavelengths of light, with typical UV wavelengths only penetrating an estimated 100 µm.[119] It has been widely reported however that as the wavelength of light is increased, its penetration within biological tissues also rises. This is summarised in **Figure 1.47**. Therefore, an attractive benefit of multiphoton imaging is that due to the longer wavelengths used, to excite the same fluorophores as traditional confocal microscopy, information can be gained at much deeper penetration depths.[120]

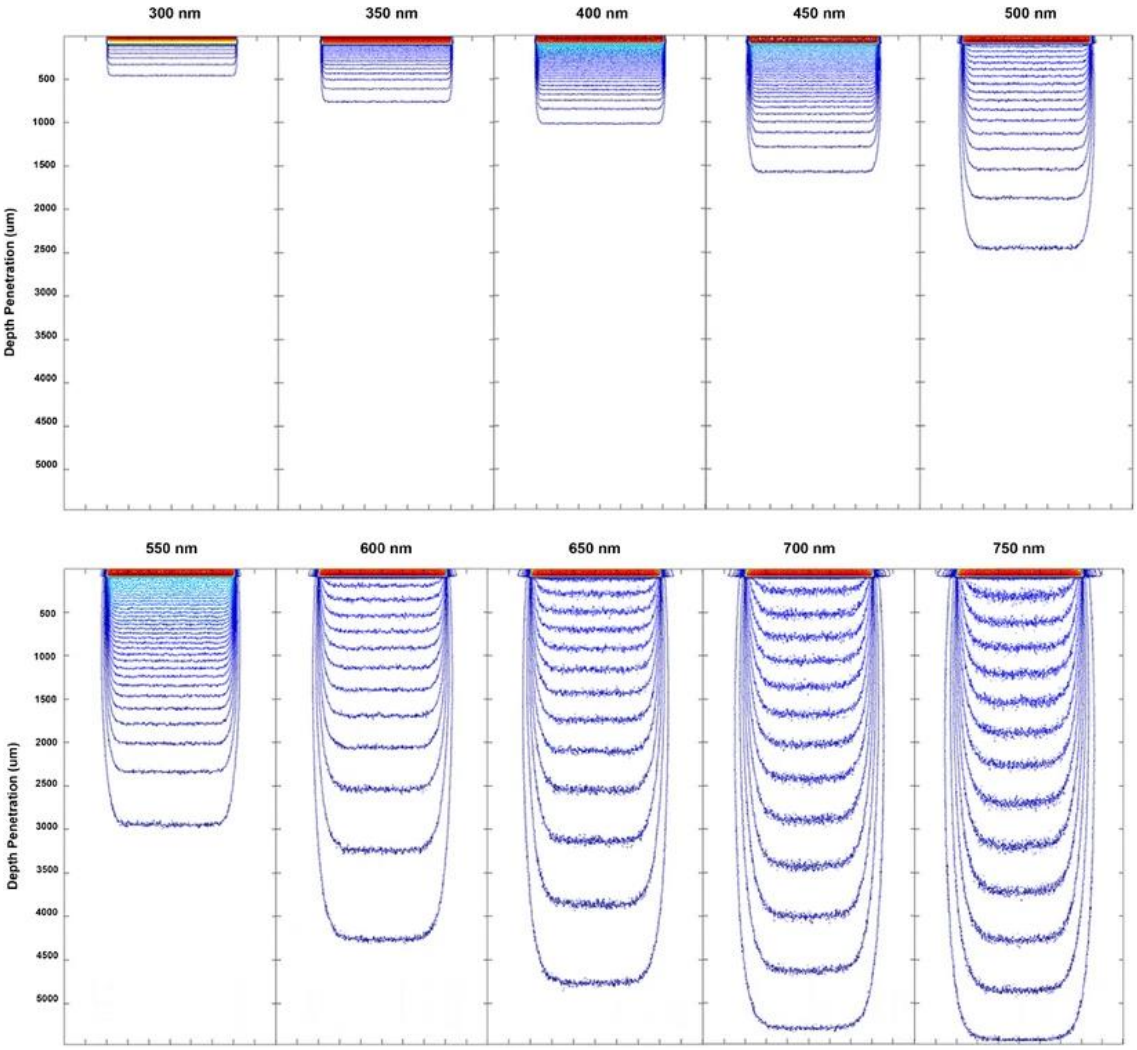

Figure 1.47 Penetration of 300-750 nm photons into tissue matrix illustrated by photon distribution. Image taken from Ash *et al*.[120]

It should be noted however, that while higher wavelength photons are able to penetrate further, it can still prove a challenge to collect the information produced by the excited fluorophore due to the scattering of any emitted light.

1.5 Project Specification

1.5.1 Project motivation and rationale

This work utilises specifically functionalised second-generation Feringa molecular motors - known as molecular nanomachines (MNMs) and shown in **Figure 1.48** - developed in collaboration with the Tour group at Rice university[121], for cell specific destruction *via* disruption of the phospholipid bilayer. With the overarching goal of working toward next generation targeted cancer therapeutics by way of multiple, distinct but overlapping, aims.

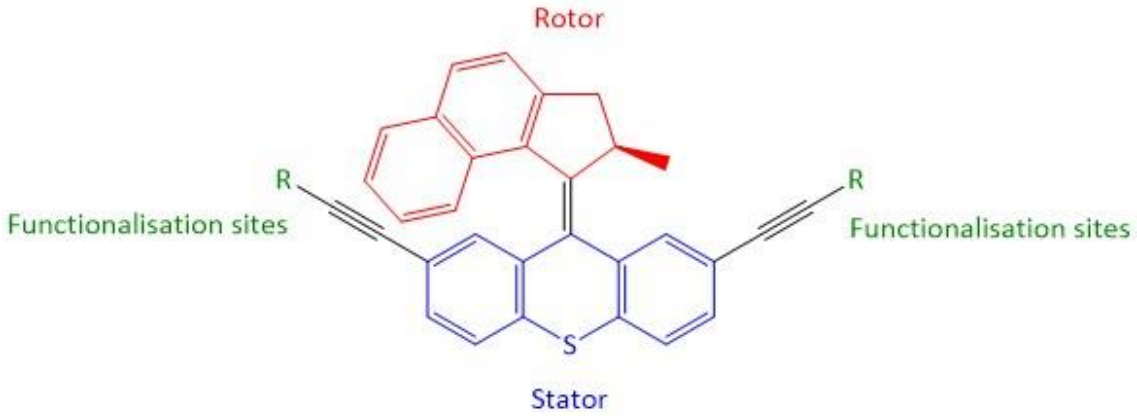

Figure 1.48 General structure of Tour MNMs, based upon second generation Feringa molecular motors.

Previously it has been shown that the nanoscale motion caused *via* the UV activation of the MNMs rotor is capable of triggering effects on the microscale, and beyond, by damaging targeted cell membranes. **Figure 1.49** illustrates this with microscopy images taken of control samples, and with the addition of an unfunctionalized (R = CH_2OH) MNM.[122]

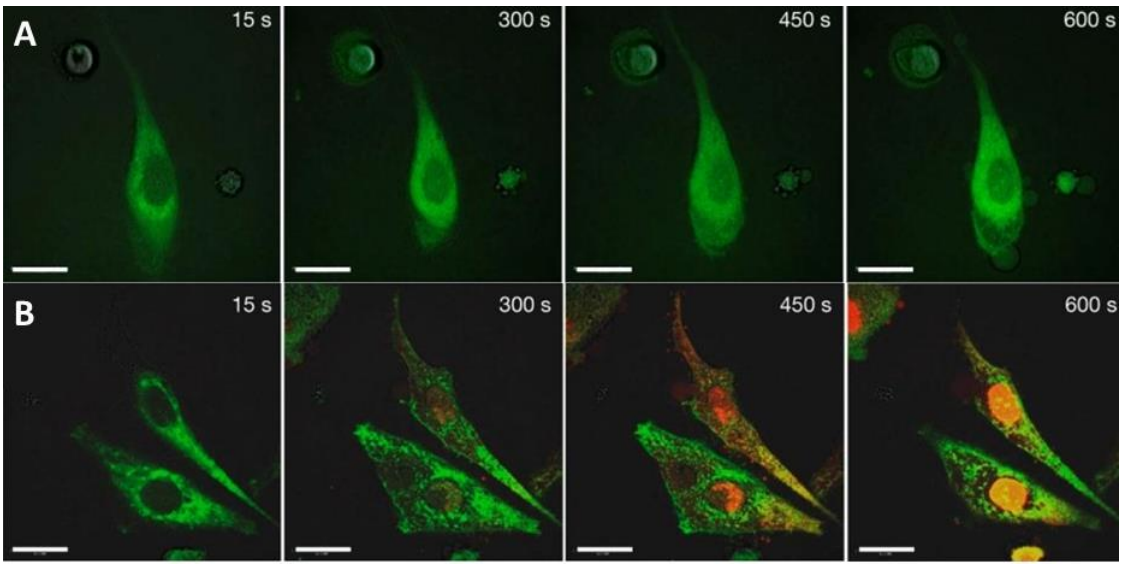

Figure 1.49 Live-cell microscopy images of NIH 3T3 cells all collected with 0.1% v/v DMSO, 1% v/v propidium iodide (λ_{ex} 543 nm, λ_{em} 600-650 nm), and constant expoure to 355 nm UV light. Overlaid mitochondrial autofluroescence (λ_{ex} 355 nm, λ_{em} 450-500 nm) (green) and propidium iodide emission (red). Scale bars 20 μm. **A** – Control sample with no added MNM. **B** – Sample with 500 nM added unfunctionalised MNM. Images adapted from Garcia-Lopez *et al*.[122]

In these microscopy experiments, as well the majority of those recorded in this work, the red fluorescent nuclear and chromosome counterstain Propidium iodide (PI, **Figure 1.50**) is used to detect cells undergoing necrosis.

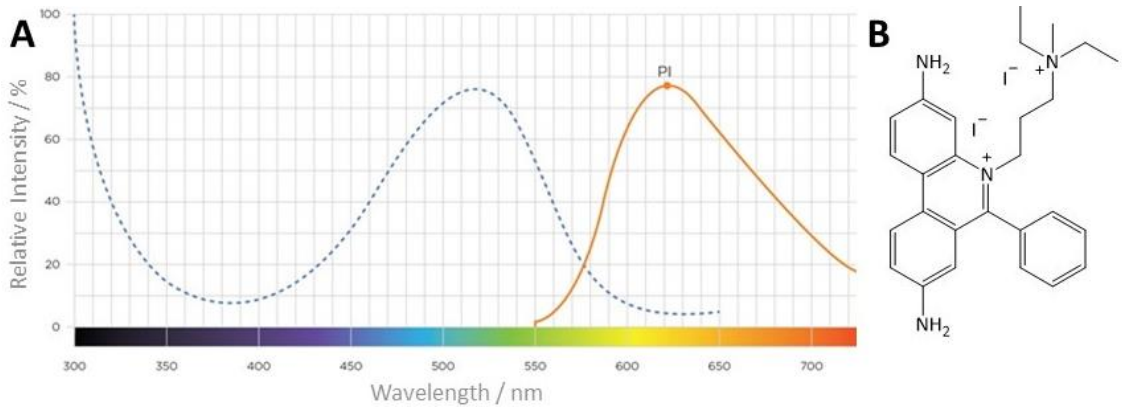

Figure 1.50 A - Absorption/emission spectrum for propidium iodide. Adapted from Beckman Coulter Life Sciences.[123] **B** - Chemical structure of propidium iodide.

PI is an intercalating agent which acts as an excellent indicator of necrotic cells, showing high levels of specificity. In aqueous solution, the dye possesses excitation/emission maxima of 493 and 636 nm respectively, however this emission is incredibly weak. Yet upon binding to DNA bases an up to 30-fold increase in fluorescence intensity is observed alongside a ~15 nm hypsochromic shift. Resulting in a bright emission maximum at ~620 nm. The key to its function is its inability to cross the cellular membrane, meaning emission will only be detected once membrane integrity is compromised – that is, the cell is undergoing necrotic cell death.

Cell visualisation is aided by characteristic green autofluorescence of the mitochondria, caused by stored nicotinamide adenine (pyridine) dinucleotide (NAD(P)H),[124] when exposed to the UV light (355 nm) used for MNM activation. This is illustrated by the absorption emission spectrum in **Figure 1.51**.

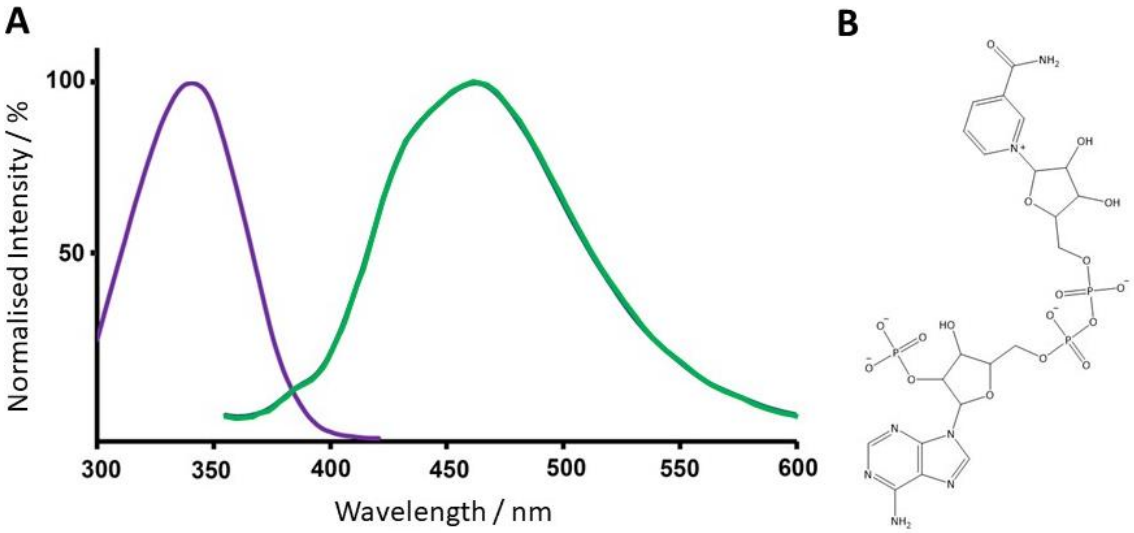

Figure 1.51 A - Absorption/emission spectrum for NAD(P)H. Adapted from Blacker *et al*.[125] **B** - Chemical structure of NAD(P)H.

The images presented in **Figure 1.49** show that mouse skin fibroblast (NIH 3T3) cells, dosed with 0.1% v/v DMSO, will tolerate exposure to 355 nm UV light for a minimum of 600 seconds (**A**). However, upon the addition of 500 nM unfunctionalised MNM necrosis will start from as early as 300 s as indicated by red PI fluorescence from within the nucleus (**B**). These results illustrate the possibility of utilising MNMs for cell specific necrosis induction.

Previous work has also been carried out validating that these MNMs can be successfully activated by a two-photon process, effectively shifting the activation wavelength from 355 nm UV to a more biologically compatible 710 nm NIR. These results are shown in the microscopy images in **Figure 1.52**.

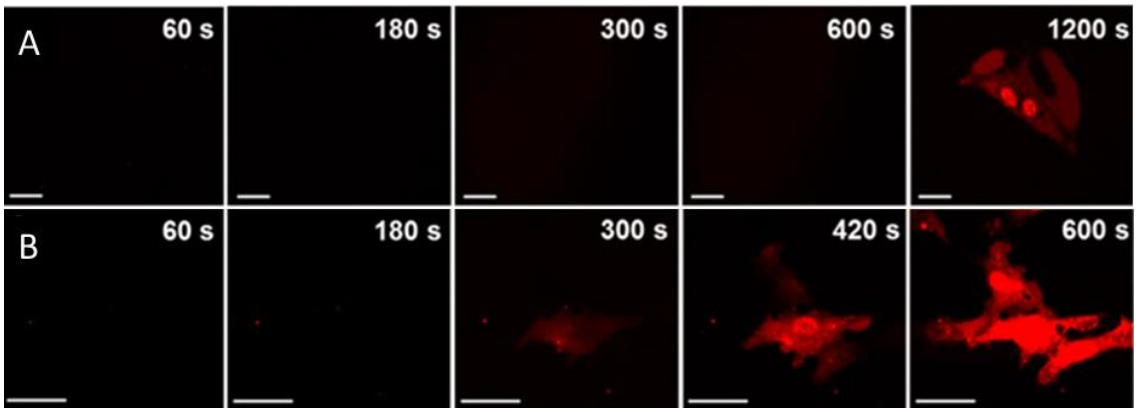

Figure 1.52 Live-cell microscopy images of PC3 cells all collected with 0.1% v/v DMSO, 1% v/v propidium iodide (λ_{ex} 543 nm, λ_{em} 600-650 nm), and constant expoure to 710 nm NIR light. PI emission shown in red. Scale bars 20 µm. **A** – Control sample with no added MNM. **B** – Sample with 500 nM added unfunctionalised MNM. Images adapted from Liu *et al*.[117]

Here, human prostate cancer (PC3) cells are shown to tolerate 1200 seconds of 710 nm light exposure before undergoing necrosis, shown again by bright PI emission at ~620 nm. However, when dosed with 1µM unfunctionalised MNM the time to necrosis onset (TTN) falls to 300 seconds. Thereby confirming that the fundamental Tour MNM structure can both undergo two photon activation (2PA), and that this activation is great enough to achieve a similar cell killing effect as previously seen with single photon UV activation.

1.5.2 Project aims and objectives

The aims of this project continue off this previously established work to build towards the overarching goal of developing this technology into a next generation cancer therapeutic. In brief, these aims are as follows:

I. Establish methods to identify and categorise photophysical, photodynamic, and photothermal impact of molecular machines on biological systems, and determine MNM mechanism of action.

II. Examine the properties for several diamine functionalised MNMs, with particular focus on shifting the activation wavelength.

III. Investigate MNMs functionalised with addends known for increase cell uptake, such as polyethylene glycol (PEG) and triphenylphosphine (TPP) to assess whether activation of MNMs from within a cell is possible.

IV. Develop of a new system and procedure for multiphoton activation of MNMs using for biologically favourable wavelengths, achieving consistency in results based upon proof-of-concept work.

V. Combine the previous aims to enable multiphoton activation of MNMs within cells as a method of induce previously unavailable cell death pathways such as apoptosis.

The following chapters detail work carried out towards these aims described above. In chapter two, studies into the MNMs used throughout this work are carried out to determine a specific mechanism of action. Attempting to separate, and study individually, any effects caused by photodynamic, photomechanical, and photothermal processes when activating the rotary process of MNMs. Chapter three summarises a systemic investigation into how functionalisation of these MNMs with various diamine addends, on both the rotor and stator, effect the activation wavelength, internalisation properties, and cell killing ability of the nanomachines. In chapter four the lengthy process behind deigning and troubleshooting a novel method for NIR activation of MNMs on a newly installed multiphoton capable system is presented. Chapter five uses

all the previously acquired data and knowledge to study MNM functionalised with specifically designed groups aimed at promoting internalisation within the cellular targets, activate them with 710 nm NIR light *via* the non-linear multiphoton process, and use these principles to induce previously impossible routes towards cell death. All with the goal of designing new, cell specific, biologically favourable, MNM based therapeutics.

1.6 Molecular nanomachine database

Below is a catalogue of the specifically functionalised MNMs used throughout the work that follows. These will be re-presented during the relevant chapters of work in more appropriate sizes. Throughout this work references will be made back to the "MNM database", this is simply a way of collecting all the MNMs used throughout the project in one place for the convenience of the reader.

The compounds presented herein were synthesised by our collaborators in Prof. James Tour's lab at Rice university. However, for comprehensiveness the synthetic methods utilised are reported in methods **Chapter 6**. The relevant published works covering the synthesis of each MNM are also referenced within **Table 1.1**.

Table 1.1 The MNM database – a catalogue of MNM structures relevant to this work.

Similarly functionalised MNMs have been grouped together for conciseness.

MNM Number	Chemical Structure
MNM 1[126]	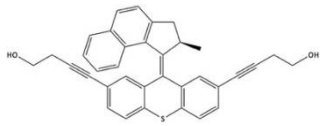
MNM 2, 3, 4[127]	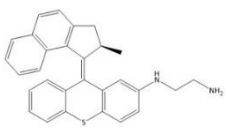 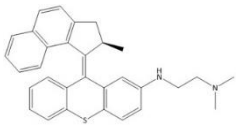 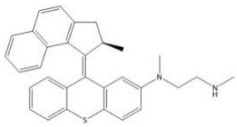
MNM 5, 6[127]	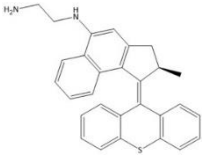 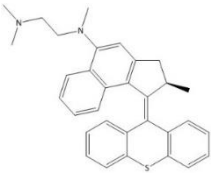
MNM 7[128]	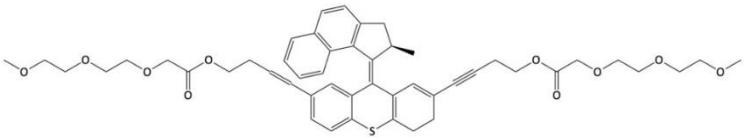
MNM 8[128]	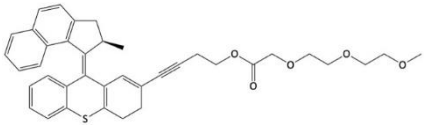
MNM 9[129]	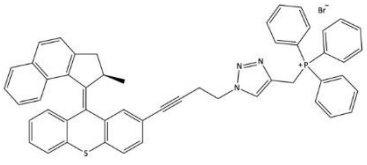
MNM 10[129]	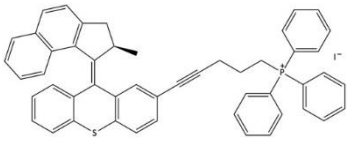

1.7 References

1 T. I. A. for R. on Cancer (IARC), Global Cancer Observatory, https://gco.iarc.fr/, (accessed 16 October 2023).

2 S. Dattani, F. Spooner, H. Ritchie and M. Roser, *Our World Data*.

3 A.-M. Florea and D. Büsselberg, *Cancers*, 2011, **3**, 1351–1371.

4 F. P. Harmers, W. H. Gispen and J. P. Neijt, *Eur. J. Cancer Oxf. Engl. 1990*, 1991, **27**, 372–376.

5 R. M. Lowenthal and K. Eaton, *Hematol. Clin.*, 1996, **10**, 967–990.

6 M. S. Ricci and W.-X. Zong, *The Oncologist*, 2006, **11**, 342–357.

7 S. Lakshmanan, G. K. Gupta, P. Avci, R. Chandran, M. Sadasivam, A. E. S. Jorge and M. R. Hamblin, *Adv. Drug Deliv. Rev.*, 2014, **71**, 98–114.

8 G. Chu, H. Hayakawa and P. Berg, *Nucleic Acids Res.*, 1987, **15**, 1311–1326.

9 D. Liu, L. Wang, Z. Wang and A. Cuschieri, *Nano Lett.*, 2012, **12**, 5117–5121.

10 Y. Zhou, *J. Healthc. Eng.*, 2012, **4**, 223–254.

11 D. Popescu, I. Stelian, A. G. Popescu, N. Neac and M.-L. Flonta, 2006, **16**, 39–56.

12 P. Soman, W. Zhang, A. Umeda, Z. J. Zhang and S. Chen, *J. Biomed. Nanotechnol.*, 2011, **7**, 334–341.

13 F. Peng, Y. Tu and D. A. Wilson, *Chem. Soc. Rev.*, 2017, **46**, 5289–5310.

14 J. F. Kelly, M. E. Snell and M. C. Berenbaum, *Br. J. Cancer*, 1975, **31**, 237–244.

15 P. Agostinis, K. Berg, K. A. Cengel, T. H. Foster, A. W. Girotti, S. O. Gollnick, S. M. Hahn, M. R. Hamblin, A. Juzeniene, D. Kessel, M. Korbelik, J. Moan, P. Mroz, D. Nowis, J. Piette, B. C. Wilson and J. Golab, *CA. Cancer J. Clin.*, 2011, **61**, 250–281.

16 United States, US5002962A, 1991.

17 J. Glaeser, A. M. Nuss, B. A. Berghoff and G. Klug, in *Advances in Microbial Physiology*, ed. R. K. Poole, Academic Press, 2011, vol. 58, pp. 141–173.

18 S. Grapengiesser, F. Gudmundsson, O. Larkö, M. Ericson, A. Rosén and A.-M. Wennberg, *Clin. Exp. Dermatol.*, 2002, **27**, 493–497.

19 G. Jori and J. D. Spikes, *J. Photochem. Photobiol. B*, 1990, **6**, 93–101.

20 H. Shibaguchi, H. Tsuru, M. Kuroki and M. Kuroki, *Anticancer Res.*, 2011, **31**, 2425–2430.

21 J. R. McCarthy, *Nanomed.*, 2009, **4**, 693–695.

22 T. Sasaki and J. M. Tour, *Tetrahedron Lett.*, 2007, **48**, 5821–5824.

23 V. Balzani, A. Credi, F. M. Raymo and J. F. Stoddart, *Angew. Chem. Int. Ed.*, 2000, **39**, 3348–3391.

24 W. Kühne, *Untersuchungen über das Protoplasma und die Contractilität*, W. Engelmann, Leipzig, 1864.

25 I. Rayment, W. R. Rypniewski, K. Schmidt-Bäse, R. Smith, D. R. Tomchick, M. M. Benning, D. A. Winkelmann, G. Wesenberg and H. M. Holden, *Science*, 1993, **261**, 50–58.

26 K. Kinbara and T. Aida, *Chem. Rev.*, 2005, **105**, 1377–1400.

27 R. P. Feynman, *APS Annu. Meet.*

28 H. Rau, *J. Photochem.*, 1984, **26**, 221–225.

29 S. Shinkai, A. Yoshioka, H. Nakayama and O. Manabe, *J. Chem. Soc. Perkin Trans. 2*, 1990, **0**, 1905–1909.

30 G. Binnig and H. Rohrer, *Angew. Chem.*, 1987, **99**, 622–631.

31 J.-M. Lehn, *Angew. Chem. Int. Ed. Engl.*, 1990, **29**, 1304–1319.

32 P. D. Boyer, *Angew. Chem. Int. Ed Engl.*, 1998, **37**, 2296–2307.

33 The Nobel Prize in Chemistry 2016, https://www.nobelprize.org/prizes/chemistry/2016/summary/, (accessed 17 October 2023).

34 J.-P. Sauvage and C. Dietrich-Buchecker, *Molecular Catenanes, Rotaxanes and Knots: A Journey Through the World of Molecular Topology*, John Wiley & Sons, 2008.

35 D. B. Amabilino and J. F. Stoddart, *Chem. Rev.*, 1995, **95**, 2725–2828.

36 B. L. Feringa and W. R. Browne, *Molecular Switches*, John Wiley & Sons, 2011.

37 J. Howard, *Nature*, 1997, **389**, 561–567.

38 W. E. Moerner and M. Orrit, *Science*, 1999, **283**, 1670–1676.

39 R. H. Fillingame, *Science*, 1999, **286**, 1687–1688.

40 R. L. Cross and T. M. Duncan, *J. Bioenerg. Biomembr.*, 1996, **28**, 403–408.

41 D. Stock, A. G. W. Leslie and J. E. Walker, *Science*, 1999, **286**, 1700–1705.

42 R. Yasuda, H. Noji, K. Kinosita and M. Yoshida, *Cell*, 1998, **93**, 1117–1124.

43 I. Stupka, Y. Azuma, A. P. Biela, M. Imamura, S. Scheuring, E. Pyza, O. Woźnicka, D. P. Maskell and J. G. Heddle, *Sci. Adv.*, 2022, **8**, eabj9424.

44 J.-M. Lehn, *Angew. Chem. Int. Ed. Engl.*, 1988, **27**, 89–112.

45 S. Anderson and H. L. Anderson, in *Templated Organic Synthesis*, John Wiley & Sons, Ltd, 1999, pp. 1–38.

46 M.-J. Blanco, M. Consuelo Jiménez, J.-C. Chambron, V. Heitz, M. Linke and J.-P. Sauvage, *Chem. Soc. Rev.*, 1999, **28**, 293–305.

47 P. R. Ashton, T. T. Goodnow, A. E. Kaifer, M. V. Reddington, A. M. Z. Slawin, N. Spencer, J. F. Stoddart, C. Vicent and D. J. Williams, *Angew. Chem. Int. Ed. Engl.*, 1989, **28**, 1396–1399.

48 I. Thomas. Harrison and Shuyen. Harrison, *J. Am. Chem. Soc.*, 1967, **89**, 5723–5724.

49 P. L. Anelli, N. Spencer and J. F. Stoddart, *J. Am. Chem. Soc.*, 1991, **113**, 5131–5133.

50 W. Clegg, C. Gimenez-Saiz, D. A. Leigh, A. Murphy, A. M. Z. Slawin and S. J. Teat, *J. Am. Chem. Soc.*, 1999, **121**, 4124–4129.

51 C. Gong and H. W. Gibson, *Angew. Chem. Int. Ed. Engl.*, 1997, **36**, 2331–2333.

52 E. Wasserman, *J. Am. Chem. Soc.*, 1960, **82**, 4433–4434.

53 A. S. Baluna, A. Galan, D. A. Leigh, G. D. Smith, J. T. J. Spence, D. J. Tetlow, I. J. Vitorica-Yrezabal and M. Zhang, *J. Am. Chem. Soc.*, 2023, **145**, 9825–9833.

54 D. A. Leigh, A. Murphy, J. P. Smart, M. S. Deleuze and F. Zerbetto, *J. Am. Chem. Soc.*, 1998, **120**, 6458–6467.

55 D. A. Leigh, K. Moody, J. P. Smart, K. J. Watson and A. M. Z. Slawin, *Angew. Chem. Int. Ed. Engl.*, 1996, **35**, 306–310.

56 W. Yang, Y. Li, H. Liu, L. Chi and Y. Li, *Small*, 2012, **8**, 504–516.

57 F. d'Orchymont and J. P. Holland, *Angew. Chem.*, 2022, **134**, e202204072.

58 L. Kortekaas and W. R. Browne, *Chem. Soc. Rev.*, 2019, **48**, 3406–3424.

59 W. Zhou, D. Chen, J. Li, J. Xu, J. Lv, H. Liu and Y. Li, *Org. Lett.*, 2007, **9**, 3929–3932.

60 J. Berná, D. A. Leigh, M. Lubomska, S. M. Mendoza, E. M. Pérez, P. Rudolf, G. Teobaldi and F. Zerbetto, *Nat. Mater.*, 2005, **4**, 704–710.

61 K. Kinbara, T. Muraoka and T. Aida, *Org. Biomol. Chem.*, 2008, **6**, 1871–1876.

62 A. B. Gardner, S. Howard, T. C. Waddington, R. M. Richardson and J. Tomkinson, *Chem. Phys.*, 1981, **57**, 453–460.

63 T. Muraoka and K. Kinbara, *J. Photochem. Photobiol. C Photochem. Rev.*, 2012, **13**, 136–147.

64 T. Muraoka, K. Kinbara and T. Aida, *Nature*, 2006, **440**, 512–515.

65 D. J. Cárdenas, A. Livoreil and J.-P. Sauvage, *J. Am. Chem. Soc.*, 1996, **118**, 11980–11981.

66 A. Livoreil, J.-P. Sauvage, N. Armaroli, V. Balzani, L. Flamigni and B. Ventura, *J. Am. Chem. Soc.*, 1997, **119**, 12114–12124.

67 D. A. Leigh, J. K. Y. Wong, F. Dehez and F. Zerbetto, *Nature*, 2003, **424**, 174–179.

68 S. Kassem, T. van Leeuwen, A. S. Lubbe, M. R. Wilson, B. L. Feringa and D. A. Leigh, *Chem. Soc. Rev.*, 2017, **46**, 2592–2621.

69 E. R. Kay and D. A. Leigh, *Pure Appl. Chem.*, 2008, **80**, 17–29.

70 M. Baroncini, S. Silvi and A. Credi, *Chem. Rev.*, 2020, **120**, 200–268.

71 W. Gao and J. Wang, *Nanoscale*, 2014, **6**, 10486–10494.

72 S. Balasubramanian, D. Kagan, C.-M. Jack Hu, S. Campuzano, M. J. Lobo-Castañon, N. Lim, D. Y. Kang, M. Zimmerman, L. Zhang and J. Wang, *Angew. Chem. Int. Ed.*, 2011, **50**, 4161–4164.

73 J. Wu, S. Balasubramanian, D. Kagan, K. M. Manesh, S. Campuzano and J. Wang, *Nat. Commun.*, 2010, **1**, 36.

74 B. Jurado-Sánchez, M. Pacheco, R. Maria-Hormigos and A. Escarpa, *Appl. Mater. Today*, 2017, **9**, 407–418.

75 Y. Wu, X. Lin, Z. Wu, H. Möhwald and Q. He, *ACS Appl. Mater. Interfaces*, 2014, **6**, 10476–10481.

76 Y. Wu, Z. Wu, X. Lin, Q. He and J. Li, *ACS Nano*, 2012, **6**, 10910–10916.

77 T. Xu, W. Gao, L.-P. Xu, X. Zhang and S. Wang, *Adv. Mater.*, 2017, **29**, 1603250.

78 J. T. McIlwain, *An Introduction to the Biology of Vision*, Cambridge University Press, 1996.

79 D. Polli, P. Altoè, O. Weingart, K. M. Spillane, C. Manzoni, D. Brida, G. Tomasello, G. Orlandi, P. Kukura, R. A. Mathies, M. Garavelli and G. Cerullo, *Nature*, 2010, **467**, 440–443.

80 B. Feringa and H. Wynberg, *J. Am. Chem. Soc.*, 1977, **99**, 602–603.

81 N. P. M. Huck and B. L. Feringa, *J. Chem. Soc. Chem. Commun.*, 1995, 1095.

82 N. Koumura, R. W. J. Zijlstra, R. A. van Delden, N. Harada and B. L. Feringa, *Nature*, 1999, **401**, 152–155.

83 M. M. Pollard, M. Klok, D. Pijper and B. L. Feringa, *Adv. Funct. Mater.*, 2007, **17**, 718–729.

84 M. K. J. ter Wiel, R. A. van Delden, A. Meetsma and B. L. Feringa, *J. Am. Chem. Soc.*, 2005, **127**, 14208–14222.

85 J. Vicario, A. Meetsma and B. L. Feringa, *Chem. Commun.*, 2005, 5910–5912.

86 N. Koumura, E. M. Geertsema, M. B. van Gelder, A. Meetsma and B. L. Feringa, *J. Am. Chem. Soc.*, 2002, **124**, 5037–5051.

87 M. Klok, M. Walko, E. M. Geertsema, N. Ruangsupapichat, J. C. M. Kistemaker, A. Meetsma and B. L. Feringa, *Chem. – Eur. J.*, 2008, **14**, 11183–11193.

88 J. C. M. Kistemaker, P. Štacko, J. Visser and B. L. Feringa, *Nat. Chem.*, 2015, **7**, 890–896.

89 P. Roy, W. R. Browne, B. L. Feringa and S. R. Meech, *Nat. Commun.*, 2023, **14**, 1253.

90 V. García-López, P.-L. E. Chu, P.-T. Chiang, J. Sun, A. A. Martí and J. M. Tour, *Asian J. Org. Chem.*, 2015, **4**, 1308–1314.

91 Y. Shirai, A. J. Osgood, Y. Zhao, K. F. Kelly and J. M. Tour, *Nano Lett.*, 2005, **5**, 2330–2334.

92 M. W. Davidson, *Microsc. Today*, 2009, **17**, 44–47.

93 R. Hooke, J. Allestry and J. Martyn, *Micrographia, or, Some physiological descriptions of minute bodies made by magnifying glasses :with observations and inquiries thereupon*, Printed by Jo. Martyn and Ja. Allestry, printers to the Royal Society, London, 1665.

94 D. L. Spector and R. D. Goldman, *Basic Methods in Microscopy: Protocols and Concepts from Cells : a Laboratory Manual*, CSHL Press, 2006.

95 null Rayleigh, *Lond. Edinb. Dublin Philos. Mag. J. Sci.*, 1879, **8**, 261–274.

96 E. Abbe, *J. R. Microsc. Soc.*, 1883, **3**, 790–812.

97 C. M. Sparrow, *Astrophys. J.*, 1916, **44**, 76.

98 Super-Resolution Tutorial - Education - Advanced Microscopy, https://advanced-microscopy.utah.edu/education/super-res/, (accessed 30 October 2023).

99 S. S. Kaderuppan, E. W. L. Wong, A. Sharma and W. L. Woo, *IEEE Access*, 2020, **8**, 214801–214831.

100 L. Schermelleh, A. Ferrand, T. Huser, C. Eggeling, M. Sauer, O. Biehlmaier and G. P. C. Drummen, *Nat. Cell Biol.*, 2019, **21**, 72–84.

101 Granite, Stokes Shift, Fluorescence Spectroscopy, https://www.edinst.com/us/blog/what-is-the-stokes-shift/, (accessed 30 October 2023).

102 A. H. Coons, H. J. Creech, R. N. Jones and E. Berliner, *J. Immunol.*, 1942, **45**, 159–170.

103 S. J. Butler, L. Lamarque, R. Pal and D. Parker, *Chem. Sci.*, 2014, **5**, 1750–1756.

104 K. W. Dunn, M. M. Kamocka and J. H. McDonald, *Am. J. Physiol. - Cell Physiol.*, 2011, **300**, C723–C742.

105 United States, US3013467A, 1961.

106 B. Libberton, The Power HyD Detector Family, https://www.leica-microsystems.com/science-lab/life-science/power-hyd-detectors/, (accessed 31 October 2023).

107 M. Göppert-Mayer, *Ann. Phys.*, 1931, **401**, 273–294.

108 A. L. Schawlow and C. H. Townes, *Phys. Rev.*, 1958, **112**, 1940–1949.

109 W. Kaiser and C. G. B. Garrett, *Phys. Rev. Lett.*, 1961, **7**, 229–231.

110 K. W. Dunn and P. A. Young, *Nephron Exp. Nephrol.*, 2006, **103**, e33–e40.

111 W. Denk and K. Svoboda, *Neuron*, 1997, **18**, 351–357.

112 In *Oxford Dictionary of Biochemistry and Molecular Biology*, Oxford University Press, 2006.

113 C. Xu and W. W. Webb, *JOSA B*, 1996, **13**, 481–491.

114 W. Denk, J. H. Strickler and W. W. Webb, *Science*, 1990, **248**, 73–76.

115 A. Schönle and S. W. Hell, *Opt. Lett.*, 1998, **23**, 325–327.

116 V. E. Centonze and J. G. White, *Biophys. J.*, 1998, **75**, 2015–2024.

117 D. Liu, V. García-López, R. S. Gunasekera, L. Greer Nilewski, L. B. Alemany, A. Aliyan, T. Jin, G. Wang, J. M. Tour and R. Pal, *ACS Nano*, 2019, **13**, 6813–6823.

118 S. Maiti, J. B. Shear, R. M. Williams, W. R. Zipfel and W. W. Webb, *Science*, 1997, **275**, 530–532.

119 A review of the optical properties of biological tissues | IEEE Journals & Magazine | IEEE Xplore, https://ieeexplore.ieee.org/abstract/document/64354, (accessed 1 November 2023).

120 C. Ash, M. Dubec, K. Donne and T. Bashford, *Lasers Med. Sci.*, 2017, **32**, 1909–1918.

121 V. García-López, P.-T. Chiang, F. Chen, G. Ruan, A. A. Martí, A. B. Kolomeisky, G. Wang and J. M. Tour, *Nano Lett.*, 2015, **15**, 8229–8239.

122 V. García-López, F. Chen, L. G. Nilewski, G. Duret, A. Aliyan, A. B. Kolomeisky, J. T. Robinson, G. Wang, R. Pal and J. M. Tour, *Nature*, 2017, **548**, 567–572.

123 Propidium Iodide Excitation and Emission Spectrum, https://www.beckman.com/reagents/coulter-flow-cytometry/cell-health-research-assays/propidium-Iodide-spectrum, (accessed 3 November 2023).

124 O. I. Kolenc and K. P. Quinn, *Antioxid. Redox Signal.*, 2019, **30**, 875–889.

125 T. Blacker, T. Berecz, M. Duchen and G. Szabadkai, *BIO-Protoc.*, , DOI:10.21769/BioProtoc.2105.

126 V. García-López, P.-T. Chiang, F. Chen, G. Ruan, A. A. Martí, A. B. Kolomeisky, G. Wang and J. M. Tour, *Nano Lett.*, 2015, **15**, 8229–8239.

127 A. L. Santos, D. Liu, A. K. Reed, A. M. Wyderka, A. van Venrooy, J. T. Li, V. D. Li, M. Misiura, O. Samoylova, J. L. Beckham, C. Ayala-Orozco, A. B. Kolomeisky, L. B. Alemany, A. Oliver, G. P. Tegos and J. M. Tour, *Sci. Adv.*, 2022, **8**, eabm2055.

128 C. Ayala Orozco, D. Liu, Y. Li, L. B. Alemany, R. Pal, S. Krishnan and J. M. Tour, *ACS Appl. Mater. Interfaces*, 2020, **12**, 410–417.

129 T. Galbadage, D. Liu, L. B. Alemany, R. Pal, J. M. Tour, R. S. Gunasekera and J. D. Cirillo, *ACS Nano*, 2019, **13**, 14377–14387.

Chapter 2: Identifying and categorising photophysical, photodynamic, and photothermal effects of molecular machines on biological systems

Summary: *This chapter is based upon previously published co-first author work in Advanced Materials: "Distinguishing Molecular Mechanical Action from Photothermal and Photodynamic Behavior by Thomas S. Bradford, Jacob L. Beckham, Ciceron Ayala-Orozco, Ana L. Santos, Dallin Arnold, Alexis R. van Venrooy, Victor Garcia-Lopez, Robert Pal, and James M. Tour.*[1] *First acting as a perspective on the various methods by which molecular machines can impact biological systems and how to distinguish between them by using examples from this project as well as previous work. Secondly, providing an investigation specifically into the behaviour of Tour MNMs in an effort to illuminate their mechanism of action. By undertaking experiments focusing on ROS generation (photodynamic behaviour), and localised heating (photothermal effects), to determine if our proposed justification, the MNM induced cellular damage is caused by light induced rotary motion (photophysical behaviour), holds true.*

2.1 Introduction

Since investigations began on Tour MNMs, a wide range of biological applications have been illustrated. Including facilitating cellular ion transport[2,3], controlling mechanosensitive cell signalling pathways[4], destruction of microorganisms[5,6], as well as the targeted opening of cellular membranes.[7] MNMs are appealing for therapeutic applications due to the principle that the effects they exhibit depend in some way on the ability of the molecule to actuate in response to irradiation; a topic covered extensively in Chapter 1. In some cases the impact of the MNM on the biological system is considered to be directly caused *via* the rotary motion exerting a mechanical force on tissue.[8] However, in other instances while the induced effect is similar it is believed that

the outcome is caused by an additional "downstream effect" such as increase in local temperature (photothermal) caused by the MHz rotation of the MNM.[9] Isolating the mechanism behind the effects of molecular actuation present a significant challenge, especially when the outcome – i.e. membrane disruption – is the same regardless of process.

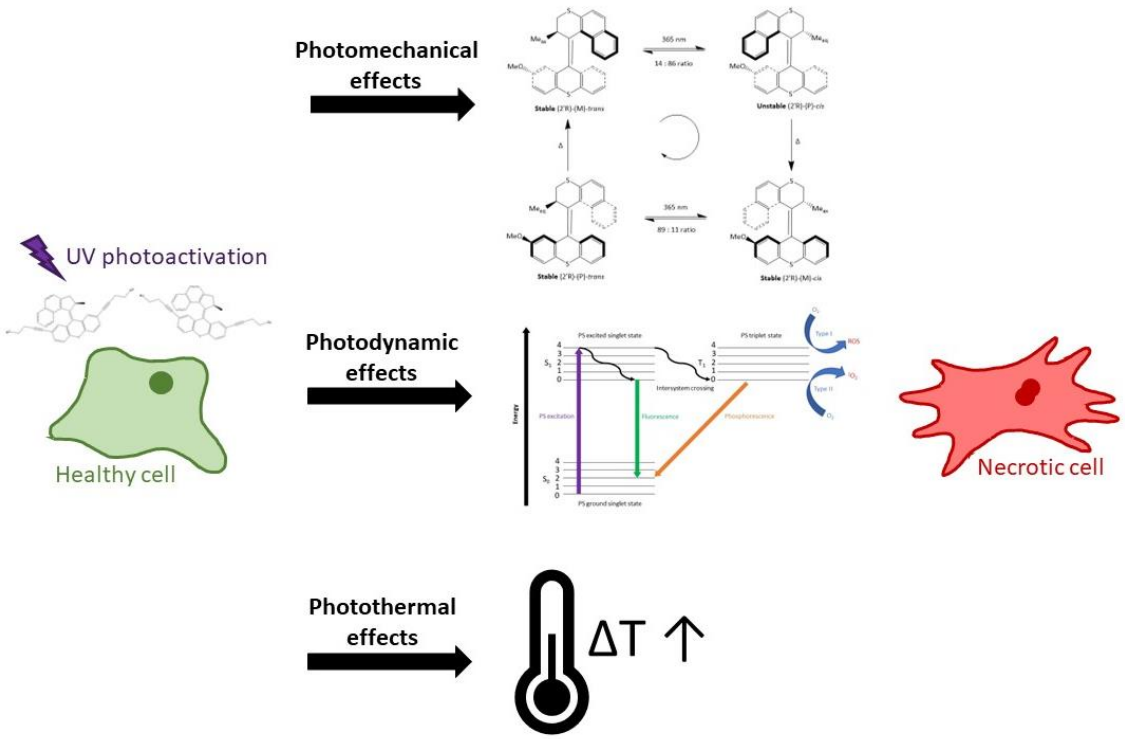

Figure 2.1 An illustrative example of the difficulty in distinguishing between multiple photoinduced mechanisms of action all resulting in the same observable result - induced necrotic cell death *via* the photoactivation of MNMs.

The irradiation of light-absorbing molecules, such as MNMs, within biological systems has previously been shown to drive a wide array of effects outside of molecular motion. With photothermal and photodynamic being the most widely studied and utilised for therapeutic applications, covered extensively in a number of review articles.[10,11] Photothermal systems generate the desired biological outcome *via* the generation of heat by light activation, whereas photodynamic technologies use ROS such as

superoxides or other reactive radical species to achieve the same – as illustrated when discussing PDT in Chapter 1. To effectively develop further treatments leveraging the unique photomechanical properties of MNMs it is vital to be able to distinguish between those biological effects caused by molecular movement, and any potential photothermal and photodynamic processes with any photostimulation experiments.

It is non-trivial to distinguish between these various phenomena that can be caused by the irradiation of fluorophores in cellular environments, and to isolate which effects are caused solely by unique MNM photomechanical action. Herein a combination of new experiments and previous work will be evaluated to provide both an experimental roadmap for investigating the underlying mechanisms of photoinduced therapeutics, and to conclusively understand the impact shown on cells by the MNMs used within this project.

2.2 Isolating photomechanical action of Tour MNMs

The highly tuneable rotary properties of second-generation Feringa motors that Tour MNMs base their core structure upon allow for the study of so-called negative control molecules. An idea which acts as the linchpin when attempting to isolate therapeutic effects arising solely from photoinduced molecular motion. The ideal negative control is designed to mimic the properties of the experimental system as closely as possible whilst changing a single photomechanical property in a known way to detect sources of spurious causal inference.[12] In the example of MNM induced cell death, to detect any additional properties of the MNM that can trigger necrosis onset without molecular rotation. This is achieved using molecules with altered rotor properties, such as much slower rotation speeds – in the Hz, compared to MHz range – or lacking unidirectionality.

An illustrative example of this experimental process is shown by a set of MNMs used in recent work triggering intercellular calcium waves (ICW) *via* the activation of inositol-triphosphate-mediated signalling pathways. In this case, HEK293 cell membranes were mechanically perturbed by the activation of amine functionalised MNMs to stimulate calcium release from the endoplasmic reticulum. Fluorescent tracker Fluo-4 (**Figure 2.2**), which shows switch-on fluorescence when binding to [Ca^{2+}] was employed to track changes in intracellular calcium concentrations.[13]

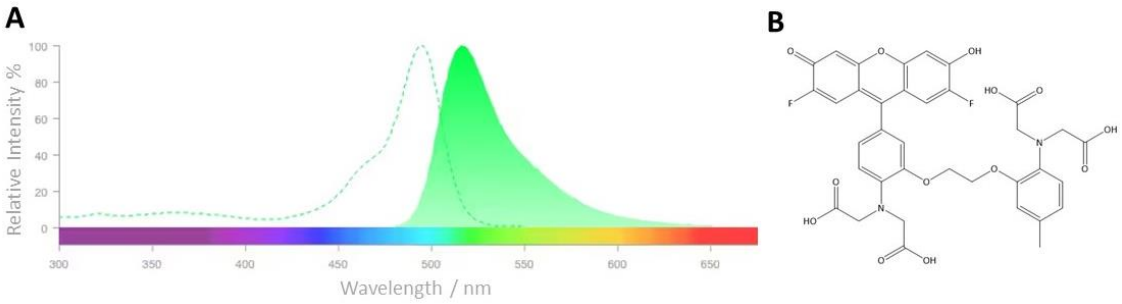

Figure 2.2 A - Absorption emission spectrum of Fluo-4 Ca^{2+} responsive dye, adapted from ThermoFisher Scientific.[14] **B** - Chemical structure of Fluo-4.

Figure 2.3 summarises the MNMs utilised for this experiment as an example of the targeted rotor modifications used to determine if the observed phenomena, in this case increased intracellular calcium concentration, are triggered by photomechanical effects and to aid in the separation of possible intertwined photodynamic, mechanical, and thermal processes.

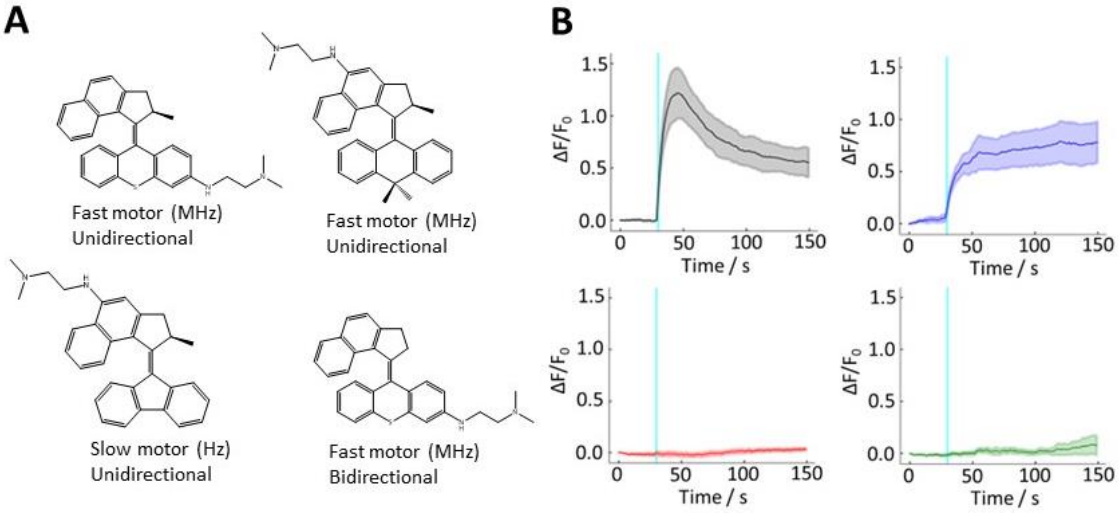

Figure 2.3 A - MNM set used to determine which phenomena result from photomechanical action-based effects; containing multiple fast, slow, and non-unidirectional motors. **B** - Representative normalised fluorescence intensity plots for HEK293 internalised fluo-4 treated with 8 µM of the corresponding MNM (increased to 24 µM for the slow control species). Each solid trace represents average data from 6 individual cells, with the shaded area illustrating standard deviation from the mean. All cell exposed to a 250 ms pulse width delivered to a circular area of diameter 5 µm at 3.2×10^2 W cm^{-2}. Irradiation of 400 nm, 15 mW photodiode laser, pixel dwell time of 140 ms with a 212 µm x 212 µm field of view. For all plots, the cyan line indicates the time of stimulus presentation. Results adapted from Beckham, J. L. *et al*.[4]

This work employed two distinct classes of fast rotating MNMs with different stator structures, as well as vital slow rotating and non-unidirectional control species. One of the key principles when working to isolate the effects of molecular motion is to ensure the experimental conditions between the positive results and the negative control remain consistent, with only the rotary properties of the MNM being altered. In this example the slow rotating unidirectional control species possessed a lower absorption coefficient for the employed wavelength of light. As such, the working concentration added to cell samples was increased by a factor of three. Double the intensity of laser

light was also employed to activate the rotor in a further effort to maintain consistency between all species under investigation. In addition to absorption coefficients, the partition coefficient and polar surface area of each MNM was monitored to ensure all control species were as chemically similar to the lead compounds as possible.

The resulting fluorescent traces shown in **Figure 2.3** found that increased fluo-4 intensity was only observed with MNMs with fast rotating (MHz) uni-directional properties. Slower MNMs (Hz) displayed no appreciable increase in intercellular Ca^{2+} concentration, and similarly fast rotating bi-directional rotors also failed to illicit any discernible ICW response. Working under the proposition that any molecules that only differentiate by rotation speed / directionality will possess near identical photodynamic and photothermal properties, allows for it to be drawn that ICW effects are solely due to this MNM species' photomechanical capabilities. This illustrates a general strategy employed when selecting MNMs for a coherent study of photomechanical behavior. Similar methodology is used for all work carried out on the possible biological application of MNMs, summarised in **Table 2.1**, providing a solid basis for eliminating the possibility of photodynamic and photothermal interference.

Table 2.1 A summary of previous MNMs core structures designed to have differing rotation speeds with similar chemical properties. Used following the previously described strategy to study photomechanical processes by separating photodynamic and photothermal effects. Specific side chain functionalisation removed for clarity.

Previous study:	Fast (MHz) unidirectional	Fast (MHz) bidirectional	Slow (Hz) control #1	Slow (Hz) control #2
UV activation of the rotor[15]				
Mammalian cell necrosis[7]				
Bacterial cell death[5]			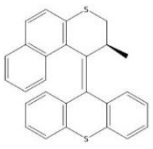	
Fungal cell death[16]				

When taken in aggregate across the whole area of research a consistent hierarchy of effectiveness for MNMs to exhibit photomechanical action is shown; fast unidirectional MNMs drive more activity – i.e., faster TTN – than MNMs with the same speed but with bidirectional motion, which in turn drive more activity than slow MNMs or switches who rarely show any difference when compared with solvent-only controls.

Results that are found not to follow this observed pattern indicate that other light driven phenomena are having an impact. An example of this was seen using a different class of hemithioindigo (HTI) molecular motor, shown in **Figure 2.4**, for antibacterial applications. Here it was found that molecules that underwent a switch-like motion (HTI v,vi,vii) demonstrated increased antibacterial activity instead of the usually preferred full rotation (HTI i, ii, iii, iv),.[17]

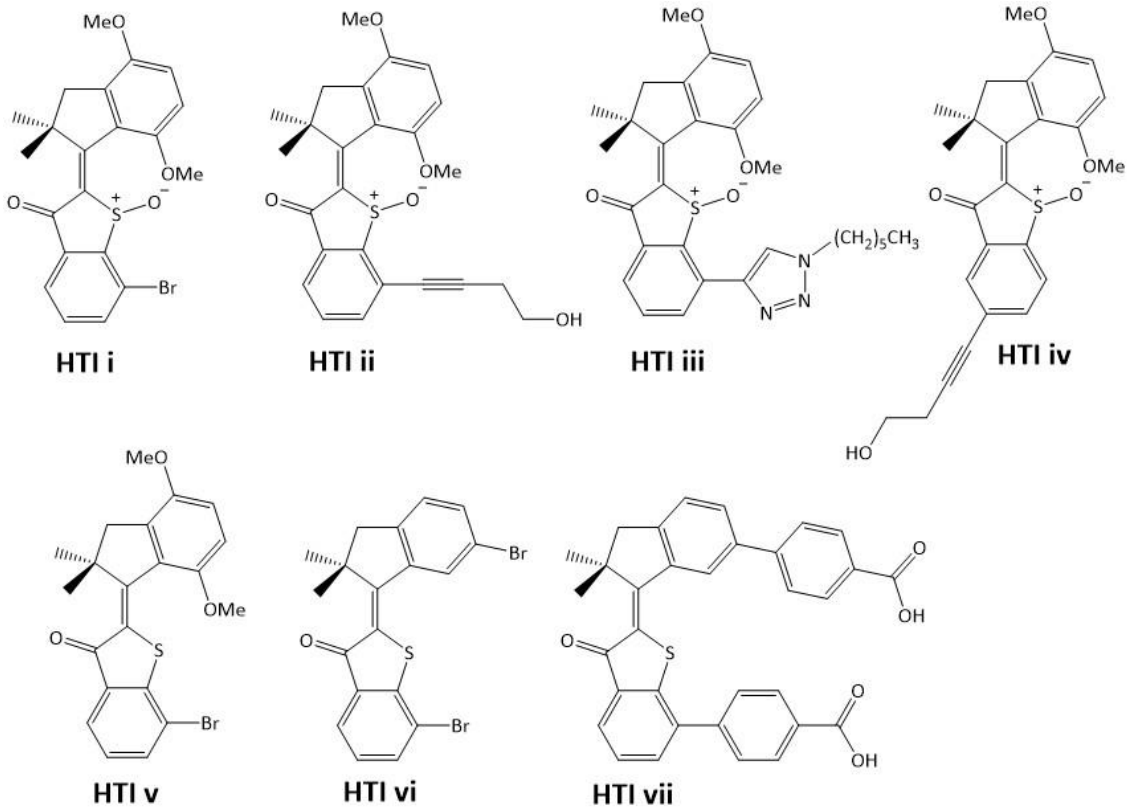

Figure 2.4 Structures of HTI based molecular motors (i-iv), and molecular switches (v-vii).

The use of non-rotating negative control species resulted in the detection of this anomalous result, and further investigation found that the antibacterial properties for this class of molecular motor was incredibly sensitive to the presence of ROS scavenging species (**Figure 2.5**).

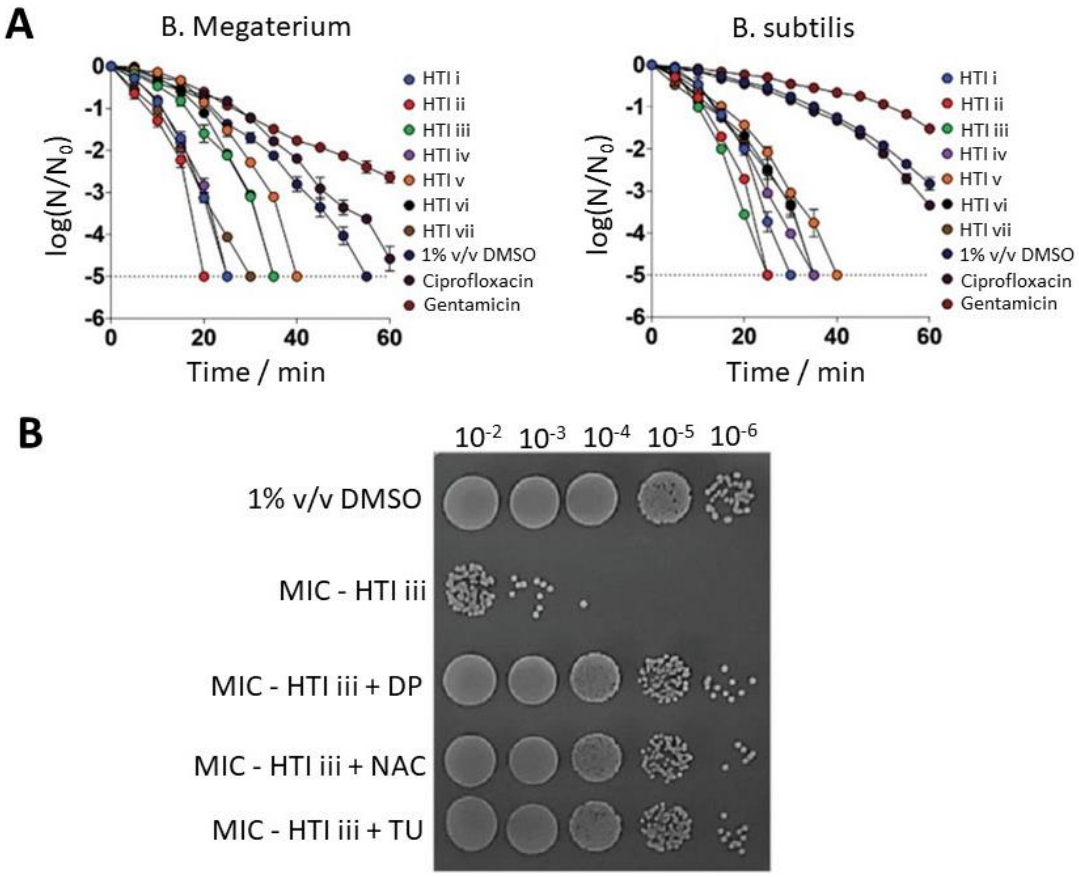

Figure 2.5 A – Time-dependent reduction in bacterial colonies (expressed as the logarithm of base 10 of the ratio between the colony forming unit value at every time point and the colony forming unit value at time zero) for two exponentially growing gram-positive bacterial strains excited with 455 nm light at 65 mW cm^{-2} with each HTI compound as well as a solvent control and two tested conventional antibodies. **B** - Representative spot plate of *S. aureus* grown with and without iron supplementation, iron scavenger 2,2'-dipyridyl (DP, 0.5 × 10−3 M) representative ROS scavengers (NAC, TU) followed by addition of 1% DMSO solvent control or 1× MIC of HTI iii and irradiated with 455 nm light (39 J cm^{-2}). Adapted from Santos *et al*.[17]

These results led to the conclusion that HTI type motors in fact lead to cell death *via* a predominantly photodynamic pathway; in stark contrast to the Feringa based Tour MNMs studied throughout this project. Where, as previously discussed, slow rotating switch-like analogues show greater TTN compared to fast rotating motors. This is

despite some results showing that slow rotor based Tour MNMs can produce higher levels of singlet oxygen when compared to their fast rotor analogues (illustrated by the UV-Vis spectra of the singlet oxygen trap 1,3-diphenylisobenzofuran[18] (DPBF) in the presence of both compounds, shown in **Figure 2.6**)[6], further illustrating the dominance of photomechanical processes in the biological applications of this class of molecule. These results do, however, underpin the importance of the negative controls within the experimental set up of this work and, as with any photoactivated process, ROS production is possible and should be thoroughly considered when determining the mechanism of action.

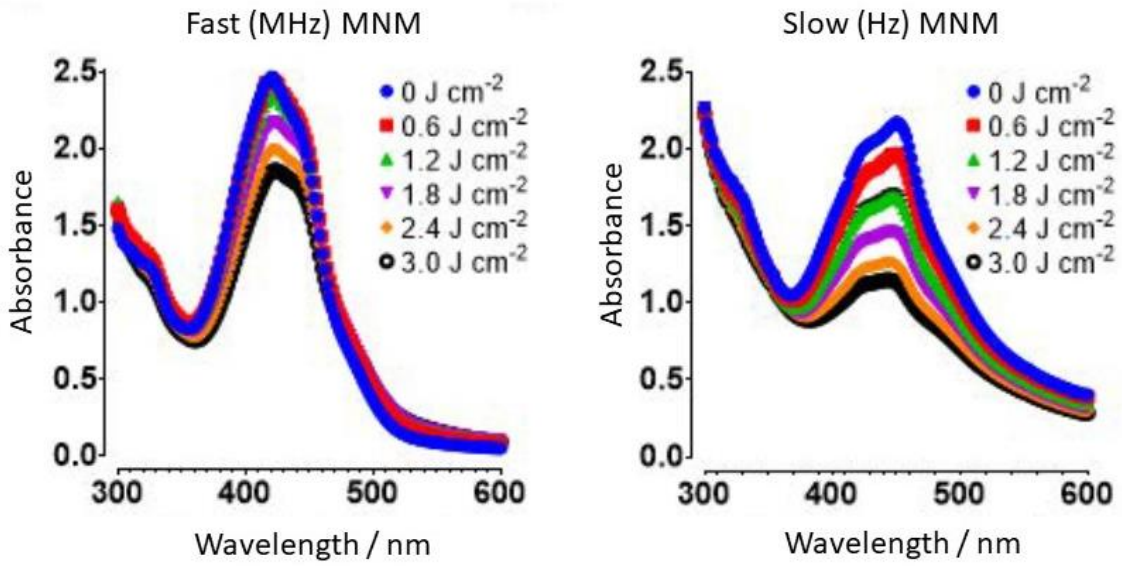

Figure 2.6 UV-Vis spectra of singlet oxygen trap DPBF in the presence of fast motor (left) and slow motor (right). Showing a greater reduction in peak intensity for the slow motor sample, implying higher levels of singlet oxygen generation.

2.3 Investigations into possible photodynamic effects by Tour MNMs

When irradiating any light-absorbing species, even MNMs which have had their photomechanical properties thoroughly studied as discussed previously, it is critical to consider the generation of ROS. This importance is raised further in this project due to

the use of UV radiation which has the possibility of ROS generation independent of any MNM addition. Specifically, UV wavelengths have been reported to alter catalase within biological systems, up-regulating nitric oxide synthase synthesis; as well as causing a decrease in protein kinase K expression, again leading to increased levels of ROS production within the cell.[19] Previous work[20] has utilised oxidative stress detection reagents to track the presence of any ROS species within prostatic adenocarcinoma PC-3 cells during 405 nm activated MNMs TTN experiments. Achieved using the proprietary, oxygen sensitive, CellROX™ green reagent (**Figure 2.7**, structure under patent) which is weakly fluorescent in its reduced form but exhibits bright green fluorescence upon oxidation by ROS and subsequent binding to DNA within the cell.

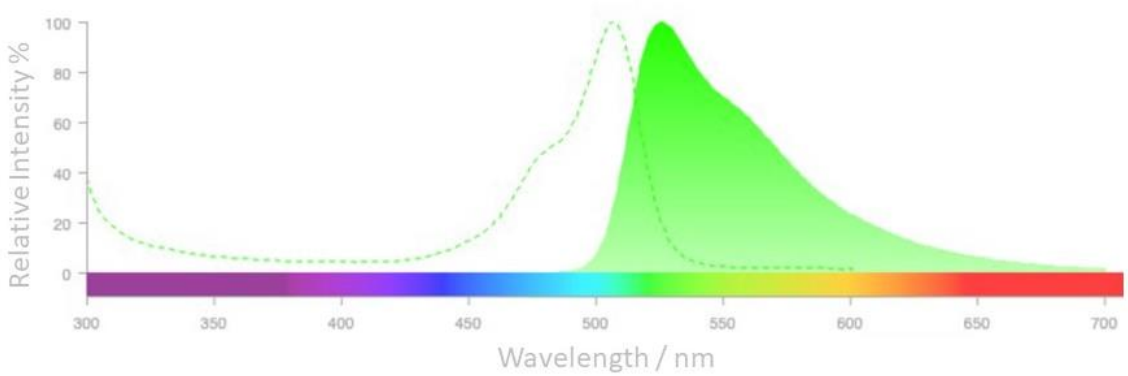

Figure 2.7 Absorption emission spectrum for CellROX™ green reagent.

Interestingly the results of this investigation found that for various MNMs with different rotor properties (**Figure 2.8**) ROS production – indicated by intensity of CellROX™ emission at 520 nm – was suppressed relative to 405 nm light exposure alone.

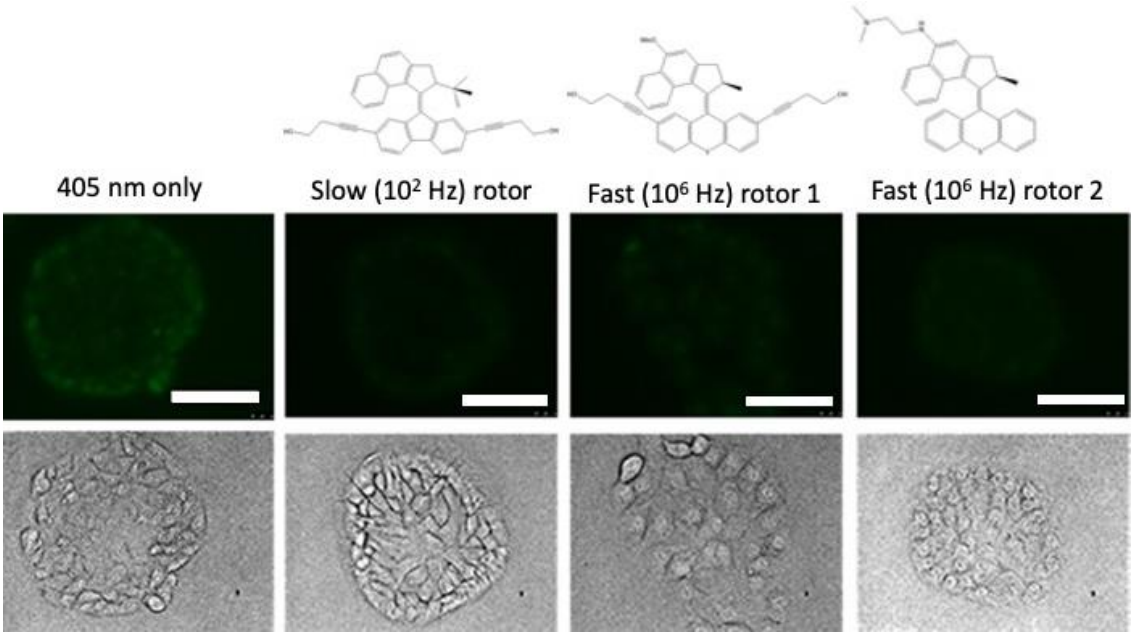

Figure 2.8 Fluorescence microscopy images illustrating ROS quenching by MNMs *via* the tracking of CellROX™ green intensity within KPC cells. Images taken after 5 minutes of treatment with 405 nm light under a fluorescence microscope at a light power of 25 mW (estimated light flux of 500 mW cm^{-2}). MNMs added at 8 µM with all samples including control having 0.1% v/v DMSO. Scale bars 100 µm

This can be rationalised by the UV-induced addition of singlet oxygen across carbon–carbon double bonds, which has been extensively studied for the photooxidation of perylene structures.[21] Rationalising that the twisted alkene axle at the core of the MNM structure can act as an ROS quencher by the proposed scheme for a illustrative unfunctionalised MNM core in **Figure 2.9**, regardless of rotation speed.

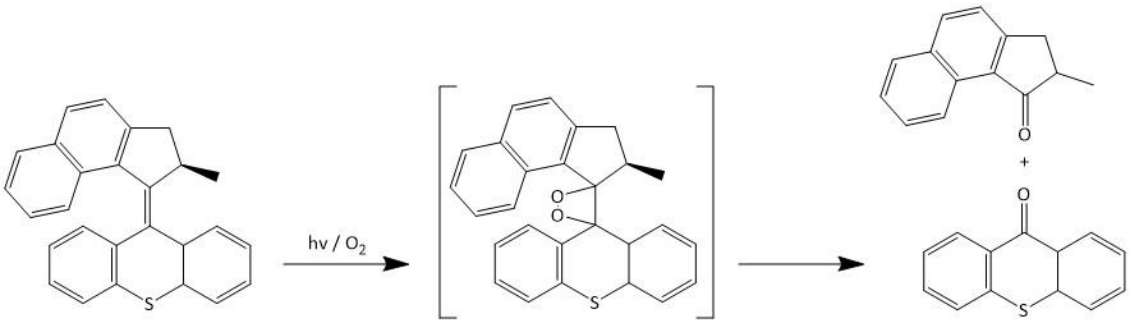

Figure 2.9 Proposed scheme illustrating possible MNM ROS scavenging ability.

This previous work with ROS sensitive fluorescent dyes attempts to track the production of ROS in mammalian cells during MNM experiments. However, the most useful methods for isolating the effects of ROS during photostimulation experiments and separating these from similar processes driven by molecular mechanical action, are those utilising ROS scavengers and measuring the effect they impart on the results; especially applicable for TTN experiments. Importantly, scavenger based methods remain applicable for both lipophilic and hydrophilic motor design.[22,23]

The first step towards constructing free radical scavenger-based experiments is the careful consideration of which species to use. One of the key points of consideration is the purported low cell permeability of commonly utilised free radical scavengers, such as N-acetyl cysteine (NAC) and Thiourea (TU), shown in **Figure 2.10**. Whose free radical scavenging ability comes either directly from the redox potential of thiols, or *via* secondary effects from increasing glutathione levels in the cells.[24] Suggesting that experiments with these molecules cannot be used to conclusively discount photodynamic involvement in MNM induced necrosis.

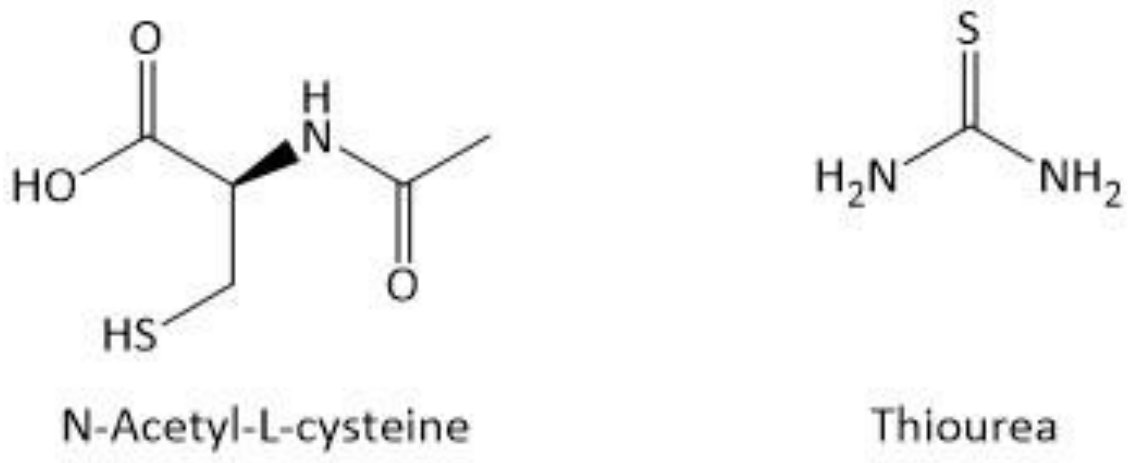

Figure 2.10 Structures of common ROS scavenging species NAC and TU.

While it is true that there are conflicting reports on the readiness of these antioxidant molecules to internalise within cells; with numerous reports claiming NAC to be a membrane-permeable cysteine precursor[25–27], while others suggesting the observed enhancement of intracellular thiol levels upon NAC dosing are due to cellular penetration of cysteine formed extracellularly by N-deacetylation.[28] It is important to note that there are many examples within previously reported literature showing these ROS scavenging molecules being used to great effect as a means of mitigating photodynamically induced cell death.[22,23] Furthermore, it should be stated that for unfunctionalised MNMs little to no cellular internalisation is shown. With the nanomachines instead showing pit-like cell-surface localisation, as described in previously published work.[7] Thus, it is reasonable to conclude that the membrane permeability of the utilised antioxidant would have a negligible effect on its ability to prevent any possible photodynamic process behind MNM-induced necrosis.

Following this, it can be confidently assumed that provided a MNM with no internalising functionalisation is used dosing with therapeutically active concentrations of NAC / TU would reduce cellular damage caused by any proposed photodynamic processes. Allowing for further separation of photomechanical and photodynamic results. It has been shown in previous literature that NAC has an appreciable antioxidant effect in NIH 3T3 cell lines, with concentrations tested up to 40 mM.[29] Utilising this principle, experiments were carried out using two different concentrations of unfunctionalised Tour machine **MNM 1** (as seen in the molecular nanomachine database – Chapter 1); 0.5 µM in line with previously discussed, and further reported, work and 50 µM to further investigate any possible concentration dependent photodynamic effects. Allowing an opportunity to observe if there is an appreciable difference in mechanism

of action, either photomechanical, photodynamic, or a combination of the two, between these two regimes.

First, 0.5 µM **MNM 1** was applied to samples of NIH 3T3 - a fibroblast cell line isolated from a mouse NIH/Swiss embryo – with and without both 1 mM added NAC (compared to control samples in **Figure 2.11**) and 1 mM TU (**Figure 2.12**). Followed by excitation of the rotor with 355 nm UV light. As in previously summarised work, cell necrosis is qualified by the fluorescence intensity of propidium iodide (λ_{max} = 615 nm) within the nucleus.

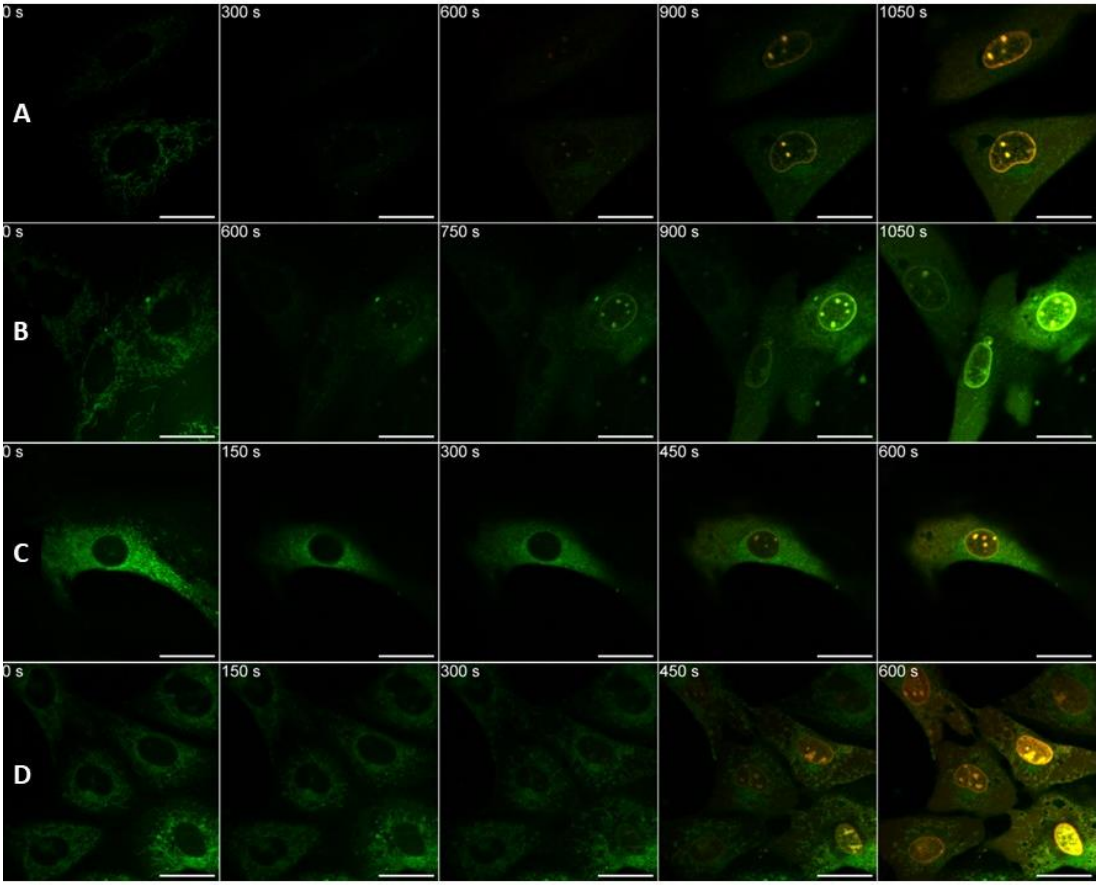

Figure 2.11 Microscopic observation of cell death caused by excitation at 355 nm (UV-exposure times are shown for each image), quantified by the observation of PI fluorescence within the nucleus. **A** – Control sample: NIH 3T3 cells loaded with 100 nM PI and 0.1% DMSO. **B** – NIH 3T3 cells loaded with 100 nM PI, 0.1% DMSO, and 1 mM NAC. **C** - NIH 3T3 cells loaded with 0.5 µM **MNM 1**, 100 nM PI. **D** - NIH 3T3 cells loaded with 0.5 µM **MNM 1**, 100 nM PI, and 1 mM NAC. All image sets collected after 30 minutes incubation after dosing procedure. Overlaid channels of PI fluorescence (λ_{ex} = 543 nm, 0.2 mW; λ_{em} = 600-700 nm), and mitochondrial autofluorescence (λ_{ex} = 355 nm, 20 mW, 400 nJ per voxel; λ_{em} = 440-460 nm). All scale bars set to 25 µm.

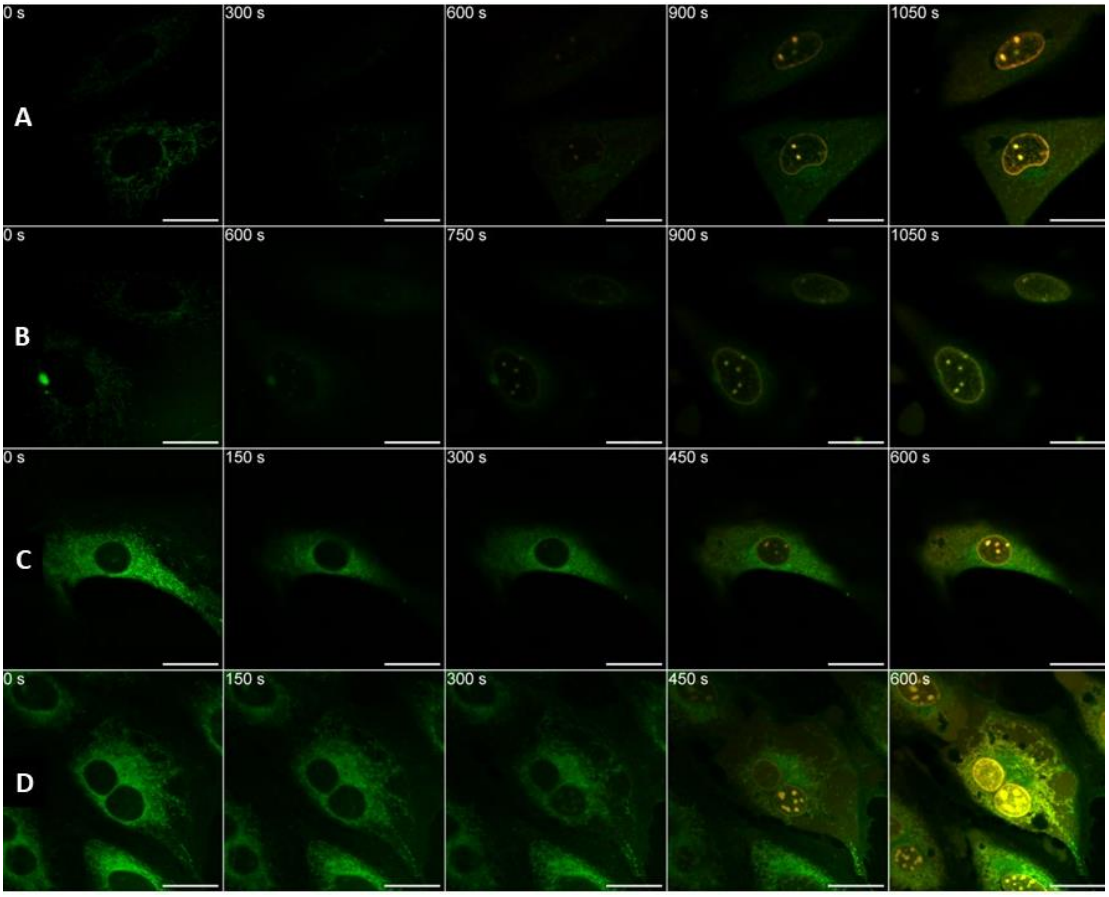

Figure 2.12 Microscopic observation of cell death caused by excitation at 355 nm (UV-exposure times are shown for each image), quantified by the observation of PI fluorescence within the nucleus. **A** – Control sample: NIH 3T3 cells loaded with 100 nM PI and 0.1% DMSO. **B** – NIH 3T3 cells loaded with 100 nM PI, 0.1% DMSO, and 1 mM TU. **C** - NIH 3T3 cells loaded with 0.5 µM **MNM 1**, 100 nM PI. **D** - NIH 3T3 cells loaded with 0.5 µM **MNM 1**, 100 nM PI, and 1 mM TU. All image sets collected after 30 minutes incubation after dosing procedure. Overlaid channels of PI fluorescence (λ_{ex} = 543 nm, 0.2 mW; λ_{em} = 600-700 nm), and mitochondrial autofluorescence (λ_{ex} = 355 nm, 20 mW, 400 nJ per voxel; λ_{em} = 440-460 nm). All scale bars set to 25 µm.

It can clearly be seen that supplementing the samples with 1 mM of either of the discussed ROS scavenging molecules had a negligible effect on the TTN caused by the UV activation of 0.5 µM **MNM 1**. First PI fluorescence is observed by eye by ~ 450 s for

all samples where photoactivated MNM 1 is present, regardless of any additional NAC or TU added.

Interesting results are observed however for NAC dosed control samples; it is shown that the addition of NAC has a non-negligible impact on the time taken for MNM free UV-induced necrosis to occur – i.e., samples with the addition of only 100 nM PI and 0.1% v/v DMSO. PI fluorescence first exhibits an increase in intensity within the nucleus of the studied cell after 510 seconds of constant 355 nm irradiation of the control slide (**Figure 2.11 A**), compared to 690 seconds upon the addition of 1 mM NAC (**Figure 2.11 B**). This further confirms that the scavenger molecules selected for this series of experiments can effectively reduce ROS generation under these conditions, meaning they are able to cross the cell membrane and alter the TTN if any photodynamic effects are in play. Considering one of the primary accepted mechanisms behind UV-induced necrosis in mammalian cells is the photochemical generation of ROS within the phospholipid bilayer.[19] This combination of results helps to illustrate that at these concentrations, used in all previous TTN experiments, photomechanical effects dominate the mechanism behind MNM induced cell death.

To further assess this, and conclusively invalidate the presence of any photodynamic processes impacting these results the concentration of ROS scavenger was raised to 5 mM. The highest concentration tolerated before overall cellular health was found to be negatively impacted by either compound, indicated by a dimmer, less uniform, mitochondrial network when using this amount of NAC (**Figure 2.13 B**) showing that this was indeed the maximum concentration possible before impacting on the results (TTN) of the experiment. However, even at these higher levels of scavenger no additional antioxidant effect was shown; 0.5 µM **MNM 1** still showed effective acceleration of

necrosis onset with both NAC (**Figure 2.13**) and TU (**Figure 2.14**) consistent with previous experiments with 1 mM, and no additional, antioxidant species.

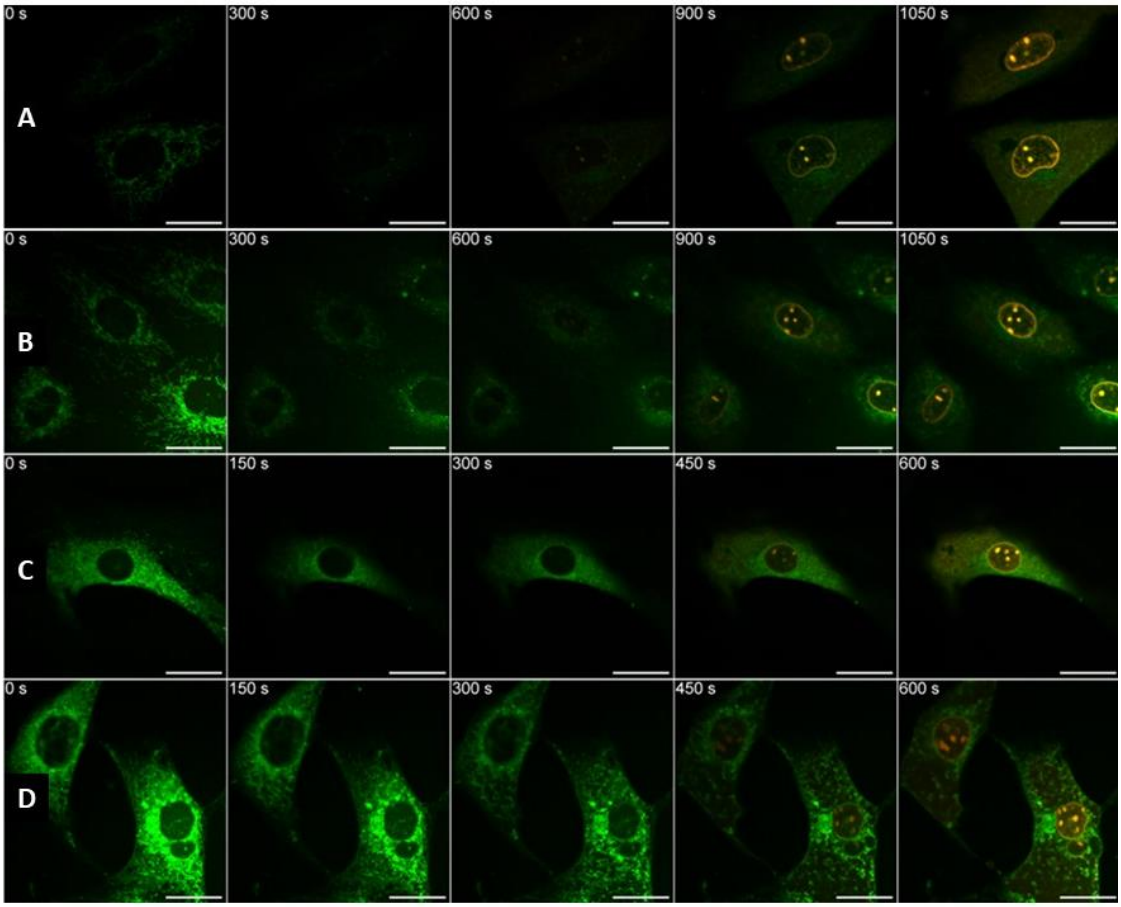

Figure 2.13 Microscopic observation of cell death caused by excitation at 355 nm (UV-exposure times are shown for each image), quantified by the observation of PI fluorescence within the nucleus. **A** – Control sample: NIH 3T3 cells loaded with 100 nM PI and 0.1% DMSO. **B** – NIH 3T3 cells loaded with 100 nM PI, 0.1% DMSO, and 5 mM NAC. **C** - NIH 3T3 cells loaded with 0.5 µM **MNM 1**, 100 nM PI. **D** - NIH 3T3 cells loaded with 0.5 µM **MNM 1**, 100 nM PI, and 5 mM NAC. All image sets collected after 30 minutes incubation after dosing procedure. Overlaid channels of PI fluorescence (λ_{ex} = 543 nm, 0.2 mW; λ_{em} = 600-700 nm), and mitochondrial autofluorescence (λ_{ex} = 355 nm, 20 mW, 400 nJ per voxel; λ_{em} = 440-460 nm). All scale bars set to 25 µm.

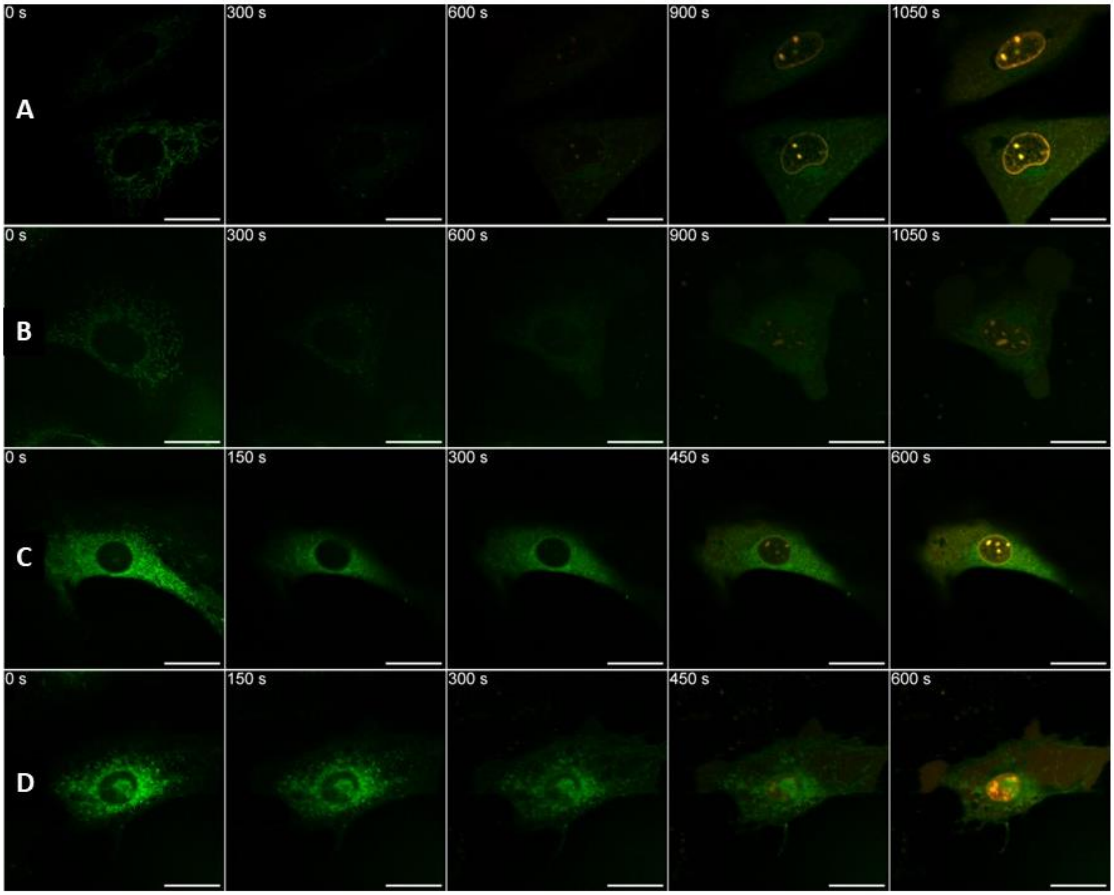

Figure 2.14 Microscopic observation of cell death caused by excitation at 355 nm (UV-exposure times are shown for each image), quantified by the observation of PI fluorescence within the nucleus. **A** – Control sample: NIH 3T3 cells loaded with 100 nM PI and 0.1% DMSO. **B** – NIH 3T3 cells loaded with 100 nM PI, 0.1% DMSO, and 5 mM TU. **C** - NIH 3T3 cells loaded with 0.5 µM **MNM 1**, 100 nM PI. **D** - NIH 3T3 cells loaded with 0.5 µM **MNM 1**, 100 nM PI, and 5 mM TU. All image sets collected after 30 minutes incubation after dosing procedure. Overlaid channels of PI fluorescence (λ_{ex} = 543 nm, 0.2 mW; λ_{em} = 600-700 nm), and mitochondrial autofluorescence (λ_{ex} = 355 nm, 20 mW, 400 nJ per voxel; λ_{em} = 440-460 nm). All scale bars set to 25 µm.

Following this, interesting results were found when investigating what effect, if any, MNM concentration imparts on the combination of photomechanical, photodynamic, and photothermal aspects involved in MNM induced necrosis. Greatly increasing the

concentration of added MNM by 100x (0.5 µM to 50 µM), as has been attempted by recent work using Feringa based molecular motors for supposed photodynamic therapies[30], allows the possibility of any different regimes existing at much higher concentrations than previously considered to be probed. Experiments were repeated with both ROS scavengers under study, again at 1 and 5 mM, using 50 µM **MNM 1**.

Any purported photodynamic effects first seem to remain negligible as shown by **Figure 2.15** and **Figure 2.16** where little to no appreciable change is observed in TTN between 50 µM **MNM 1** dosed samples with, and without, both concentrations of NAC.

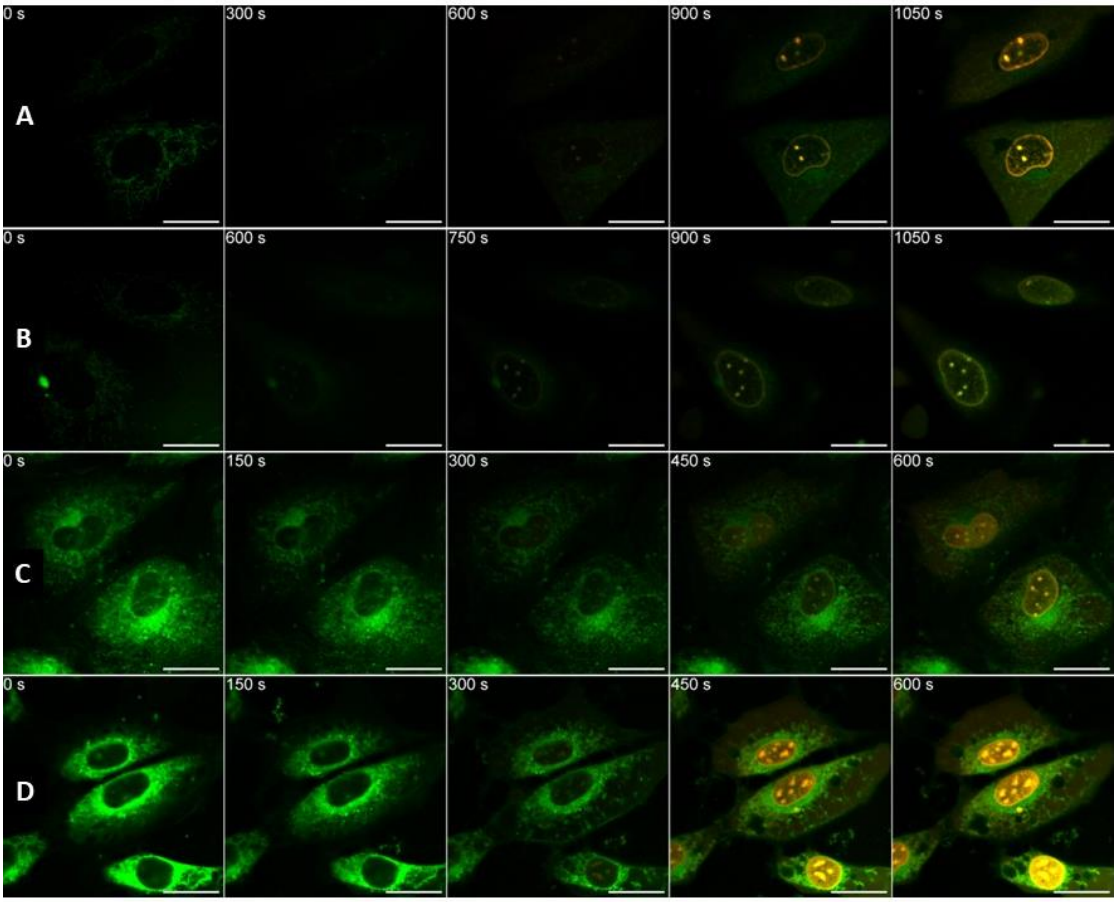

Figure 2.15 Microscopic observation of cell death caused by excitation at 355 nm (UV-exposure times are shown for each image), quantified by the observation of PI fluorescence within the nucleus. **A** – Control sample: NIH 3T3 cells loaded with 100 nM PI and 0.1% DMSO. **B** – NIH 3T3 cells loaded with 100 nM PI, 0.1% DMSO, and 1 mM NAC. **C** - NIH 3T3 cells loaded with 50 µM **MNM 1**, 100 nM PI. **D** - NIH 3T3 cells loaded with 50 µM **MNM 1**, 100 nM PI, and 1 mM NAC. All image sets collected after 30 minutes incubation after dosing procedure. Overlaid channels of PI fluorescence (λ_{ex} = 543 nm, 0.2 mW; λ_{em} = 600-700 nm), and mitochondrial autofluorescence (λ_{ex} = 355 nm, 20 mW, 400 nJ per voxel; λ_{em} = 440-460 nm). All scale bars set to 25 µm.

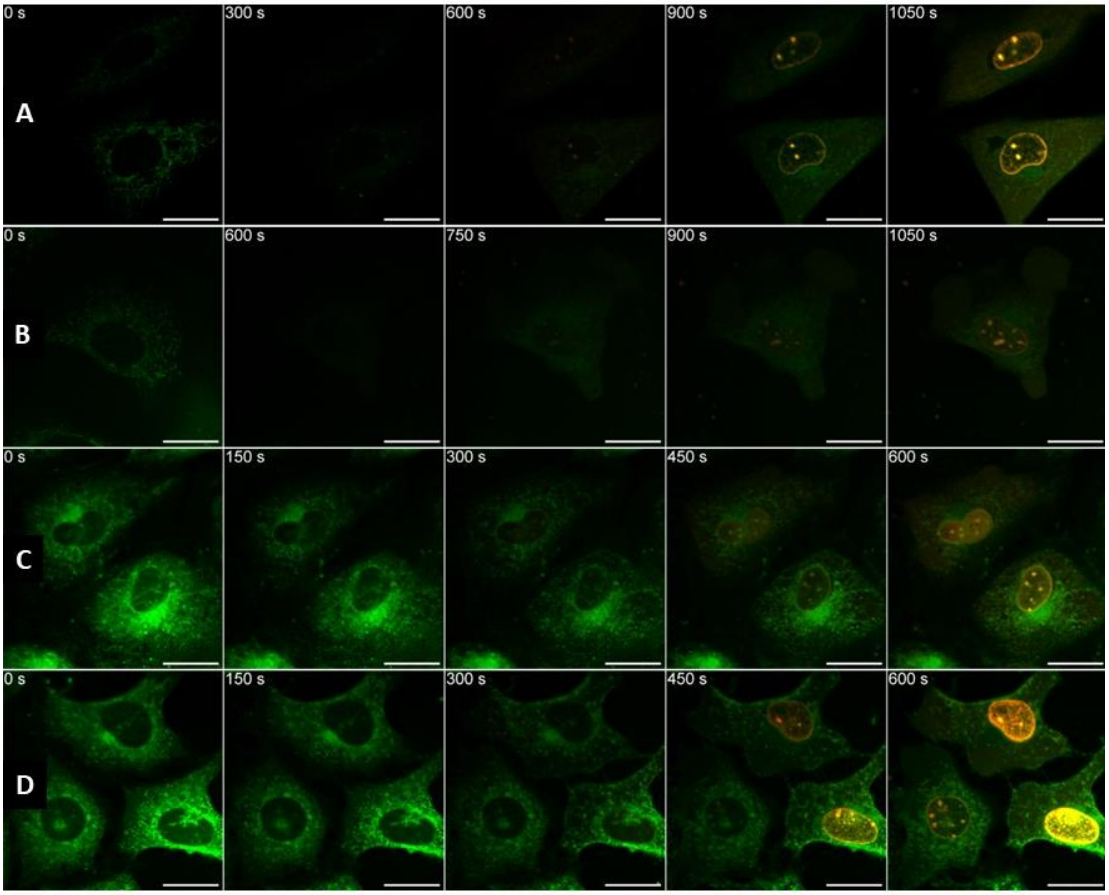

Figure 2.16 Microscopic observation of cell death caused by excitation at 355 nm (UV-exposure times are shown for each image), quantified by the observation of PI fluorescence within the nucleus. **A** – Control sample: NIH 3T3 cells loaded with 100 nM PI and 0.1% DMSO. **B** – NIH 3T3 cells loaded with 100 nM PI, 0.1% DMSO, and 5 mM NAC. **C** - NIH 3T3 cells loaded with 50 µM **MNM 1**, 100 nM PI. **D** - NIH 3T3 cells loaded with 50 µM **MNM 1**, 100 nM PI, and 5 mM NAC. All image sets collected after 30 minutes incubation after dosing procedure. Overlaid channels of PI fluorescence (λ_{ex} = 543 nm, 0.2 mW; λ_{em} = 600-700 nm), and mitochondrial autofluorescence (λ_{ex} = 355 nm, 20 mW, 400 nJ per voxel; λ_{em} = 440-460 nm). All scale bars set to 25 µm.

However, a slight effect is shown upon the repeat of these high MNM concentration experiments when using TU as the preferred ROS scavenger. The TTN appears to be increased, at both 1 and 5 mM antioxidant concentrations, as summarised in **Figure 2.17**

and **Figure 2.18**. This may indicate that at much higher MNM concentrations than normally used for therapeutic studies, there is an aspect of photodynamic behaviour contributing to the observed effect alongside the previously investigated mechanical drilling mechanism. It must be stressed however, that the impact of TUs observed ROS scavenging behaviour does not prevent the added nanomachine from accelerating cell death completely, when compared with the control sample. Illustrating that any additional photodynamic mechanism involved in accelerating TTN in mammalian cells does not outcompete the impact of the photomechanical drilling process that also exists at lower concentrations. The difference in results achieved with TU compared with NAC is interesting and may imply that TU is more readily available within cells under these experimental conditions; showing a greater ability to prevent the build-up of harmful ROS and prevent any photodynamic process from damaging the cell.

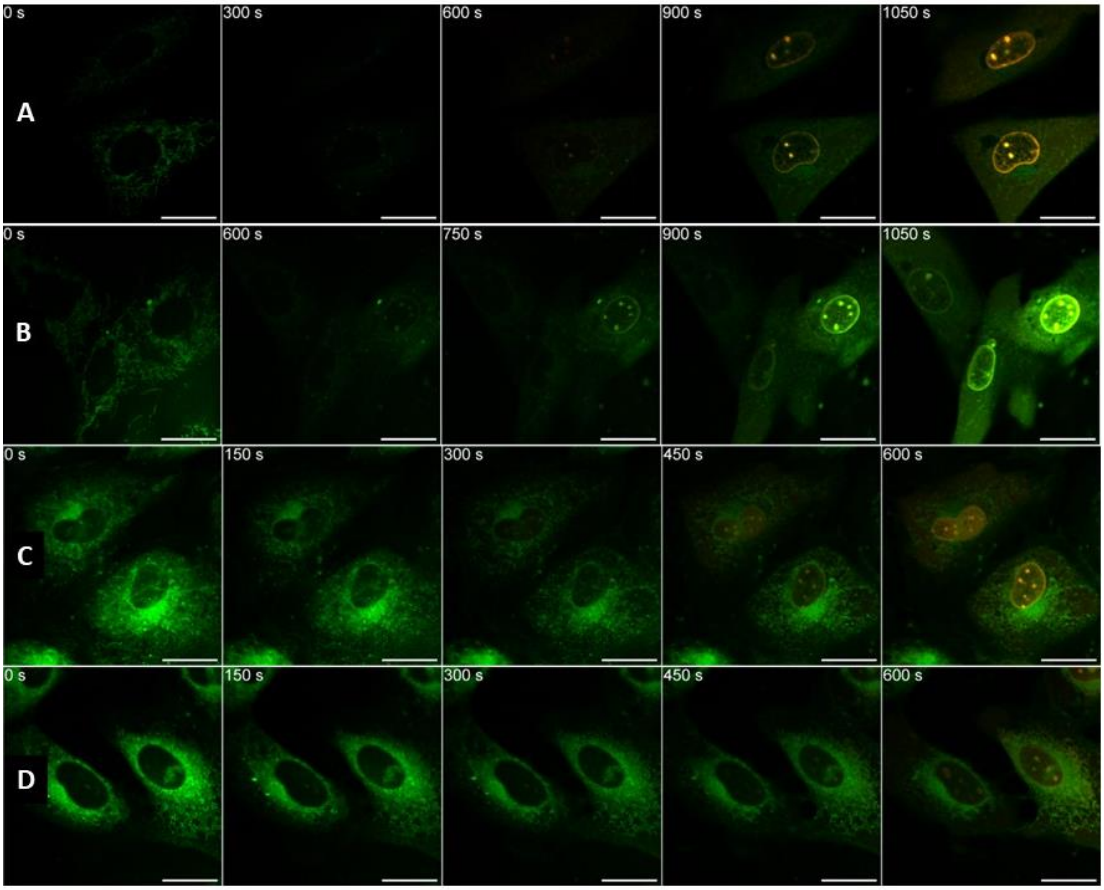

Figure 2.17 Microscopic observation of cell death caused by excitation at 355 nm (UV-exposure times are shown for each image), quantified by the observation of PI fluorescence within the nucleus. **A** – Control sample: NIH 3T3 cells loaded with 100 nM PI and 0.1% DMSO. **B** – NIH 3T3 cells loaded with 100 nM PI, 0.1% DMSO, and 1 mM TU. **C** - NIH 3T3 cells loaded with 50 µM **MNM 1**, 100 nM PI. **D** - NIH 3T3 cells loaded with 50 µM **MNM 1**, 100 nM PI, and 1 mM TU. All image sets collected after 30 minutes incubation after dosing procedure. Overlaid channels of PI fluorescence (λ_{ex} = 543 nm, 0.2 mW; λ_{em} = 600-700 nm), and mitochondrial autofluorescence (λ_{ex} = 355 nm, 20 mW, 400 nJ per voxel; λ_{em} = 440-460 nm). All scale bars set to 25 µm.

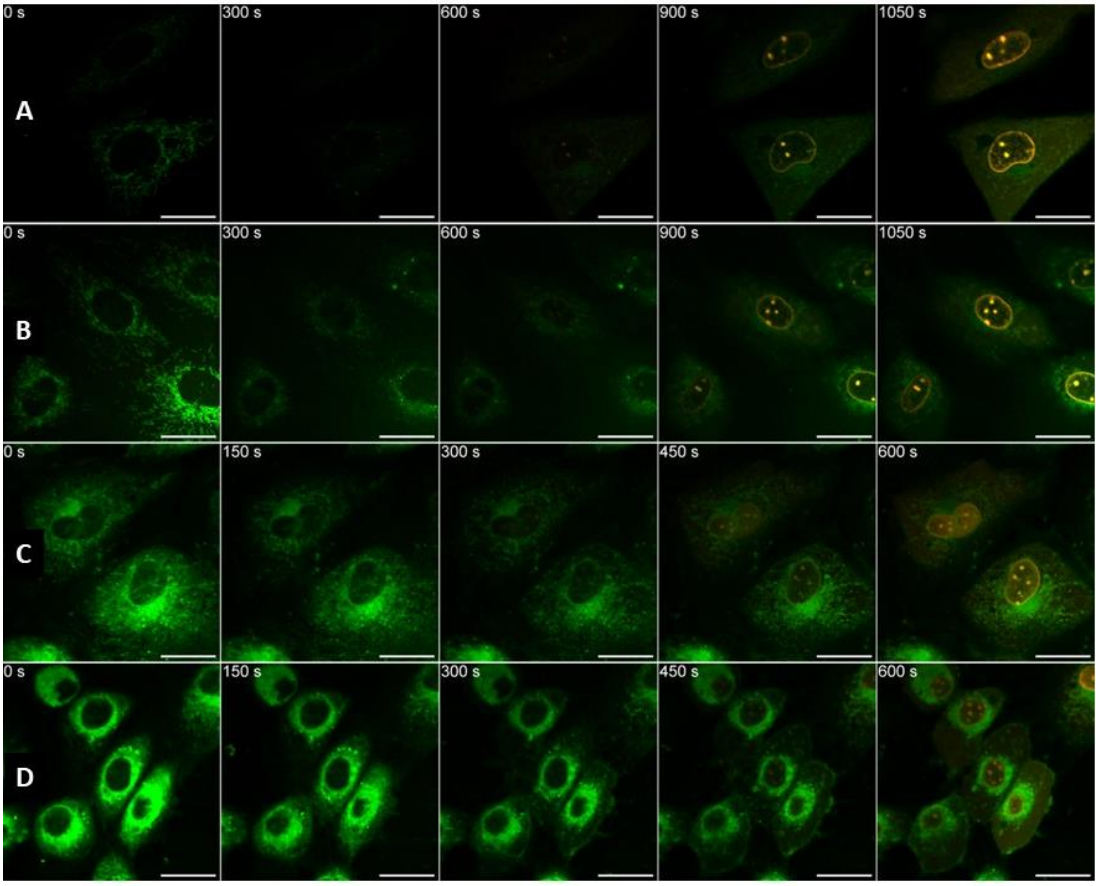

Figure 2.18 Microscopic observation of cell death caused by excitation at 355 nm (UV-exposure times are shown for each image), quantified by the observation of PI fluorescence within the nucleus. **A** – Control sample: NIH 3T3 cells loaded with 100 nM PI and 0.1% DMSO. **B** – NIH 3T3 cells loaded with 100 nM PI, 0.1% DMSO, and 5 mM TU. **C** - NIH 3T3 cells loaded with 50 µM **MNM 1**, 100 nM PI. **D** - NIH 3T3 cells loaded with 50 µM **MNM 1**, 100 nM PI, and 5 mM TU. All image sets collected after 30 minutes incubation after dosing procedure. Overlaid channels of PI fluorescence (λ_{ex} = 543 nm, 0.2 mW; λ_{em} = 600-700 nm), and mitochondrial autofluorescence (λ_{ex} = 355 nm, 20 mW, 400 nJ per voxel; λ_{em} = 440-460 nm). All scale bars set to 25 µm.

These results may indicate that, as observed in work where significantly higher than normal concentrations of molecular machine are studied, additional photodynamic effects may by observed. However, even under these extreme conditions, this is one of

many factors that must be considered, and it would be incorrect to assert that photo induced ROS production is the only cause of early onset necrosis. Clearly illustrated when high concentrations of antioxidant are employed; it is still apparent that nanomechanical action is responsible for the increase in the rate of necrosis onset. Of great importance is the conclusion that under the conditions used in the work contained within this thesis (concentrations of MNM at 0.5-5 μM) ROS generation *via* MNM photoactivation has little to no observable impact on the viability of the cellular samples.

The previously analysed microscopy results are summarised graphically in **Figure 2.19**, by plotting the mean PI (600-690 nm) fluorescence intensity of pixels within the cell's nucleus, against time, for each experiment discussed. This representation of data shows two clear regimes regardless of MNM concentration or antioxidant used; early onset necrosis caused by addition of MNM, and later necrosis caused by irreversible 355 nm UV damage.

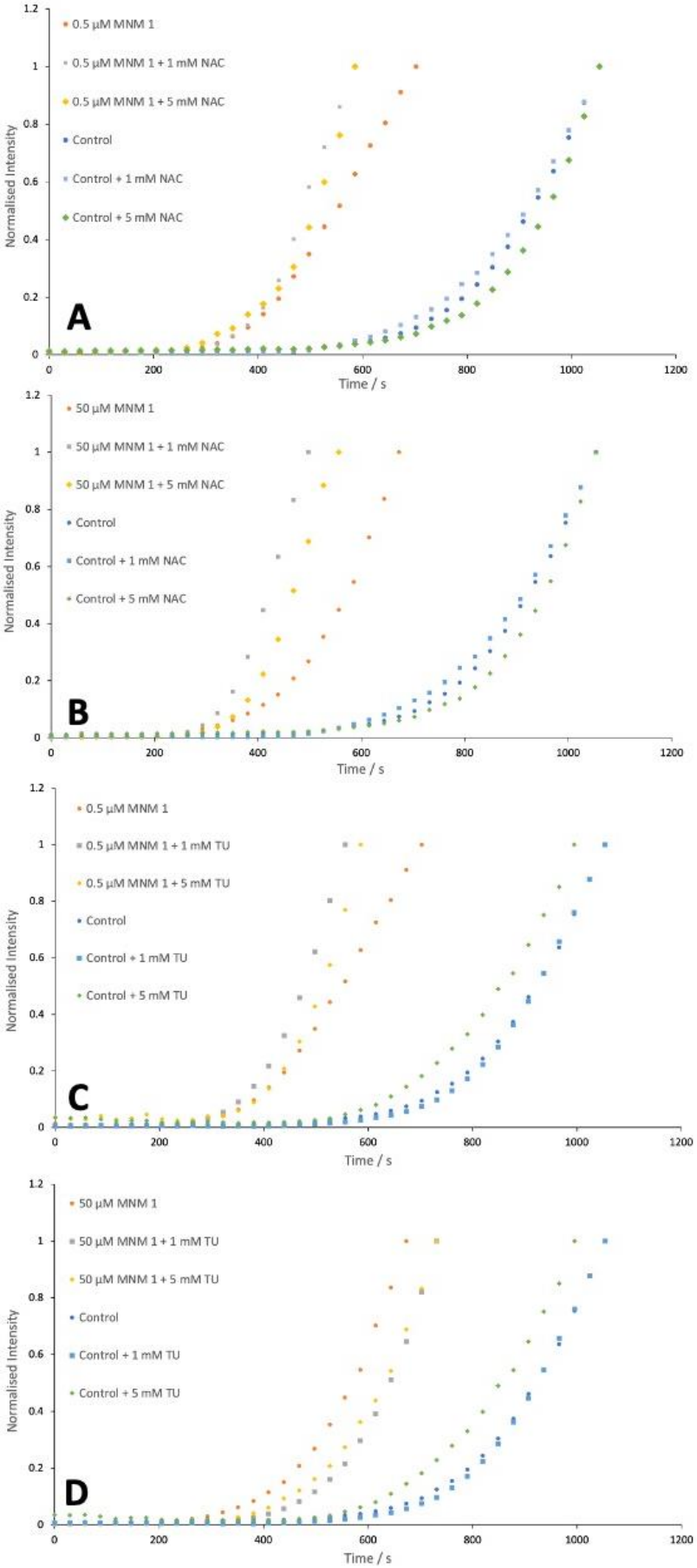
0.5 µM MNM 1
0.5 µM MNM 1 + 1 mM NAC
0.5 µM MNM 1 + 5 mM NAC
Control
Control + 1 mM NAC
Control + 5 mM NAC
Normalised Intensity
Time / s
A
50 µM MNM 1
50 µM MNM 1 + 1 mM NAC
50 µM MNM 1 + 5 mM NAC
Control
Control + 1 mM NAC
Control + 5 mM NAC
Normalised Intensity
Time / s
B
0.5 µM MNM 1
0.5 µM MNM 1 + 1 mM TU
0.5 µM MNM 1 + 5 mM TU
Control
Control + 1 mM TU
Control + 5 mM TU
Normalised Intensity
Time / s
C
50 µM MNM 1
50 µM MNM 1 + 1 mM TU
50 µM MNM 1 + 5 mM TU
Control
Control + 1 mM TU
Control + 5 mM TU
Normalised Intensity
Time / s
D

Figure 2.19 Normalised intensity data for mean PI fluorescence of pixels within the cell's nucleus. **A** – 0.5 μM MNM 1 with NAC. **B** – 50 μM MNM 1 with NAC. **C** – 0.5 μM MNM 1 with TU. **D** – 50 μM MNM 1 with TU.

When studying the lower concentration regimes (0.5 μM **MNM 1**) the addition of NAC or TU at either 1 or 5 mM concentrations (**Figure 2.19 A and C**) has no appreciable impact on the measured TTN. This is most clearly illustrated each by the normalised fluorescence curves leaving the baseline within the same 30 second window, meaning the first frame with detectable PI within the nucleus remains consistent. The higher concentration regime (50 μM **MNM 1**) again sees no impact on TTN – the first frame with detectable PI within the nucleus – upon the addition of NAC (**Figure 2.19 B**). However, when using TU as the chosen ROS scavenger a +120 second shift (four frames) is seen in the time taken to first detect an increase in PI intensity, illustrated by a delay in these traces in coming off the baseline in the normalised intensity plots. This further illustrates the previous conclusions drawn from the analysis of the obtained microscopy images; at extremely higher than normal concentrations of MNM a slight photodynamic impact is observed alongside the previously well-established photomechanical effect. However, this is a relatively small contribution and when counteracted by the addition of widely used antioxidant compounds, cells still undergo accelerated necrosis compared to the control experiments, implying the photomechanical effect still dominates.

2.4 Photothermal studies using a circularly polarised luminescence probe

2.4.1 Circularly polarised luminescence theory

Circularly polarised luminescence (CPL) is a phenomenon wherein emissive species emit light with a combination of both left and right-handed circularly polarised light with incongruent intensities. Initially observed by Samoilov in 1948[31], the measurement of this emission event (CPL spectroscopy) is commonly thought of as the emission alternative of the absorbance based technique Circular Dichroism (CD) spectroscopy – the differential absorbance of circularly polarised light. Polarised light is most simply considered as a propagating wave composed of both an electric and a magnetic vector component moving perpendicular to each other, and to the direction of propagation. The electric field component can be further deconstructed into two additional perpendicular components; the amplitude and phase of which can be studied. In traditional linear polarised light these electronic components maintain phase with each other but differ in amplitude. Circularly polarised light is generated when this principle is inverted; the electric field vectors are out of phase by a quarter of a wavelength while preserving identical amplitude. This is illustrated in **Figure 2.20**. This phase difference causes one component to fall to zero, while the other reaches a minimum or maximum value causing the light to propagate with a defined helicity.[32]

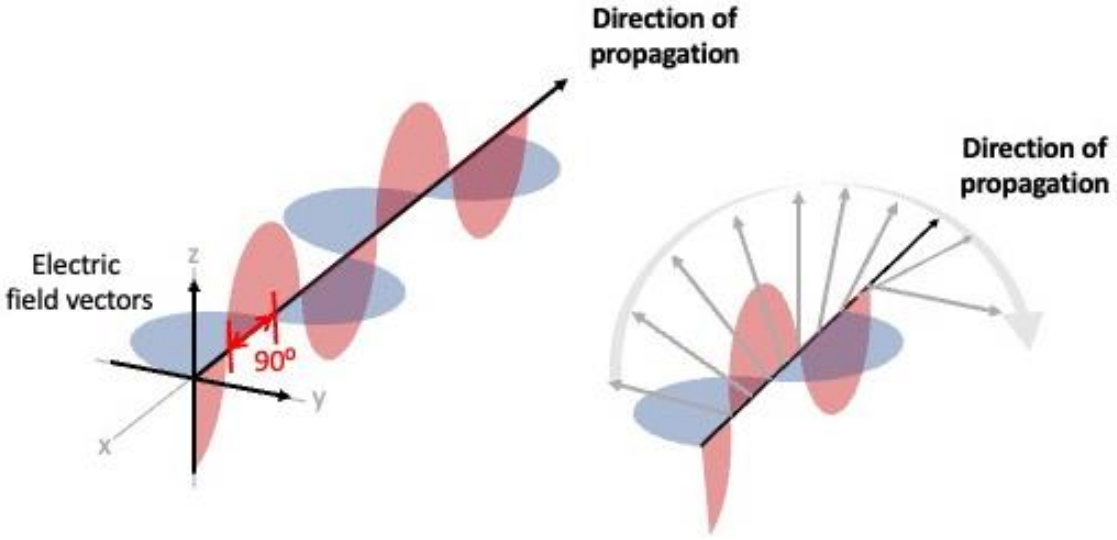

Figure 2.20 Summary of electric field vectors in circular polarised light. If the wave were approaching the observer its electric vector would appear to be rotating anticlockwise, right circular polarisation.

Lanthanide emitter complexes such as Europium(III) are commonly utilised as strong CPL probes due to Eu(III)'s intense emission, however excitation is often highly inefficient. As such coordinated ligand molecules can be used to induce sensitised emission *via* the antenna effect (briefly illustrated in **Figure 2.21**), with the added benefit of adding chirality to the overall structure resulting in unusually strong CPL emission.[33]

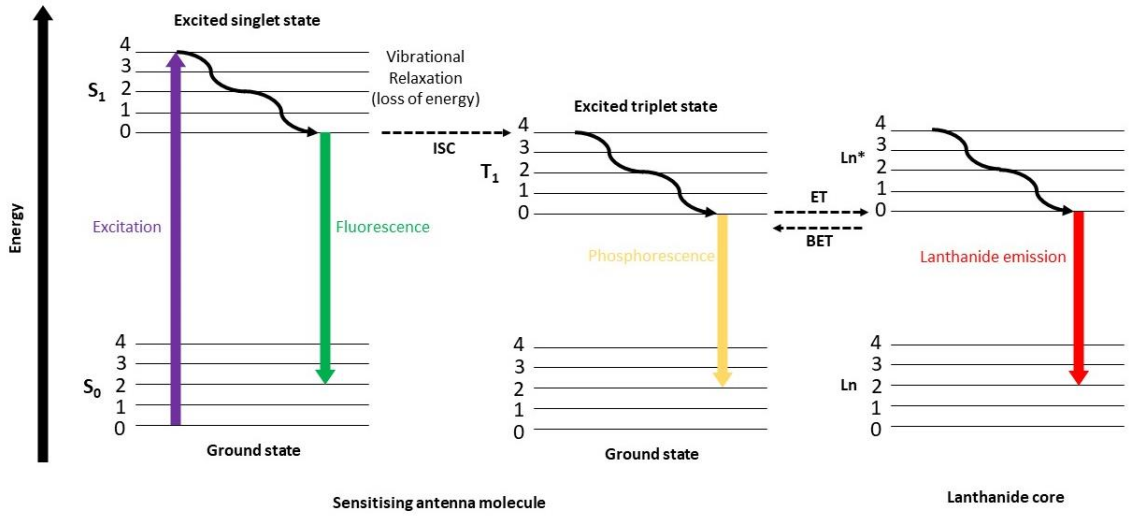

Figure 2.21 Jablonski diagram illustrating the major processes involved in sensitised lanthanide emission. Energy transfer (ET) and back energy transfer (BET) shown as lanthanide processes.

The chirality imparted by the coordinated ligand molecules allows for resolved isomers to generate incredibly strong CPL signals. If these compounds are forced to lose this chiral specificity the produced CPL signal will fall as the proportions of left and right-handed light become closer to equality; importantly the total emission remains unchanged in comparison to sample destruction or photobleaching. Exploiting this phenomenon may allow for any proposed photothermal effects to be studied.

2.4.2 Using CPL emitters to study photothermal effects

Photothermal therapy (PTT) is an area that utilises nanomaterials, and more recently small organic molecules, to artificially elevate local temperatures as a form of cancer treatment.[34] After photoexcitation, the energy of the excited species is released through nonradiative decay processes – these can be either unimolecular or caused *via* collisions with other molecules – instead of the previously discussed photon emission (fluorescence / phosphorescence) or photodynamic reactions. Leading to the aforementioned increase in local temperature, often without any measurable raise in

macro-level temperature of the sample[35]; making this phenomenon difficult to conclusively study. In the case of Feringa type molecular motors, it could be theorised that the rapid rotation of the molecule may be leading to increased molecular collisions, with both the solvent system and additional MNMs, resulting in a PTT type system. Any such system would produce results indistinguishable from those caused by mechanical processes, with faster rotor speeds causing more rapid TTN.

By using highly polarised emitters that readily racemise under heating, the presence of any localised heating phenomena caused by proposed photothermal MNM effects could be studied. The chirally resolved complex, **Eu(III) complex 1** (shown in **Figure 2.22**), has been observed to racemise readily in water under heating at 60 ^{o}C for 12 hours, resulting in a reduction in resolved CPL signal while maintaining a comparable overall emission of light.

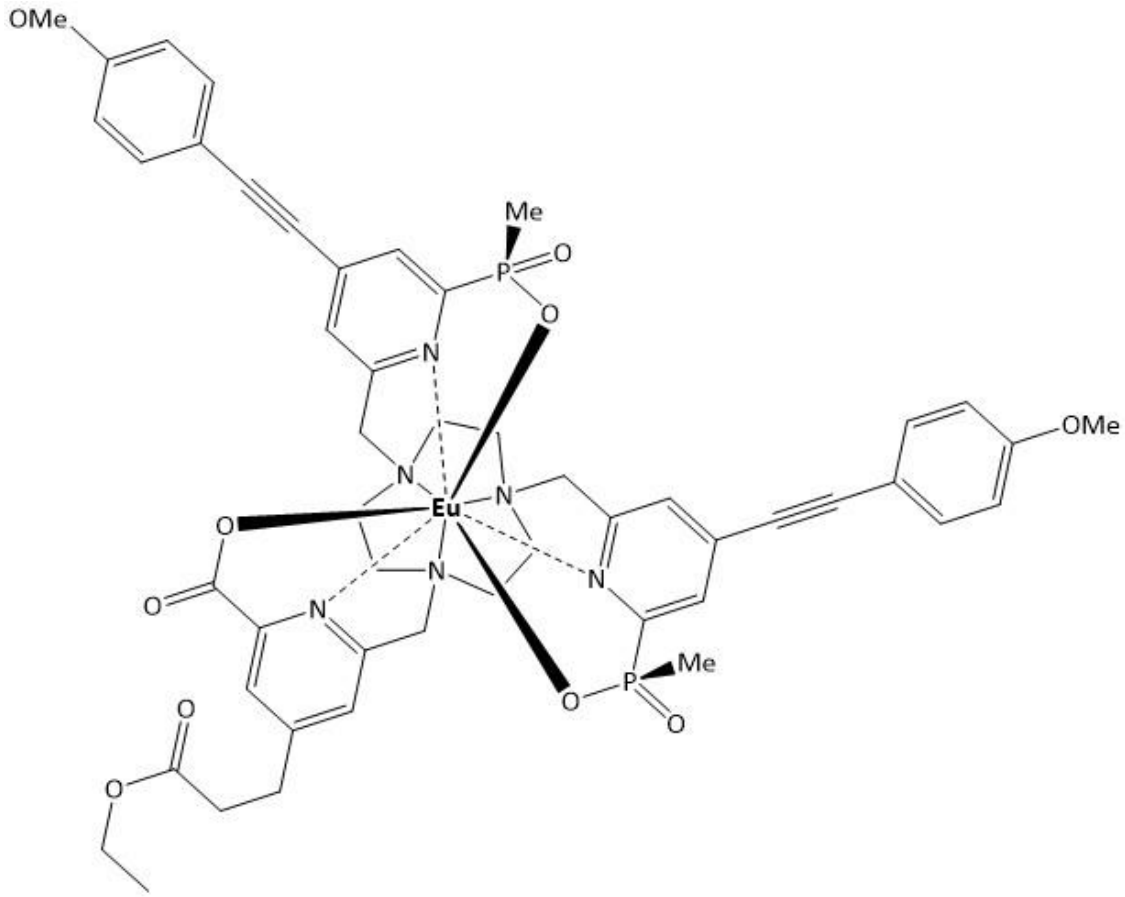

Figure 2.22 Structure of **Eu(III) complex 1**.

These results are shown by the overlaid spectra for the isolated Δ isomer in **Figure 2.23** – overlaid total emission is also shown illustrating the observed effect is indeed due to heat induced racemisation and not sample degradation.

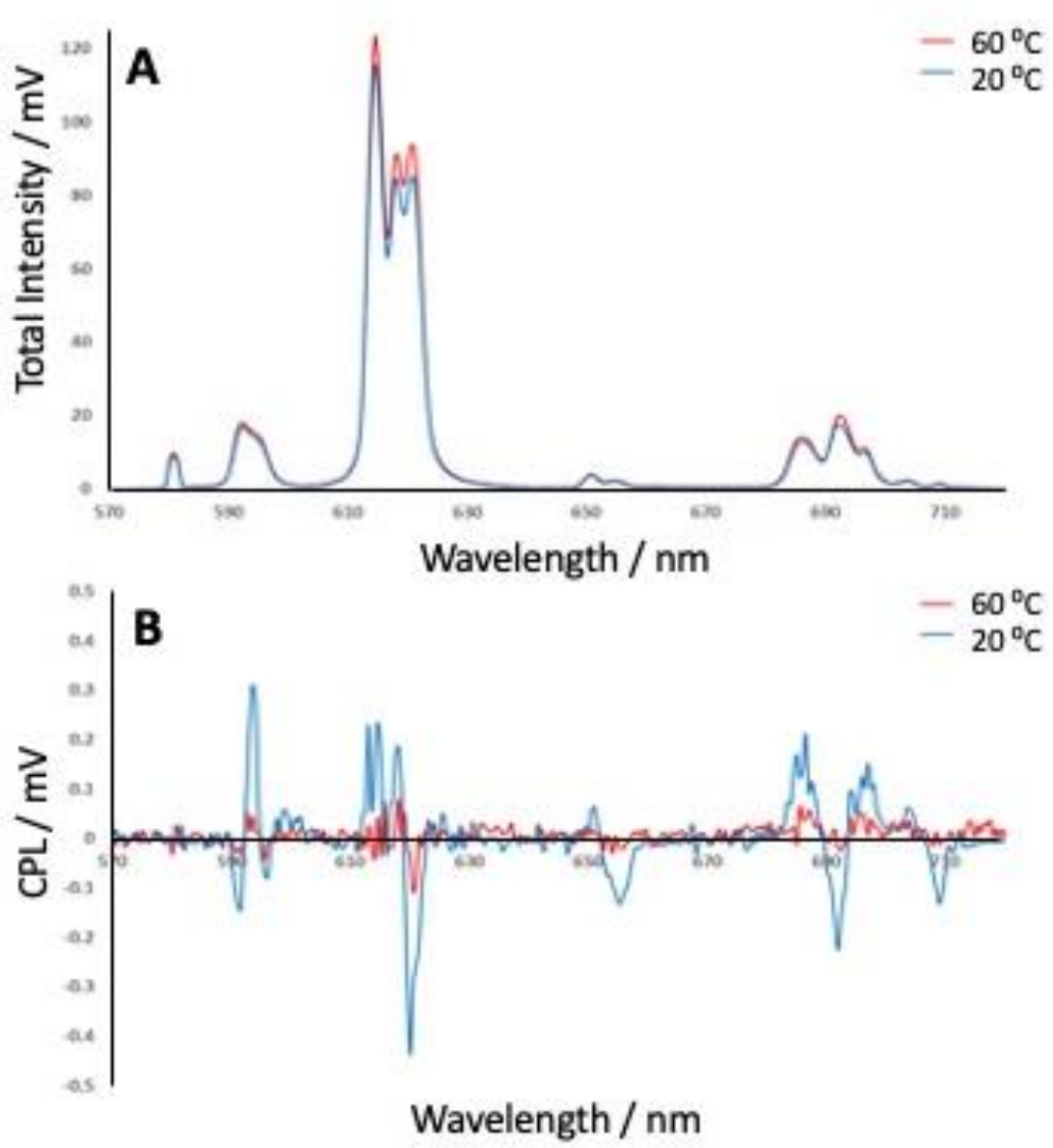

Figure 2.23 A - Total emission of **Eu(III) complex 1 Δ** at both 20 °C (blue) and 60 °C (red) showing little change in overall emission properties. **B** - CPL spectra of **Eu(III) complex 1 Δ** at 20 °C (blue) and 60 °C (red) showing a dramatic reduction in CPL upon heating.

This sensitivity to temperature induced racemisation may allow for any heat generated by MNMs to be identified. If a high enough concentration of MNM is in solution such that the number of rotary molecules outnumber the amount of **Eu(III) complex 1 Δ**, the proposed generated heating effect will cause any probe complexes in close proximity to

racemise. Resulting in a drop in measured CPL signal, while maintaining comparable total emission intensity.

For this complex to be suitable for testing with activated MNMs, it is vital that the emission properties remain consistent after prolonged exposure to 355 nm light to allow for MNMs to be activated for extended periods of time without adversely affecting the complex itself. The overlaid spectra in **Figure 2.24** compares the CPL emission of **Eu(III) complex 1 Δ** over 5 hours of constant UV exposure.

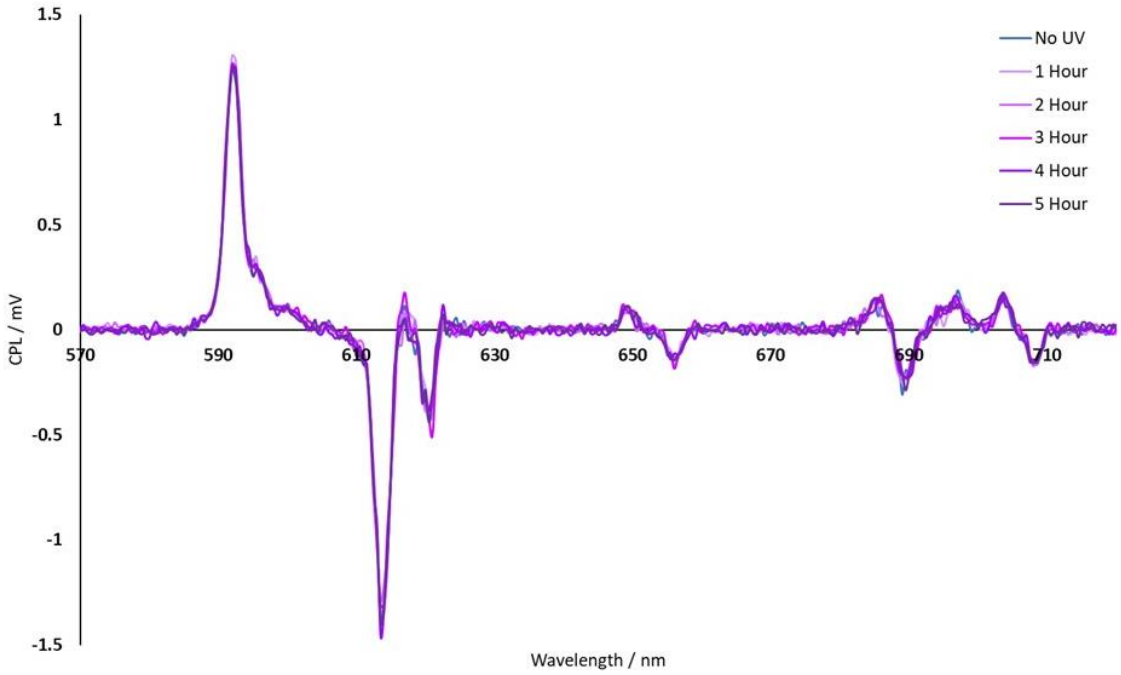

Figure 2.24 Overlaid CPL spectra of **Eu(III) complex 1 Δ** when exposed to 355 nm UV for 5 hours, showing no degradation in emission

No change in the CPL spectra were observed after prolonged UV excitation, leading to the conclusion that this complex was resistant both to UV-induced racemisation and to photobleaching or degradation. Making it a suitable candidate for probing the presence of any photothermal effects caused by UV activation of MNMs. To achieve this, **MNM 1** was added at 10× the concentration of the CPL probe, held at 20 ^{o}C, and activated with

355 nm UV light for 8 hours. The comparative total emission and CPL spectra are shown in **Figure 2.25**.

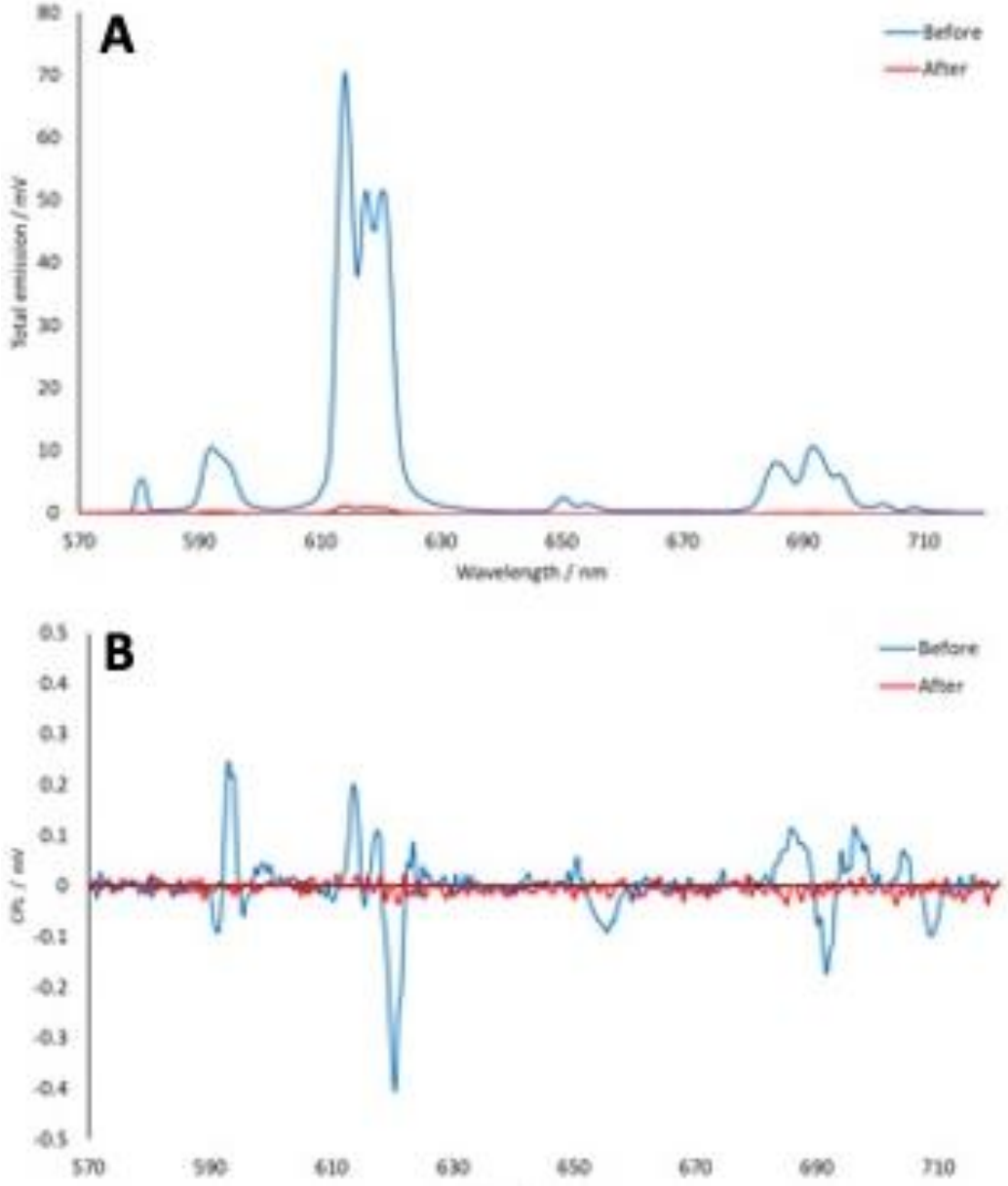

Figure 2.25 A – Total emission of **Eu(III) complex 1 Δ** with the addition of 10× concentration **MNM 1**, before (blue) and after (red) 8 hours of 355 nm UV activation. **B** – CPL spectra of **Eu(III) complex 1 Δ** with the addition of 10× concentration **MNM 1**, before (blue) and after (red) 8 hours of 355 nm UV activation.

A clear reduction in CPL signal was indeed observed (**Figure 2.25 B**), while dramatic reduction in overall emission was also seen (**Figure 2.25 A**) implying that the probe has been fundamentally altered instead of undergoing purely heat induced racemisation. This may imply that photothermal effects are not the predominant factor during MNM activation under these conditions, and the photomechanical action of the rotor's motion is mechanically changing the coordination of the Eu(III) complex, reducing its emission properties. While these experiments provide a good basis for understanding the mechanism behind MNM induced cell necrosis, repeat experiments under differing conditions could be undertaken to conclusively detect any photothermal processes.

2.5 Conclusions

This chapter has made initial attempts at exploring the processes involved in MNM induced cell death. By systematically altering the chemical structure of various MNMs to change the rotor properties it can be shown that rotation speed of the machine is directly related to the speed at which necrosis is induced. Strongly implying that photomechanical effects are predominantly responsible for the ability of this class of molecule to induce cell death.

The possible presence of any photodynamic effects are further diminished by repeated live-cell microscopy experiments of MNM samples dosed with various ROS scavenger compounds. Little to no impact was seen on the measured TTN in the presence of these antioxidants, up to incredibly high concentrations of 5 mM, at micromolar concentrations of MNM; the same concentration range used for all further microscopy experiments within this work. While the possibility of some photodynamic impact is found at 100× MNM concentration, this impact is still shown to be small and readily resolved *via* ROS scavenger addition.

Any photothermal contribution to MNM induced cell death is harder to study, however strides have been made utilising resolved Eu(III) CPL probes to detect any change in local temperature during UV activation of MNMs. A photostable complex that readily racemises when heated - reducing the imbalance in left- and right-handed light emitted lowering the intensity of CPL signal measured, while maintaining comparable total emission - was used to probe any increase in temperature around activated MNM molecules. The CPL signal was found to diminish, but total intensity of emission also fell to negligible levels. This may imply that the CPL active complex was mechanically altered, fundamentally changing its photophysical properties. As such any photothermal processes that may exist are insignificant in respect to the impact of the photomechanical driving force of MNM action. However, the existence of any photothermal possibility has not been disproved.

2.6 References

1 J. L. Beckham, T. S. Bradford, C. Ayala-Orozco, A. L. Santos, D. Arnold, A. R. van Venrooy, V. García-López, R. Pal and J. M. Tour, *Adv. Mater.*, **n/a**, 2306669.

2 W.-Z. Wang, L.-B. Huang, S.-P. Zheng, E. Moulin, O. Gavat, M. Barboiu and N. Giuseppone, *J. Am. Chem. Soc.*, 2021, **143**, 15653–15660.

3 J. Sun, C. Ma, S. Maity, F. Wang, Y. Zhou, G. Portale, R. Göstl, W. H. Roos, H. Zhang, K. Liu and A. Herrmann, *Angew. Chem. Int. Ed.*, 2021, **60**, 3222–3228.

4 J. L. Beckham, A. R. van Venrooy, S. Kim, G. Li, B. Li, G. Duret, D. Arnold, X. Zhao, J. T. Li, A. L. Santos, G. Chaudhry, D. Liu, J. T. Robinson and J. M. Tour, *Nat. Nanotechnol.*, 2023, **18**, 1051–1059.

5 T. Galbadage, D. Liu, L. B. Alemany, R. Pal, J. M. Tour, R. S. Gunasekera and J. D. Cirillo, *ACS Nano*, 2019, **13**, 14377–14387.

6 A. L. Santos, D. Liu, A. K. Reed, A. M. Wyderka, A. van Venrooy, J. T. Li, V. D. Li, M. Misiura, O. Samoylova, J. L. Beckham, C. Ayala-Orozco, A. B. Kolomeisky, L. B. Alemany, A. Oliver, G. P. Tegos and J. M. Tour, *Sci. Adv.*, 2022, **8**, eabm2055.

7 V. García-López, F. Chen, L. G. Nilewski, G. Duret, A. Aliyan, A. B. Kolomeisky, J. T. Robinson, G. Wang, R. Pal and J. M. Tour, *Nature*, 2017, **548**, 567–572.

8 L. Ribovski, Q. Zhou, J. Chen, B. L. Feringa, P. van Rijn and I. S. Zuhorn, *Chem. Commun.*, 2020, **56**, 8774–8777.

9 B. Guo, Z. Huang, Q. Shi, E. Middha, S. Xu, L. Li, M. Wu, J. Jiang, Q. Hu, Z. Fu and B. Liu, *Adv. Funct. Mater.*, 2020, **30**, 1907093.

10 D. Zhi, T. Yang, J. O'Hagan, S. Zhang and R. F. Donnelly, *J. Controlled Release*, 2020, **325**, 52–71.

11 S. S. Lucky, K. C. Soo and Y. Zhang, *Chem. Rev.*, 2015, **115**, 1990–2042.

12 M. Lipsitch, E. T. Tchetgen and T. Cohen, *Epidemiol. Camb. Mass*, 2010, **21**, 383–388.

13 K. R. Gee, K. A. Brown, W.-N. U. Chen, J. Bishop-Stewart, D. Gray and I. Johnson, *Cell Calcium*, 2000, **27**, 97–106.

14 Fluo-4, AM, cell permeant, https://www.thermofisher.com/order/catalog/product/F14201, (accessed 7 November 2023).

15 V. García-López, P.-T. Chiang, F. Chen, G. Ruan, A. A. Martí, A. B. Kolomeisky, G. Wang and J. M. Tour, *Nano Lett.*, 2015, **15**, 8229–8239.

16 A. L. Santos, J. L. Beckham, D. Liu, G. Li, A. van Venrooy, A. Oliver, G. P. Tegos and J. M. Tour, *Adv. Sci.*, 2023, **10**, 2205781.

17 A. L. Santos, A. van Venrooy, A. K. Reed, A. M. Wyderka, V. García-López, L. B. Alemany, A. Oliver, G. P. Tegos and J. M. Tour, *Adv. Sci.*, 2022, **9**, 2203242.

18 J. A. Howard and G. D. Mendenhall, *Can. J. Chem.*, 1975, **53**, 2199–2201.

19 T. L. de Jager, A. E. Cockrell and S. S. Du Plessis, in *Ultraviolet Light in Human Health, Diseases and Environment*, ed. S. I. Ahmad, Springer International Publishing, Cham, 2017, pp. 15–23.

20 C. Ayala Orozco, D. Liu, Y. Li, L. B. Alemany, R. Pal, S. Krishnan and J. M. Tour, *ACS Appl. Mater. Interfaces*, 2020, **12**, 410–417.

21 W. M. Abdou, Y. O. Elkhoshnieh and M. M. Sidky, *Tetrahedron*, 1994, **50**, 3595–3602.

22 H. Kim, J. Lee, C. Oh and J.-H. Park, *Nat. Commun.*, 2017, **8**, 15880.

23 Y. Bu, T. Xu, X. Zhu, J. Zhang, L. Wang, Z. Yu, J. Yu, A. Wang, Y. Tian, H. Zhou and Y. Xie, *Chem. Sci.*, 2020, **11**, 10279–10286.

24 S.-Y. Sun, *Cancer Biol. Ther.*, 2010, **9**, 109–110.

25 Y. Samuni, S. Goldstein, O. M. Dean and M. Berk, *Biochim. Biophys. Acta BBA - Gen. Subj.*, 2013, **1830**, 4117–4129.

26 M. P. Murphy, A. Holmgren, N.-G. Larsson, B. Halliwell, C. J. Chang, B. Kalyanaraman, S. G. Rhee, P. J. Thornalley, L. Partridge, D. Gems, T. Nyström, V. Belousov, P. T. Schumacker and C. C. Winterbourn, *Cell Metab.*, 2011, **13**, 361–366.

27 M. Arakawa, N. Ushimaru, N. Osada, T. Oda, K. Ishige and Y. Ito, *Neurosci. Res.*, 2006, **55**, 255–263.

28 D. Mazor, E. Golan, V. Philip, M. Katz, A. Jafe, Z. Ben-Zvi and N. Meyerstein, *Eur. J. Haematol.*, 1996, **57**, 241–246.

29 S. Y. Hong, J. O. Yang, E. Y. Lee and Z. W. Lee, *J. Korean Med. Sci.*, 2003, **18**, 649–654.

30 A. M. Firsov, J. Pfeffermann, A. S. Benditkis, T. I. Rokitskaya, A. S. Kozlov, E. A. Kotova, A. A. Krasnovsky, P. Pohl and Y. N. Antonenko, *J. Photochem. Photobiol. B*, 2023, **239**, 112633.

31 B. N. Samoilov, *Zhur Eksptl Teor. Fiz*, 1948, **18**, 1030–1039.

32 J. P. Riehl and G. Muller, in *Comprehensive Chiroptical Spectroscopy*, John Wiley & Sons, Ltd, 2011, pp. 65–90.

33 L. E. MacKenzie and R. Pal, *Nat. Rev. Chem.*, 2021, **5**, 109–124.

34 H. Sung Jung, P. Verwilst, A. Sharma, J. Shin, J. L. Sessler and J. Seung Kim, *Chem. Soc. Rev.*, 2018, **47**, 2280–2297.

35 X. Yi, Q.-Y. Duan and F.-G. Wu, *Research*, 2021, 1-38.

Chapter 3: Investigation into various diamine functionalised MNMs and their photophysical properties

Summary: *This chapter investigates MNMs functionalised by diamine chains upon both the stator and rotor halves of the molecule, with varying levels of substitution about the nitrogen atoms. Live cell confocal microscopy is utilised to investigate what effect, if any, these synthetic modifications have on the MNMs ability to promote cell death upon activation. The ability of the various analogues to cross the phospholipid bilayer and localise within the cell are considered as well as the cells capability of responding to this internalisation and how this impacts any future possible therapeutic applications. Photophysical properties of each compound are also studied to determine how the activation wavelength is altered. Any changes in the emission properties of the MNM are also observed to assess the possibility of fluorescent tracking within the cell.*

3.1 Introduction

Amine based electron donating substituents have previously been used at the C4 position of the upper naphthalene system (rotor), and the C8/C7 carbons of the bottom anthracene ring (stator) of Tour MNMs (**Figure 3.1**) to induce a bathochromic shift in the wavelength required for motor excitation. Allowing the use of a widely used, biologically accepted and adopted, 405 nm UV light emitting diode (LED) to "switch on" the rotors functionality and induce necrosis in samples of PC3 cells, and trigger mitochondrial disfunction and calcium overload in various fungi respectively.[1,2] This shift towards less phototoxic wavelengths of light is vital when working towards possible therapeutic applications for MNMs, while also inherently shifting their 2PE activation wavelength. Enabling lower energy excitations with greater tissue penetration.

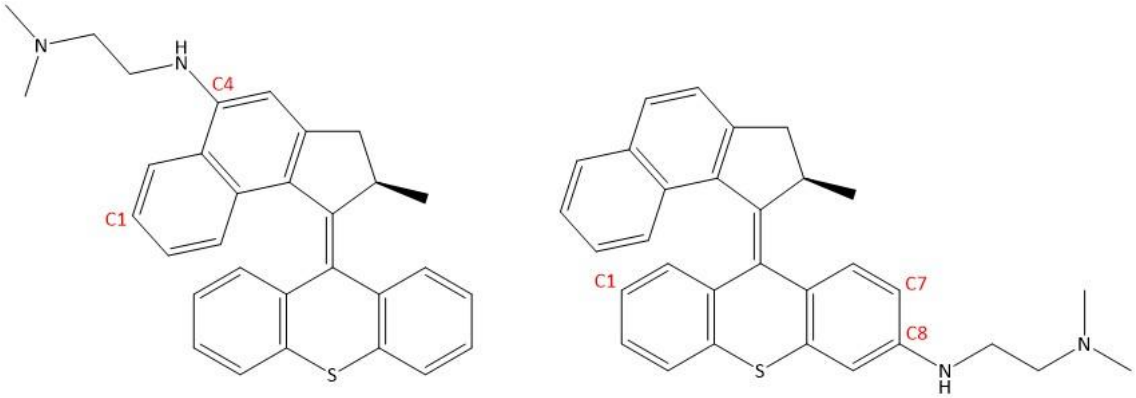

Figure 3.1 Structure of the previously studied 405 nm activated fast motor (MHz) Tour MNMs. Carbon functionalisation position numbering indicated in red.

Other related functional groups at the C4 rotor position, including the addition of a secondary light-gated dithienylethene switch[3] possessing the ability to turn the rotary function on and off, have previously been shown to also allow for visible light activation. The impact on the excitation wavelength caused by these functionalisations have recently been rationalised by the proposal of an electronic "push-pull" system across the central overcrowded olefin axle. A series of compounds, shown in **Figure 3.2**, were synthesised containing highly electron withdrawing -CN, and electron donating -OMe groups in the C4 and C8 positions to observe the impact of manipulating electron density across the motor.[4]

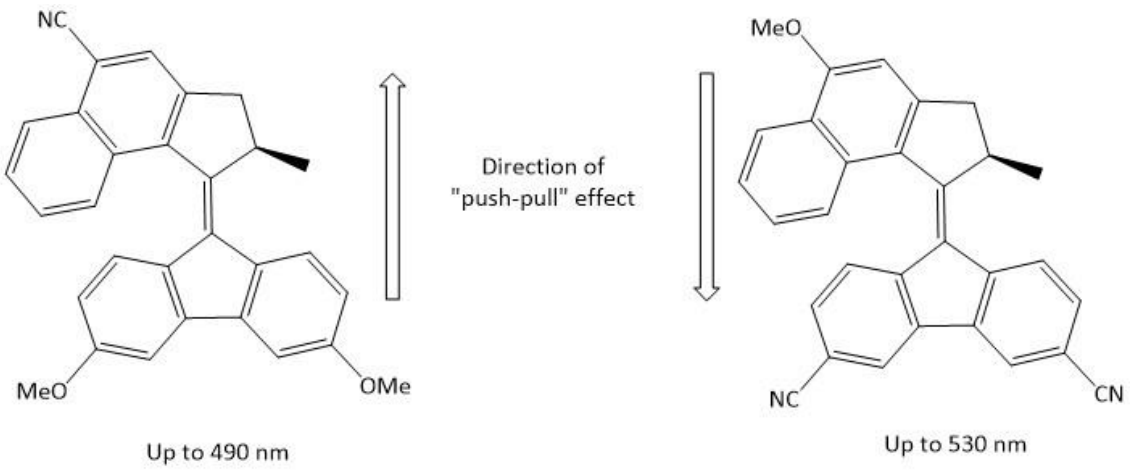

Figure 3.2 Structure of species used to investigate electronic effects on Feringa motor activation wavelengths. Wavelengths stated refer to the low-energy onset of absorption.

Time-dependent density-functional theory (TD-DFT) calculation carried out in Gaussian showed that the HOMO-LUMO energy gap was decreased upon addition of -CN moieties pulling electron density onto one half, either the rotor or stator, of the molecule. This was further intensified *via* the addition of -OMe functionalisation on the alternate half of the molecular motor pushing electron density from the other side. Crucially, the electron density on the frontier orbitals closely resembles those present in the unfunctionalised form, indicating that the process behind the photoisomerisation of the central alkene is unaffected. The observed HOMO-LUMO energy gap reduction is found to be more potent when the electron density is pushed from the stator and pulled toward the rotor half of the compound, as shown in **Figure 3.3**.

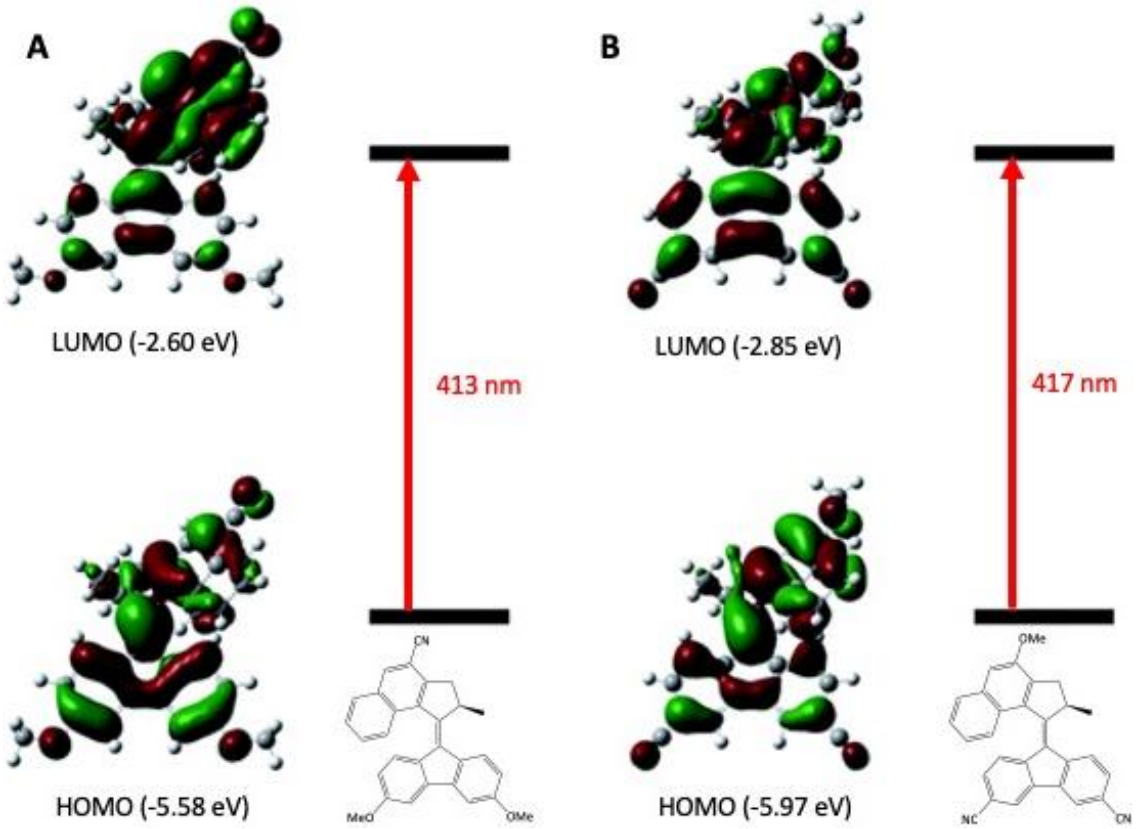

Figure 3.3 Structures and calculated (TD-DFT, CAM-B3LYP, 6-311G++(d,p)) frontier orbitals for -CN rotor -OMe stator (left), and -CN stator -OMe rotor (right) 2nd generation Feringa molecular motors. Adapted from Pfrifer *et al*.[4]

It is important to note that several additional methods for tuning the activation wavelength of second and third generation Feringa molecular motors have been extensively investigated. Functionalisation with palladium tetraphenylporphyrin (PdTPP), also at the C4 position of the rotor (**Figure 3.4**), was shown by Feringa to dramatically shift the activation wavelength to 530 nm.[5] This PdTPP module behaves differently to the smaller functionalisation investigated in this chapter by acting as a triplet sensitiser. Due to its relatively long-lived triplet lifetime a triplet-triplet energy transfer between PdTPP and the porphyrin based molecular motor is possible allowing for sensitised photoisomerisation with the same behaviour as the previously explained isomerisation *via* direct irradiation. While this is an incredible shift in wavelength a

number of concessions are made to the other properties of the molecular machine, making it incompatible with biological applications. The extra steric bulk and addition of palladium lead to solubility problems in aqueous environments, while the added molecular weight to the rotor half of the molecule reduces rotor speed making disruption of the phospholipid bilayer incredibly challenging.

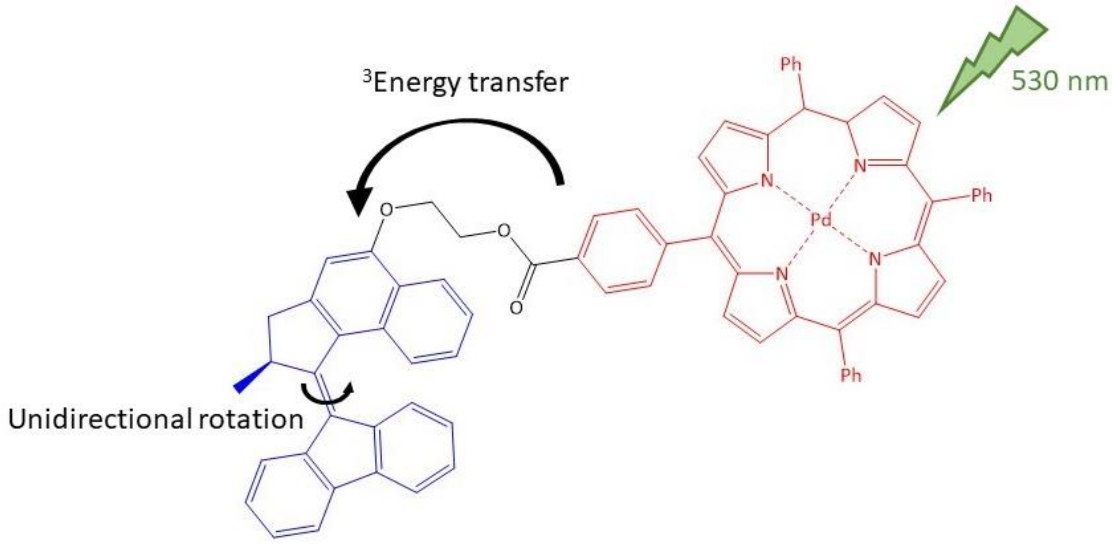

Figure 3.4 Structure and photosensitised activation process for PdTPP (red) functionalised Feringa molecular motor (blue). Adapted from Cnossen *et al*.[5]

Feringa molecular motors have also been coordinated to Ru(II) bipyridine compounds, resulting in a complex (**Figure 3.5**) that not only shows a substantial bathochromic shift (450 nm) but also a 50-fold increase in rotation speed.[6] This red shift is attributed to a predicted ligand-to-metal charge transfer process, indicated by a dramatic reduction seen in the luminescence properties of the coordinated $[Ru(bpy)_3]^{2+}$ complex. Again, while promising, this technology is limited in its biological applications due to the high likelihood of de-coordination in complex aqueous media.

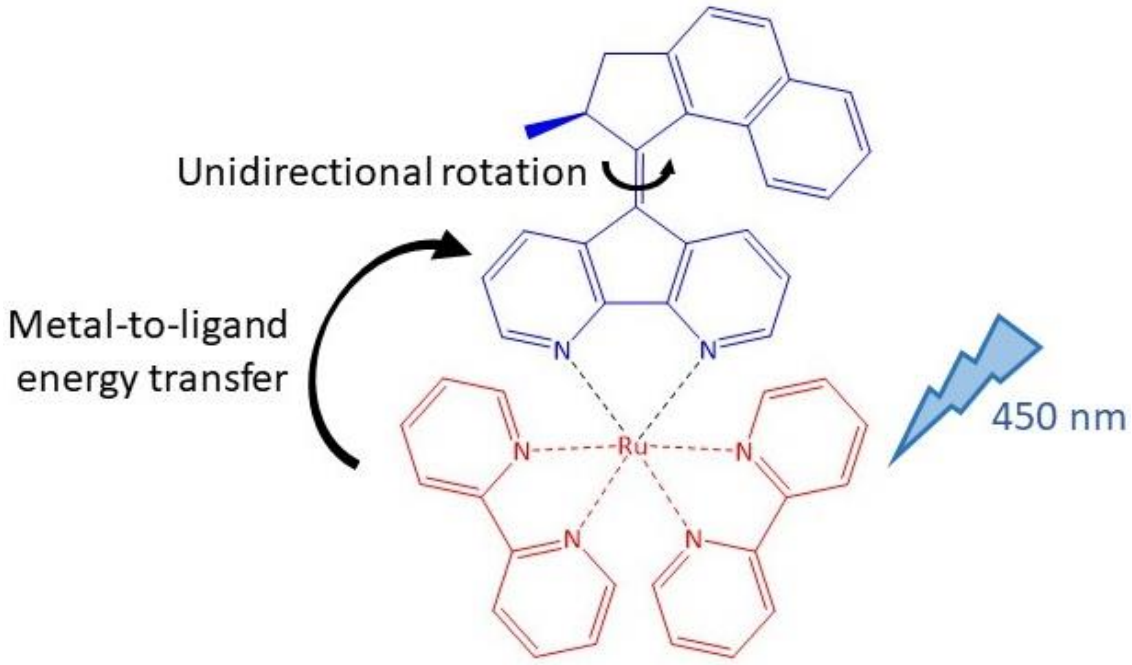

Figure 3.5 Structure and photosensitised activation for Ru(II) bipyridine (red) functionalised Feringa molecular motor (blue). Adapted from Wezenberg *et* al.[6]

Additionally, extension of the aromatic core of the molecular motors has been shown to pose an efficient strategy for wavelength shifting.[7] **Figure 3.6** shows two illustrative examples, extending the aromatic system on either the rotor or stator side of the double bond axle. While this strategy poses less issues for biological applications compared to the previously discussed, the quantum yield for the photochemical *cis/trans* isomerisation is slightly lower. In addition, the rotation speeds are slowed due to the increased steric bulk about the fjord region.

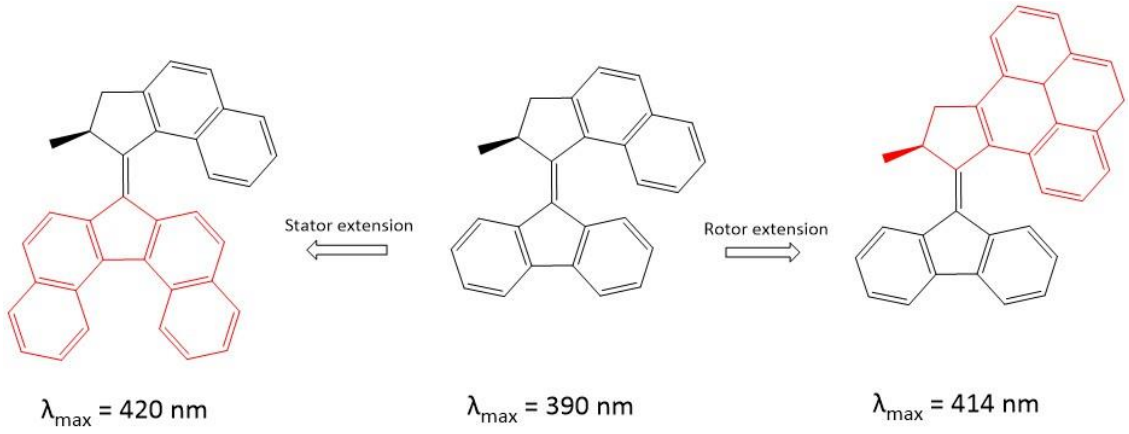

Figure 3.6 Stator (left) and rotor (right) extensions of Feringa motors with their accompanying maximum excitation wavelengths, 420 and 414 nm respectively.

This chapter focuses on C4 rotor and C7 stator functionalisation of Tour MNMs as this has been seen to introduce additional benefits alongside the red shifted rotor activation wavelength and lacks the various drawbacks of the other methods covered above, making it a promising route for use with the MNMs used for this project. It is reported that functionalisation of this kind is also able to promote cellular internalisation and an increase in fluorescence intensity while maintaining good rotation speeds and biologically compatible properties.[8] Promoting observable fluorescence in Tour MNMs without the addition of emissive side chains, such as BODIPY functionalisation, poses a challenge due to the majority of the absorbed energy being consumed in the non-radiative processes involved in the motion of the rotor.[9] The possible increase in cellular uptake is also worthy of further study as the activation of MNMs from within the cell may allow for more biologically favourable routes towards cell death to be accessed. Thus, the benefits of these MNMs are of great interest to the field. However, these advantages haven't been thoroughly investigated, and a systematic study of the impact on the nitrogen substitution of these diamine-based analogue has yet to be carried out.

The work presented in this chapter aims to assess the impact of increasing the substitution of the diamine nitrogens, at both the C4 rotor and C7 stator positions, on photoactivation, cellular internalisation, and emission properties. While also ensuring that the ability of the MNM to accelerate necrosis onset is minimally affected. Firstly, C7 stator functionalised MNMs will be investigated (**MNM 2, 3,** and **4** in the molecular nanomachine database), followed by C4 rotor-based diamines (**MNM 5** and **6**). These MNMs are illustrated again in **Table 3.1** for ease of interpretation.

Table 3.1 Excerpt of structures from the MNM database (found in Chapter 1) relevant to this chapter of work.

MNM Number	Chemical structure
MNM 2	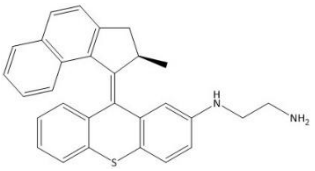
MNM 3	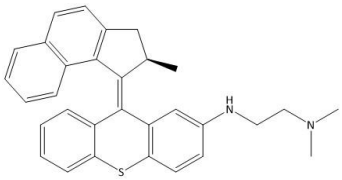
MNM 4	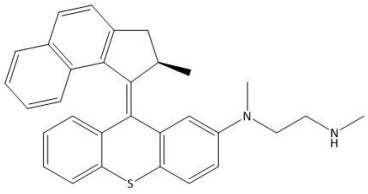
MNM 5	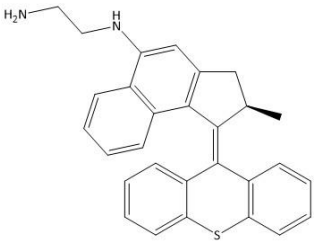
MNM 6	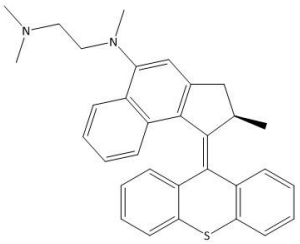

3.2 Stator “C7” diamine functionalisation

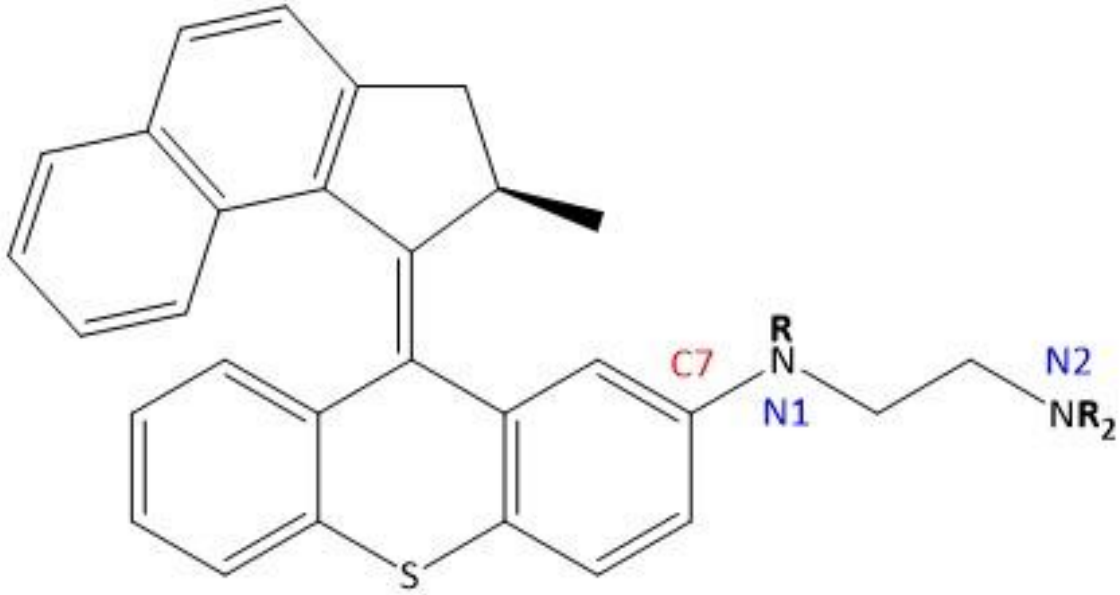

Figure 3.7 General structure for the family of stator "C7" bound diamine MNMs. R = H, Me.

MNMs 2, **3**, and **4** possess various diamine functionalisations at the C7 position on the stator. Varying only by the level of methyl substitution about the two nitrogen atoms. It is predicted that by increasing the level of substitution on either nitrogen, the lipophilicity of the compound will increase, allowing the MNM to cross the cell membrane more efficiently and internalise within cells at greater levels. However, it should be considered that this substitution – especially at the N1 nitrogen – will increase steric bulk within the previously defined “fjord region”, resulting in possible adverse effects on the rotary properties of the MNM.

The earlier cited “push-pull” effect suggested to be behind MNM activation wavelength tuning suggests that the addition of electron donating groups within the stator half of the molecule has the possibility of enabling a bathochromic shift. Leading to the prediction that the availability of the conjugated N1 nitrogen lone pair may result in altered activation wavelengths, with analogues showing greater levels methyl substitution having lower energy onsets of activation due to hyperconjugation. The

availability of MNMs to emit an observable percentage of absorbed energy instead of using the vast majority in the non-radiative process of rotation is not fully understood. It is the hope that this study will pose some answers to how a motors stereo-electronic structure relate to its fluorescence properties.

3.2.1 MNM 2

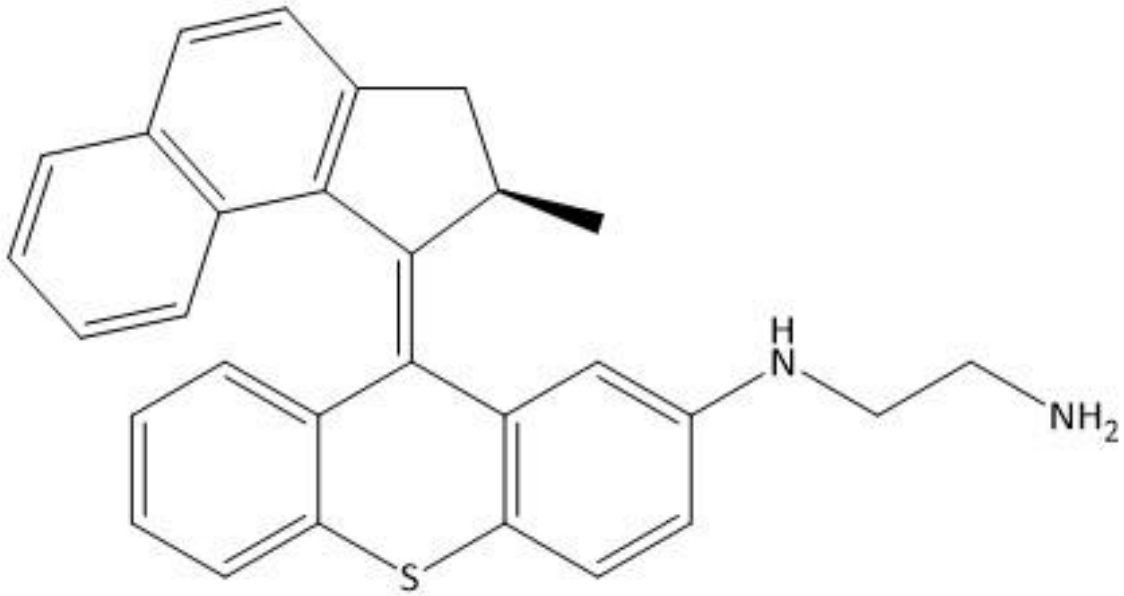

Figure 3.8 Chemical structure of **MNM 2**.

The first stator functionalised MNM studied, **MNM 2**, is the least substituted in this, diamine addend, class of machines. The absorption spectrum of **MNM 2** in DMSO is shown in **Figure 3.9**.

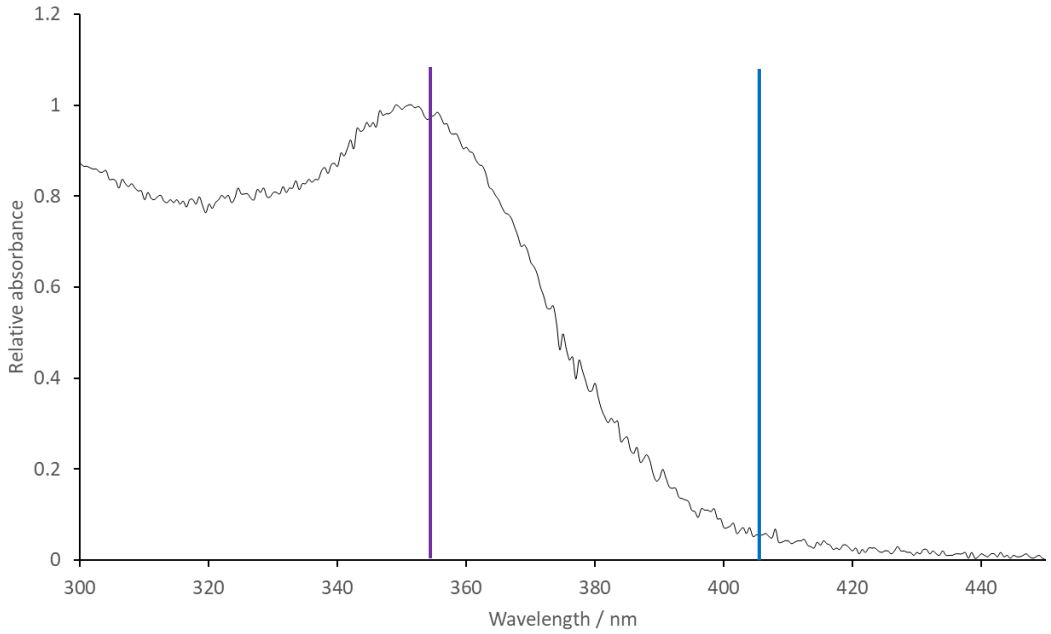

Figure 3.9 UV-Vis absorbance spectrum of **MNM 2** in DMSO with purple and blue lines indicating 355 and 405 nm absorbance respectively.

A fairly broad peak is observed with a maximum at ~355 nm, showing similar properties to the standard unfunctionalised machine **MNM 1** (overlaid spectra are given in **Figure 3.10**). Low energy onset of absorbance is unchanged while λ_{max} is seen to be slightly blue shifted. These results seem to suggest that the addition of the unsubstituted diamine results in little change in the photophysical properties of the motor, regardless of the electron donating conjugated lone pair on N1. A result that fit the initial hypothesis of this chapter of work, as it was initially predicted that the most substituted analogue had the greatest chance of promoting a bathochromic shift due to the increased availability of the lone pair caused by the hyperconjugation of the additional methyl electrons.

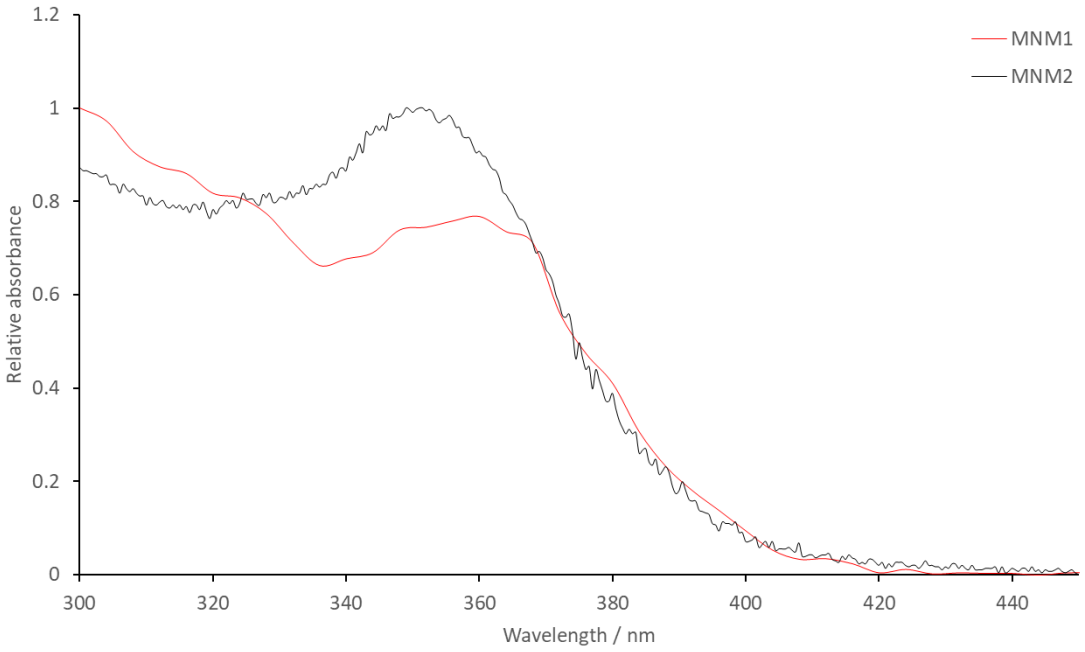

Figure 3.10 Overlaid UV-Vis absorbance spectra of unfunctionalised **MNM 1** (red) and C7 stator diamine **MNM 2** (black).

An emission spectrum was generated, exciting at 340 nm, however no emission was observed. Implying that this structure behaves in an identical way to its unfunctionalised counterpart. The vast majority of absorbed energy is utilised in the rotation mechanism leaving a negligible amount to promote fluorescence; this may be compensated for by using highly viscous solvents or low temperatures to slow down the rotation, however this would severely limit the biological applications. Making **MNM 2** unsuitable for fluorescent tracking.

Initial live cell microscopy experiments were carried out, using methods previously surmised in Chapter 2 (for full experimental procedures see methods Chapter 6), to assess **MNM 2**'s ability to promote necrosis in samples of NIH 3T3 cells. **Figure 3.11** shows these results alongside both a control sample containing a comparable concentration of DMSO (0.1% v/v), and a sample containing the widely investigated, unfunctionalised, **MNM 1**.

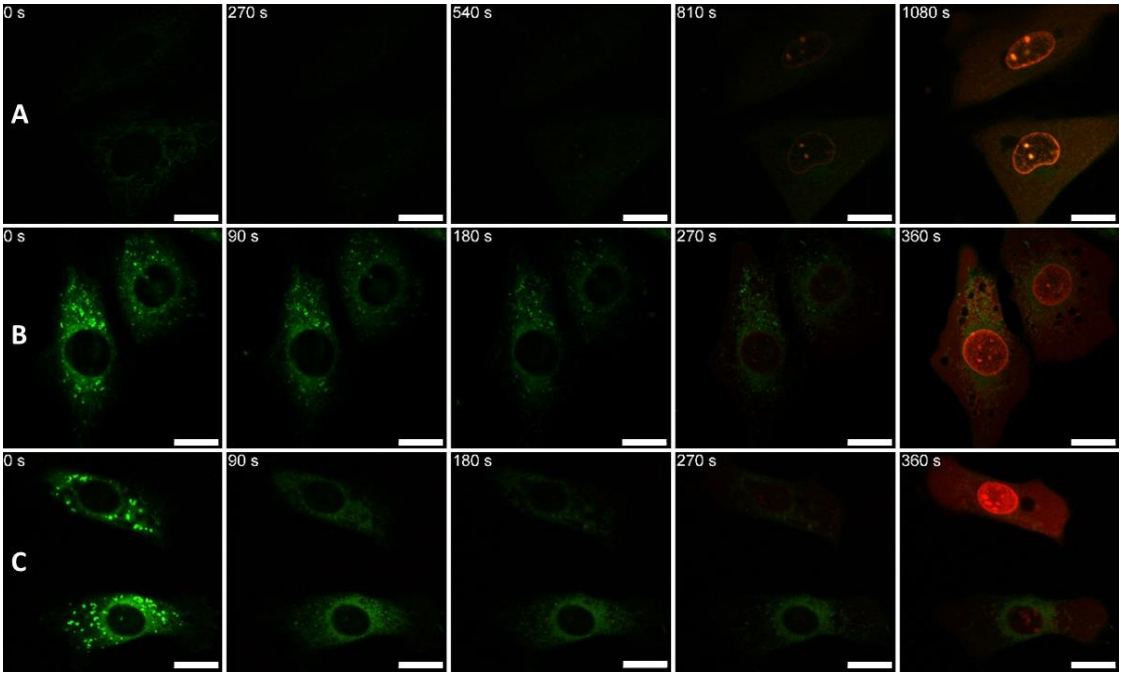

Figure 3.11 Microscopic observation of cell death caused by excitation at 355 nm (UV-exposure times are shown for each image), quantified by the observation of PI fluorescence within the nucleus. **A** – Control sample: NIH 3T3 cells loaded with 100 nM PI and 0.1% DMSO. **B** – NIH 3T3 cells loaded with 100 nM PI and 0.5 µM **MNM 1**. **C** - NIH 3T3 cells loaded with 100 nM PI and 0.5 µM **MNM 2**. All image sets collected after 30 minutes incubation after dosing procedure. Overlaid channels of PI fluorescence (λ_{ex} = 543 nm, 0.2 mW; λ_{em} = 600-700 nm), and mitochondrial autofluorescence (λ_{ex} = 355 nm, 20 mW, 400 nJ per voxel; λ_{em} = 440-460 nm). All scale bars set to 20 µm.

As expected, a dramatic reduction in TTN was observed – *via* first onset of PI emission within the nucleus - when compared to the control sample (**Figure 3.11 A**). The acceleration of cell death caused by **MNM 2** (**Figure 3.11 C**) was shown to be almost identical to that seen for the previously studied **MNM 1** (**Figure 3.11 B**), with the control first showing PI emission at 1080 s and both MNMs reducing this to 360 s. This suggests that the addition of the minimally substituted diamine moiety has little to no observable

impact on the MNM's ability to disrupt the cells membrane. Allowing for the conclusion that the rotation speed of the rotor is unaffected in a significant way, and thus that the steric bulk within the fjord region is unchanged.

In order to determine the capability of a MNM to internalise within cells – either by crossing, or by getting lodged within the phospholipid bilayer – a series of experiments were designed. These are summarised in **Figure 3.12**. In brief, after incubating the cellular sample with 0.5 μM of MNM, for various periods of time, the sample is washed with MNM free media – removing any MNM in solution. Imaging then takes place as normal after the required staining procedures. Any observed decrease in the TTN can then be rationalised as being caused by MNMs left behind within the cell or stuck within the cellular membrane; the magnitude of this necrosis acceleration will be proportional to the levels of internalised MNM and therefore will act as a measure of the machines ability to cross the membrane. A clearance procedure is also used, whereby a MNM dosed, and subsequently washed, cellular sample is left for the period of one cell division cycle (16-hour average for NIH 3T3) with regular media changes. Allowing for the observation of the ability of the cells to: 1) Eject any internal MNMs over the course of a cell cycle, and 2) maintain good cellular health after being dosed with MNMs. A complete breakdown of these experimental procedures is found in Chapter 6.

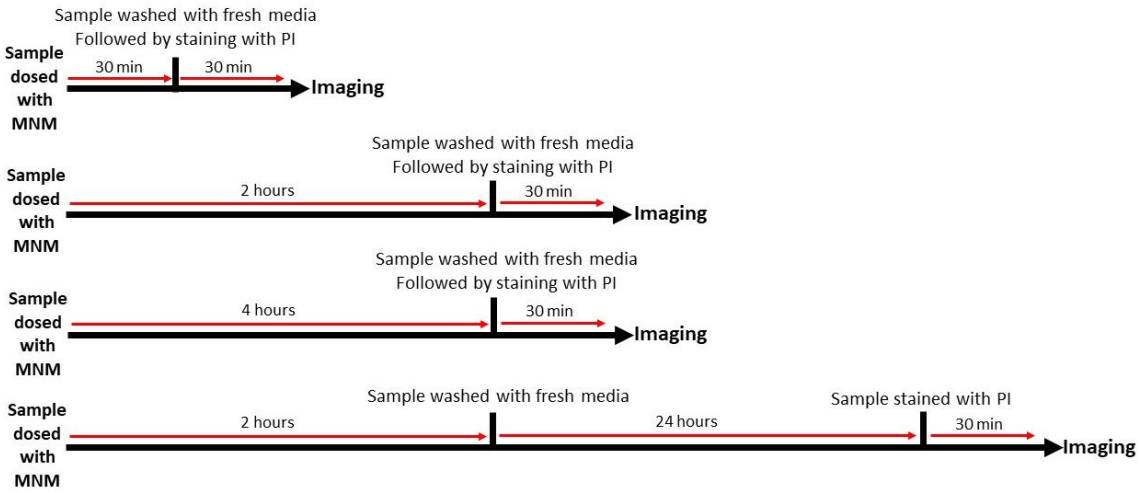

Figure 3.12 Summary of cellular internalisation experiment timelines.

The live cell microscopy results of these **MNM 2** internalisation studies are shown in **Figure 3.13**.

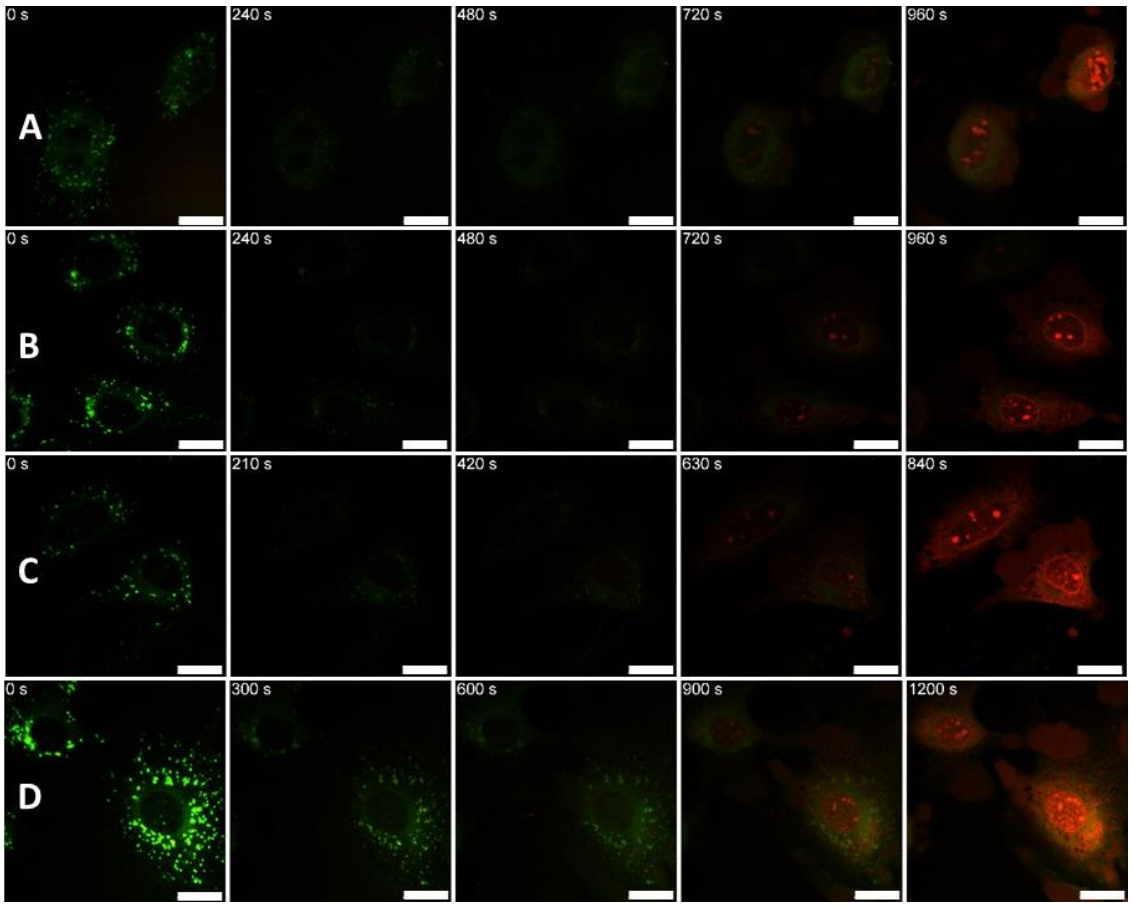

Figure 3.13 Microscopic observation of cell death caused by excitation at 355 nm (UV-exposure times are shown for each image), quantified by the observation of PI fluorescence within the nucleus. **A** – NIH 3T3 loaded with 0.5 µM **MNM 2**, followed by 30 minutes incubation and washing with MNM free media, and subsequent staining with 100 nM PI. **B** – NIH 3T3 loaded with 0.5 µM **MNM 2**, followed by 2-hour incubation and washing with MNM free media, and subsequent staining with 100 nM PI. **C** - NIH 3T3 loaded with 0.5 µM **MNM 2**, followed by 4-hour incubation and washing with MNM free media, and subsequent staining with 100 nM PI. **D** - NIH 3T3 loaded with 0.5 µM **MNM 2**, followed by 2-hour incubation, washing with MNM free media, 16-hour clearance, and subsequent staining with 100 nM PI. All image sets collected after 30 minutes incubation after staining procedure. Overlaid channels of PI fluorescence (λ_{ex} = 543 nm, 0.2 mW; λ_{em} = 600-700 nm), and mitochondrial

autofluorescence (λ_{ex} = 355 nm, 20 mW, 400 nJ per voxel; λ_{em} = 440-460 nm). All scale bars set to 20 μm.

Comparing these results to the previously evaluated images for both the control sample and the standard dosing procedure for **MNM 2**, conclusions about the internalisation properties of **MNM 2** can be drawn. Firstly, it is clearly shown that a significantly less noticeable increase in the TTN is observed after washing the cell samples with MNM free media for all incubation times (~600 – 700 s) when compared with experiments where **MNM 2** remains in solution (~350 s). A slight increase in TTN is seen from as little as 30 minutes of incubation (~720 compared with ~810 s) with **MNM 2** compared to the control sample, implying that a small amount of **MNM 2** does indeed remain after media changes. When considering previous findings of cell surface pit-like localisation of MNMs, this can be rationalised as small numbers of **MNM 2** becoming lodged on the membranes surface and cannot be conclusively rationalised by any proposed internalisation effects. Additionally, increasing the incubation time before removal of MNMs from the media doesn't result in a dramatic increase in the apparent internalisation, with no observable difference shown between 30 minute and 2-hour incubation. A slight further reduction in TTN is seen after 4 hours of incubation before MNM removal (~630 s) implying small amounts of MNM may be fully trapped within the phospholipid bilayer or possibly internalised within the cell itself. However, the exact location of these molecules isn't possible to determine due to their previously discussed lack of emission and low concentrations. No further increase in necrosis acceleration was observed for longer incubation times up to 24 hours.

After incubating cells with **MNM 2** for 2 hours and washing with MNM free media, followed by a complete cell division cycle with regular media changes, it is shown that

the TTN dramatically rises back to pre-experiment levels (**Figure 3.13 D**). Implying that any internalised MNMs have been cleared from the system and that no detriment to overall cellular health was caused by the experiment.

A summary of the induced TTN for each of the previously discussed experiments with **MNM 2** is shown in **Figure 3.14**.

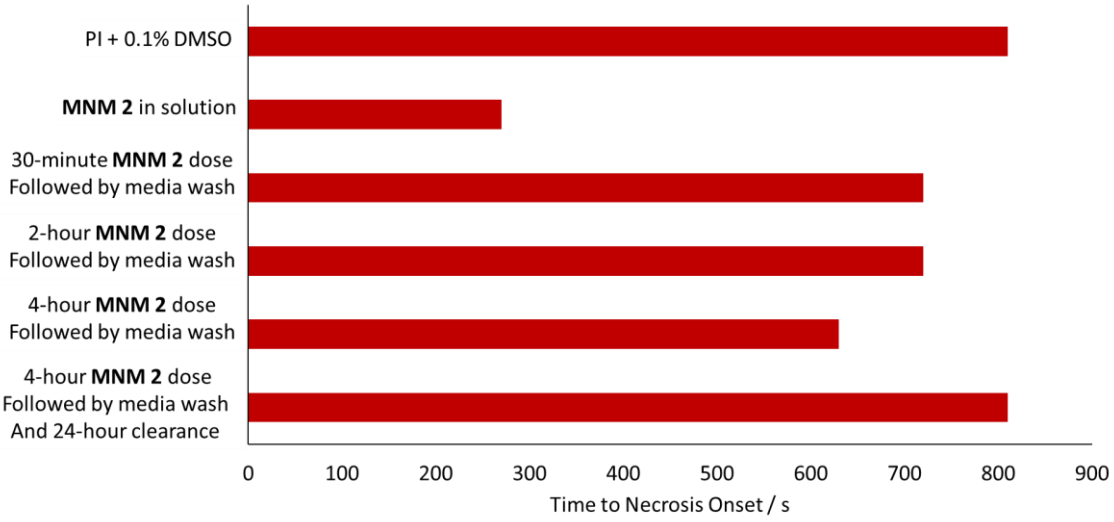

Figure 3.14 Graphical summary of TTN data based upon first observable PI emission detected within the nucleus for **MNM 2** internalisation studies.

Interestingly, experiments with longer MNM incubation times lead to an unexpected distortion of the mitochondrial autofluorescence. Instead of the anticipated web-like appearance, the network appears balled up with inconsistent fluorescent intensity throughout. A comparison is shown in **Figure 3.15**. This effect is shown for all the MNMs studied throughout this chapter, suggesting the diamine functionalisation in responsible for this phenomenon. However, it is important to note that this appears to have no effect on cell viability as consistent results are obtained regardless of mitochondrial appearance. While samples of NIH3T3 cells exposed to longer incubation times of **MNM 2** have been place back into the incubator and been shown to be healthy for multiple

cell division cycles after experimentation, it should be noted that no further cell viability studies have been carried out after those initially reported by García-López *et al*.[9]

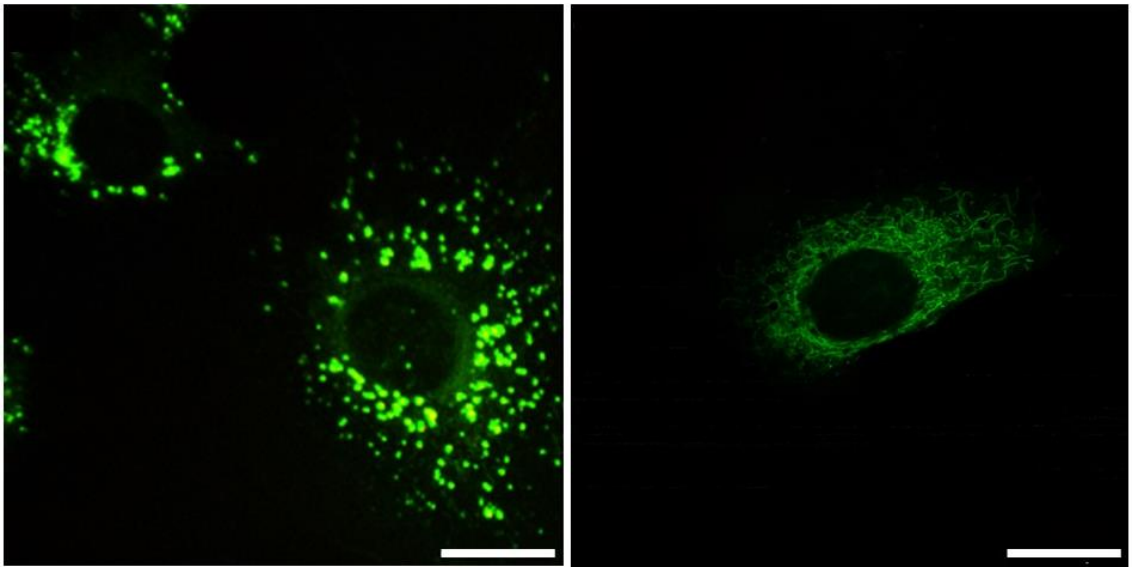

Figure 3.15 Microscopic observation of mitochondrial autofluorescence (λ_{ex} = 355 nm, 20 mW, 400 nJ per voxel; λ_{em} = 440-460 nm) for NIH 3T3 cells when dosed with **MNM 2** (left) and **MNM 1** (right). Scale bars set to 20 µm.

This change in appearance could be rationalised by some binding mechanism between the dosed MNM and the mitochondria itself; possibly implying the nitrogen atoms become protonated within the cell leading to electrostatic attraction to the negative mitochondrial membrane. However, the low amount of internalisation seen for **MNM 2** makes such a strong effect unlikely. Another possible explanation for the unexpected appearance of the cells is any internalised MNMs becoming trapped within lysosomes; the acidic (pH 4.5) membrane bound organelles responsible for receiving and disposing of molecules entering the cell, which extensively sequester lipophilic and basic compounds.[10,11] If the rotation of the MNMs rotor is hindered significantly while held within the lysosomes, the absorbed energy may promote fluorescence of the molecule

in the same range as mitochondrial autofluorescence (440 – 460 nm) as illustrated further in this chapter by emission spectra of **MNMs 5** and **6**. **Figure 3.16** shows a comparison between the effect observed by diamine MNM dosing of NIH 3T3 cells and staining of the lysosomes by Lysoview 488™.[12]

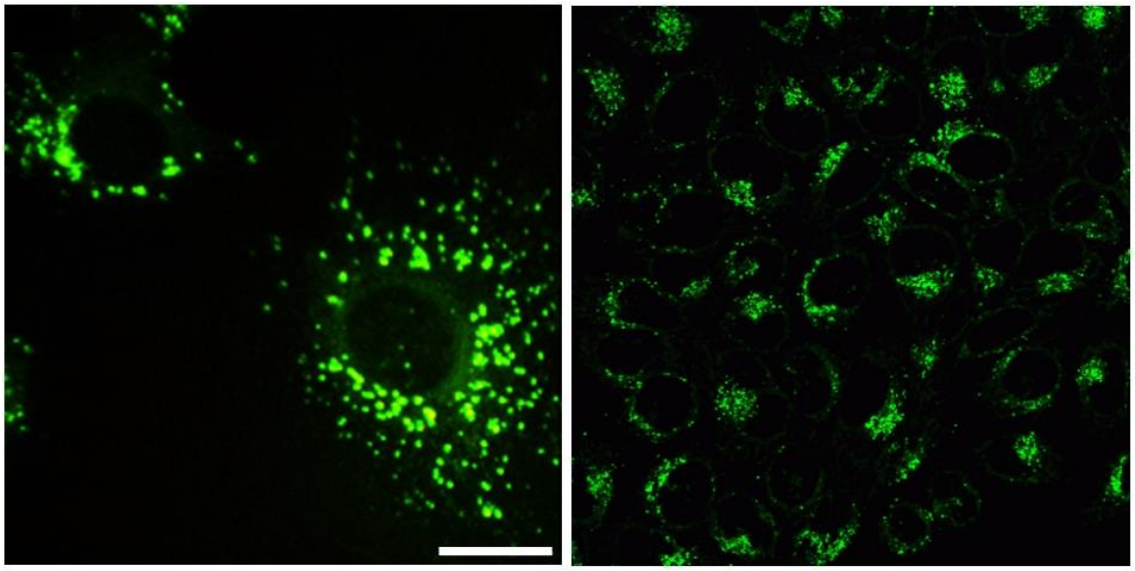

Figure 3.16 Microscopic observation of mitochondrial autofluorescence (λ_{ex} = 355 nm, 20 mW, 400 nJ per voxel; λ_{em} = 440-460 nm) for NIH 3T3 cells when dosed with **MNM 2** (left) and emission of LysoView 488 adapted from Cambridge bioscience (right).[12] Scale bar set to 20 µm (left), with no scale bar provided by Cambridge bioscience (right).

3.2.2 MNM 3

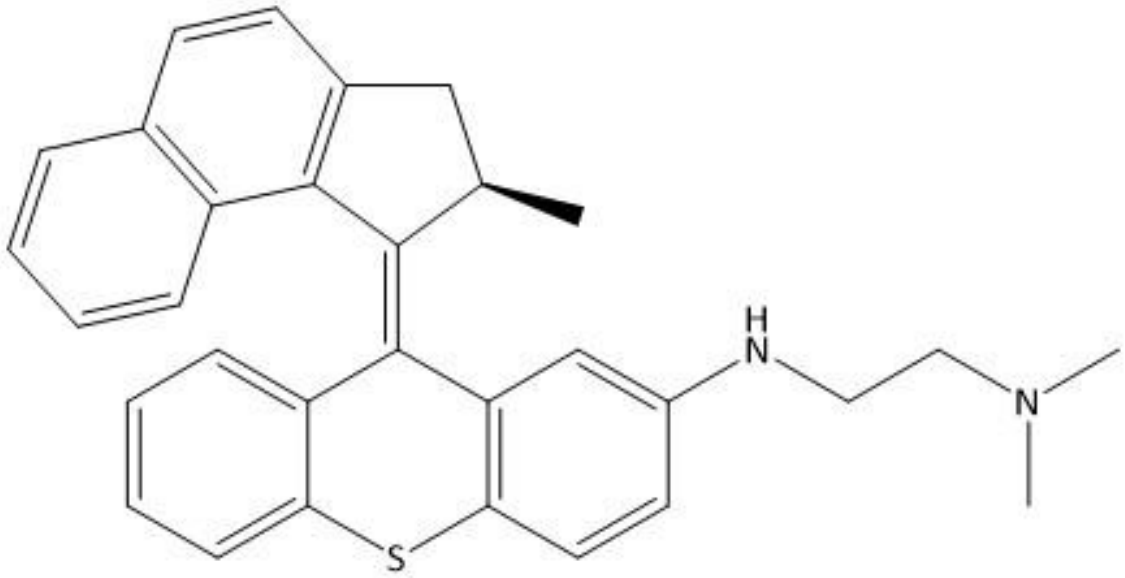

Figure 3.17 Chemical structure of MNM **3**.

MNM 3 is another example of a stator functionalised diamine, maintaining the secondary amine at the N1 position but possesses a fully substituted tertiary amine at N2. Based on the hypothesis covered at the start of this chapter, it is predicted that this slight increase in lipophilicity should result in increased internalisation of the MNM. Due to the additional substitution being added at the N2 position - further away from the fjord region than the corresponding N1 – it is hoped that little to no slowing down of the rotor should occur, thereby maintaining a good ability to disrupt the cellular membrane and induce early onset necrosis. The photophysics of the molecule are harder to predict with the results for **MNM 2** implying that the diamine addition has little impact; the absorption spectrum for **MNM 3** is shown in **Figure 3.18**.

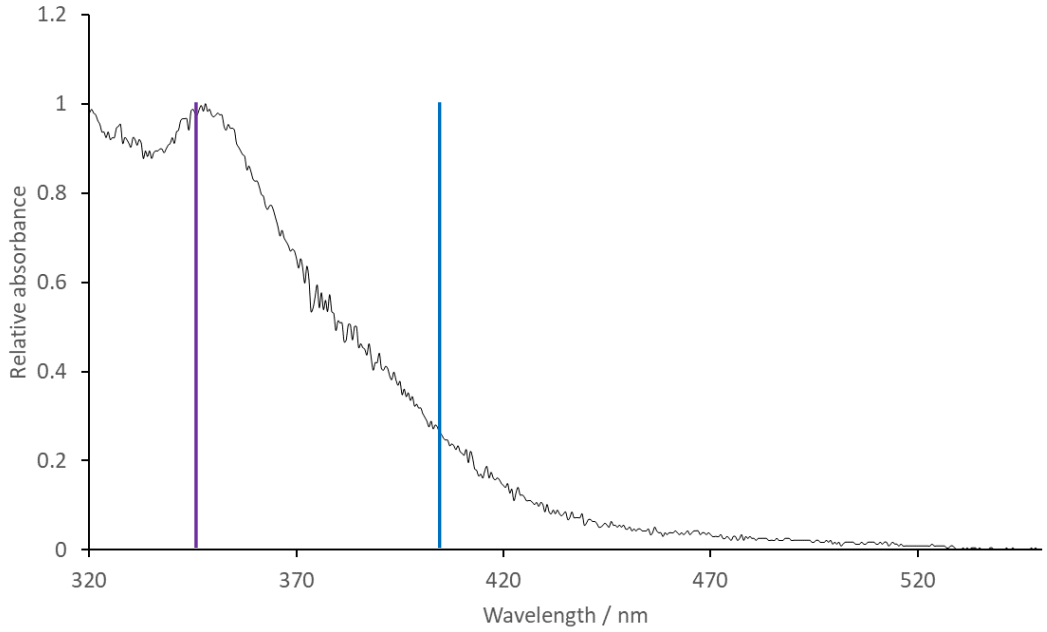

Figure 3.18 UV-Vis absorbance spectrum of **MNM 3** in DMSO with purple and blue lines indicating 355 and 405 nm absorbance respectively.

Similarly to **MNM 2**, the absorbance spectrum of **MNM 3** shows an absorbance maximum of ~350 nm, showing no observable bathochromic shift caused by diamine functionalisation at the C7 stator position. In general, the absorbance peak is narrower than that seen for other MNMs, but efficient activation is still shown when excited with 355 nm wavelengths. As with **MNM 2**, an emission spectrum was attempted at 340 nm excitation. Despite a slight increase in average intensity, the presence of any emission was not discernible from noise under standard conditions. Once again implying that this method of MNM functionalisation is not altering the mechanics of rotor photoactivation in any meaningful way.

The same experimental rationale was carried out for this MNM, with initial experiments measuring the acceleration of necrosis with **MNM 3** in solution. These results are shown and compared to both the control sample and unfunctionalised **MNM 1** in **Figure 3.19**.

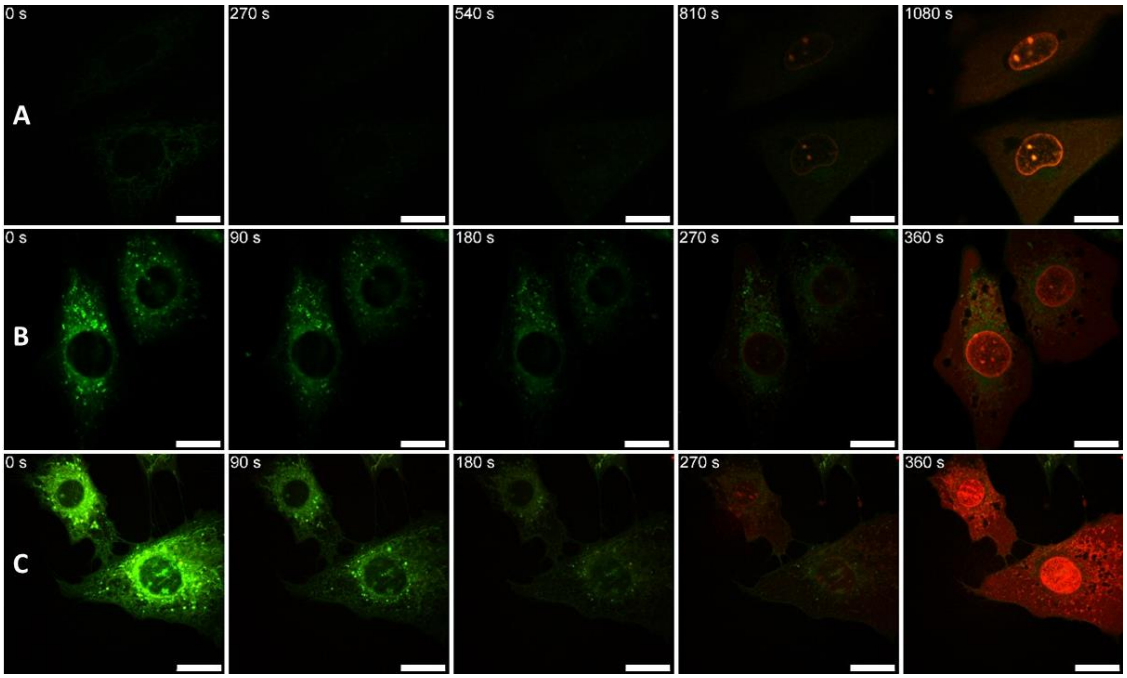

Figure 3.19 Microscopic observation of cell death caused by excitation at 355 nm (UV-exposure times are shown for each image), quantified by the observation of PI fluorescence within the nucleus. **A** – Control sample: NIH 3T3 cells loaded with 100 nM PI and 0.1% DMSO. **B** – NIH 3T3 cells loaded with 100 nM PI and 0.5 µM **MNM 1**. **C** - NIH 3T3 cells loaded with 100 nM PI and 0.5 µM **MNM 3**. All image sets collected after 30 minutes incubation after dosing procedure. Overlaid channels of PI fluorescence (λ_{ex} = 543 nm, 0.2 mW; λ_{em} = 600-700 nm), and mitochondrial autofluorescence (λ_{ex} = 355 nm, 20 mW, 400 nJ per voxel; λ_{em} = 440-460 nm). All scale bars set to 20 µm.

The results found agree with both the outcomes of studies with **MNM 2**, and previous work with **MNM 1**. A dramatic increase in TTN is seen when **MNM 3** is left in solution and activated with 355 nm UV light when compared with the control sample; first observable necrosis is detected in the nucleus at 270 s (**Figure 3.19 C**), compared with 810 s (**Figure 3.19 A**). A ~66% reduction in TTN, comparable with results obtained with **MNM 1** in solution. Showing that the addition of the diamine functional group does not

hinder the movement of the rotor when the N2 position is fully saturated with methyl groups. It should be noted that the mitochondria autofluorescence channel again appears altered and shows an increase in brightness. While no conclusion can reasonably be drawn from this due to normal fluctuations in brightness seen between separate experiments, it may again suggest diamine functionalised MNMs are able to fluoresce if held within the cells with their rotation hindered.

Internalisation studies were carried out *via* the same procedures as those followed for **MNM 2** to identify any changes in **MNM 3**'s ability to cross, or get stuck within, the cell membrane caused by the additional lipophilicity caused by the methyl functionalisation of the N2 amine. These results are shown in **Figure 3.20**.

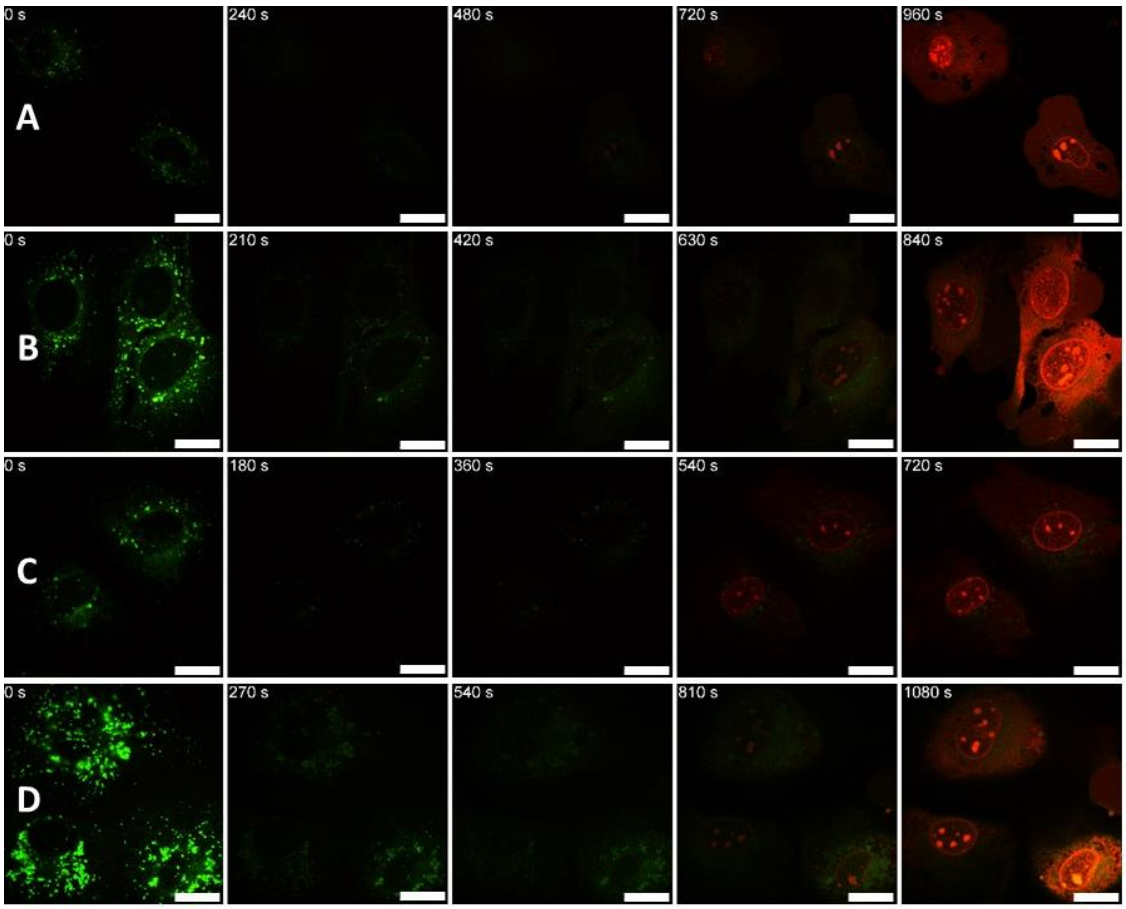

Figure 3.20 Microscopic observation of cell death caused by excitation at 355 nm (UV-exposure times are shown for each image), quantified by the observation of PI fluorescence within the nucleus. **A** – NIH 3T3 loaded with 0.5 µM **MNM 3**, followed by 30 minutes incubation and washing with MNM free media, and subsequent staining with 100 nM PI. **B** – NIH 3T3 loaded with 0.5 µM **MNM 3**, followed by 2-hour incubation and washing with MNM free media, and subsequent staining with 100 nM PI. **C** - NIH 3T3 loaded with 0.5 µM **MNM 3**, followed by 4-hour incubation and washing with MNM free media, and subsequent staining with 100 nM PI. **D** - NIH 3T3 loaded with 0.5 µM **MNM 3**, followed by 2-hour incubation, washing with MNM free media, 16-hour clearance, and subsequent staining with 100 nM PI. All image sets collected after 30 minutes incubation after staining procedure. Overlaid channels of PI fluorescence (λ_{ex} = 543 nm, 0.2 mW; λ_{em} = 600-700 nm), and mitochondrial

autofluorescence (λ_{ex} = 355 nm, 20 mW, 400 nJ per voxel; λ_{em} = 440-460 nm). All scale bars set to 20 µm.

While a similar trend to that of **MNM 2** is observed, some key differences give insight into what effect switching N2 from a primary to tertiary amine has imparted on the internalisation properties of **MNM 3**. Firstly, while the ability to promote early onset necrosis does not reach the levels seen when the MNM is in solution, a faster TTN is observed when compared to the result seen when studying **MNM 2**. For example, after just 30 minutes of incubation before changing the media **MNM 3** causes first emission of PI to be detected at ~630 s (a 22% reduction in TTN compared to the control sample) compared to **MNM 2** triggering the same condition at 720 s (11% reduction). This relationship of increased reduction in TTN between **MNM's 2 and 3** remains true for all studied incubation times. Implying that, as predicted, the additional methyl substituents has indeed resulted in a higher percentage of MNM internalisation. Additionally, after incubation followed by the 16-hour clearance period results were found completely in line with a standard control sample. Suggesting that this increased ability to cross, or get stuck within, the cell membrane does not impact the cells capability to remove **MNM 3** from the system.

As previously these results are summarised, using the UV exposure time of the specific frame of first detected PI emission in **Figure 3.21** for ease of comparison.

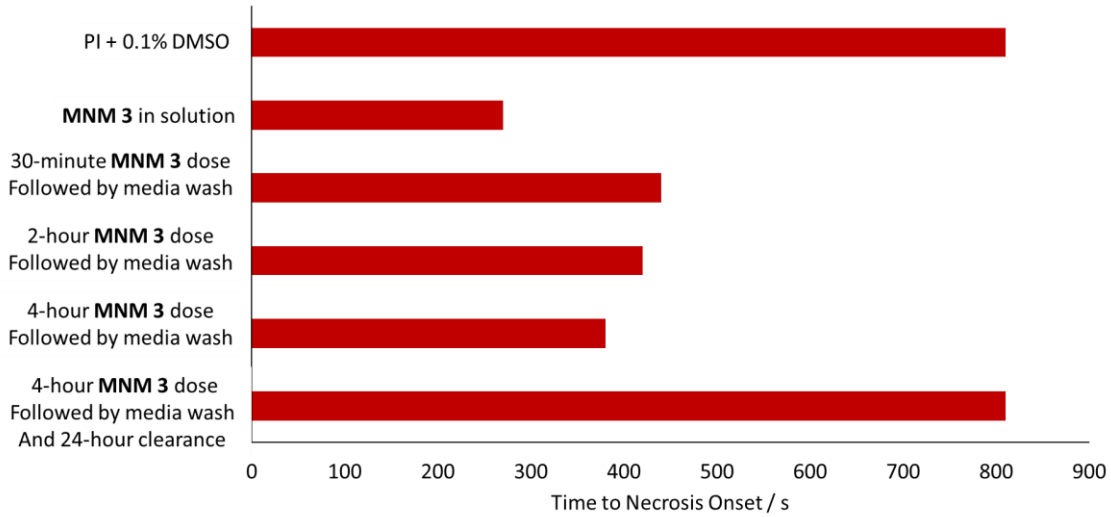

Figure 3.21 Graphical summary of TTN data based upon first observable PI emission detected within the nucleus for **MNM 3** internalisation studies.

3.2.3 MNM 4

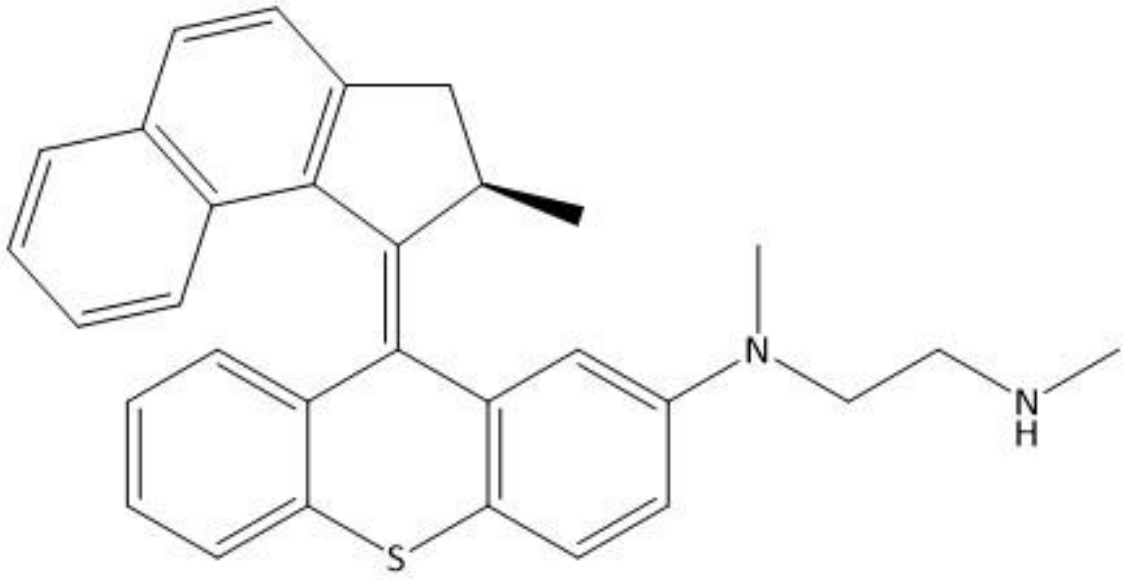

Figure 3.22 Chemical structure of **MNM 4**.

MNM 4 is designed with the same number of additional methyl groups as **MNM 3** but split between both amine sites. Resulting in a tertiary amine at the N1 position and a secondary at N2. This structure allows the effect of increased substitution about the N1 position – the nitrogen closer to the fjord region – to be studied. It is predicted that comparable internalisation behaviour to **MNMs 2 and 3** will be found. However, due to

the proximity of the functionalisation to the aforementioned fjord region a reduction in rotation speed, and thus a reduction in ability to accelerate necrosis onset is possible. It is assumed that similar photophysical properties to the previously studied MNMs will be observed as only conformation changes are found between **MNMs 3 and 4**. The absorption spectrum for **MNM 4** is shown in **Figure 3.23**.

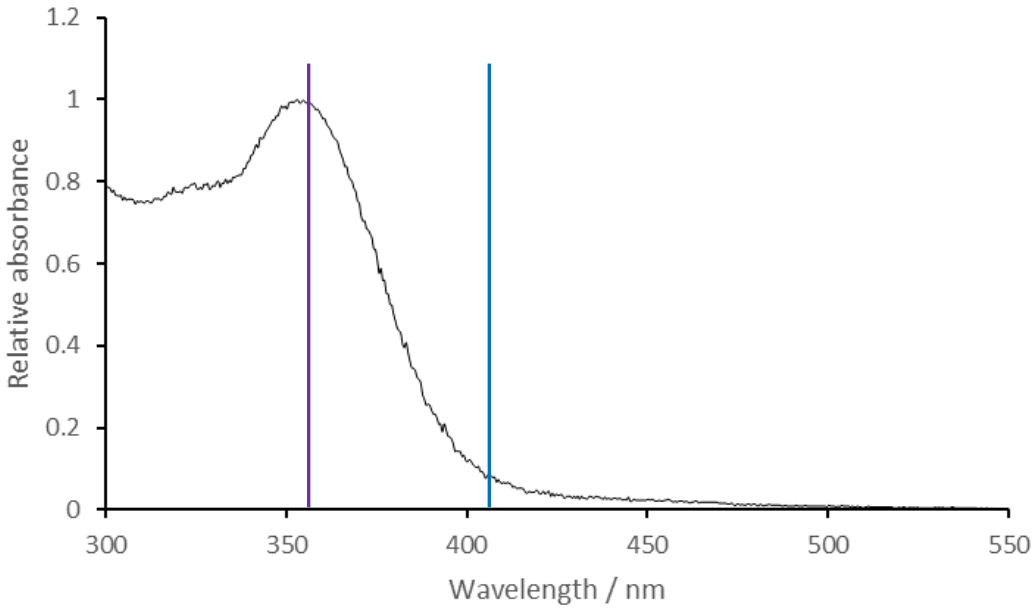

Figure 3.23 UV-Vis absorbance spectrum of **MNM 4** in DMSO with purple and blue lines representing 355 and 405 nm absorbance respectively.

Importantly, the absorbance maximum of **MNM 4** is shown to be very slightly red shifted. Possibly implying that functionalisation about the N1 amine position has an impact on the photoactivation of the rotary cycle; however, without additional analogues and further study this cannot be conclusively stated. The addition of the methyl group causes this small bathochromic shift as the N1 transformation from secondary to tertiary amine will increase the availability of the lone pair due to the inductive effect of the alkyl group. Which, based on previous discussion of the "push-pull" mechanism, would indeed be predicted to induce a slight redshift as it was found

that electron donating stator substituents caused a greater reduction in HOMO-LUMO energy gap. This observation may also be rationalised by a steric effect - due to the proximity of this additional methyl group to the fjord region - manipulating the mechanism of rotation and subsequently altering the activation wavelength and not an electronic effect caused by the lone pair donation of the diamine. In line with the other stator functionalisation diamine MNMs no discernible peaks were shown in the emission spectrum corresponding to 340 nm excitation. Implying that the rotor is not slowed to a significant enough extent to promote radiative processes above the non-radiative rotation mechanism.

Live-cell microscopy was carried out in the same fashion as previous MNM studies and did however show a possible change to the rotation speed, shown in **Figure 3.24**.

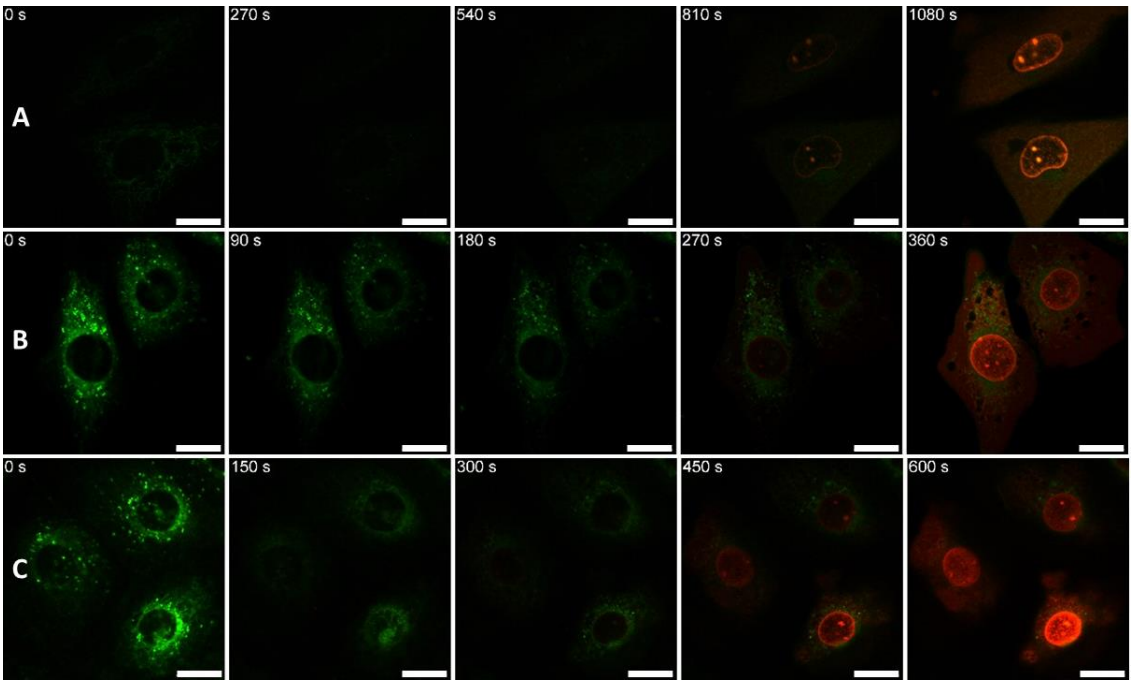

Figure 3.24 Microscopic observation of cell death caused by excitation at 355 nm (UV-exposure times are shown for each image), quantified by the observation of PI fluorescence within the nucleus. **A** – Control sample: NIH 3T3 cells loaded with 100 nM PI and 0.1% DMSO. **B** – NIH 3T3 cells loaded with 100 nM PI and 0.5 µM **MNM 1**. **C** - NIH 3T3 cells loaded with 100 nM PI and 0.5 µM **MNM 4**. All image sets collected after 30 minutes incubation after dosing procedure. Overlaid channels of PI fluorescence (λ_{ex} = 543 nm, 0.2 mW; λ_{em} = 600-700 nm), and mitochondrial autofluorescence (λ_{ex} = 355 nm, 20 mW, 400 nJ per voxel; λ_{em} = 440-460 nm). All scale bars set to 20 µm.

MNM 4, while still promoting necrosis onset at a significantly faster rate than the control sample (44% reduction in TTN), was shown to be less effective than both other stator functionalised diamines **MNM 2 and 3** (~70 and ~66% reduction in TTN respectively). Leading to the possible conclusion that the steric hindrance added by functionalising the N1 position has impacted the fjord region. However, this effect is relatively small as seen by a lack of fluorescence from the compound, implying most absorbed energy is still

going towards the rotation cycle. Critically, any reduction in rotation rate does not stop **MNM 4** from promoting early necrosis in NIH 3T3 cells.

In line with previous analogues, the internalisation properties of **MNM 4** were measured by the same microscopy experimental series, illustrated in **Figure 3.25**.

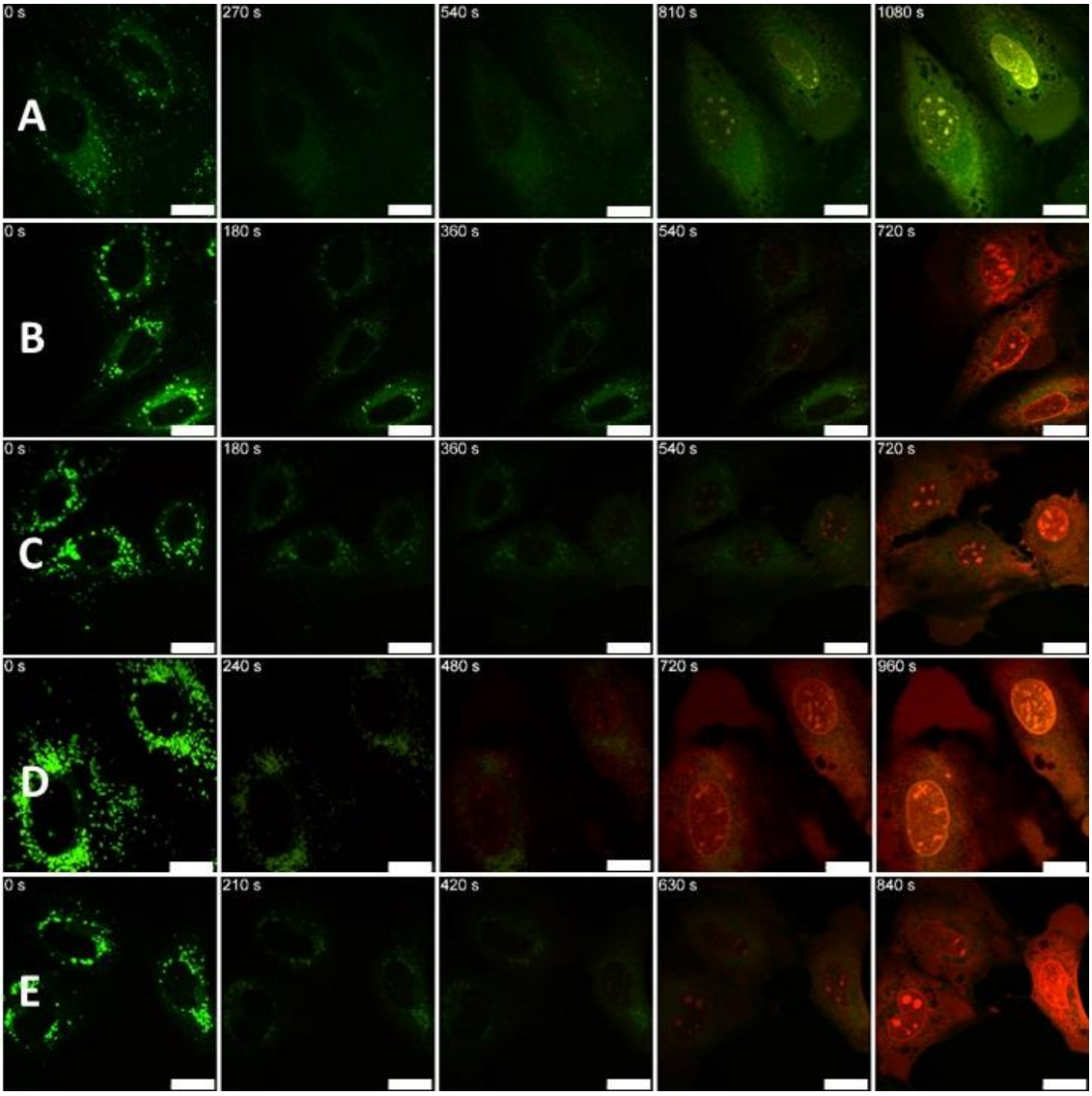

Figure 3.25 Microscopic observation of cell death caused by excitation at 355 nm (UV-exposure times are shown for each image), quantified by the observation of PI fluorescence within the nucleus. **A** – NIH 3T3 loaded with 0.5 µM **MNM 4**, followed by 30 minutes incubation and washing with MNM free media, and subsequent staining with 100 nM PI. **B** – NIH 3T3 loaded with 0.5 µM **MNM 4**, followed by 2-hour incubation and washing with MNM free media, and subsequent staining with 100 nM PI. **C** - NIH 3T3 loaded with 0.5 µM **MNM 4**, followed by 4-hour incubation and washing with MNM free media, and subsequent staining with 100 nM PI. **D** - NIH 3T3 loaded with 0.5 µM **MNM 4**, followed by 24-hour incubation and washing with MNM free

media, and subsequent staining with 100 nM PI **E** - NIH 3T3 loaded with 0.5 µM **MNM 4**, followed by 2-hour incubation, washing with MNM free media, 16-hour clearance, and subsequent staining with 100 nM PI. All image sets collected after 30 minutes incubation after staining procedure. Overlaid channels of PI fluorescence (λ_{ex} = 543 nm, 0.2 mW; λ_{em} = 600-700 nm), and mitochondrial autofluorescence (λ_{ex} = 355 nm, 20 mW, 400 nJ per voxel; λ_{em} = 440-460 nm). All scale bars set to 20 µm.

These internalisation studies present some interesting findings compared to the previously investigated MNMs, surprising due to the relatively minor structural change of **MNM 4**. First, it is clear that **MNM 4** does not show as dramatic a decrease in the TTN as the incubation time is increased - when compared with **MNMs 2** and **3**. This could be due to a number of possibilities; **MNM 4** may not cross the phospholipid bilayer as efficiently resulting in lower concentrations being left behind after washes with fresh MNM free media. Alternatively, this decrease in potency may simply be caused by the MNMs previously discussed slower rotation speed limiting the disruption caused to the membrane. To further understand this possible lower rate of internalisation **MNM 4** was left to incubate with the cellular sample for 24 hours before washing with fresh media (**Figure 3.25 D**). Very little increase in the ability to promote early onset necrosis was observed between this experiment and the previous 2 and 4-hour incubations, implying the maximum internal cellular concentration of **MNM 4** is reached within the first few hours of incubation and that this is not potent enough to cause sufficient enough membrane disruption to rapidly cause cell death.

The second surprising result is found in the results of the 16-hour clearance procedure (**Figure 3.25 E**). Here, a clear reduction in the TTN compared to the control sample is observed after allowing the cells a full division cycle with regular MNM free media

changes. In all experiments with previous MNMs this has been sufficient to clear any withheld MNM from the system resulting in almost identical results to a standard control sample. This strongly implies that **MNM 4** is either not sufficiently cleared from within cells / cell membranes, or prolonged exposure to **MNM 4** is toxic to the cells under study. This stark contrast with results obtained for previous **MNMs 2** and **3** is again surprising as the structural change is relatively minor. These results are again summarised graphically in **Figure 3.26** for ease of comparison.

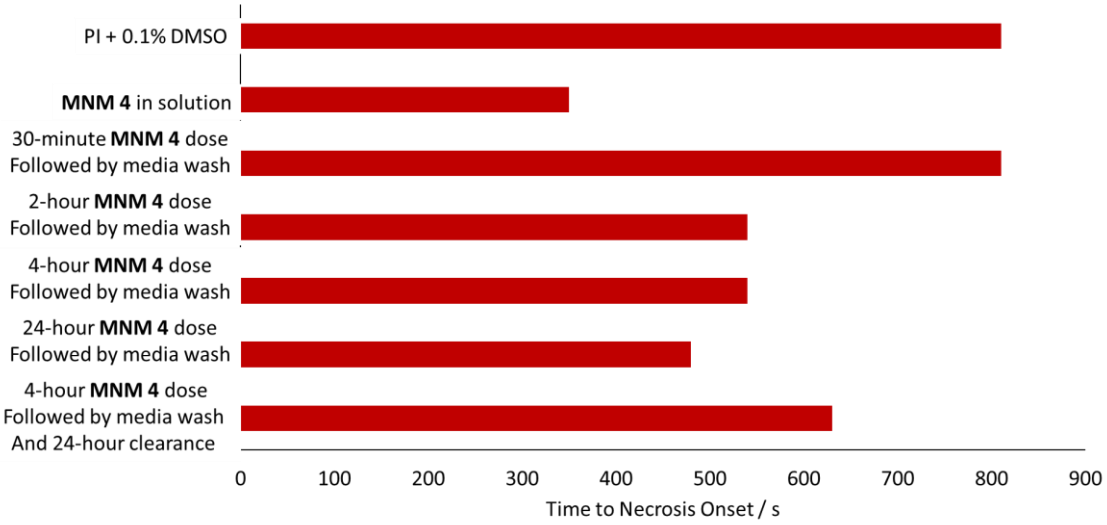

Figure 3.26 Graphical summary of TTN data based upon first observable PI emission detected within the nucleus for **MNM 4** internalisation studies.

3.3 Rotor "C4" diamine functionalisation

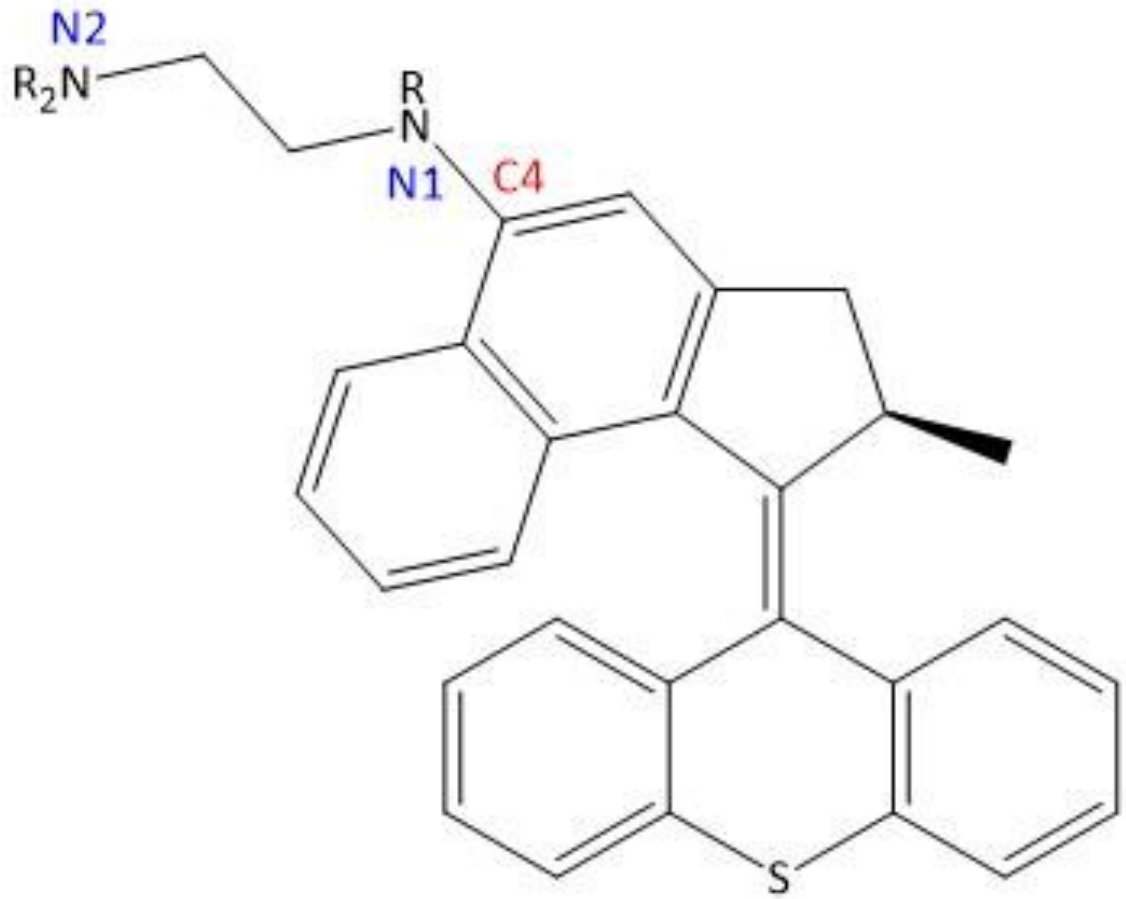

Figure 3.27 General structure for the family of stator "C7" bound diamine MNMs. R = H, Me.

MNMs 5 and **6** are functionalised with similar diamine addends to the previously covered **MNMs 2**, **3**, and **4**, on the C4 rotor position as opposed to the C7 stator site. Containing the least and most methyl substitutions respectively. As previously discussed, functionalisation with both electron donating and electron withdrawing moieties at the C4 position on the rotor has been shown to promote significantly red shifted activation of MNMs within the literature.

It is predicted that this class of MNM have a greater chance of showing bathochromic shift in their activation wavelength compared to the previous stator functionalised family. **MNM 6** is fully saturated with methyl groups, possessing tertiary amines both

the N1 and N2 positions. This increase in lipophilicity is anticipated to aid in the passive crossing of the phospholipid bilayer and allow for good levels of MNM internalisation within the cell when compared with the fully unsubstituted **MNM 5**. It is also hoped, based on previously discussed literature, that a sufficient increase in fluorescence properties will be shown - allowing emission spectra to be collected.

An interesting dynamic is found specifically with this class of MNMs. Due to the lack of functionalised "arms" on the stator – like those seen on **MNM 1** – these C4 rotor functionalisations result in the molecular weight of the rotor being higher than the stator. This is not the case for any other MNM investigated throughout this project. While the nomenclature for the halves of the molecule separated by the double bond axle will not be altered, it is important to consider that in these specific cases it is likely the "stator" that is rotating about the "rotor" half of the molecule. This distinction may lead to unique rotary and photophysical properties for **MNM 5** and **6**, which will be hard to distinguish from any effects caused by the diamine functionalisation.

3.3.1 MNM 5

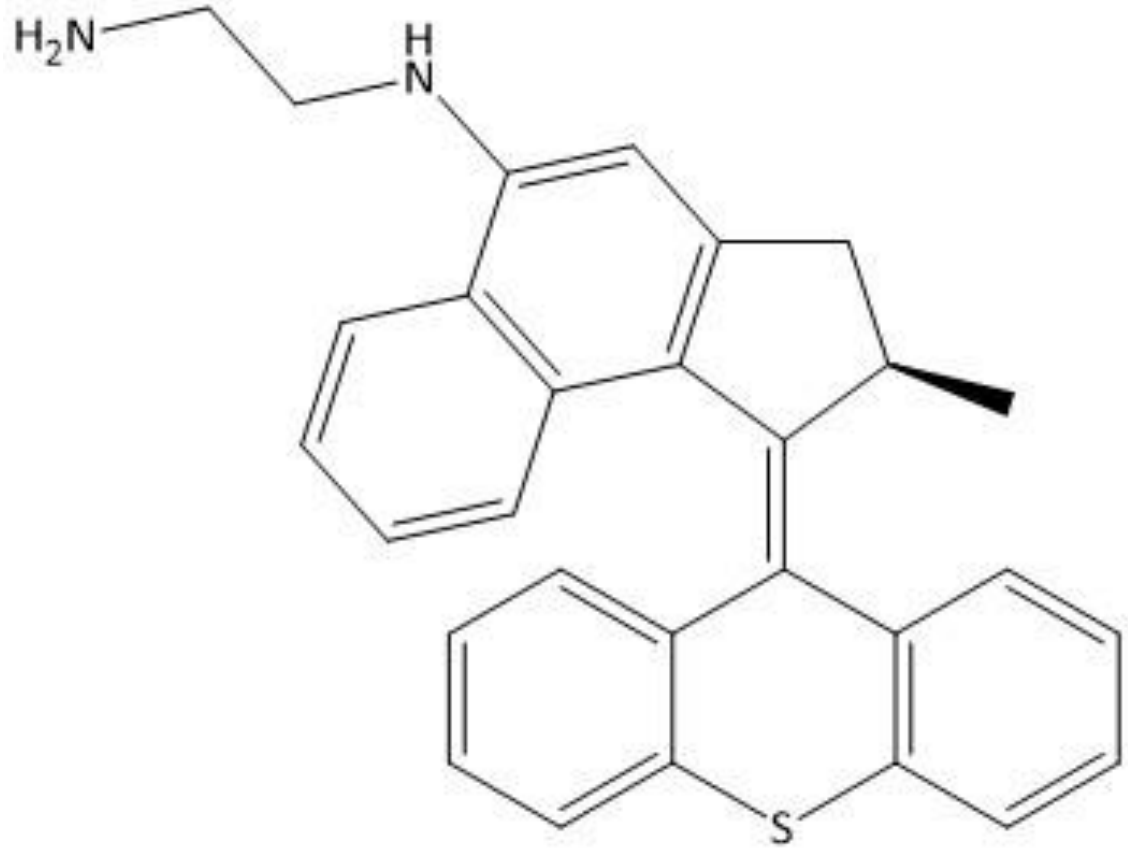

Figure 3.28 Chemical structure of **MNM 5**.

The first rotor modified machine to be studied, **MNM 5**, has the least substituted structure. Consisting of a secondary amine at the N1 nitrogen, and a primary amine at N2. Functionalisation at the C4 rotor position is not predicted to have any influence over the fjord region due to the geometry of the molecule, however rotor speed may still be affected due to the previously evaluated imbalance in molecular weight. The addition of the electron donating secondary amine at the C4 position is predicted to have a greater red shifting effect that the corresponding functionalisation at the stator's C7. The absorbance spectrum is shown in **Figure 3.29**.

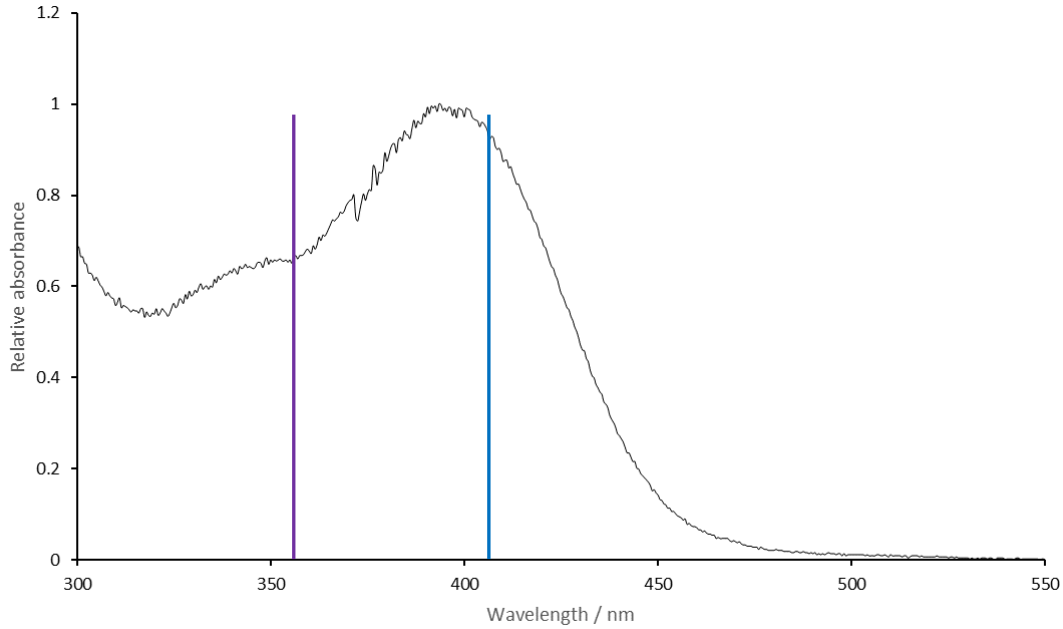

Figure 3.29 UV-Vis absorbance spectrum of **MNM 5** in DMSO with purple and blue lines indicating 355 and 405 nm absorbance respectively.

This absorbance spectrum shows significant bathochromic shift, with maximum absorbance seen at 393.5 nm; significantly higher than the previous stator functionalised MNMs. This is concordant with previous results seen for machines functionalised with other electron donating groups - such as -OMe - at the C4 rotor position, opening the possibility of activating this class of MNM with more biologically safe wavelengths of light.

Weak emission was also detected, and separated from noise, at ~415 nm using an excitation of 340 nm. The observed peak is very broad with clearly shown emission between ~310 and 400 nm, with the corresponding excitation spectrum exhibiting a broad peak with an excitation maximum of ~360 nm. Excitation was able to be observed for **MNM 5** at wavelengths as high as 405 nm, showing significant bathochromic shift. The collected excitation emission spectra are shown in **Figure 3.30**.

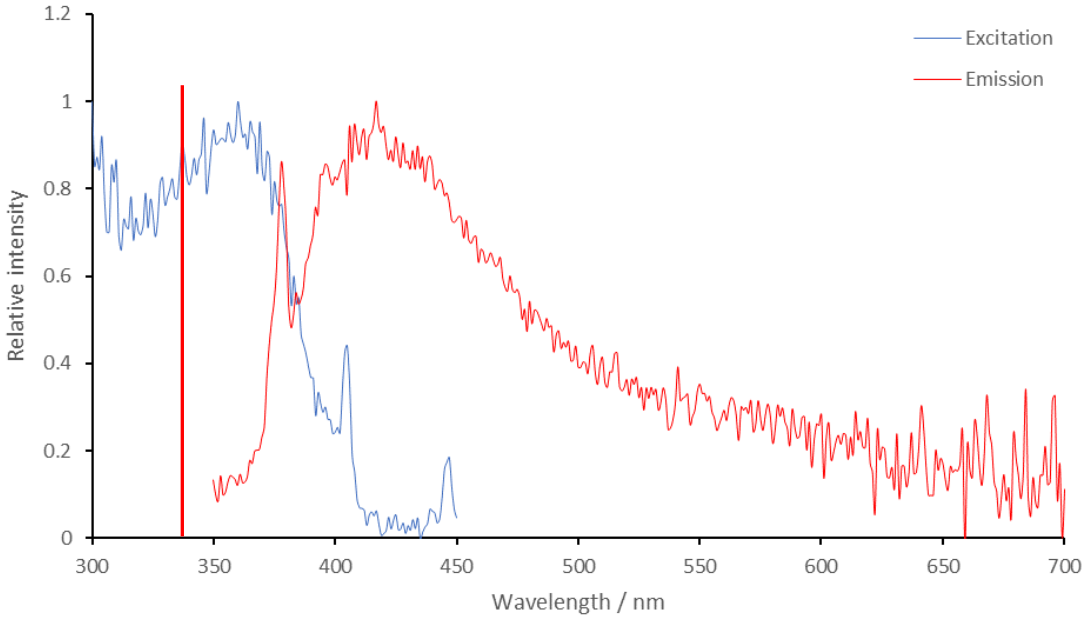

Figure 3.30 Excitation emission spectra for **MNM 5** in DMSO. Red line indicates 340 nm excitation.

While the shift in activation wavelength is rationalised easily with respect to the existing literature covered previously, the increase in emission is less well understood. While plausible that this effect is caused by the change in electronics caused by the availability of the amine lone pair, it is important not to discount the idea that the rotation mechanism is fundamentally altered by the increase in mass of the "rotor" compared to the "stator". This may also play a role in altering the fraction of absorbed energy that is available for radiative processes.

As with the previous studies into stator bound diamine MNMs initial work was carried out comparing the effectiveness of **MNM 5** to induce early onset necrosis in NIH 3T3 cell samples, compared to both a control sample and the well understood unfunctionalised **MNM 1**. These live cell microscopy images are shown in **Figure 3.31**.

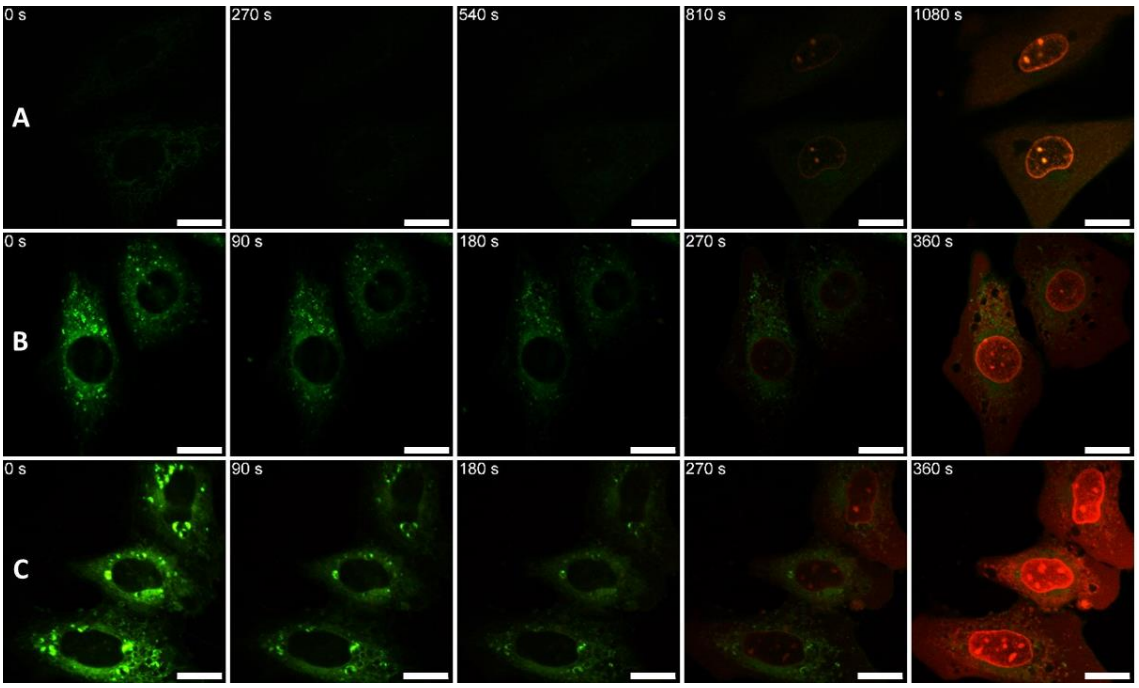

Figure 3.31 Microscopic observation of cell death caused by excitation at 355 nm (UV-exposure times are shown for each image), quantified by the observation of PI fluorescence within the nucleus. **A** – Control sample: NIH 3T3 cells loaded with 100 nM PI and 0.1% DMSO. **B** – NIH 3T3 cells loaded with 100 nM PI and 0.5 µM **MNM 1**. **C** - NIH 3T3 cells loaded with 100 nM PI and 0.5 µM **MNM 5**. All image sets collected after 30 minutes incubation after dosing procedure. Overlaid channels of PI fluorescence (λ_{ex} = 543 nm, 0.2 mW; λ_{em} = 600-700 nm), and mitochondrial autofluorescence (λ_{ex} = 355 nm, 20 mW, 400 nJ per voxel; λ_{em} = 440-460 nm). All scale bars set to 20 µm.

MNM 5 was shown to promote early onset necrosis faster than any of the previously tested stator functionalised machines, with a significant 67% acceleration of necrosis when compared to the control sample. This may be rationalised by the lack of any steric interactions within the machine's fjord region resulting in no possible slowing down of the rotation. The images in **Figure 3.32** show further results for the internalisation experiments.

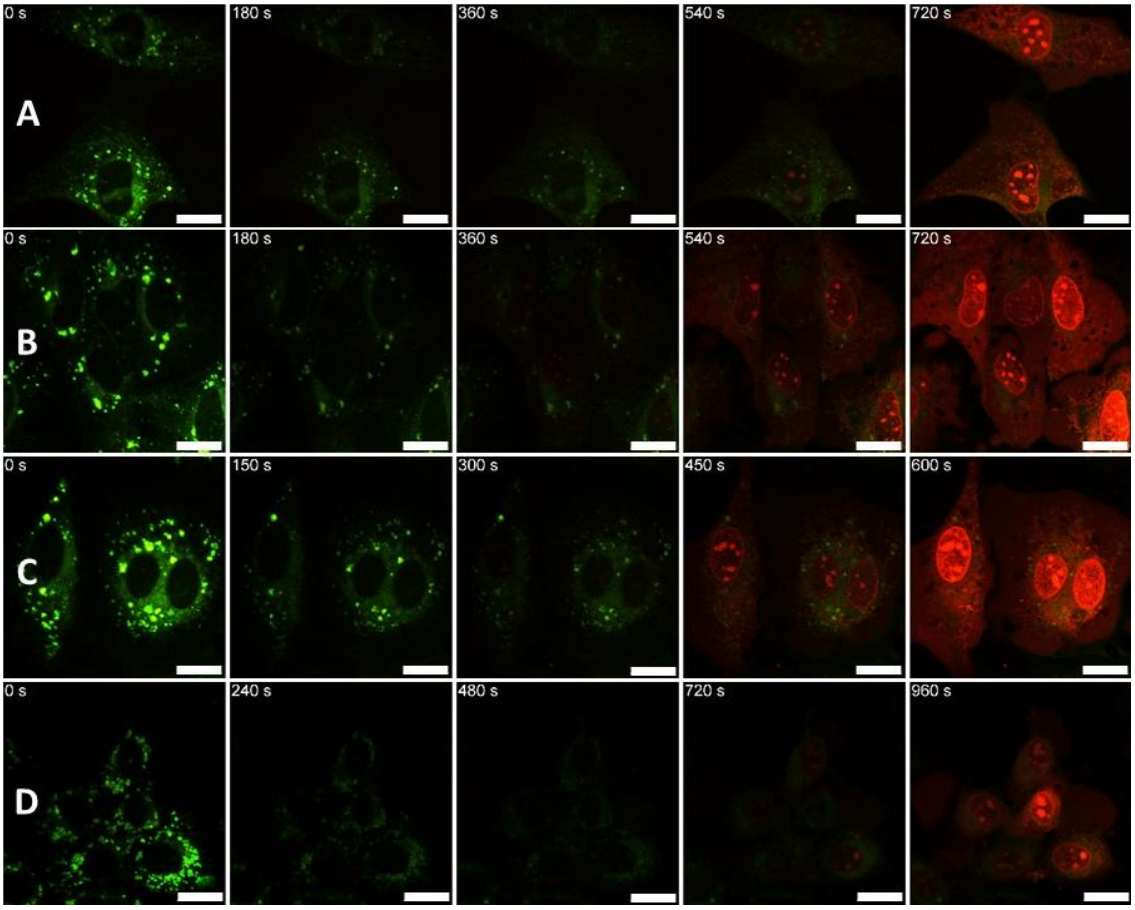

Figure 3.32 Microscopic observation of cell death caused by excitation at 355 nm (UV-exposure times are shown for each image), quantified by the observation of PI fluorescence within the nucleus. **A** – NIH 3T3 loaded with 0.5 µM **MNM 5**, followed by 30 minutes incubation and washing with MNM free media, and subsequent staining with 100 nM PI. **B** – NIH 3T3 loaded with 0.5 µM **MNM 5**, followed by 2-hour incubation and washing with MNM free media, and subsequent staining with 100 nM PI. **C** - NIH 3T3 loaded with 0.5 µM **MNM 5**, followed by 4-hour incubation and washing with MNM free media, and subsequent staining with 100 nM PI. **D** - NIH 3T3 loaded with 0.5 µM **MNM 5**, followed by 2-hour incubation, washing with MNM free media, 16-hour clearance, and subsequent staining with 100 nM PI. All image sets collected after 30 minutes incubation after staining procedure. Overlaid channels of PI fluorescence (λ_{ex} = 543 nm, 0.2 mW; λ_{em} = 600-700 nm), and mitochondrial

autofluorescence (λ_{ex} = 355 nm, 20 mW, 400 nJ per voxel; λ_{em} = 440-460 nm). All scale bars set to 20 μm.

These results first show small amounts of internalisation under short (30 minutes) incubation times with **MNM 5**. Slight PI fluorescence is detected within the nucleus at 540 seconds after initial UV (355 nm) exposure; a 33% acceleration of necrosis compared to the control sample. After 2 hours of incubation with **MNM 5**, detectable necrosis was clearly seen after a shorter period of UV excitation, reaching up to 45% acceleration of TTN after 4 hours of incubation before fresh media washes. While not as effective as experiments with **MNM 5** in solution (**Figure 3.31 D**), **MNM 5** shows promising internalisation properties. Interestingly, these results are shockingly dissimilar to those obtained with **MNM 2**, the C7 stator bound equivalent containing a fully unsaturated diamine. This again implies that functionalising the rotor in this way has a stronger effect on the rotary properties of the machine than the corresponding stator analogue. Rationalised by either more effective rotor activation with 355 nm wavelengths, or the previously discussed imbalance in molecular weight across the overcrowded double bond axle. It should also be noted that clearance studies for **MNM 5** (**Figure 3.32 D**) do not show a complete return to control experiment TTN, with a small (11%) decrease still observed after a 16-hour cell division cycle with MNM free media. Leading to the possible conclusion that **MNM 5** either does not completely clear from NIH 3T3 cells or has a lasting negative impact on cellular health. Reducing any possible future applications despite promising photophysical and internalisation results. Results of these discussed live cell microscopy experiments are again summarised graphically in **Figure 3.33**.

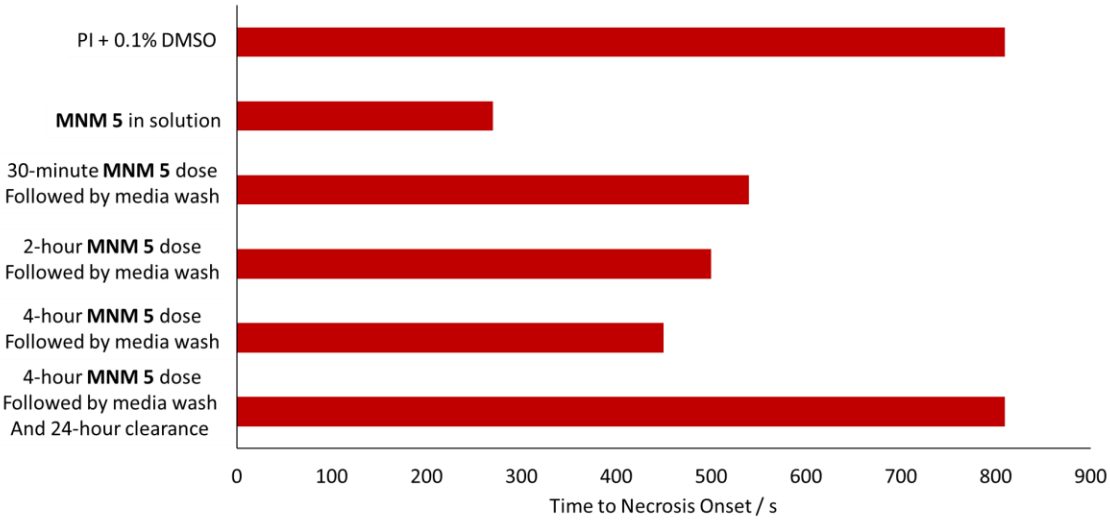

Figure 3.33 Graphical summary of TTN data based upon first observable PI emission detected within the nucleus for **MNM 5** internalisation studies.

3.3.2 MNM 6

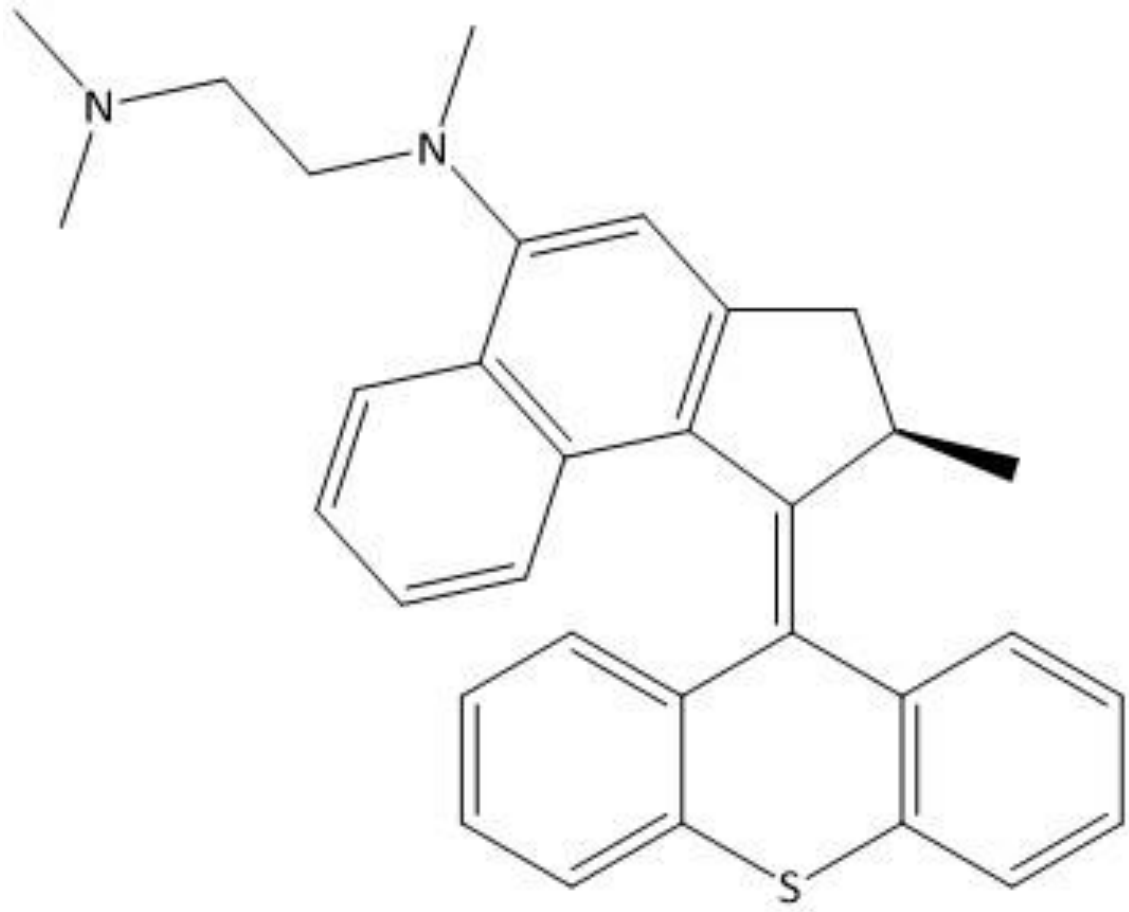

Figure 3.34 Chemical structure of MNM 6.

MNM 6 contains the maximum methyl substitution at both amine sites; tertiary at both N1 and N2. Based on previous results obtained from the studies of the other C4 rotor functionalised molecule, **MNM 5**, it is expected that this machine will also show good absorbance at higher-than-normal wavelengths. The additional alkyl group found at the N1 position will generally increase the availability of the lone pair *via* hyperconjugation, so it may be predicted that this MNM could show a further bathochromic shift than previously studied diamine functionalised machines – similar to the differences seen in the absorbance spectra of **MNMs 2** and **4**. The absorbance spectrum for **MNM 6** is shown in **Figure 3.35**.

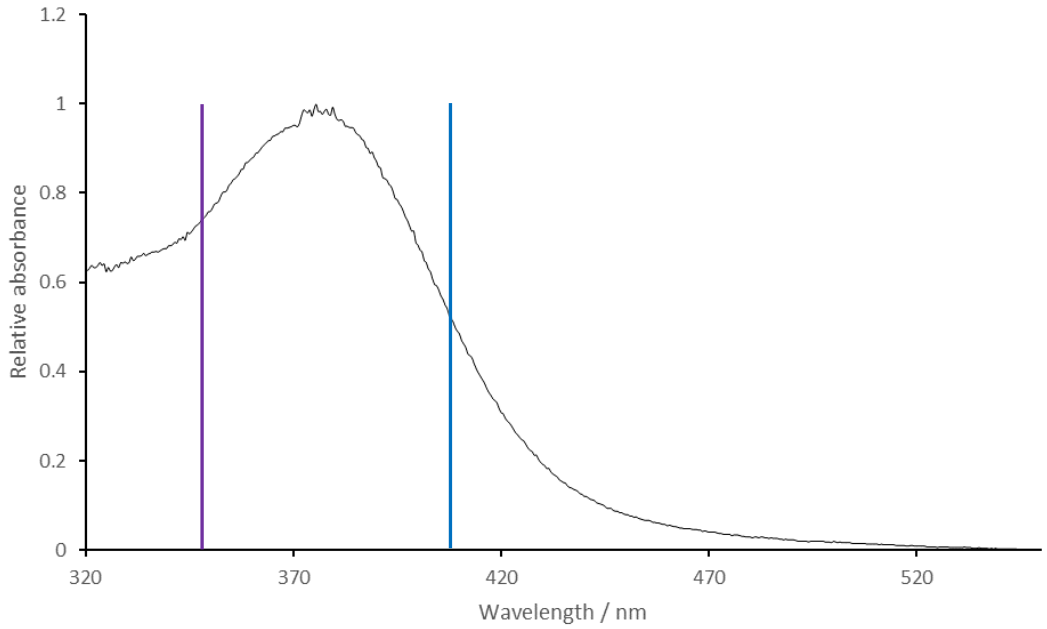

Figure 3.35 UV-Vis absorbance spectrum of **MNM 6** in DMSO with purple and blue lines indicating 355 and 405 nm absorbance respectively.

Surprisingly, the opposite is observed. While **MNM 6**'s absorbance spectrum still shows a significantly higher low energy onset than any C7 stator bound MNM, this is in fact redshifted to a lesser extent than the less substituted analogue **MNM 5**. This could pose more evidence to a new rotary mechanism whereby the stator is rotating about the rotor due to its lower molecular weight. Emission was again able to be detected at 340 nm excitation as shown by the excitation emission spectra in **Figure 3.36**.

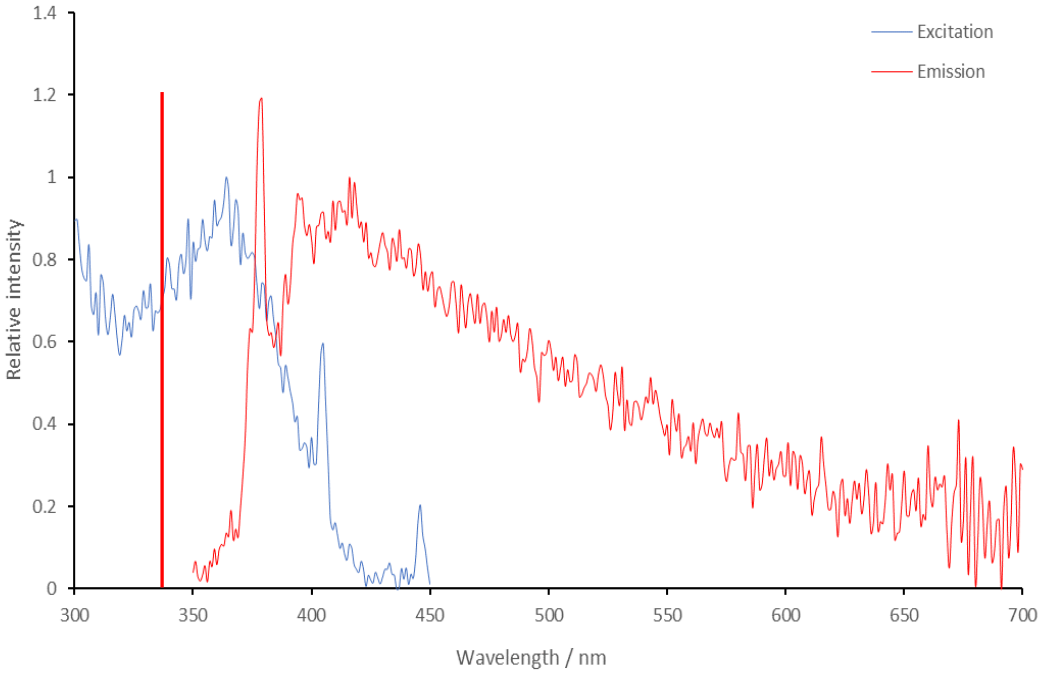

Figure 3.36 Excitation emission spectra for **MNM 6** in DMSO. Red line indicates 340 nm excitation.

Similar photophysical properties to **MNM 5** are seen, with a broad emission peak at around 415 nm when excited by 340 nm light. While this peak was considerably shallower than what was seen for **MNM 5**, detectable emission was still observed at wavelengths as high as 460 nm. The excitation spectrum corresponding to 460 nm emission showed that activation may be possible with 405 nm lasers, again showing promise when looking towards more biologically favourable treatments. It can be interpreted that a bathochromic shift in the excitation wavelength is observed when the Tour MNM cores are functionalised with a diamine addend at the rotor's fourth carbon, but the level of substitution about each nitrogen, N1 and N2, does not pose significant impact on the magnitude of this shift.

Initial live cell microscopy results, with **MNM 6** in solution, are shown in **Figure 3.37** compared as previously with both the control sample and unfunctionalised **MNM 1**.

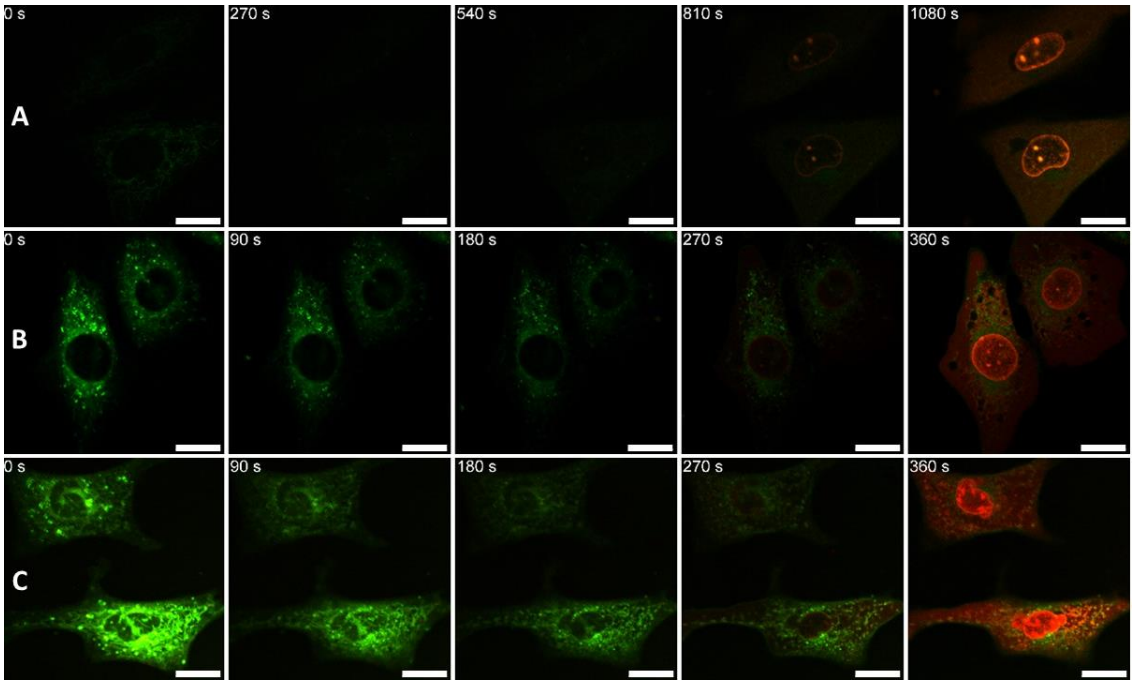

Figure 3.37 Microscopic observation of cell death caused by excitation at 355 nm (UV-exposure times are shown for each image), quantified by the observation of PI fluorescence within the nucleus. **A** – Control sample: NIH 3T3 cells loaded with 100 nM PI and 0.1% DMSO. **B** – NIH 3T3 cells loaded with 100 nM PI and 0.5 µM **MNM 1**. **C** - NIH 3T3 cells loaded with 100 nM PI and 0.5 µM **MNM 6**. All image sets collected after 30 minutes incubation after dosing procedure. Overlaid channels of PI fluorescence (λ_{ex} = 543 nm, 0.2 mW; λ_{em} = 600-700 nm), and mitochondrial autofluorescence (λ_{ex} = 355 nm, 20 mW, 400 nJ per voxel; λ_{em} = 440-460 nm). All scale bars set to 20 µm.

MNM 6 shows almost identical necrosis acceleration to both **MNM 5** and **MNM 1**, showing detectable PI emission from within the nucleus of the studied cells after 240 s of UV excitation. The lack of substantial change in TTN between experiments with **MNMs 5** and **6** despite the increased bulk of the rotor again bolster the prediction that, in the case of this family of MNMs, it is the stator rotating and causing the membrane

disruption responsible for the early onset of cell death. The added lipophilicity of the three additional methyl substituents on the diamine is predicted to have an impact on the internalisation properties of the molecule. These results are illustrated in **Figure 3.38**.

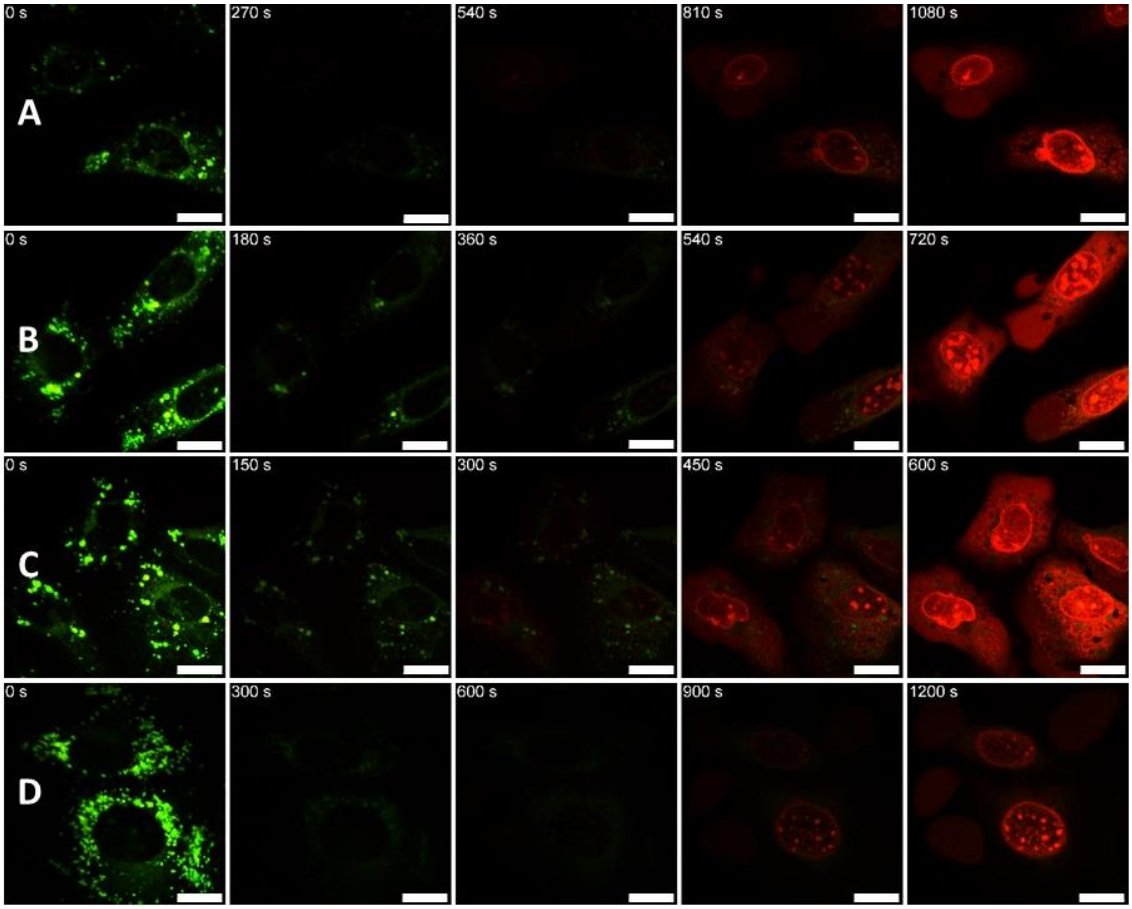

Figure 3.38 Microscopic observation of cell death caused by excitation at 355 nm (UV-exposure times are shown for each image), quantified by the observation of PI fluorescence within the nucleus. **A** – NIH 3T3 loaded with 0.5 µM **MNM 6**, followed by 30 minutes incubation and washing with MNM free media, and subsequent staining with 100 nM PI. **B** – NIH 3T3 loaded with 0.5 µM **MNM 6**, followed by 2-hour incubation and washing with MNM free media, and subsequent staining with 100 nM PI. **C** - NIH 3T3 loaded with 0.5 µM **MNM 6**, followed by 4-hour incubation and washing with MNM free media, and subsequent staining with 100 nM PI. **D** - NIH 3T3 loaded with 0.5 µM **MNM 6**, followed by 2-hour incubation, washing with MNM free media, 16-hour clearance, and subsequent staining with 100 nM PI. All image sets collected after 30 minutes incubation after staining procedure. Overlaid channels of PI fluorescence (λ_{ex} = 543 nm, 0.2 mW; λ_{em} = 600-700 nm), and mitochondrial

autofluorescence (λ_{ex} = 355 nm, 20 mW, 400 nJ per voxel; λ_{em} = 440-460 nm). All scale bars set to 20 μm.

After 30 minutes of incubation with **MNM 6** in solution, followed by washes with fresh MNM free media and the addition of PI, the studied cells showed a negligible reduction in TTN when compared to the control experiment. Implying that for such short incubation times little MNM can passively cross the cell membrane. However, upon further incubation times, 2- and 4-hour, a significantly greater acceleration of necrosis is observed; 540 seconds (33% reduction in TTN compared to 0.1% DMSO only) and 300 seconds (63%) of 355 nm UV excitation respectively. These results suggest that **MNM 6** internalises at a slower rate than the previously tested rotor functionalised analogue, but more effectively. Reaching an overall higher level of internalisation at longer incubation times. This observation can be easily rationalised by the predicted increase in lipophilicity by fully saturating the diamine addend with methyl groups, resulting in a compound that is able to enter the phospholipid bilayer more readily but with an increased steric bulk slowing down passage within the cell. After a complete cell division cycle with MNM free media it appears that **MNM 6** is completely cleared from within the cells studied, leaving behind no noticeable ill effects on overall cellular health. Exhibiting negligible change in the TTN measured when exposed to UV light when compared to the blank sample loaded with only 0.1% control DMSO. Once more these results are summarised for easy comparison in **Figure 3.39**.

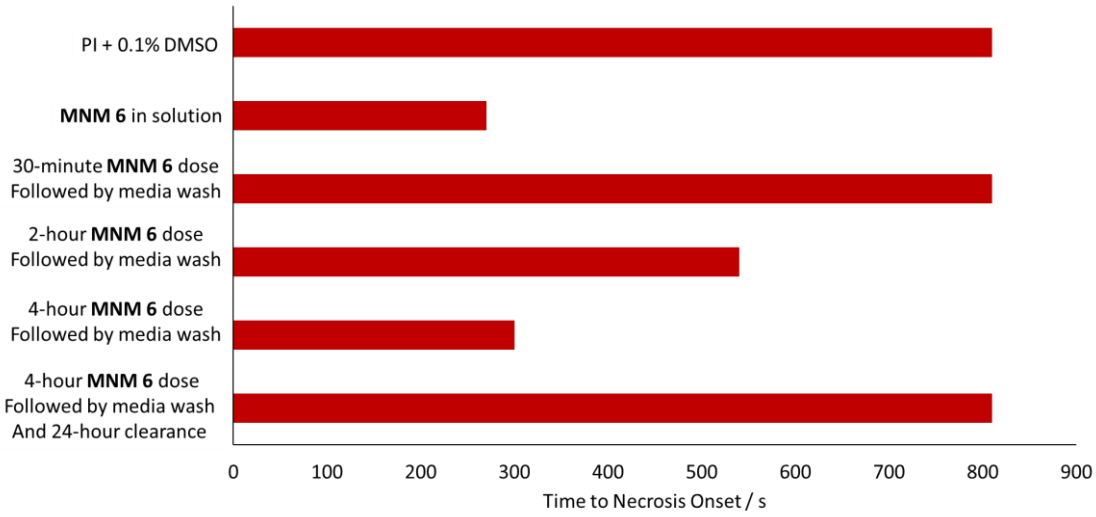

Figure 3.39 Graphical summary of TTN data based upon first observable PI emission detected within the nucleus for **MNM 6** internalisation studies.

3.4 Conclusions

The results presented in this chapter have shown that diamine functionalisation of Tour MNM core molecules enables at least partial crossing of the cell membrane. Allowing these functionalised MNMs to either localise within the cells or at minimum lodge within the phospholipid bilayer itself, allowing an acceleration of early onset necrosis caused by 355 nm UV activation of the rotor to be observed after all MNMs in solution have been removed. Based on a change in cell morphology observed in the mitochondrial autofluorescence (green) channel - λ_{ex} = 355 nm, λ_{em} = 440-460 nm – seen with all variations of diamine functionalised MNMs, it can be assumed that full internalisation is occurring over partial membrane crossing. Whether this effect is induced by physical changes in the mitochondrial network, or fluorescence from non-rotating MNMs held within the lysosomes is not fully understood. However, the observation of this morphological change after MNM clearance experiments where no acceleration of

necrosis, and thus no presence of MNMs, is detected strongly implies direct changes in the formation of the mitochondrial network. Importantly, this is shown to have no meaningful effect on cellular health with these samples undergoing UV-induced necrosis at comparable exposure time to control samples. As well as being further cultivated on the microscope slide for 48 hours without noticeable decrease in cell viability.

Stator functionalised MNMs were found to increase in the internalisation properties upon the addition of addition methyl groups. However, the proximity of these to the fjord region that impact the rotation mechanism of the machines results in less potent acceleration of necrosis, implying a slower rotor rotation. This effect was seen to be more potent when functionalising the N1 position, further implying that the observed impact is due to steric interactions within the fjord region increasing the energy barrier of the rotary process.

When functionalised at the C4 position of the rotor this increased rate of internalisation was also observed, without the apparent drawback of slower MNM rotation speeds. In addition to this, substantial bathochromic shift in the activation wavelength was also observed to as far as 405 nm. As well as an unexpected increase in emission intensity allowing for emission spectra, albeit weak, to be recorded for both rotor functionalised compounds. These unexpected results open the possibly of an altered rotation mechanism dominating this subclass of MNM structure. The disparity of molecular weights across the double bond axle, resulting in a heavier rotor half, is only found within these rotor functionalised MNMs, **MNM 5** and **6**. As they do not possess the traditional functional arms on the stator half, as seen in **MNM 1**. This is proposed to cause the “stator” half of the compound to rotate about the “rotor” half, possibly resulting in an altered mechanism. As the stator half of the molecule is symmetrical with

a sulphur atom at its centre this proposed rotation may show completely different mechanics. Which may explain the difference observed in the utilisation of absorbed energy, resulting in a small increase in emitted light.

MNM 6 presents comparable TTN acceleration when activated in solution to **MNM 1** while also showing a brilliant ability to passively cross the phospholipid bilayer, resulting in good necrosis induction after 4 hours of incubation with the studied sample. Importantly, without showing any adverse effect on the overall health of the sample after being removed. These results, coupled with a sizeable red shift in excitation wavelength, suggest that of all the diamine functionalised MNMs tested **MNM 6** is most promising as a more biologically favourable candidate for further functionalisation in the development of cell specific targeted cancer therapeutics.

3.5 References

1 A. L. Santos, J. L. Beckham, D. Liu, G. Li, A. van Venrooy, A. Oliver, G. P. Tegos and J. M. Tour, *Adv. Sci.*, 2023, **10**, 2205781.

2 C. Ayala Orozco, D. Liu, Y. Li, L. B. Alemany, R. Pal, S. Krishnan and J. M. Tour, *ACS Appl. Mater. Interfaces*, 2020, **12**, 410–417.

3 D. Roke, C. Stuckhardt, W. Danowski, S. J. Wezenberg and B. L. Feringa, *Angew. Chem. Int. Ed.*, 2018, **57**, 10515–10519.

4 L. Pfeifer, M. Scherübl, M. Fellert, W. Danowski, J. Cheng, J. Pol and B. L. Feringa, *Chem. Sci.*, 2019, **10**, 8768–8773.

5 A. Cnossen, L. Hou, M. M. Pollard, P. V. Wesenhagen, W. R. Browne and B. L. Feringa, *J. Am. Chem. Soc.*, 2012, **134**, 17613–17619.

6 S. J. Wezenberg, K.-Y. Chen and B. L. Feringa, *Angew. Chem. Int. Ed.*, 2015, **54**, 11457–11461.

7 D. Roke, B. L. Feringa and S. J. Wezenberg, *Helv. Chim. Acta*, 2019, **102**, e1800221.

8 J. L. Beckham, A. R. van Venrooy, S. Kim, G. Li, B. Li, G. Duret, D. Arnold, X. Zhao, J. T. Li, A. L. Santos, G. Chaudhry, D. Liu, J. T. Robinson and J. M. Tour, *Nat. Nanotechnol.*, 2023, **18**, 1051–1059.

9 V. García-López, F. Chen, L. G. Nilewski, G. Duret, A. Aliyan, A. B. Kolomeisky, J. T. Robinson, G. Wang, R. Pal and J. M. Tour, *Nature*, 2017, **548**, 567–572.

10 J. P. Luzio, P. R. Pryor and N. A. Bright, *Nat. Rev. Mol. Cell Biol.*, 2007, **8**, 622–632.

11 L. Francis, A. Harrell, D. Hallifax and A. Galetin, *J. Pharm. Sci.*, 2020, **109**, 2891–2901.

12 LysoView™ 488 - Biotium, https://www.bioscience.co.uk/product~829073, (accessed 24 November 2023).

Chapter 4: Procedure and system development for the activation of MNMs via two-photon excitation

Summary: *This chapter offers an overview of the process followed when installing and designing novel experimental procedures for a new multiphoton laser built into an existing live cell microscopy system - used for MNM activation and study. It will be split into two distinct sections, for clarity of explanation; first covering the instrumental problems that arose after initial installation and the adaptations made attempting rectify them, and second presenting a summary of the changes in experimental procedure and methodology that were required to obtain comparable results to previously undertaken single- and two- photon proof of concept work. The main difficulties encountered during the optimisation of this new two-photon capable set-up arose in the pursuit of consistency in the results obtained. With large variances initially found in the observed time to necrosis onset for repeat experiments under identical conditions.*

4.1 Introduction

Previous proof on concept work has been carried out - using **MNM 1** as a model candidate - confirming the possibility of activating Tour style MNMs *via* a two-photon process, using two separate systems.[1] First, a Nikon E600 upright microscope equipped with a BioRad MicroRadiance 2000 multiphoton head coupled to a Spectra-Physics MaiTai tunable (710–950 nm, 80 mW @ 720 nm, 80 MHz, 100 fs) multiphoton laser using a ×60 1.4NA water immersion IR objective (operating at 166 lines/s scan speed and 128 × 128 pixel FOV), and second a Leica SP8 multiphoton microscope (DM5000 CS upright chassis) equipped with a quad HyD NDD Leica TCS MP scan head coupled to a Coherent Chameleon tuneable (680–1050 nm, 65 mW @ 710 nm, 80 MHz, 100 fs) multiphoton laser using a ×20 0.95NA IMM CORR objective (operating at 100 Hz scan speed with 2

line accumulation unidirectional 1024 × 1024 pixel FOV). Measurements have also been taken to obtain a 2PE cross-section of σ^2 10.3 GM for **MNM 1** using this 2PA capable Leica microscope, the experimental results of which are shown in **Figure 4.1**.

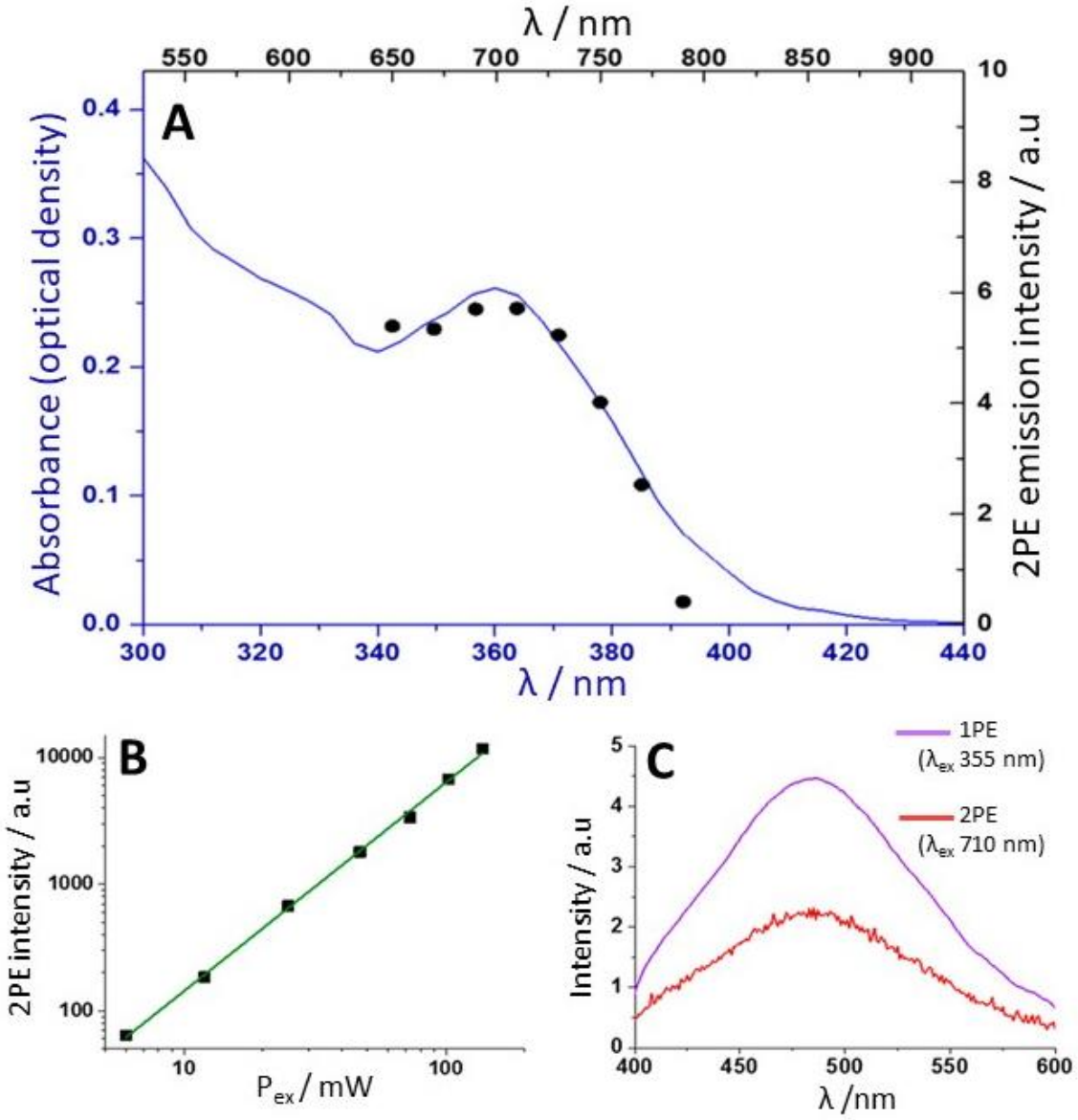

Figure 4.1 Summary of photophysical studies used to measure the 2PE cross-section of **MNM 1**. **A** – One- (blue) and two- (black) photon excitation spectra (λ_{em} 500 nm) for **MNM 1** (Φ_f = 3.7 × 10^{-3}, Σ = 15400 $dm^3\ mol^{-1}\ cm^{-1}$). **B** – Excitation power dependence plot of the measured maximum two-photon induced emission (10^{-50} $cm^4 s\ photon^{-1}$), gradient 1.96 ± 0.1 in DMSO. C – One- (purple, λ_{ex} 355 nm) and two- (red, λ_{ex} 710 nm) photon emission spectra of **MNM 1** (σ^2 = 10.3 GM).

The theoretical basis for measuring a multiphoton cross-section – the quantification for the probability of 2PA at a given wavelength[2] - was outlined by Webb *et al.*, using the ratio between a known reference emitter and the sample.[3] Presented in **Equation 4.1**.

$$\frac{\sigma_2^S \phi^S}{\sigma_2^R \phi^R} = \frac{C_R n_S F^S(\lambda)}{C_S n_R F^R(\lambda)}$$

Equation 4.1

Where $\boldsymbol{\sigma_2}$ is the two-photon cross-section (2PCS), $\boldsymbol{\phi}$ is the photoluminescence quantum yield, ***C*** is the concentration, ***n*** is the refractive index, and ***F*(λ)** is the integrated photoluminescence spectrum of the sample (**S**) and reference (**R**) respectively. Fluorescein/NaOH (Fl), excited at 760 nm, was used as the reference compound. With a literature 2PE cross-section of 36 GM, and a reported fluorescence quantum yield of 0.9.[4] Alongside another widely utilised fluorophore Rhodamine B/methanol (Rh), σ_2 = 210 GM, ϕ = 0.7.[3] Resulting in a literature ratio (R_{lit}), shown in **Equation 4.2.**

$$\frac{\sigma_2^{Rh} \phi_{Rh}}{\sigma_2^{Fl} \phi_{Fl}} = R_{lit}$$

Equation 4.2

Used to validate the experimental procedure used, by comparison to the experimental ratio - **Equation 4.3**.

$$\frac{C_{Fl} n_{Rh} F_{Rh}(\lambda)}{C_{Rh} n_{Fl} F_{Fl}(\lambda)} = R_{exp}$$

Equation 4.3

Resulting in identical ratios within a degree of error, $R_{lit} \approx R_{exp}$, validating the experimental set up as comparable with existing, wildly trusted data. Thereby confirming that the Tour style MNM core structure possesses an appreciable two-photon cross-section and can be activated with 710 nm wavelengths of light.

While attempts have been carried out to directly measure the 2PE cross-section of other various functionalised MNMs, their lack of fluorescence makes this a difficult prospect. However, their ability to cause early onset necrosis when activated by NIR wavelengths – as illustrated by the work covered in Chapter 5 – serves as verification of their capability to effectively absorb highly pulsed light *via* a two-photon process, in a mechanism comparable to their unfunctionalised counterpart. It may be possible to measure two-photon cross-sections for additional MNMs by limiting the speed of the motor - thereby increasing fluorescence intensity – by employing highly viscous solvent systems or low temperatures. However, these conditions would not be comparable to the biologically compatible systems used throughout all the experimentation carried out for this project. Thus, it is deemed appropriate that the observation of accelerated time to induced cell death *via* 2PA is sufficient to conclude good 2PCS for each MNM studied throughout the project, but an investigation into determining a method for measuring 2PCS of weakly fluorescence MNMs may be a promising route for further study.

The initial work carried out using the previously described 2PA capable system (Leica SP8 chassis coupled with Coherent Chameleon multiphoton laser) obtained preliminary live-cell microscopy data illustrating the clear capability of **MNM 1** to induce early onset necrosis in samples of both NIH 3T3 and PC3 cells, shown in **Figure 4.2**.

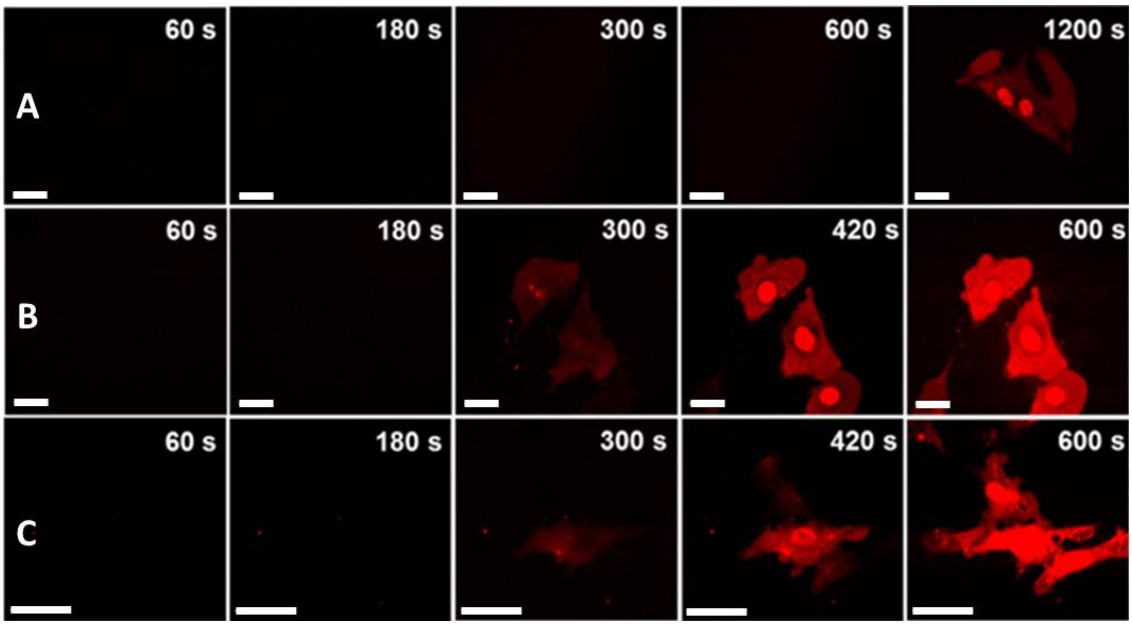

Figure 4.2 Microscopic observation of cell death (PC3 and NIH 3T3) caused by excitation at 710 nm (NIR-exposure times are shown for each image), quantified by the observation of PI fluorescence within the nucleus. **A** – Control sample: NIH 3T3 and PC3 cells loaded with 100 nM PI and 0.1% DMSO. **B** – NIH 3T3 cells loaded with 100 nM PI and 1 µM **MNM 1**. **C** – PC3 cells loaded with 100 nM PI and 1 µM **MNM 1**. All image sets collected after 30 minutes incubation after staining procedure. Red channel shows PI fluorescence (λ_{ex} = 543 nm, 0.2 mW; λ_{em} = 600-700 nm). All scale bars set to 20 µm. Images adapted from Liu *et al*.[1]

Showing a remarkable 75% reduction in TTN for **MNM 1** dosed samples activated with 710 nm NIR wavelengths. Initial aims for this chapter of work required installing a new laser system capable of obtaining comparable results to these proof-of-concept studies and ensuring that these results were consistent across multiple experimental sessions when using the same procedures. To this end, a tuneable (680 – 1080 nm) Coherent Chameleon Vision II femtosecond Ti:sapphire multiphoton laser[5] was installed onto the existing Leica TCS SP5 imaging system[6] used to collect the results for all work covered

throughout this thesis. For a full equipment summary and breakdown see methods in Chapter 6.

This chapter provides both a presentation of preliminary multiphoton results - which are comparable with the previously depicted proof-of-concept work - and a summary of the extensive experimentation that was required to produce a consistent methodology for their acquisition. The myriad of hurdles encountered when troubleshooting this new laser system is best explained if divided into two general categories. Firstly, problems arising due to the instrument itself, such as inconsistent power or changes in focal distance. Most often rectified by additional understanding of the nature of the system – such as the warmup time required for MNM specific use cases - or by troubleshooting / changing individual components, such as the installation of additional filters. Secondly, issues caused by the methodology and experimental procedure followed and the nature of working with biological systems. These include problems such as selecting a consistent focal plane, the balance between scan speed and laser power, and inconsistent condition of cellular samples leading to unacceptable variance in TTN measurements. Resolved by enacting changes to various experimental procedures.

4.2 Instrumentation development and troubleshooting

A number of issues arise when utilising the Chameleon Vision II femtosecond Ti:sapphire multiphoton laser for the purpose of prolonged activation and *in vivo* study of MNMs. The vast majority of published examples of multiphoton laser scanning confocal microscopy (MPLSCM) are used for purely imaging applications, where the laser is utilised to induce emission in studied fluorophores over relatively short (seconds timescale) excitation windows.[7–10] In contrast, experiments in this work use the multiphoton laser to continuously activate the rotary mechanism of the MNMs to induce

cell death, with observation times of up to 20 minutes. Meaning, any small changes in photon flux - be it from laser power or pulse train fluctuations – are inevitably amplified, leading to inconsistent results. Alongside this, the window of laser intensity between two extremes - causing almost immediate thermal damage to the biological samples and having little to no activation effect of the MNMs - is surprisingly small. This again means any minute experiment-to-experiment fluctuations have a dramatic effect on the TTN observed, and in general greater fine control over the photon flux at the focal plane is required when compared to the more standard applications. Due to MNM study being such a niche example of multiphoton laser use adapting the system poses a major challenge; after installation, providing no direct problems with the instrumentation, the Coherent engineers can also offer little troubleshooting advice.

After initial installation, preliminary experiments were carried out using the previously standardized control samples; NIH 3T3 cells loaded with 0.1% v/v DMSO and 100 nM PI to be used for necrosis detection. To obtain baseline measurements for the capacity of the biological sample to withstand 710 nm wavelengths of light with such high photon flux, as well as to ensure that these results remained consistent throughout repeated experimentation. It was predicted that the cells would be able to survive constant exposure to this new NIR laser line for longer excitation periods than the previously studied 355 nm UV due to the widely reported drop in phototoxicity for these lower energy wavelengths. However, after some time necrosis would still be observed due to localised heating caused by the roughly tenfold increase in absorption by water between 355 and 710 nm light, illustrated in **Figure 4.3**.

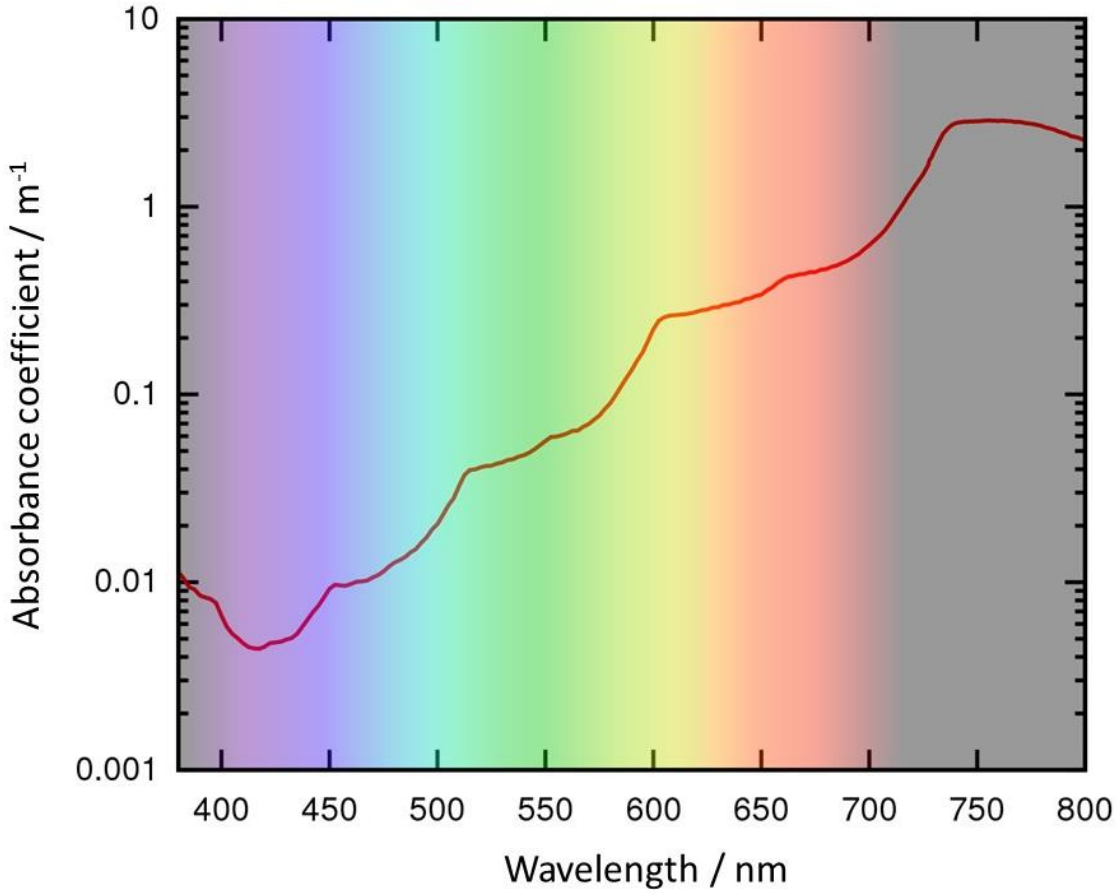

Figure 4.3 Absorption spectrum of pure water in the visible region. Adapted from both Fry, and Querry *et al*.[11,12]

The first control experiment carried out with this new laser set up initially appeared to give promising results, with no appreciable necrosis (indicated by PI fluorescence) observed for the cells under study within 10 minutes of constant exposure to 710 nm light. Presenting results in line with predictions that the highly pulsed 710 nm laser line is less phototoxic than the 355 nm UV. However, when repeating this trial under identical experimental conditions immediate necrosis coupled with large bubble formation on the surface of the cell was observed. In addition, burning around the edges of the imaging window was also found after only 30 seconds of 710 nm exposure. **Figure 4.4** shows the PI emission channel obtained for these experiments, overlaid with the standard brightfield image to easily show the aforementioned bubble formation.

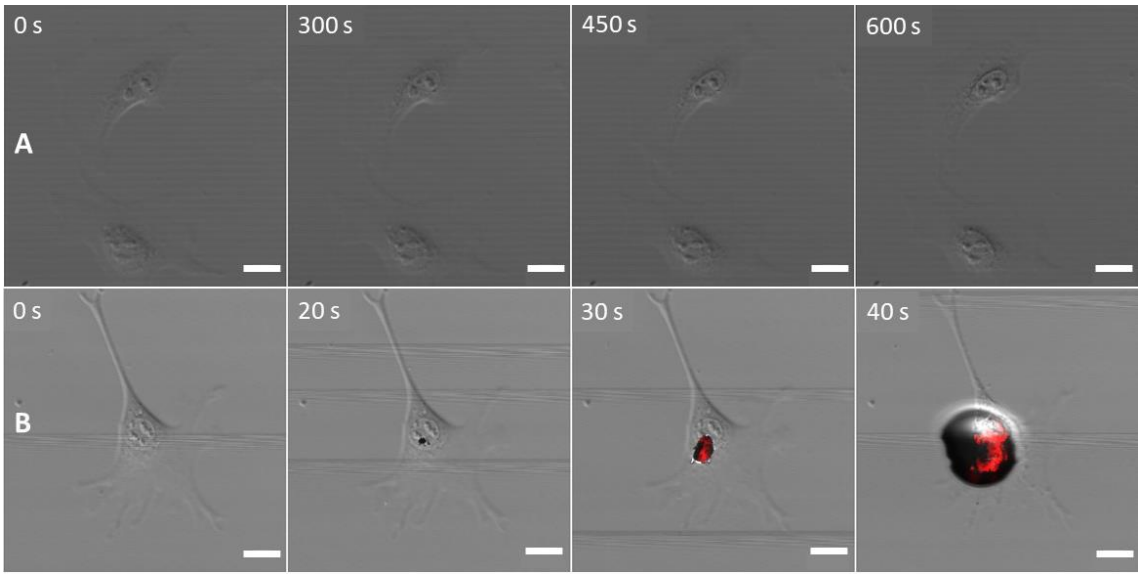

Figure 4.4 Microscopic observation of cell death caused by excitation at 710 nm (NIR-exposure times are shown for each image), quantified by the observation of PI fluorescence within the nucleus. **A** – NIH 3T3 cells loaded with 100 nM PI and 0.1% DMSO, experiment 1. **B** – NIH 3T3 cells loaded with 100 nM PI and 0.1% DMSO, experiment 2. All image sets collected after 30 minutes incubation after dosing procedure. Overlaid channels of PI fluorescence (λ_{ex} = 543 nm, 0.2 mW; λ_{em} = 600-700 nm), and brightfield (transmission) image. All scale bars set to 20 µm.

This inconsistency in the results obtained under identical conditions continued both for samples studied within the same experimental window, as well as for experiments carried out following laser shut down and start up procedures. Initial steps to solve this were taken first by utilising the lasers internal ocean optics HR4000 spectrometer to measure the power generated when set to 710 nm emission after initial warm up procedures – i.e., when the system itself indicated the laser was fully stabilised. The graph shown in **Figure 4.5** illustrates these measurements taken every minute for the two hours immediately after laser initialisation.

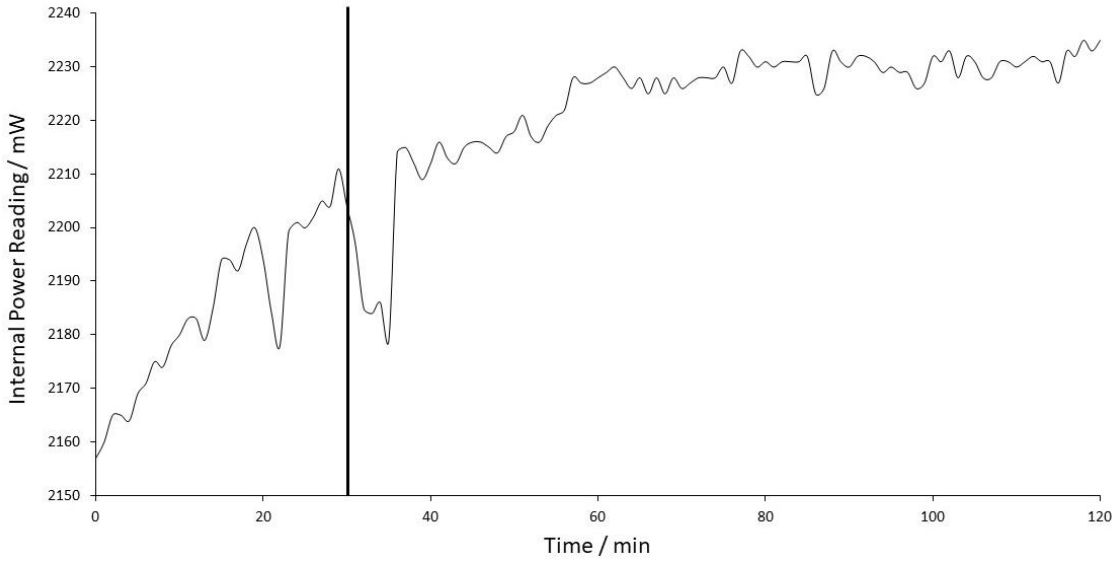

Figure 4.5 Graph logging internal power readings, measured *via* internal ocean optics HR4000 spectrometer, for the multiphoton laser taken every minute immediately after initialisation. Line added at 30 minutes, where the system reads as fully stabilised.

The line added onto **Figure 4.5** at 30 minutes show the time from which the system reads as fully initialised and ready to use. It is clearly shown that for a minimum of 30 additional minutes, fluctuations of up to 2.5% laser power are occurring. While not a massive variance, over a period of 10 minutes constant excitation this may cause some irregularities in the results obtained. However, this would not fully explain the dramatic differences seen in experiment-to-experiment variance. Indeed, after consistently waiting two hours after laser initialisation before starting experimental work significant changes in results were still observed for identical experimental conditions.

Next, laser power measurements were taken at the focal plane using a Thorlabs microscope slide high power meter sensor head coupled to a PM400 power metre console.[13] While these appeared to remain constant over multiple experimental

windows, after waiting a minimum of two hours after laser initialisation, an interesting observation was made. The graph presented in **Figure 4.6** shows measurements taken at the focal plane at 710 nm, selecting powers in 10% increments from 0 to 50% total laser power.

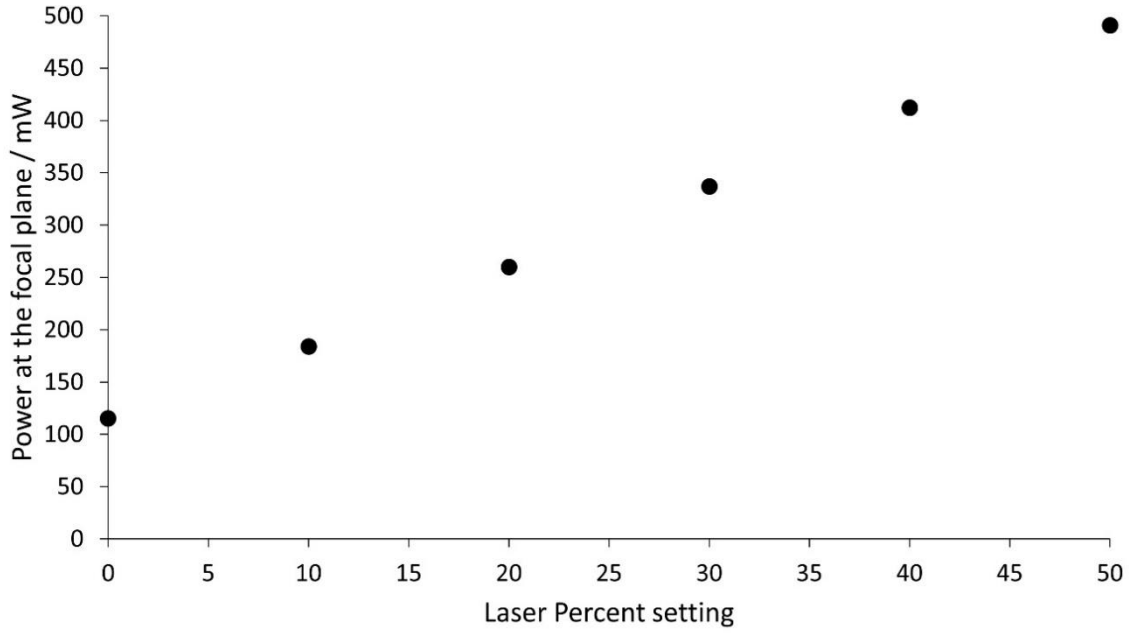

Figure 4.6 Recorded power measurements taken at the focal plane for the multiphoton laser set 710 nm, in 10% increments.

With the system set to zero, 115 mV of laser power is still detected at the focal plane using this instrumentation. This power is much higher than any previous experiments and can cause direct damage to the sample, and crucially to the coating on the slide itself which leaves very little room for focus adjustment without ruining the experiment. Due to the longer than standard exposure times used in MNM experiments when compared with more standard imaging techniques, coupled with the random variance in biological samples, this power is far too high to acquire consistent results due to the

constrained ability to adjust power below ~100 mW, as well the dramatic differences caused by any minor changes in the stages z position.

To account for this, and ensure adequate room for further adjustment of power between experiments, a neutral-density (ND) filter with an optical density of 0.3 was installed along the beam path to reduce the intensity of the laser line across all wavelengths equally.[14] For an optical density, d, the fractional transmittance of light across the ND filter is given by **Equation 4.4**.

$$Fractional\ transmittance = \frac{I}{I_0} = 10^{-d}$$

Equation 4.4

Figure 4.7 shows measurements at the focal plane taken after installation of ND filter ND503B taken at the beginning of multiple experimental sessions.

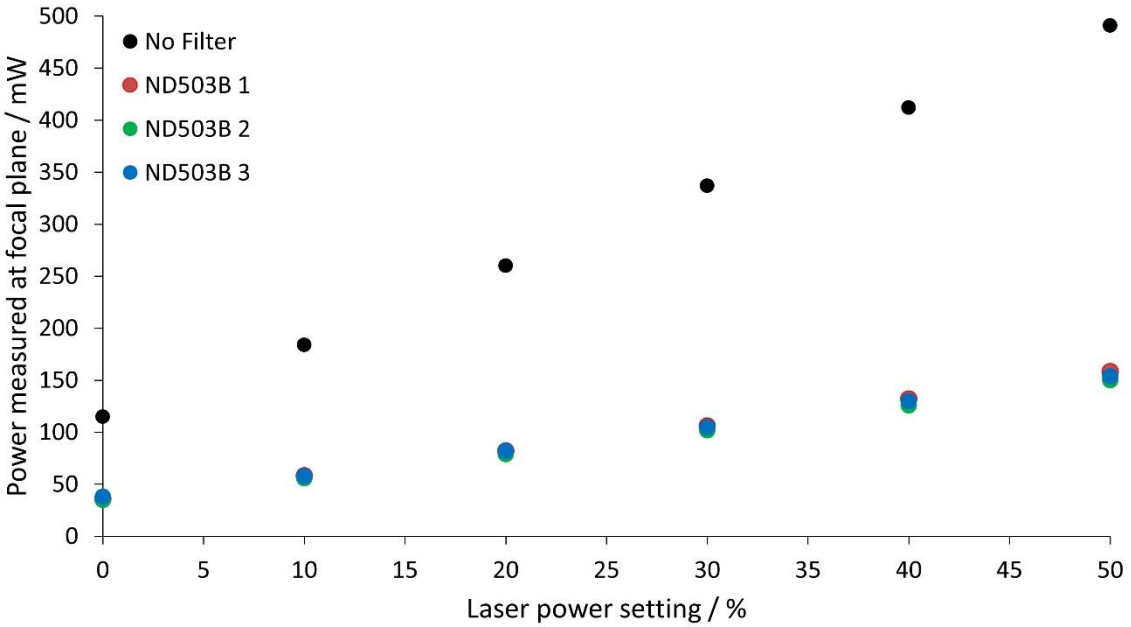

Figure 4.7 Recorded power measurements taken at the focal plane for the multiphoton laser set at 710 nm, in 10% increments, after installation of ND503B.

After installation of ND503B, 35 mW of power was still measured at the focal plane. While not ideal, this allows for studies to be carried out on biological samples without immediate damage being observed. Importantly, several sets of measurements were taken over multiple days to ensure the high power and pulse train of the chameleon vision ii laser did not cause any degradation in filter quality, and its ability to reduce the intensity of light passing through the system. It is clearly seen by the reported data that little to no observable change is found in the power of light measured, allowing for the conclusion that this style of filter can effectively limit the power of a multiphoton system without substantial alteration occurring to the filter. For at least a small period of time, however further regular monitoring during the day-to-day running of the system would be required to ensure no detrimental effects of highly pulsed light on the filter. **Figure 4.8** shows live cell microscopy images collected for both the control sample, and a sample dosed with **MNM 1**, using the MP system with ND503B added.

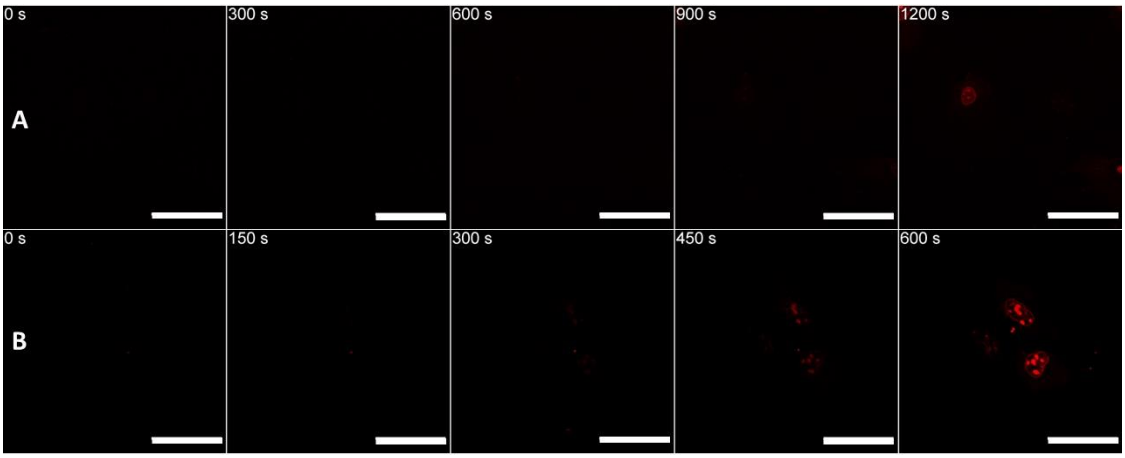

Figure 4.8 Microscopic observation of cell death caused by excitation at 710 nm (NIR-exposure times are shown for each image), quantified by the observation of PI fluorescence within the nucleus. Using Coherent Chameleon Vision II laser system fitted with **ND503B** filter. **A** – Control sample: NIH 3T3 cells loaded with 100 nM PI and 0.1% DMSO. **B** – NIH 3T3 cells loaded with 100 nM PI and 0.1% DMSO, and 1µM **MNM 1**. All image sets collected after 30 minutes incubation after dosing procedure. Red channel showing detection of PI fluorescence (λ_{ex} = 543 nm, 0.2 mW; λ_{em} = 600-700 nm). All scale bars set to 50 µm.

These results, while able to maintain a level of consistency not previously obtainable, were collected with the laser set to 0% within the control software. If raised even to 1%, similar problems were encountered as those previously discussed; a lack of consistency in measured TTN, slide burning, and results that were incredibly sensitive to changes in focus. Importantly, due to the relatively long run times of the MNM studies (20 minutes and above), any sensitivity to changes in focus pose a significant problem as cell morphology may change within the experimental time frame – changing the focal point and altering any results collected. More troubleshooting around the problems arising from changes in focus are discussed in section 4.3 where changes in methodology and

experimental set up are covered in detail. In an effort to increase the range of laser powers available during methodology testing an ND filter with an increased optical density (0.9) was installed, ND509B, further reducing the power at the focal plane.[15] This was again measured over multiple days of experimentation to ensure no degradation in filter quality and compared to previous measurements, shown in **Figure 4.9**.

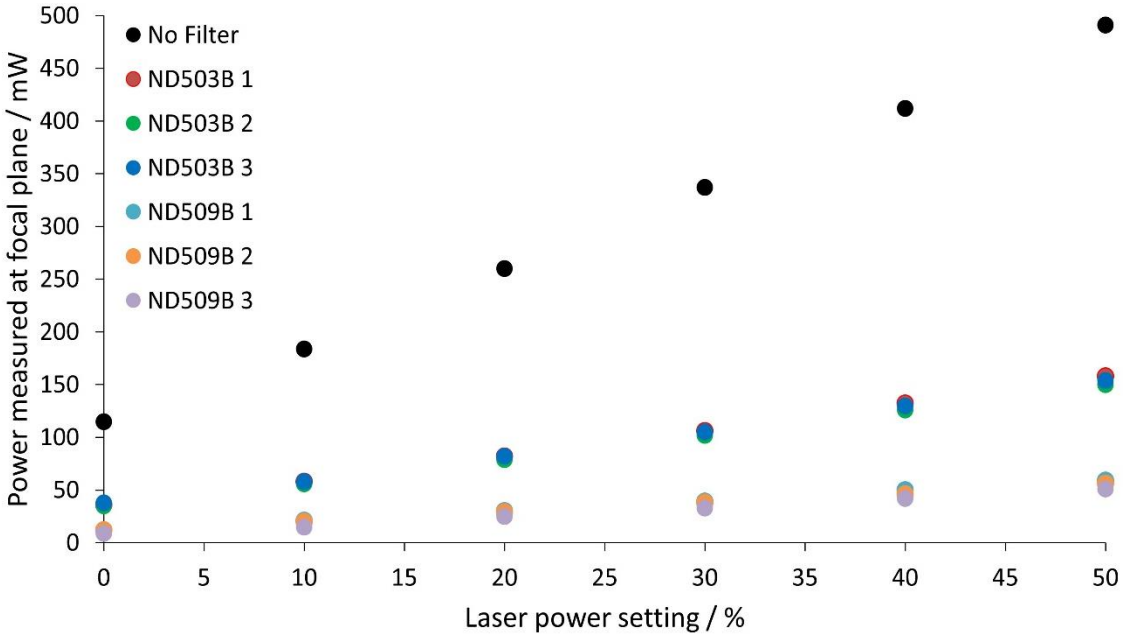

Figure 4.9 Recorded power measurements taken at the focal plane for the multiphoton laser set at 710 nm, in 10% increments, after installation of ND509B.

Upon increasing the optical density of the fitted ND filter the minimum power detected at the focal plane (with the system set to 0%) falls to 10 mV. This allows for more freedom when selecting appropriate powers within the graphical user interface (GUI), particularly important when small experiment-to-experiment fluctuations can pose such dramatic impacts on the collected result. It is now possibly to periodically rerun the control – MNM free – sample and compare this to previous results, making small alterations to the laser power as required to keep the observed TTN within a comparable

window. **Figure 4.10** presents both a control, and **MNM 1** dosed, sample. Showing good repeatable results, with comparable percentage changes in TTN, with previous work using ND503B.

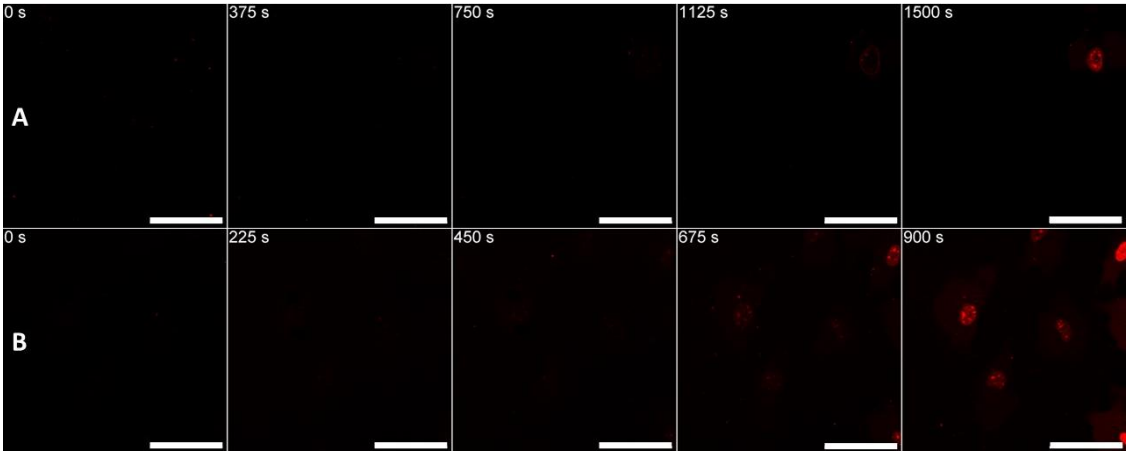

Figure 4.10 Microscopic observation of cell death caused by excitation at 710 nm (NIR-exposure times are shown for each image), quantified by the observation of PI fluorescence within the nucleus. Using Coherent Chameleon Vision II laser system fitted with **ND509B** filter. **A** – Control sample: NIH 3T3 cells loaded with 100 nM PI and 0.1% DMSO. **B** – NIH 3T3 cells loaded with 100 nM PI and 0.1% DMSO, and 1µM **MNM 1**. All image sets collected after 30 minutes incubation after dosing procedure. Red channel showing detection of PI fluorescence (λ_{ex} = 543 nm, 0.2 mW; λ_{em} = 600-700 nm). All scale bars set to 50 µm.

Using this set up a ~55% increase in TTN is observed upon the addition of **MNM 1**, comparable to work carried out with 355 nm UV excitation and with 710 nm ND503B 2PA. Critically, there is now enough manoeuvrability in laser power to allow for increased consistency in the results obtained. However, the operating window still sits between 0 and 5% and with only 1% increment available this leaves only 5 distinct power levels to select from. In addition, these ND filters are not tested for prolonged use with

laser of these powers and high pulse trains. To combat this, and further increase the tunability of the system, a Pockels cell based electro-optic modulator (EOM, PicoQuant) was installed in place of the ND filters for amplitude modulation. In short, the device consists of an electro-optic crystal through which a beam of light can propagate. The phase delay in the crystal, or the Pockels effect, is modulated in proportion to the applied electrical voltage. Resulting in what is effectively a voltage controlled waveplate. A simple intensity modulator is made when the input laser beam has its linear polarisation at a 45° angle to the optical axis of the crystal: assuming no birefringence with no electric field, and a given half-wave voltage of $\mathbf{U_\pi}$ – that is, that voltage required to induce of phase change of π, equivalent to half an optical wavelength. A polariser is placed behind the crystal, aligned to obtain either 100 or 0% transmission with no voltage applied. In the case of 100% transmission, the transmitted field is considered to be a superposition of two in-phase field components of equal strength. When an electric field is applied, these components acquire a phase difference (**Δϕ**) shown in **Equation 4.5**, the total transmitted amplitude (**T(A)**) is then proportional to **Equation 4.6**. Leading to the result for power transmission (**T(U)**), as given in **Equation 4.7**.

$$\Delta\phi = \frac{\pi U}{U_\pi}$$

Equation 4.5

$$T(A) \propto 0.5(1 + e^{i\Delta\phi})$$

Equation 4.6

$$T(U) = \left|\frac{1}{2}(1 + e^{i\Delta\phi})\right|^2 = cos^2(\frac{\pi U}{2U_\pi})$$

Equation 4.7

Demonstrating that the voltage across the crystal only needs to be modified by a single half-wave voltage to switch the total transmission from 100 to 0%. This technology has several benefits when applied to this laser system. Firstly, the added degree of control over the laser – as shown in **Figure 4.11** – allows for: 1) a much lower minimum available power solving any previous issues with burning of both the microscope slide and the sample itself, and 2) significantly finer intervals in the available laser power selection, resulting in a substantial increase in the degree of control over the experiment. Secondly, when compared to the added ND filters, the application of an EOM based amplitude modulator for the power modulation of a highly pulsed (fs) multiphoton laser is widely studied and shown to have no observable impact on the pulse train, allowing for maximum excitation within the focal spot.[16] As well as posing no possible future issues with filter degradation.

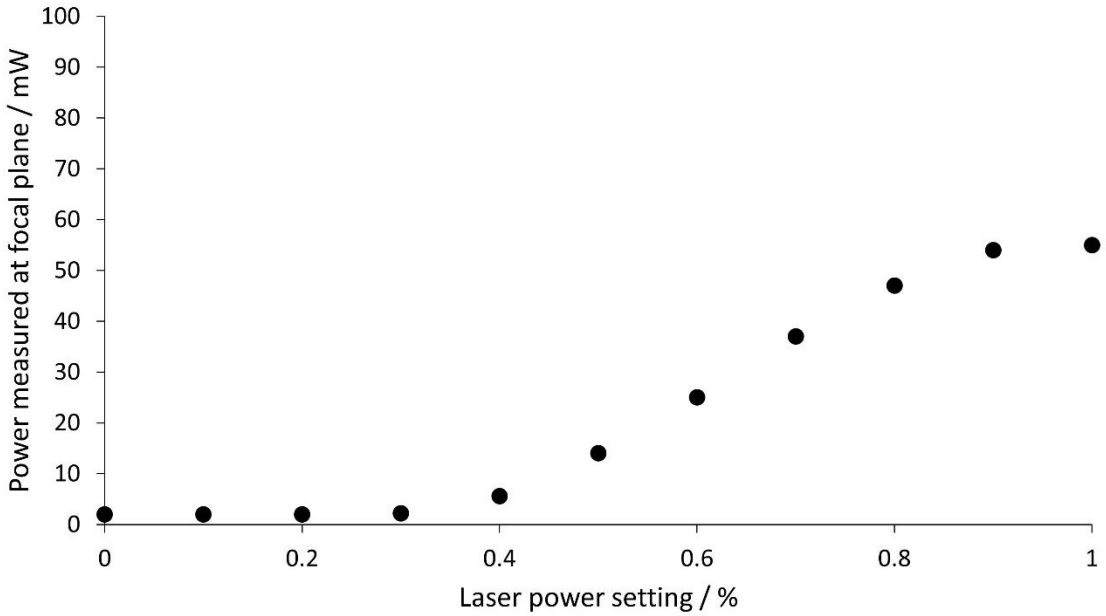

Figure 4.11 Recorded power measurements taken at the focal plane for the multiphoton laser set at 710 nm, in 0.1% increments, after installation of EOM power control.

The live cell microscopy images, for both a control sample containing no added MNM and a sample dosed with 1 µM **MNM 1** – shown in **Figure 4.12** – illustrate the highly repeatable results obtainable with this new method for power modulation, remaining comparable with both the previously well-established single photon work as well as the proof-of-concept experiments acquired using different hardware. These were all acquired with a 0.55% intensity setting (~25 mW), powers which were previously unobtainable without the installation of the EOM controller. These highly stable, and repeatable, lower power settings with micro adjustments result in an experimental procedure and workflow which is much easier to work with and allows for the acquisition of results with both a cleaner image and more consistent TTN.

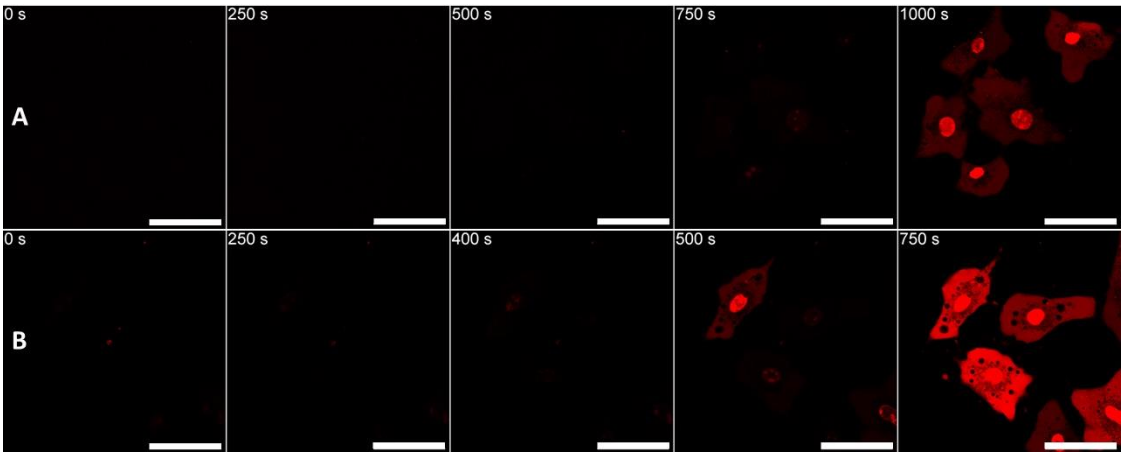

Figure 4.12 Microscopic observation of cell death caused by excitation at 710 nm (NIR-exposure times are shown for each image), quantified by the observation of PI fluorescence within the nucleus. Using Coherent Chameleon Vision II laser system fitted with an **EOM-based amplitude modulator**. **A** – Control sample: NIH 3T3 cells loaded with 100 nM PI and 0.1% DMSO. **B** – NIH 3T3 cells loaded with 100 nM PI and and 1 µM **MNM 1**. All image sets collected after 30 minutes incubation after dosing procedure. Red channel showing detection of PI fluorescence (λ_{ex} = 543 nm, 0.2 mW; λ_{em} = 600-700 nm). All scale bars set to 50 µm.

An important change to note in these results, compared to those acquired previously in this chapter, is that due to the lower powers used the experiment can continue to be run for longer periods after initial observation of PI fluorescence without risk of burning the sample and leading to unreliable results. This means a brighter end point image is found, where complete PI emission is seen throughout the entire cell in study, making the results between experiments using different MNMs easier to compare.

4.3 Methodology and sequence iteration

It is important to note that the experimental alterations presented within this section were carried out in tandem with the previously discussed instrumentational work and

are collated separately for ease of interpretation. Thus, the collected results may show initial variance in quality compared with those shown towards the end of section 4.2, however both strategies – instrument and methodology based – are vital for creating the working system and experimental procedure used throughout the rest of this work.

The majority of hurdles surrounding the development of the procedure for the multiphoton activation, and subsequent image acquisition, of MNM dosed cellular samples arise due to issues with the focus of the excitation source. Initially, problems were found due to chromatic aberration; a common problem when multiple excitation wavelengths are used in a scanning microscope system. Chromatic aberration results in a spatial shift between the foci of lasers of differing wavelengths passing through the objective.[17] Specifically in LSCM, chromatic aberration can be defined into two distinct forms: axial and lateral. Given two laser excitation sources of differing wavelengths, λ_1 and λ_2, each beam will be shifted in both the x,y (lateral) and z (axial) planes during the scanning of the image – as illustrated in **Figure 4.13**. While most modern optics attempt to correct for this phenomenon, this remains an ongoing consideration in the field. Exacerbated by the rise of two- and even three- photon microscopy extending the possible range of excitation wavelengths.

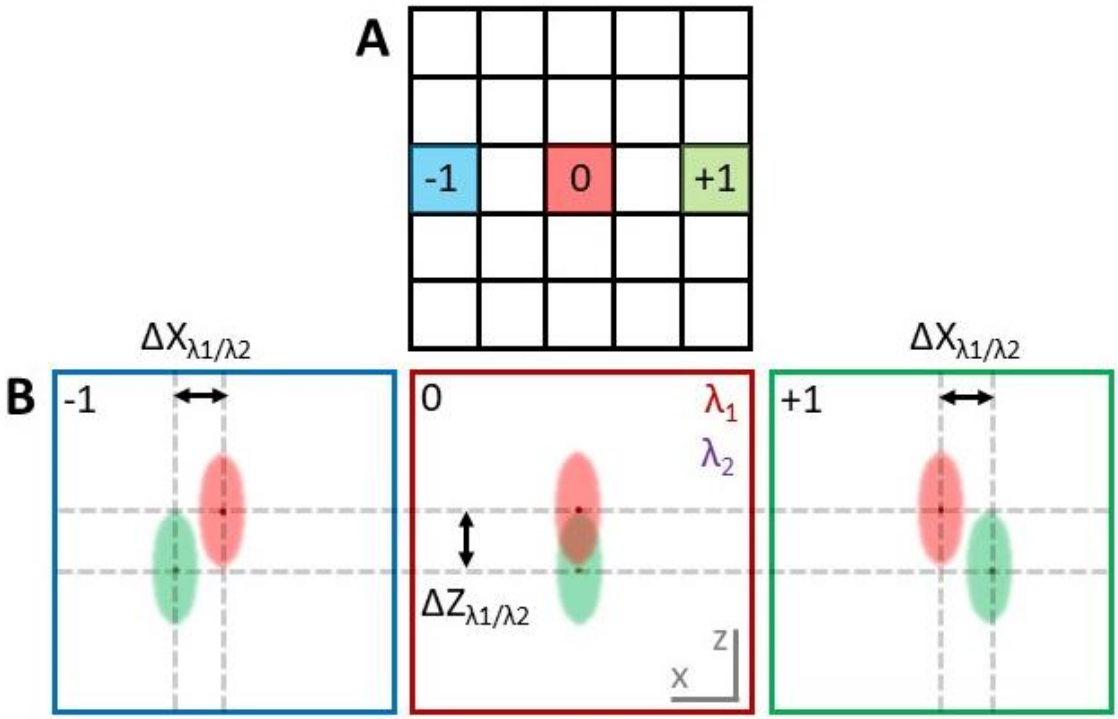

Figure 4.13 Schematic representation of chromatic aberration for a dual beam LSCM set up. **A** – Raster scanned image field of view. **B** – Axial chromatic aberration through the optics causes the two laser lines at the centre of the field of view (0) to be shifted in the Z plane by $\Delta Z_{\lambda1/\lambda2}$, while the edges of the field of view (-1, +1) are also shifted in the X dimension by $\Delta X_{\lambda1/\lambda2}$. Adapted from Blanc *et al*.[17]

In this case, lateral chromatic aberration poses no issue to the experiment. Firstly, due to the fact that the 710 nm multiphoton laser line is not being used to promote emission from a fluorophore, thereby resulting in no out of focus light being produced. Secondly, the scale of the imaging window is relatively small, with the cells in study being held predominantly in the centre of the field of view, meaning the amount of lateral chromatic aberration is kept at negligible levels. Axial chromatic aberration, however, is a significant issue with a substantial difference seen between the z axis focal planes of both the 543 nm single photon and the 710 nm two photon laser lines despite

manufacturer correction for chromatic aberration on the optics used. This is shown graphically in **Figure 4.14**.

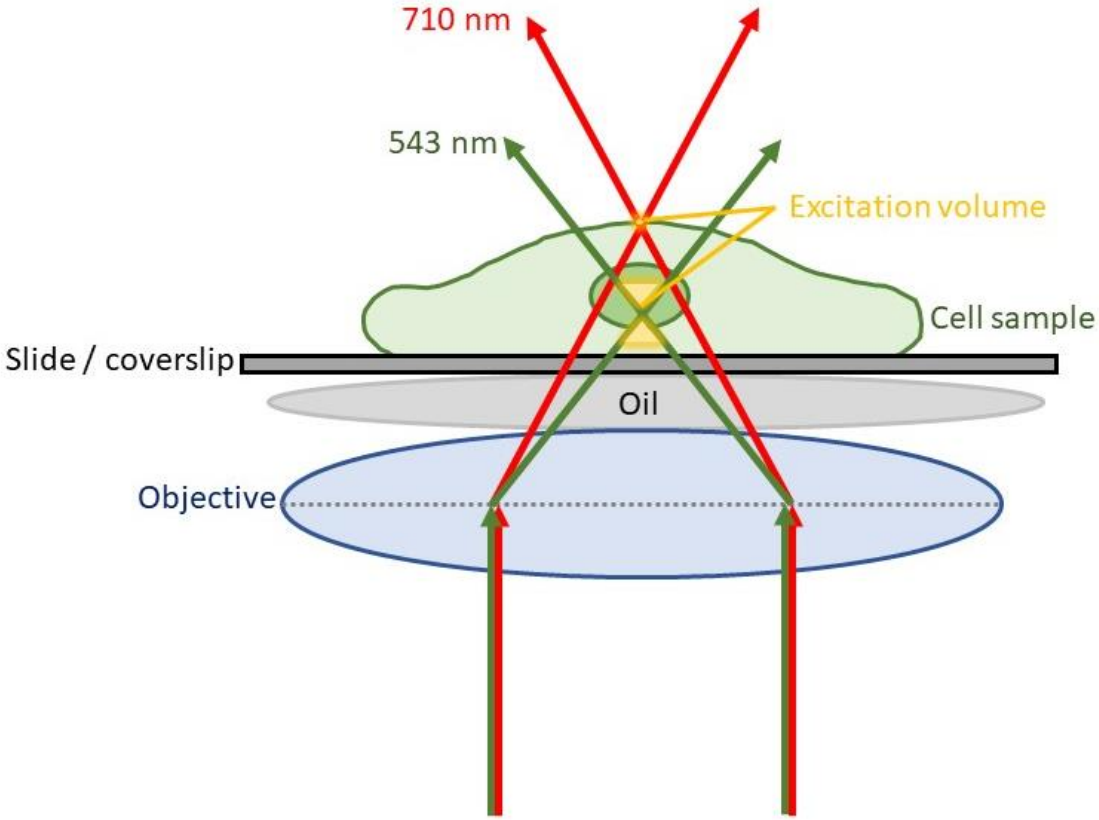

Figure 4.14 Simplified representation of axial chromatic aberration causing 543 and 710 nm laser lines to have differing focal planes.

This posed an initial question of how to correctly select the focus before starting the imaging procedure. As previously discussed, one of the key benefits to multiphoton activation is its inherent confocality caused by the non-linear absorption of two, or more, photons. This ideally allows for very specific selection of the excitation voxel and, in the case of MNM activation, highly specific cell selectivity. When utilised correctly this can show remarkable selective onset of cellular necrosis between multiple cells within the same imaging window, illustrated nicely by **Figure 4.15** obtained during the proof-of-concept work.[1]

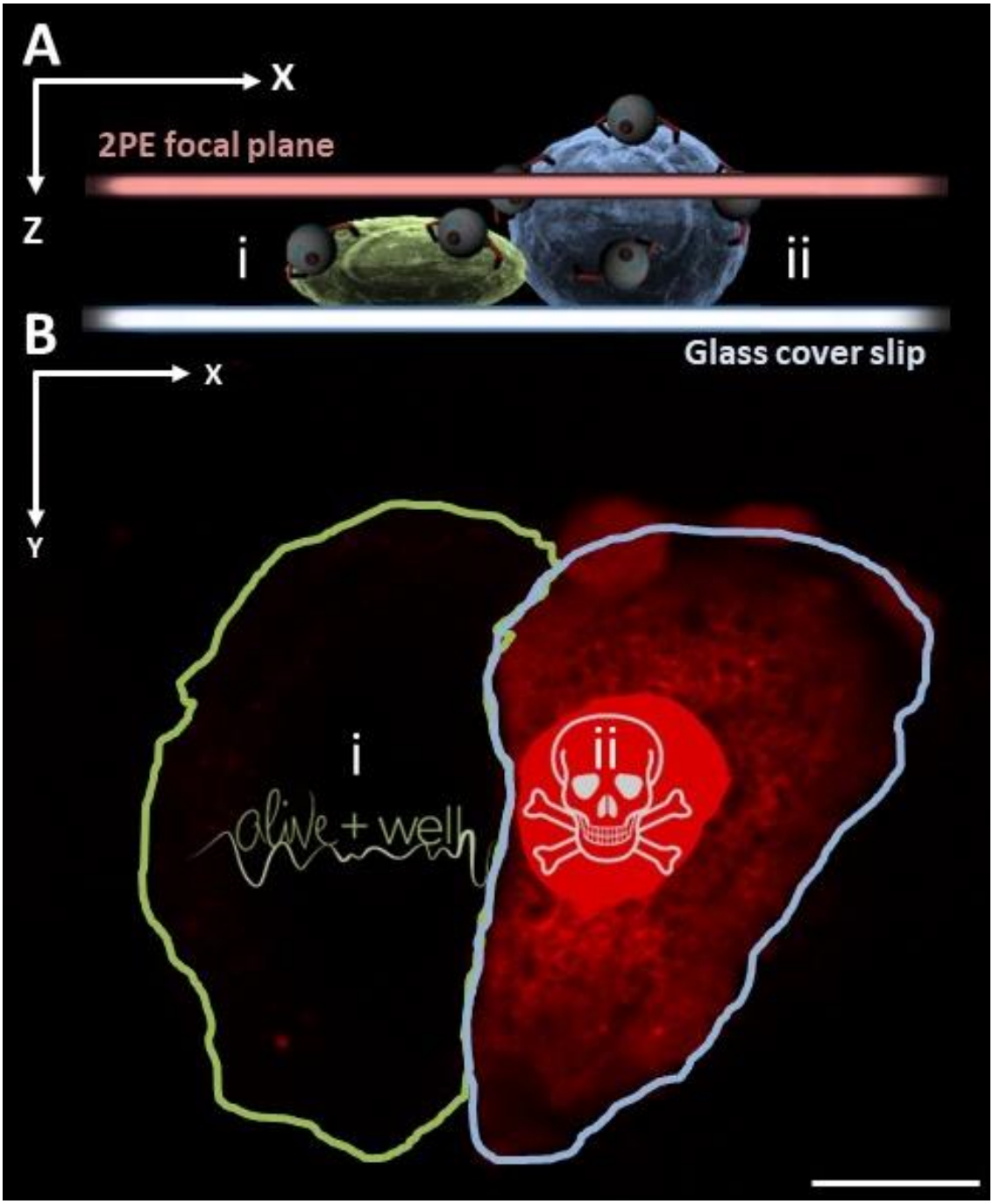

Figure 4.15 Demonstration of z-dimension precision in cell killing using 2PE NIR MNM activation. **A** - Schematic representation of a selected PC3 cell focal plane with high axial precision MNM 2PE activation (710−720 nm). **B** - Microscopic observation of cell death caused by excitation at 710 nm quantified by the observation of PI fluorescence within the nucleus (100 nM red, λ_{ex} = 543 nm, λ_{em} = 610−630 nm, 0.2 mW) confirming high-precision 3D selective-induced necrosis only by the cell occupying space in the

selective focal plane of 2PE activation (710 nm, 65 mW, 80 MHz, 100 fs, ×20 0.75NA objective). Scale bar set to 20 µm. Adapted from Liu *et al*.[1]

However, in this case the observed axial chromatic aberration combined with this high level of focus specificity brings with it some significant challenges, as any minor change in the initial focal set up will dramatically alter the results obtained when measuring the onset of necrosis. This is compounded if using higher wavelengths, such as 800 nm for the MPA of 405 nm single photon activated MNMs. The two-photon NIR laser line is now not visible requiring focusing only on the visible 543 nm excitation source used for PI visualisation. **Figure 4.16** shows the dramatic difference observed when changing the initial focusing procedure from obtaining an in-focus image using either the 543 nm single-photon or 710 nm two-photon laser line.

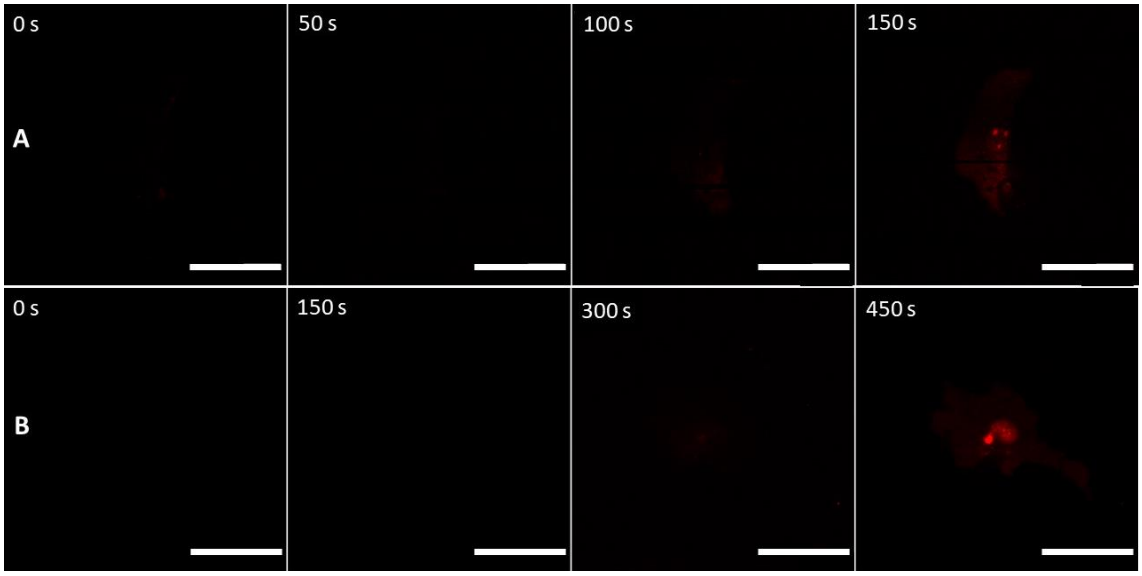

Figure 4.16 Microscopic observation of cell death caused by excitation at 710 nm (NIR-exposure times are shown for each image), quantified by the observation of PI fluorescence within the nucleus. **A** – Control sample: NIH 3T3 cells loaded with 100 nM PI and 0.1% DMSO. Focusing cells using 543 nm single-photon laser line. **B** – Control sample: NIH 3T3 cells loaded with 100 nM PI and 0.1% DMSO. Focusing cells using 710 nm two-photon laser line. All image sets collected after 30 minutes incubation after dosing procedure. Red channel showing detection of PI fluorescence (λ_{ex} = 543 nm, 0.2 mW; λ_{em} = 600-700 nm). All scale bars set to 50 µm.

A substantial disagreement of ~200 s is seen between the TTN results collected when only varying the starting focal plane, illustrating the tight focal dependence when working with non-linear processes. Both focusing procedures brought with them their own challenges. Focusing on purely on the multiphoton line caused the 543 nm induced PI fluorescence to be significantly out of focus, while this reduction in image quality may not necessarily ruin the experiment, the resultant difficulty in determining an exact first frame for PI fluorescence within the nucleus makes consistency in the obtained results difficult to maintain. Focusing on the 543 nm single-photon line elevates this concern

but introduces additional constraints. Specifically, the results obtained became much less reliable with necrosis occurring within an unacceptable timeframe. In addition, occurrences of the burning of the slide and slide coating became much more prevalent, ruining many results with seemingly no way to predict or prevent the problem. To attempt to explain this phenomenon it is important to specify the structure of the ibidi µ-slide I[18] channel slides used throughout this work – shown in **Figure 4.17**.

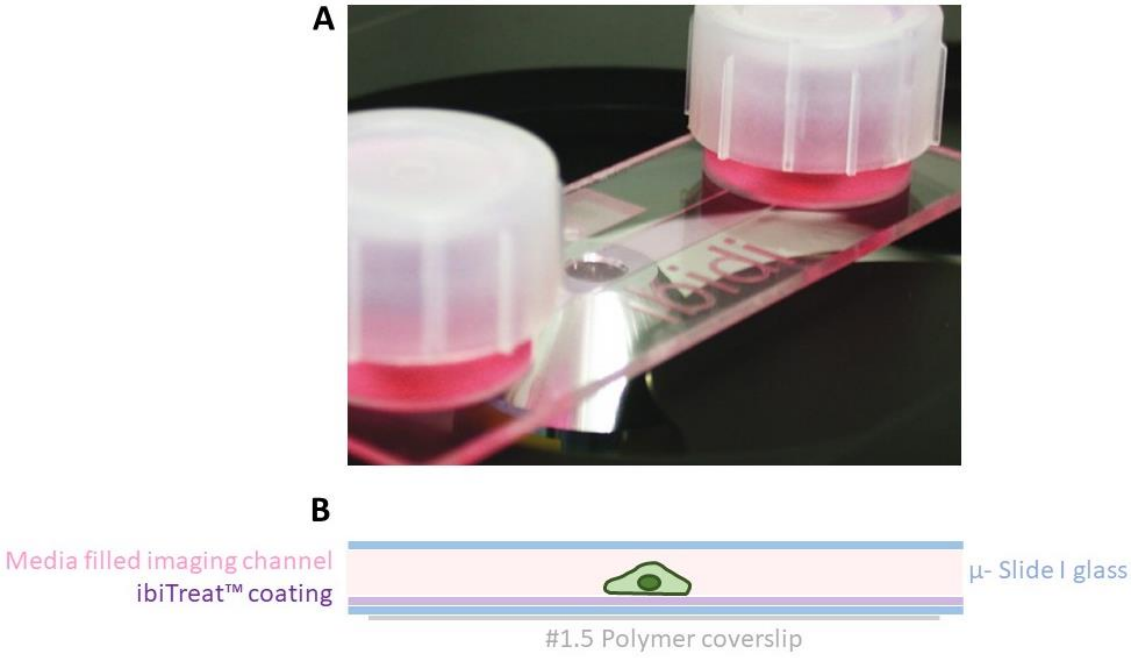

Figure 4.17 A – ibidi µ-slide I image, taken from the ibidi website.[18] **B** – Schematic breakdown of the layers contained within the channel slide.

The channel slides used to study the samples throughout this project consist of several layers, including coverslips and various coatings. While the exact make up, including any adhesive layers, of the slides is not publicly available it is shown that each slide contains a complex layered structure. When exclusively focusing on the 543 nm laser line, the exact placement of the axially shifted 710 nm MP laser is unknown. It is plausible that depending on the structure of the cell under study, and the placement of the 543 nm

focal plane, the 710 nm plane may be focused onto one of these layers. Resulting in the unpredictable burning effects shown to ruin the running experiment.

These problems are compounded further due to the inherent unpredictability when working with biological systems. Cells within the sample have the possibility of being outside of the focal plane based on morphology, caused by where they are within their division cycle or unseen factors causing differing levels of cellular stress.[19,20] When under some form of stress (be this minute changes in pH, temperature, or humidity) it is typical of NIH 3T3 cells to slightly pull away from the substrate they are growing on, with completely healthy cells lying significantly closer to the surface. This holds the possibly to lead to the 2PE focal plane covering different surface areas of the sample when brought into focus using identical techniques by the microscopist, i.e., by focusing on specific features within the cytoplasm or nucleus. This is Illustrated in **Figure 4.18**.

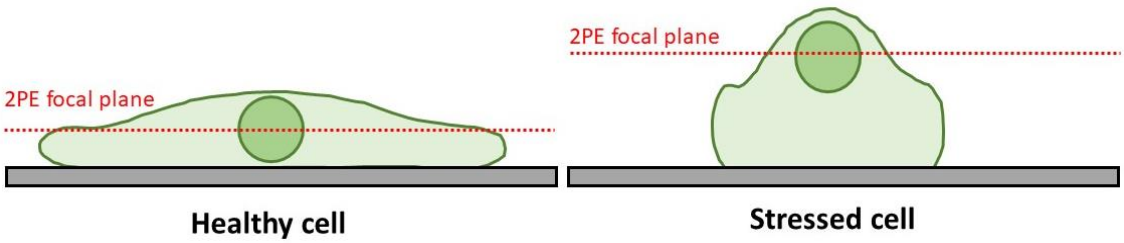

Figure 4.18 Pictorial representation showing the possible difference in surface area held within the 2PE focal plane, between healthy cells (left) and slightly stressed cells (right) when focused in such as a way as to bisect the nucleus with the focal plane.

This causes little issue in previous single-photon UV activation experiments due to the relatively large excitation voxel, but the diffraction limited excitation space of the quadratic two-photon process results in a dramatic difference. Based on previous understanding of the pit-like surface localisation of MNMs on cellular membranes it is

feasible to suggest that the greater the surface area of cell exterior exposed to 710 nm 2PA, the faster the onset of necrosis due to higher numbers of MNMs being activated. Thereby resulting in the unpredictability in the obtained previously results.

A compromise had to be reached between the intrinsic benefit of 2PE's inherent confocality, and the inconsistent results produced due to the previously described problems arises from the same concept. This was solved by enacting new methodology in the excitation of the samples, to artificially increase the size of the two-photon excitation space. By setting up a z-stack within the microscopy software the width of the focal plane can be increased enough to reduce the impact of any changes in cell morphology and maintain consistent results, providing all other experiment procedures are controlled. This is illustrated in **Figure 4.19**. Crucially, this method leaves the lateral resolution of the two-photon laser unaffected, still allowing for cell specific selection and destruction.

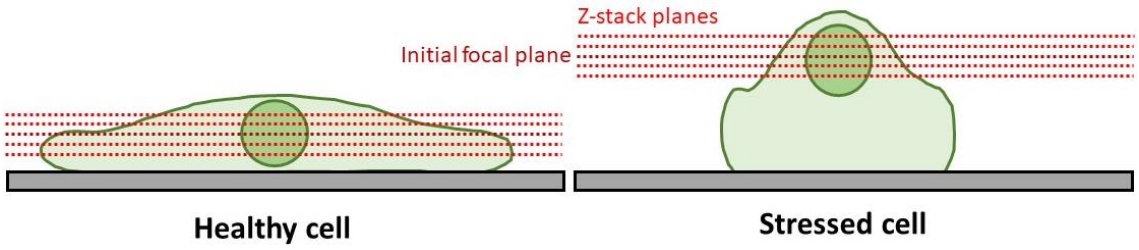

Figure 4.19 Pictorial representation of how enacting a Z-stacking procedure artificially increases the 2PE excitation space for either healthy (left) or slightly stressed (right) cells.

After repeated experimentation a 5 µm z-stack (5 steps of 1 µm) was found to strike the correct balance between reducing the impact of cell morphology changes on the obtained TTN results, while also preventing the boundaries of the highly pulsed two-

photon laser from crossing the burnable layer of the ibidi μ-slide. This procedure also has the additional benefit of giving 5 observable imaging planes; selecting the specific plane where the 543 nm laser is in focus allows for easy detection of the first frame where PI fluorescence is detectable within the cell's nucleus, further increasing the reliability and repeatability of the results. Leading to a robust methodology, used for all further MNM 2PA experiments within the reported work.

4.4 Conclusions

To briefly conclude, initial work with the newly installed multiphoton capable laser system was hampered by both instrumental problems relating to power stability and intensity, and by unavoidable focus issues which required solving with changes in experimental procedure. The highly specific use case of this MNM based work, namely incredibly long excitation times coupled with a lack of fluorescence within the 2PE channel, resulted in the utility of the standard troubleshooting procedures of both Lecia and Coherent engineers being limited. This required extensive investigations and "trial and error" work to be carried out to firstly determine the source of any problems, and secondly work on possible solutions.

Issues arising from power instability, usually producing little to no noticeable effect during the more standard imaging uses of this style of system, were first solved by longer warm up times as well as minute changes to the "startup" and "shutdown" procedures. More significant problems were caused, simply, by too great of a laser power hitting the sample. Again, under the timeframes in more standard imaging or spectroscopy-based uses for these systems this is a non-issue and as a result is difficult to solve. Initially these problems – burning slides and damage to cellular samples – were solved by the addition of ND filters into the beam path of the laser, after internal power control. This limited

the power detected at the focal plane, allowing for a significant jump in experimental reproducibility. However, power was only limited up to a certain point (10 mV when set to 0% within the GUI), leading to a very small operation window of laser power with little to no room to operate. This, alongside the worry of degradation of the filter, led to the installation of a more advanced EOM based amplitude modulator for power control, resulting in a highly tuneable instrument, capable of specific MNM activation and study.

Problems were also found when selecting the focal plane during experiment setup. Chromatic aberration caused a drift between the two lasers used within the experiment, and minute uncontrollable changes in cell morphology between experiments led to unpredictable results. This, coupled with the intrinsic high voxel specificity of the multiphoton laser system caused several problems – initially very hard to distinguish from those caused by the previously explained instrumentation issues. After vast amounts of troubleshooting, a z-stack procedure was enacted to increase the size of the 2PE space. When coupled with the previous power improvements a robust, highly consistent procedure, was developed for the two-photon investigation of Tour based MNMs. This was used in the additional work presented within future chapters.

4.5 References

1 D. Liu, V. García-López, R. S. Gunasekera, L. Greer Nilewski, L. B. Alemany, A. Aliyan, T. Jin, G. Wang, J. M. Tour and R. Pal, *ACS Nano*, 2019, **13**, 6813–6823.

2 M. Rumi and J. W. Perry, *Adv. Opt. Photonics*, 2010, **2**, 451–518.

3 C. Xu and W. W. Webb, *JOSA B*, 1996, **13**, 481–491.

4 M. A. Albota, C. Xu and W. W. Webb, *Appl. Opt.*, 1998, **37**, 7352–7356.

5 Coherent, Chameleon Ultra - Tunable Ti:Sapphire laser system, https://www.coherent.com/lasers/oscillators/chameleon-ultra, (accessed 6 December 2023).

6 Leica, Leica TCS SP5, https://www.leica-microsystems.com/products/confocal-microscopes/p/leica-tcs-sp5/, (accessed 6 December 2023).

7 K. König, *J. Microsc.*, 2000, **200**, 83–104.

8 M. J. Koehler, M. Speicher, S. Lange-Asschenfeldt, E. Stockfleth, S. Metz, P. Elsner, M. Kaatz and K. König, *Exp. Dermatol.*, 2011, **20**, 589–594.

9 K. Schenke-Layland, I. Riemann, U. A. Stock and K. König, *J. Biomed. Opt.*, 2005, **10**, 024017.

10 E. B. Brown, R. B. Campbell, Y. Tsuzuki, L. Xu, P. Carmeliet, D. Fukumura and R. K. Jain, *Nat. Med.*, 2001, **7**, 864–868.

11 R. M. Pope and E. S. Fry, *Appl. Opt.*, 1997, **36**, 8710–8723.

12 G. M. Hale and M. R. Querry, *Appl. Opt.*, 1973, **12**, 555–563.

13 Microscope Slide Power Meter Sensor Heads, https://www.thorlabs.com, (accessed 12 December 2023).

14 Thorlabs - ND503B Unmounted Reflective Ø1/2, https://www.thorlabs.com, (accessed 13 December 2023).

15 Thorlabs - ND509B Unmounted Reflective Ø1/2, https://www.thorlabs.com, (accessed 14 December 2023).

16 W. R. Zipfel, R. M. Williams and W. W. Webb, *Nat. Biotechnol.*, 2003, **21**, 1369–1377.

17 H. Blanc, G. Kaddour, N. B. David, W. Supatto, J. Livet, E. Beaurepaire and P. Mahou, *ACS Photonics*, , DOI:10.1021/acsphotonics.3c01104.

18 µ-Slide I | Channel Slide for Flow Assays, https://ibidi.com/channel-slides/49--slide-i.html, (accessed 19 December 2023).

19 S. Fulda, A. M. Gorman, O. Hori and A. Samali, *Int. J. Cell Biol.*, 2010, **2010**, 214074.

20 A. M. Schor, S. L. Schor and T. D. Allen, *J. Cell Sci.*, 1983, **62**, 267–285.

Chapter 5: Single- and two-photon evaluation of various internalising group functionalised MNMs working towards promoting more biologically favourable cell death pathways

Summary: *This chapter provides a collection of investigations surrounding two key functional groups commonly utilised within medicinal chemistry for the internalisation of various drug and drug-like molecules within cells. These are coupled to the previously well documented MNM core structure, and the ability of these new functionalised MNMs to passively cross the phospholipid bilayer are tested using the aforementioned experimental procedures; with both single- and two-photon processes. Promising candidates, with seemingly good internalisation properties, then undergo further evaluation in an effort to access new, more biologically favourable, routes towards MNM induced cell death via activation of the rotor from within the cell. In an overall effort to aid in the development of possible therapeutically compatible MNM-based procedures for cell specific destruction.*

5.1 Introduction

5.1.1 Internalising MNM addends – their structure and function

Previous work within this project, evaluating the ability of certain MNM addends to shift the activation wavelength of the rotary mechanism, noted an increased ability of MNMs functionalised with various diamine-based groups to passively cross the phospholipid bilayer. Resulting in MNMs with the remarkable ability to lodge within the membrane or completely internalise within the cell itself. These surprising results prompted a search for new functional groups specifically designed to promote cellular uptake of MNMs and open the possibility of activation from within the cell.

Polyethylene glycol (PEG) moieties, shown in **Figure 5.1**, are inert chain amphiphilic molecules constructed by the linkage of repeating units of ethylene oxide. First

developed in 1978 for the purpose of modifying enzyme properties, specifically their life time within the blood stream.[1]

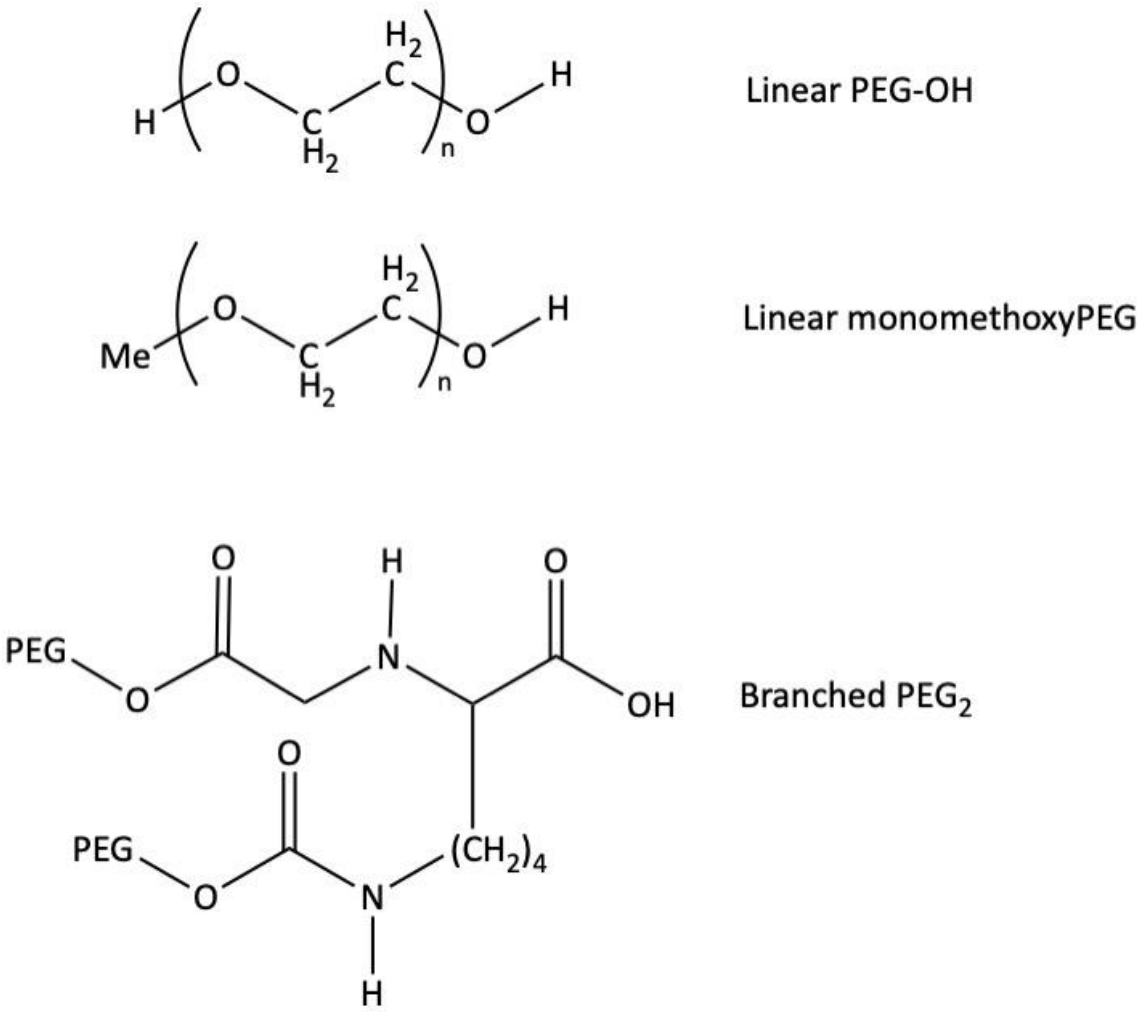

Figure 5.1 Chemical structures of selected commonly used PEG moieties for pharmacokinetic modification. Adapted from Bailon *et al*.[2]

A large number of PEG-molecule conjugates are found in medicinal chemistry where pegylation is used to increase the size and molecular weight of numerous drug and drug-like compounds, thereby altering their immunological, pharmacokinetic, and pharmacodynamic properties. **Table 5.1** presents a brief overview of these studied PEG conjugates.

Table 5.1 Summary of various types of PEG conjugates and their properties.[3]

Conjugated compound	Applications of PEG modification
Small MNM-like molecules	Improved solubility, **increased permeability across biological barriers**, increased blood stream half-life, controlled release.
Affinity ligands and cofactors	Used in aqueous 2-phase partitioning systems for purification and analysis of biological macromolecules and cells
Peptides	Improved solubility, biologically active conjugates
Proteins	Increased resistance to proteolysis, reduced immunogenicity, increased blood stream half-life
Saccharides	Novel biomaterials, drug carriers
Oligonucleotides	Improved solubility, resistance to nucleases, **increased cell membrane permeability**
Biomaterials	Reduced protein and cell adherence

Due to its common usage in the modification of biopharmaceuticals to enhance permeability through phospholipid bilayers[4], as well proposed passive targeted of cancer cells *via* increased internalisation through cancerous cell membranes[5], PEG functionalisation of MNMs was deemed a promising route. However, it is important to note that some studies have shown that PEG functionalised small molecules can exhibit an enhanced ability to cross the blood brain barrier (BBB).[6] Posing a possible drawback when looking forward to using PEG addended MNMs in therapeutic treatments. Nevertheless, several Pegylated drugs have passed clinical trials and are approved for use; the most widely known of which being PEG-adenosine deaminase (Pegademase)[7]

and PEG-asparaginase (Pegaspargase).[8] Therefore PEG functionalised MNMs (**MNM 7** and **MNM 8**), shown in **Figure 5.2**, were developed for evaluation within this chapter.

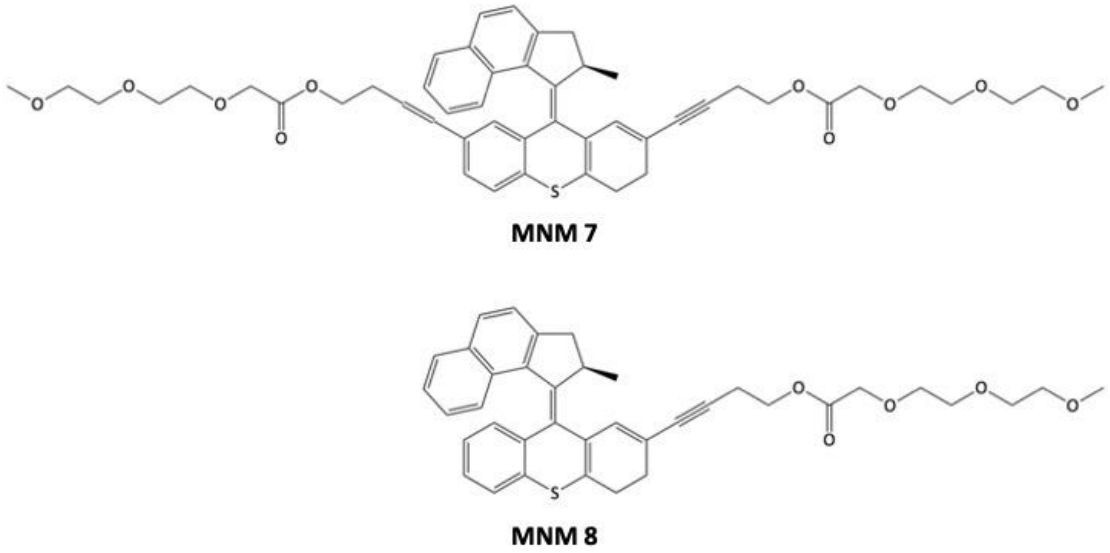

Figure 5.2 Exert from the MNM database showing the chemical structures of two pegylated MNMs used throughout this chapter, dual armed **MNM 7** and single arm functionalised **MNM 8**.

In addition to this PEG functionalisation, an alternative method has also been proposed utilising the highly lipophilic triphenyl-phosphonium cation (TPP+), **Figure 5.3**, as a mitochondriotropic carrier; not only to promote crossing of the cellular membrane but also to specifically bind within the target cells mitochondrial network.[9] TPP+ conjugates are one of the most widely used mitochondria targeting carriers[10] in modern drug development alongside rhodamine 19[11] as well as mitochondria targeted peptide techniques such as Szeto−Schiller peptides[12]. Their ability to promote rapid crossing of the cell membrane without the need for any transport proteins is afforded by both the large ionic radius, due to resonance-mediated diffusion of the positive charge, and the highly lipophilic nature of the three phenyl rings within the structure.[13] Illustrated in **Figure 5.3**.

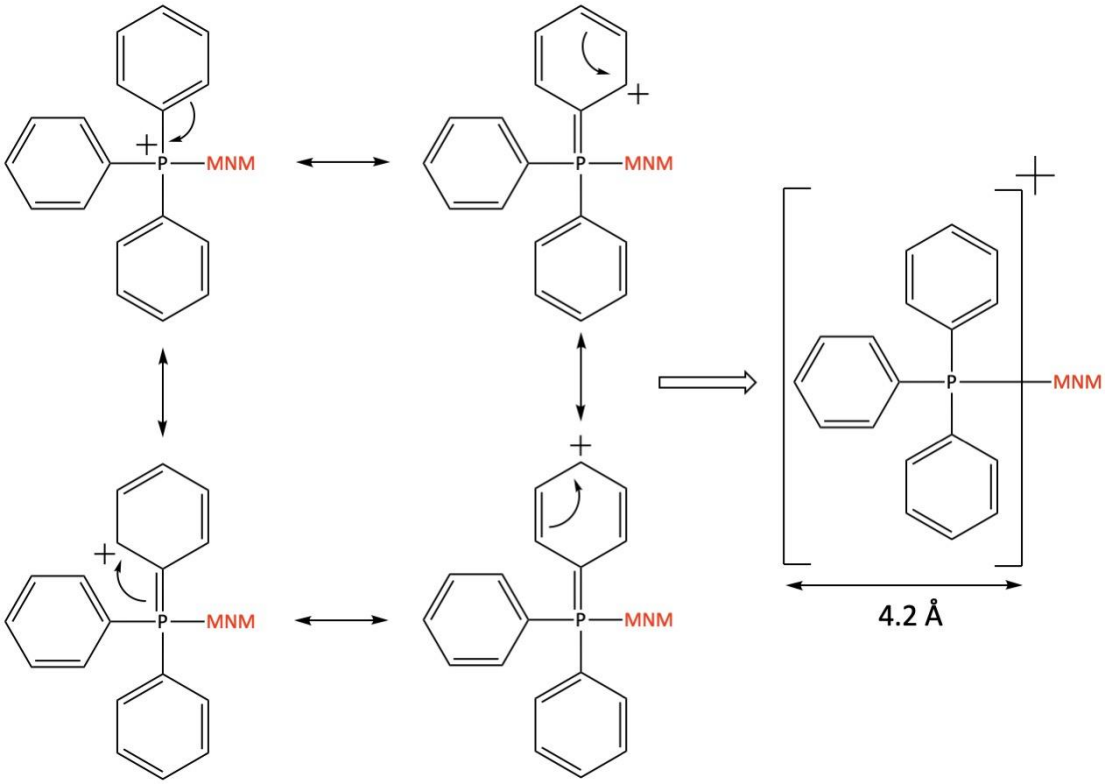

Figure 5.3 Diffusion of positive charge across the TPP+ cation *via* resonance of aryl pi electrons resulting in the observed large ionic radius of 4.2 Å. Adapted from Ross *et al*.[13]

This internalised, positively charged, TPP+ moiety is electrostatically attracted to the mitochondria due to the roughly -180 mV membrane potential across the inner mitochondrial membrane, caused by the proton pumping action of the electron transport chain.[14] Studies have shown that for every 60 mV of membrane potential across the mitochondria there is a 10-fold accumulation of small molecule functionalised TPP+ conjugates, resulting in up to a 500× accumulation within their inner membrane, illustrated in **Figure 5.4**.[9] This process has been widely exploited within the literature, resulting in several commonly available TPP+ targeted cargos; such as the anticancer drugs Mitometformin[15] and Mitoporphyrin[16], and the mitochondrial imaging probes MitoSox[17] (used for ROS detection) and 1,8-naphthalimide-TPP[18].

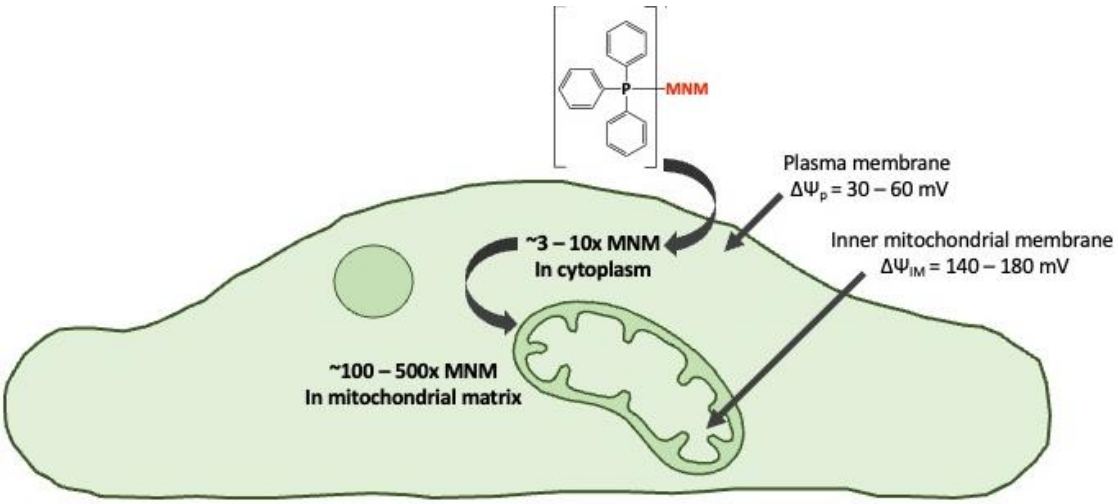

Figure 5.4 Schematic representation of the membrane potential driven uptake of TPP+ functionalised MNM conjugates within the mitochondria of cells.

This promising ability of these various reported TPP+ conjugates to cross the phospholipid bilayer and localise within the mitochondria. As well as improving generic pharmacokinetic properties, such as half-life within the blood stream, made this functionalisation technique an exciting route to explore for MNM modification. As such, **MNMs 9** and **10** (**Figure 5.5**) were developed and will be investigated for their internalisation ability herein.

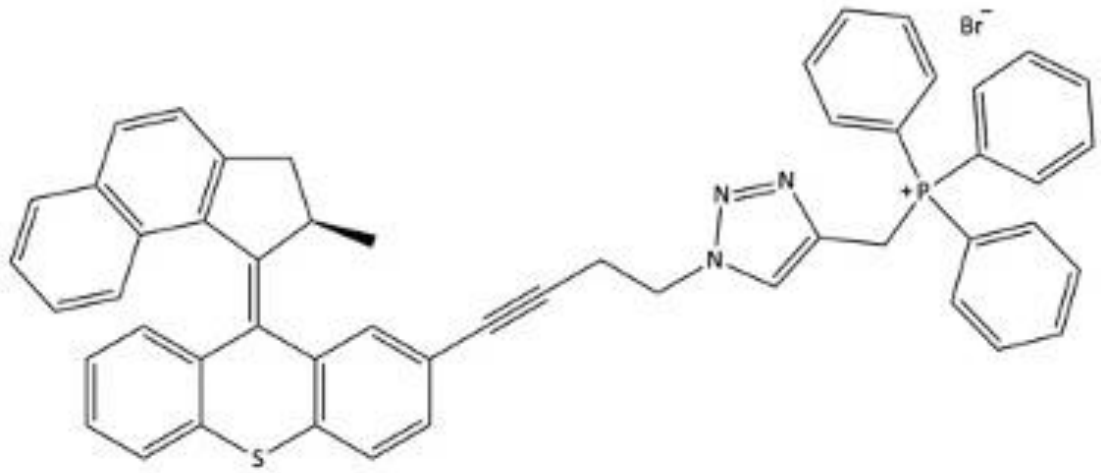

MNM 9

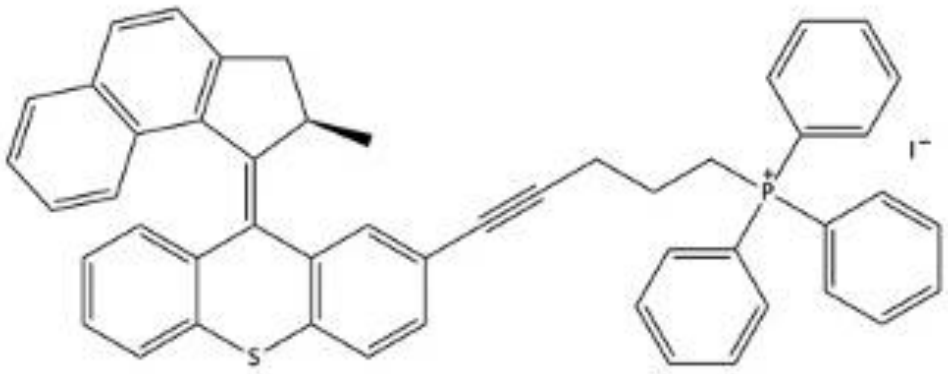

MNM 10

Figure 5.5 Exert from the MNM database showing the chemical structures of two TPP+ coupled MNMs used throughout this chapter, Br counter ion **MNM 7** and I counter ion **MNM 8**.

It is important to note however, that recent literature has proposed that TPP+ functionalisation may not be as inert as initially reported. In fact, it is reported that TPP+ targeted compounds can lead to detrimental effects on mitochondrial function by inhibiting oxidative phosphorylation, and inducing mitochondrial proton leak.[19,20] While these are not necessarily toxic to the cell in study, the synthesis of ATP may be effected. Therefore, it is important to monitor the health of any cells dosed with TPP+ containing

MNMs. Making 24-hour clearance experiments, like those discussed in previous chapters, of vital importance.

5.1.2 Differing routes towards cell death and possible methods of detection

Cell death has long been categorised into two overarching categories, with the first references to distinct cell death pathways being found as early as 1951 when Glucksmann coined the term "programmed cell death" (PCD) when referring to cell death that occurred at specifically defined points as part of the normal development cycle of cells.[21] In the 1970s this was extended when histochemical studies on lysosomal changes provided the first evidence for two distinct modalities for the death of mammalian cells; initially interpreted as two forms of necrosis, regular- and shrinkage-necrosis.[22] The term apoptosis was first introduced in 1972[23], and now necrosis and apoptosis are fully understood to be two completely separate cell death pathways. Crucially for the microscopist, with distinct morphological characteristics - such as cell shrinkage during apoptosis and cytoplasm blebbing specific to necrosis. These are illustrated by the phase contrast microscopy images of HeLa cells in **Figure 5.6**.[24]

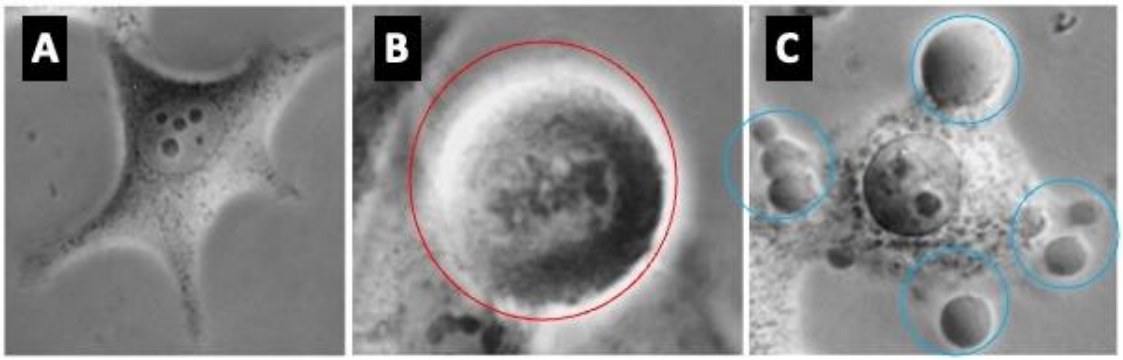

Figure 5.6 Phase contrast microscopy images of HeLa cells illustrating the different morphology changes between various cell death pathways. **A** – Healthy HeLa cell before undergoing any treatment. **B** – Apoptotic HeLa cells treated with porphyrin derivative CF3 exhibiting typical features of apoptosis; cell shrinkage and rounding (illustrated in red), as well as releasing from the surface (illustrated by the movement out of the focal plane). **C** – Necrotic HeLa cells treated with photodynamic ZnPc exhibiting the typical features of necrosis; maintain cellular boundaries (lack of cellular shrinkage) and significant blebbing of the cytoplasm (highlighted in blue). Adapted from Rello *et al*.[24]

Apoptosis, and various other PCD pathways to be elaborated upon shortly, is specifically defined as an active process involved in the physiological elimination of redundant, or otherwise damaged, cells. As well as being responsible for maintaining tissue homeostasis by compensating for normal cell proliferation. As opposed to accidental necrosis which is fully triggered by effects outside of the cells control. It should be noted that cells can trigger apoptosis, or other PCD pathways, in response to a stimulus that would normally trigger necrosis in a form of damage mitigation. The discovery of caspases, specific proteases, as the predominant executor of the cascade reactions responsible for apoptosis allowed for a more strict definition of apoptosis, and the illumination of other, non-caspase mediated forms, of PCD.[25]

The newly discovered types of PCD all have in common that they are specifically executed by active processes from within the cell itself and can be intercepted by interfering with these intracellular signalling pathways. Indeed, the majority of non-apoptotic PCD mechanism were discovered by inhibition of various caspase proteins.[26] **Figure 5.7** provides a brief summary of various models of cell death. The specifics of each of these non-apoptotic PCD mechanisms are beyond the scope of this work, as for the purposes of MNM based therapeutics there is little difference between apoptosis and other non-caspase mediated PCD mechanisms. It is vital however, to distinguish between accidental necrosis caused by external factors and cellular membrane damage (which is observed for all previous MNM experiments), and cell controlled PCD mediated by various intracellular mechanisms as these provide possible therapeutic benefits to be discussed in section 5.1.3.

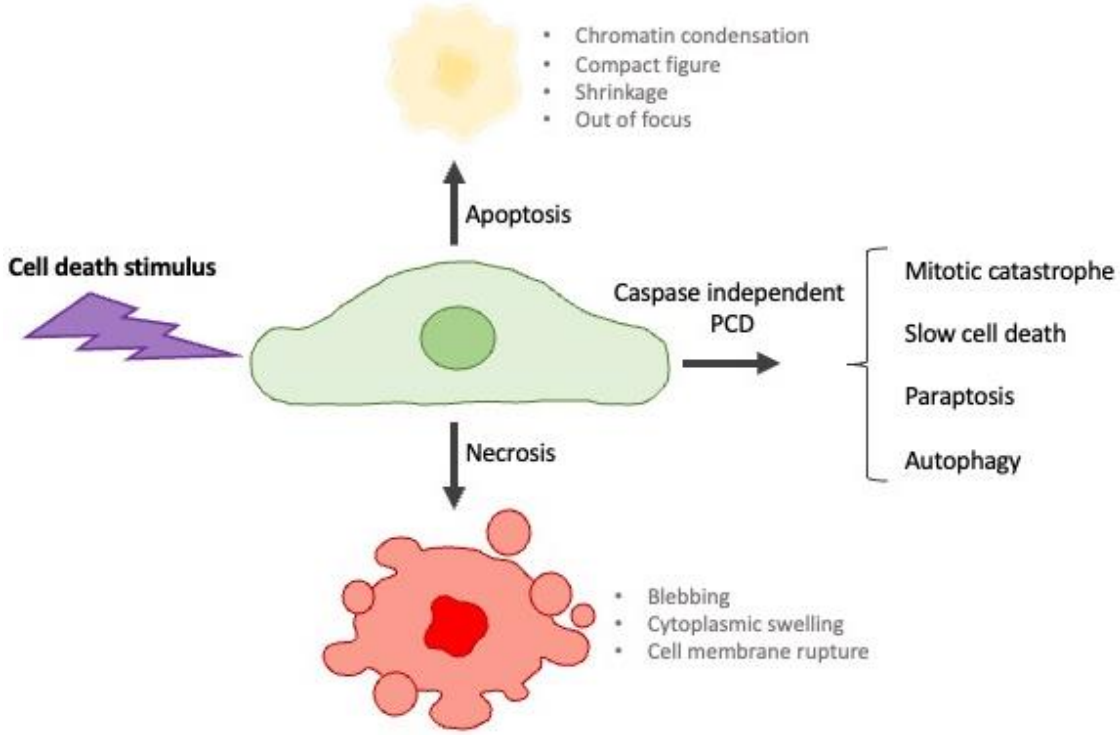

Figure 5.7 Summary of a few key mechanisms of cell death, including several proposed models of caspase independent PCD. Mitotic catastrophe is the default PCD pathway after mitotic failure, slow cell death is a proposed route to describe PCD when caspases are inhibited, paraptosis exhibits cytoplasmic vacuolation and mitochondrial swelling in the absence of caspase activation, and autophagy has been categorised by breakdown of organelles and their subsequent digestion by the cells own lysosomal system. Adapted from Bröker *et al*.[26]

To provide a comprehensive overview of the topic, **Table 5.2** shown below, includes a brief overview of defined non-apoptotic mechanisms of PCD. However, as the vast majority of these processes are nearly indistinguishable from apoptosis without monitoring the internal biochemistry of the cells under study, or directly inhibiting the caspase pathway. In addition to being specific to individual cell types. Any further detail is unnecessary for the work reported in this chapter.

Table 5.2 Brief summary of various non-caspases mediated PCD pathways. Adapted from Bröker *et al*.[26]

Cytotoxic agent	Cellular system studied	PCD mediated by:
Camptothecin	Hepatocytes	Cathepsin
Cladribine	Human leukaemia	Apoptosis inducing factor (AIF)
Doxorubicin	Cardiomyocytes	Calpains
Paclitaxel	Ovarian carcinoma	AIF
Staurosporine	Fibroblasts	Cathepsin D
Flavopiridol	Glioma cells	AIF
Vitamin D	Breast cancer cells	Calpains
Quinolone antibiotics	Various human and mice cells	Cathepsin B and D

While microscopists have historically distinguished apoptosis – and other non-caspase based PCD mechanisms – from necrosis *via* the previous illustrated morphological changes, the establishment of emissive dyes with "switch on" functionality and specific recognition properties have made differentiating between these forms of cell death a simpler affair. Allowing for immediate identification of the route towards observed cell death. However, morphological changes are still a vital tool in untangling the routes leading to cell destruction, and fluorescence – or lack thereof – of detection agents cannot always be relied upon to fully understand cell death pathways.

PI, shown again in **Figure 5.8**, has already been utilised throughout in this work as a necrosis specific detection agent and is commonly used in both live-cell microscopy and

flow cytometry.[27] A membrane impermeable dye, PI exhibits a fluorescence maximum at 617 nm (excitation and emission spectra shown in Chapter 1) when bound to nucleic acids intercalated between DNA strands.

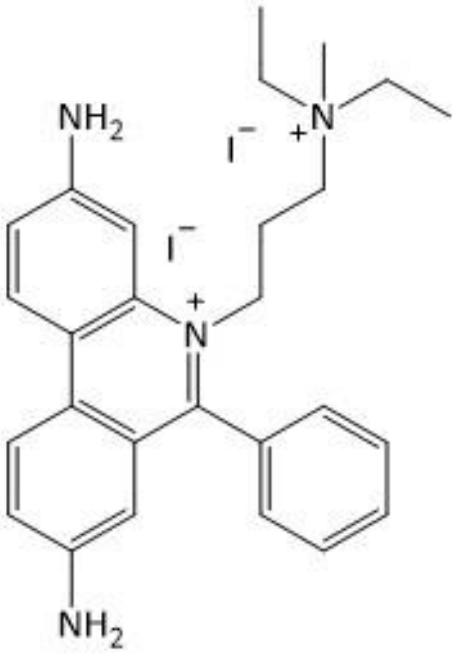

Figure 5.8 Chemical structure of Propidium iodide.

Since PI enters the cell only when membrane integrity is compromised, it has found widespread use in determining plasma membrane permeability and, by extension, the presence of necrotic cells.[28] In addition, commonly available non-specific live-dead stains often use PI, combined with other non-membrane permeable staining agents such as calcein-AM, SYTO 9™, or 4',6-diamidino-2-phenylindole (DAPI), to assess the overall health of cellular colonies.[29] As illustrated by the previous results shown within this work, PI is an incredible useful tool in live cell microscopy where immediate identification of necrotic cells is possible. However, as previously illuded to, these staining systems are not infallible; especially when used in flow cytometry. If apoptotic cells are not removed by phagocytic cells – i.e. if studied outside of the body – they can progress to secondary necrosis through passive cellular swelling.[30] Leading to false

positive readings where PI has crossed the plasma membrane of initially apoptotic cells. Illustrating the point that morphological changes should be used in conjugation with emissive dyes to fully understand the routes towards cell death in a studied system.

Apoptosis, and other PCD routes, can of course be detected by the lack of PI emission within morphologically assessed dead cells. However, a number of emissive detection regents have been developed to specifically identify apoptosis from other forms of cell death. Since apoptosis is a process controlled by the activation of caspase enzymes within the cell, the simplest method for determining apoptotic cells is to identify the presence of these proteins. Caspase detection kits often consist of fluorescent compounds, such as rhodamine 110, coupled to peptide sequences that are cleaved by specific forms of caspase. When bound to the peptide sequence these dyes are relatively non-fluorescent, however upon cleavage they exhibit "switch-on" emission and can be easily detected thereby acting as an indicator of apoptosis.[31] These methods of detection however have their own limitations, as the level of caspase within the cells under study must reach high enough levels to produce detectable amounts of emissive species and the specific form of caspase – 14 mammalian and 12 human specific forms[32] – responsible for triggering the cascade reaction within the cell type under study must be known.

Annexin V is a phospholipid binding protein that binds to phosphatidylserine. In healthy cells phosphatidyl serine is located at the cytoplasmic surface of the cellular membrane, making it inaccessible to the non-membrane permeable annexin V. Cells undergoing apoptosis expose phosphatidylserine to the outer surface of the membrane as a recognition signal for the macrophages responsible for cellular elimination – a process illustrated in **Figure 5.9**. Which can be exploited for another fluorescent based detection

method of apoptosis by attaching numerous emissive conjugates, such as Alexa Fluor 488, to samples of annexin V.[33]

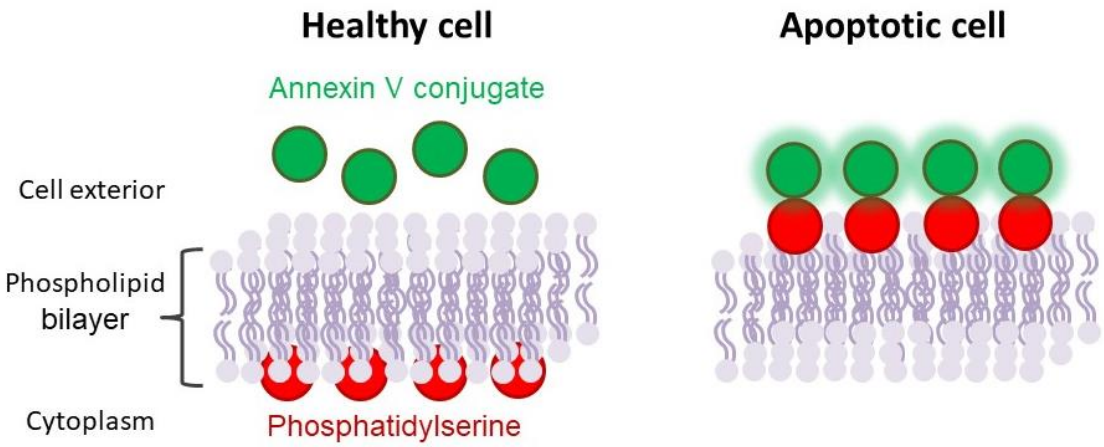

Figure 5.9 Schematic representation of the mechanism of annexin V conjugate binding to phosphatidylserine that allows for apoptosis detection.

However, there is a significant risk of false positive results when staining with annexin V conjugates. Compromised plasma membranes, such as those present in necrotic cells, will allow for the stain to leach into the interior of the cell where binding to phosphatidylserine can occur on the inner membrane. As such, co-staining with a necrotic specific dye such as PI is usually advised.

5.1.3 Looking towards possible therapeutics

The ability to use the MNM based treatments explored throughout this project to induce cellular apoptosis instead of the previously reported necrosis would represent an incredibly significant development on the path towards possible next generation targeted cancer therapeutics. Apoptosis and other controlled, PCD, pathways have the benefit of producing little to no immune response from the body; utilising the previously discussed movement of phosphatidylserine to the cell surface to signal macrophage clean up. These types of cell death are therefore reported to trigger little to no

inflammation.[34] Necrotic, or unscheduled, cell death on the other hand leads to a spillage of intracellular proteins into the extracellular space, triggering a damage response from the hosts immune system.[35] While some cancers, and cancer treatments, may benefit from an induced immune response from necrotic cell death if co-administered with forms of immunotherapy[36] most treatments aim for an induction of cleaner PCD pathways to reduce the onset of harmful side effects.[37]

One of the key morphological changes seen in MNM-induced unregulated necrotic cell death is the leakage on internal cellular material through the mechanically induced holes in the cellular membrane. It is clear when looking towards any possible future use for MNM therapies to treat cancers, that this poses a significant shortcoming compared to other widely available treatments. Uncontrolled necrotic cell death – as opposed to controlled necroptosis - has been shown to activate cancer cell survival and proliferation pathways, as well as promote angiogenesis and tumour cell migration.[38] For these reasons, this chapter focuses on developing methods to use MNMs functionalised with the previously discussed internalising groups to promote controlled apoptosis and other PCD pathways preferentially over uncontrolled necrosis.

Many toxicants have already been found to show a dose-response relationships for induced modes of cells death, as illustrated by the effects of different concentration of 2,3-dimethoxy-1,4-naphthoquinone on RINm5F cells in **Figure 5.10**.[39]

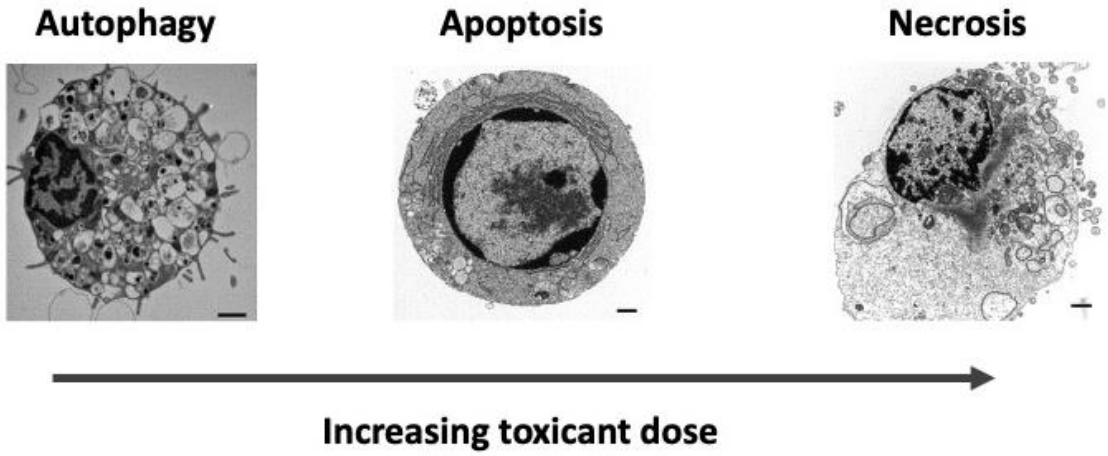

Figure 5.10 Dose dependent PC3 cell killing effect for different concentrations of toxicant. Scale bar size not reported. Adapted from Orrenius *et al*.[39]

Here it is shown that the concentration of added cell killing agent can induce reversable autophagy at low concentrations, while promoting apoptosis, followed by necrosis, at higher levels respectively. While this cannot be directly compared to MNM induced cell death, as even at low concentrations membrane integrity is affected thereby leading to necrosis, it does provide inspiration. It is proposed that if a low enough concentration of MNM, shown to efficiently cross the phospholipid bilayer and localised within cells, can be activated from within the sample and cause sufficient internal damage without damaging the cells membrane. It may be possible to trigger apoptosis or other controlled PCD without allowing the damage to reach great enough levels to cause a necrotic response. What follows is an investigation into the internalising properties of these PEG and TPP+ functionalised MNMs followed by attempts to use this hypothesis and trigger non-necrotic death in the cells studied.

5.2 Single-photon 355 nm UV activation studies of PEG functionalised MNMs

Initial work has been carried out first, on PEG functionalised **MNMs 7** and **8**, to determine if the attachment of these groups can promote internalisation within the studied cells. Crucially, it is also investigated if the levels of MNM within the cell are high enough to be activated by 355 nm excitation, and if this activation is great enough to cause cell death *via* the previously well-established necrotic pathway. As with all previous experimentation this is measured by onset of PI emission within the cell's nucleus. **MNM 7**, shown again in **Figure 5.11**, contains short PEG chains addended to both functional arms leaving the mechanics of the rotor and stator unchanged.

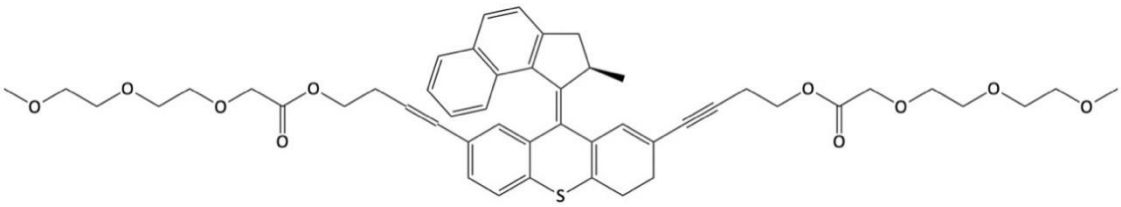

Figure 5.11 Chemical structure of **MNM 7**.

Preliminary live cell microscopy experiments were first carried out using the standard dosing procedure, extensively covered throughout this work, where the MNM under study is held within the cell media while imaging – for full experimental methods see methods Chapter 6. This was completed to ensure **MNM 7** could still promote necrotic cell death *via* induced membrane damage, comparable to the other MNMs studied in this project, despite the added molecular weight of the PEG chains. These results are summarised by the images in **Figure 5.12**.

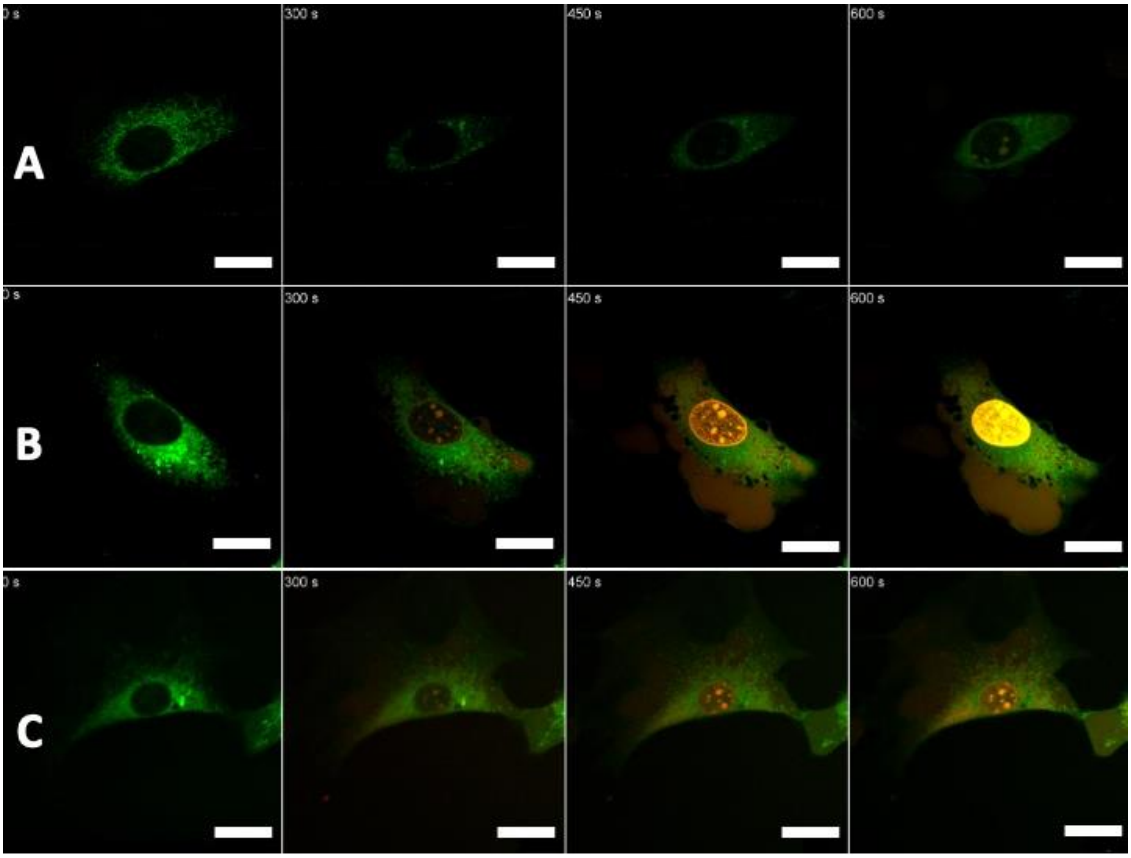

Figure 5.12 Microscopic observation of necrotic cell death caused by excitation at 355 nm (UV-exposure times are shown for each image), quantified by the observation of PI fluorescence within the nucleus. **A** – Control sample: NIH 3T3 cells loaded with 100 nM PI and 0.1% DMSO. **B** – NIH 3T3 cells loaded with 100 nM PI and 0.5 µM **MNM 1**. **C** - NIH 3T3 cells loaded with 100 nM PI and 0.5 µM **MNM 7**. All image sets collected after 30 minutes incubation after dosing procedure. Overlaid channels of PI fluorescence (λ_{ex} = 543 nm, 0.2 mW; λ_{em} = 600-700 nm), and mitochondrial autofluorescence (λ_{ex} = 355 nm, 20 mW, 400 nJ per voxel; λ_{em} = 440-460 nm). All scale bars set to 20 µm.

It can be immediately seen that **MNM 7** is able to induce necrotic cell death under constant 355 nm UV exposure faster than the control sample containing only 0.1% DMSO v/v and 100 nM PI. With at least a 50% reduction observed in the TTN. However, this cell killing effect is notable slower when compared with the results for **MNM 1** under

the same conditions, indicated by a slower increase in PI fluorescence intensity. This was not unexpected and can be rationalised when considering the increase in molecular weight upon addition of these PEG arms; an increase of 320.34 from 514.68 to 835.02 g mol^{-1}. This may affect the efficiency of the rotor, limiting its ability to mechanically disrupt the phospholipid bilayer. The increase in molecular size could also impart a similar limitation, if fewer MNM molecules are able to locate in the same area, causing less overall cellular damage. However, the ability of **MNM 7** to cause early onset necrosis, upon UV activation of the rotor, is still more than sufficient to continue studies of this nanomachine.

Following these conclusions, measurements of the internalising capabilities of **MNM 7** were taken using the experimental procedure developed in Chapter 3 (full experimental details are provided in methods Chapter 6). In short, samples of NIH 3T3 cells seeded onto microscopy slides are incubated with 0.5 μM **MNM 7** for varying time periods, before being washed completely with fresh MNM free growth media and subjected to standard imaging procedure. Any changes in the TTN when compared with the control sample are therefore due to any internalised MNM left behind after the washing procedure, either lodged within the phospholipid bilayer or held completely within the internal space of the cell. In order to ensure these internalised MNMs have no detrimental effect on overall cellular health without prior activation of the rotary mechanism a clearance experiment is also carried out. Here, cell samples are left after washing completely with fresh growth media for at least one cell division cycle – found to be anywhere from 12 to 22 hours for the NIH 3T3 cell line[40] – followed by further washing with MNM free media before being subject to the same imaging procedure as all previous experiments. Ensuring any added MNM has been cleared from the system.

The fluorescence microscopy images in **Figure 5.13** shows the results of these internalisation measurement experiments.

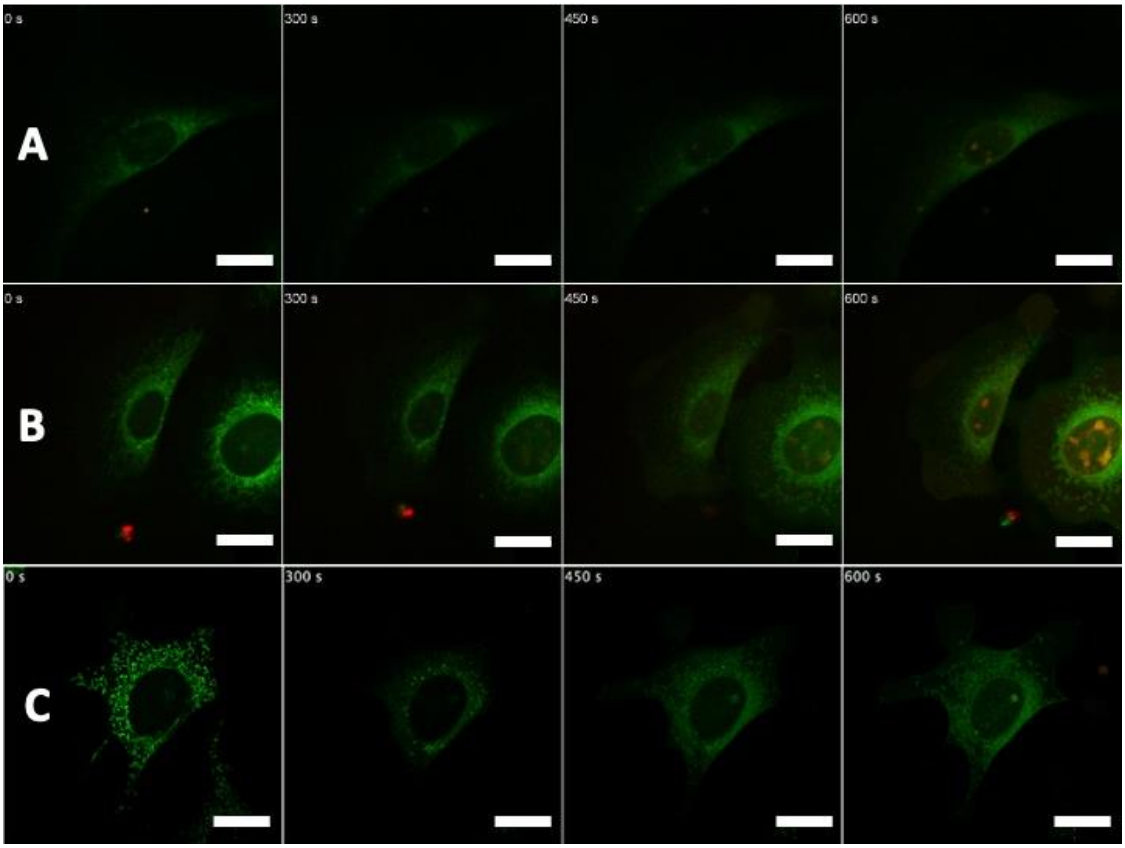

Figure 5.13 Microscopic observation of cell death caused by excitation at 355 nm (UV-exposure times are shown for each image), quantified by the observation of PI fluorescence within the nucleus. **A** – NIH 3T3 loaded with 0.5 µM **MNM 7**, followed by 30 minutes incubation and washing with MNM free media, and subsequent staining with 100 nM PI. **B** – NIH 3T3 loaded with 0.5 µM **MNM 7**, followed by 2-hour incubation and washing with MNM free media, and subsequent staining with 100 nM PI. **C** - NIH 3T3 loaded with 0.5 µM **MNM 7**, followed by 2-hour incubation, washing with MNM free media, 16-hour clearance, and subsequent staining with 100 nM PI. All image sets collected after 30 minutes incubation after staining procedure. Overlaid channels of PI fluorescence (λ_{ex} = 543 nm, 0.2 mW; λ_{em} = 600-700 nm), and mitochondrial autofluorescence (λ_{ex} = 355 nm, 20 mW, 400 nJ per voxel; λ_{em} = 440-460 nm). All scale bars set to 20 µm.

These results show little to no internalisation upon 30 minutes of incubation (**Figure 5.13 A**). PI fluoresce is detected in the frames leading up to 600 s of UV exposure, implying a slight acceleration in necrosis onset when compared to the control sample, but not a strong enough effect to imply good level of internalisation. However, after 2 hours of incubation before washing and starting the imaging procedure (**Figure 5.13 B**) a good level of TTN reduction is observed, with PI fluorescence within the cell's nucleus being seen after 450 seconds of 355 nm UV exposure, a 25% acceleration. While not as dramatic as the 50% acceleration seen when **MNM 7** is in solution, this does imply that good levels of **MNM 7** are internalised and are able to be activated by UV exposure after washing with fresh growth media. Furthermore, the clearance experiment (**Figure 5.13 C**) show a complete return to baseline levels (TTN matching that of the control sample) after 24 hours with regular MNM free media changes. Illustrating that while **MNM 7** can passively cross the membrane of the cells under study, after a complete cell division cycle the machine is efficiently cleared from the system and had no lasting impact of cellular health. Which was further confirmed by incubation of the colony for a further three days where no impact on cell division, or overall health, was observed. For ease of interpretation **Figure 5.14** shows a comparison of the UV exposure times for the first frame on PI emission within the nucleus for each experiment.

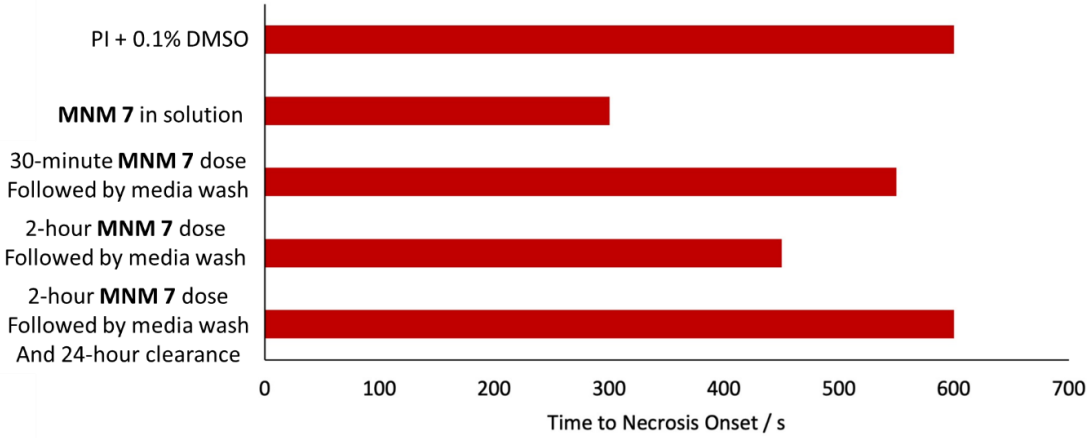

Figure 5.14 Graphical summary of TTN data obtained from 355 nm UV exposure times to first observable PI emission detected within the nucleus of studied cells for **MNM 7** internalisation studies.

Following these positive results for **MNM 7**, functionalised with two PEG based "arms", **MNM 8** (shown in **Figure 5.15**) was investigated in the same manner. This MNM consists of the same Tour MNM core structure, based upon the second-generation Feringa design, this time functionalised with the PEG addend only on one side of the molecule. Leaving the other "arm" free for further functionalisation, such as a proposed targeting peptide sequence to aid in cell specific localisation. It is hoped that the levels of internalisation of **MNM 8** will be comparable to those previously observed for **MNM 7**, without the need for multiple functionalisation sites taken up with PEG chains, allowing for future MNMs to be addended with both internalisation properties in addition to other functional groups.

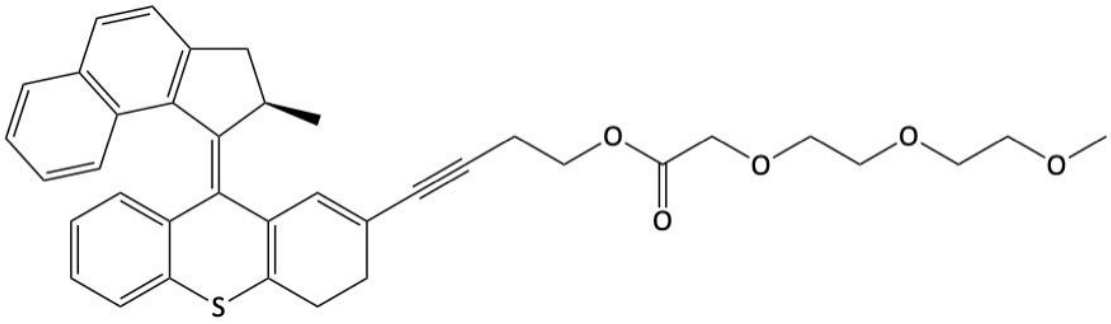

Figure 5.15 Chemical structure of **MNM 8**.

As with all previous work, when first evaluating a new MNM, initial experiments are run with 0.5 µM MNM 8 in solution and activated by 355 nm UV light. These results are then compared to both the standard MNM-free control sample as well as the previous results from work with MNM 1 to compare their ability to promote early onset necrosis. These results are shown in **Figure 5.16**.

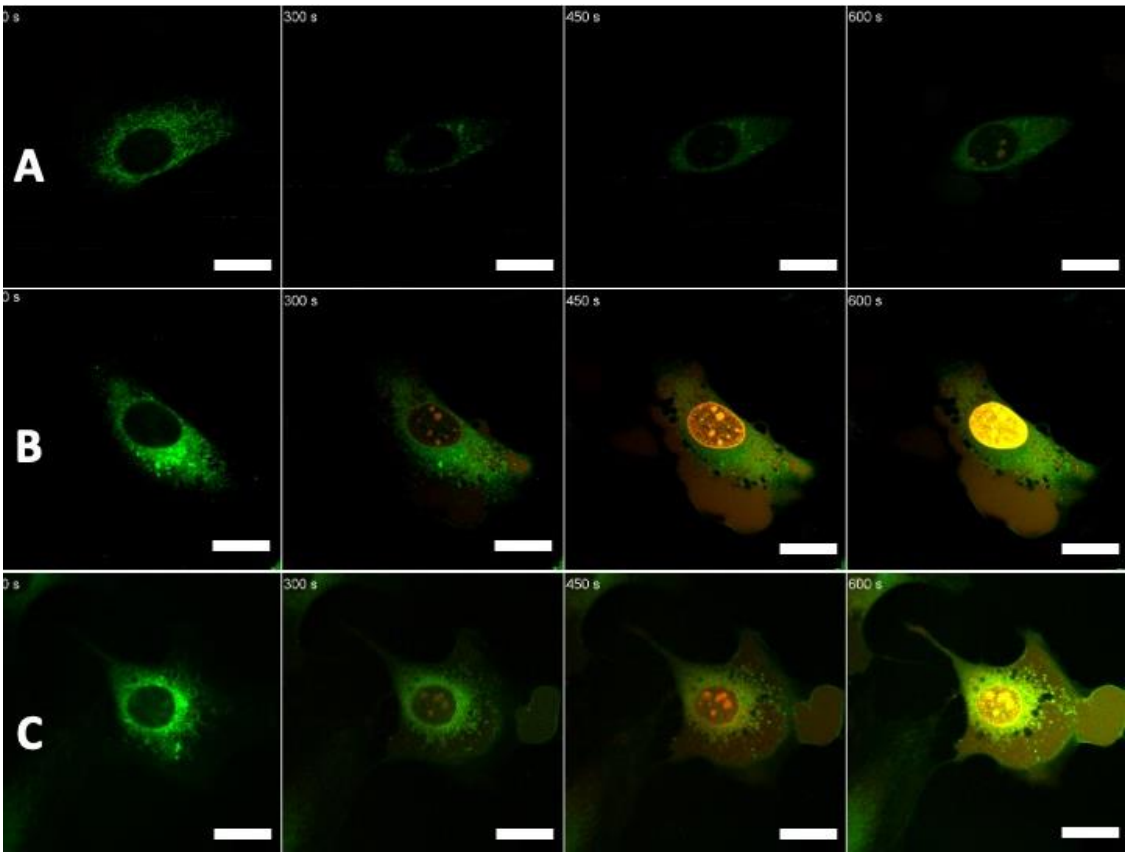

Figure 5.16 Microscopic observation of necrotic cell death caused by excitation at 355 nm (UV-exposure times are shown for each image), quantified by the observation of PI fluorescence within the nucleus. **A** – Control sample: NIH 3T3 cells loaded with 100 nM PI and 0.1% DMSO. **B** – NIH 3T3 cells loaded with 100 nM PI and 0.5 µM **MNM 1**. **C** - NIH 3T3 cells loaded with 100 nM PI and 0.5 µM **MNM 8**. All image sets collected after 30 minutes incubation after dosing procedure. Overlaid channels of PI fluorescence (λ_{ex} = 543 nm, 0.2 mW; λ_{em} = 600-700 nm), and mitochondrial autofluorescence (λ_{ex} = 355 nm, 20 mW, 400 nJ per voxel; λ_{em} = 440-460 nm). All scale bars set to 20 µm.

As expected based upon the results found for the dual arm pegylated **MNM 7**, **MNM 8** shows a necrosis acceleration remarkably close to the standard unfunctionalized **MNM 1**. Interestingly, necrosis onset does occur slightly quicker when compared with **MNM 7**. This lends credence to the previous assumption that the two pegylated arms of **MNM**

7 slightly limit the machine's ability to localise close together due to the increased molecular size, and by reducing this by only functionalising one arm in **MNM 8** a slight reduction in the measured TTN is found. This difference however is relatively small and both MNMs possess a cell killing ability, in solution, comparable with **MNM 1**. Crucially, the internalisation properties of **MNM 8** were also investigated following the same procedure as previously described to determine if one pegylation site is sufficient to promote efficient crossing of the cell membrane. These results are once again summarised in **Figure 5.17**.

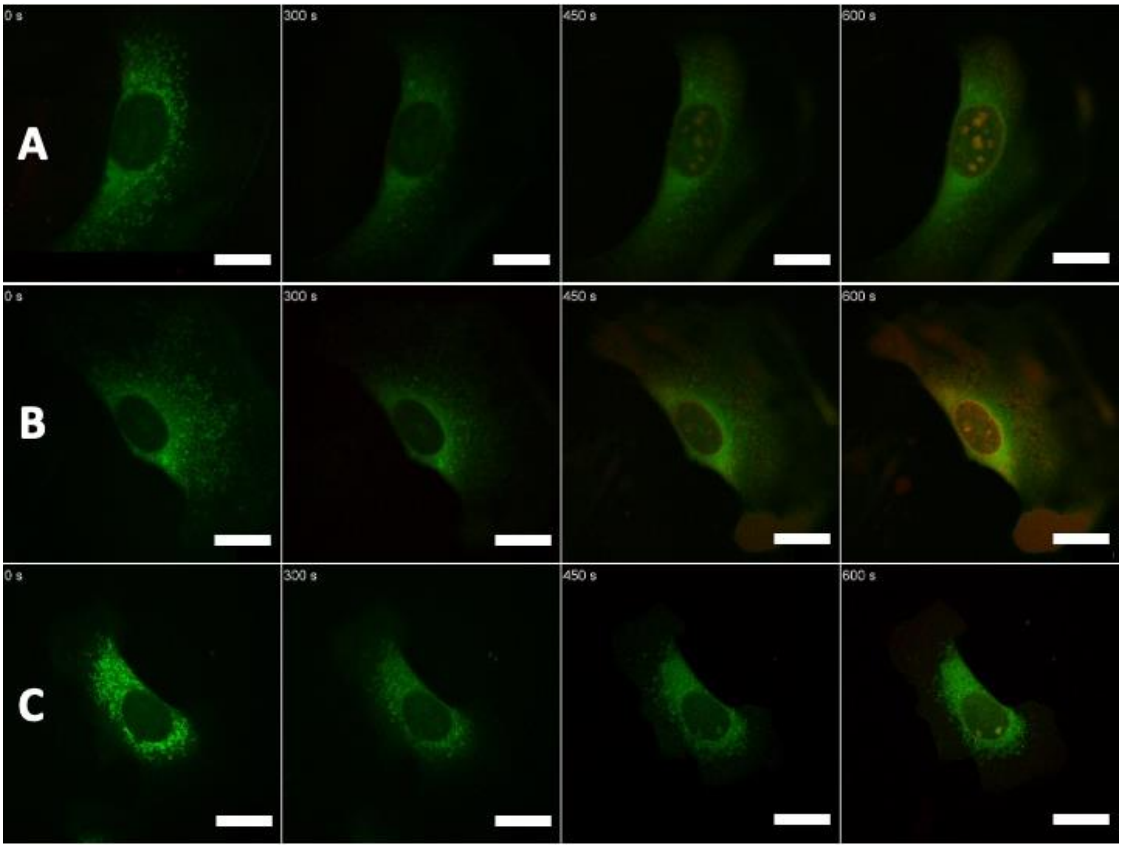

Figure 5.17 Microscopic observation of cell death caused by excitation at 355 nm (UV-exposure times are shown for each image), quantified by the observation of PI fluorescence within the nucleus. **A** – NIH 3T3 loaded with 0.5 µM **MNM 8**, followed by 30 minutes incubation and washing with MNM free media, and subsequent staining with 100 nM PI. **B** – NIH 3T3 loaded with 0.5 µM **MNM 8**, followed by 2-hour incubation and washing with MNM free media, and subsequent staining with 100 nM PI. **C** - NIH 3T3 loaded with 0.5 µM **MNM 8**, followed by 2-hour incubation, washing with MNM free media, 16-hour clearance, and subsequent staining with 100 nM PI. All image sets collected after 30 minutes incubation after staining procedure. Overlaid channels of PI fluorescence (λ_{ex} = 543 nm, 0.2 mW; λ_{em} = 600-700 nm), and mitochondrial autofluorescence (λ_{ex} = 355 nm, 20 mW, 400 nJ per voxel; λ_{em} = 440-460 nm). All scale bars set to 20 µm.

Interestingly, a greater reduction in TTN is seen with 30-minute incubation times for the one arm pegylated **MNM 8** compared to the double armed **MNM 7**, with 400 seconds and 450 seconds to first frame PI emission respectively. While this could imply greater levels of internalisation, it is also probable that this effect is again due to the ability of these smaller MNMs to localise closer together. Invoking the ability to cause greater cell damage in a smaller area, increase the rate of PI entering the cell *via* holes within the phospholipid bilayer. Reinforcing this hypothesis is the comparable times to first PI emission seen for both nanomachines upon 2-hour incubation times. However, a more rapid increase in brightness in observed for **MNM 8** leading to the possibility of an increase in perforations created in the membrane by these smaller molecules, resulting in faster PI uptake within the cell. It should be noted however, that the rate of PI channel brightness increase is not always a reliable method for investigating MNM action as this has been found to change slightly between experiments regardless of MNM procedure used.

Figure 5.18 summarises these results graphically, enabling quick comparison. As expected, based on the previous work with **MNM 7**, **MNM 8** rapidly clears from the cell upon incubation in MNM free media (**Figure 5.17 C**). Resulting in a return to necrosis onset times indeclinable from the control sample, having never been exposed to MNMs.

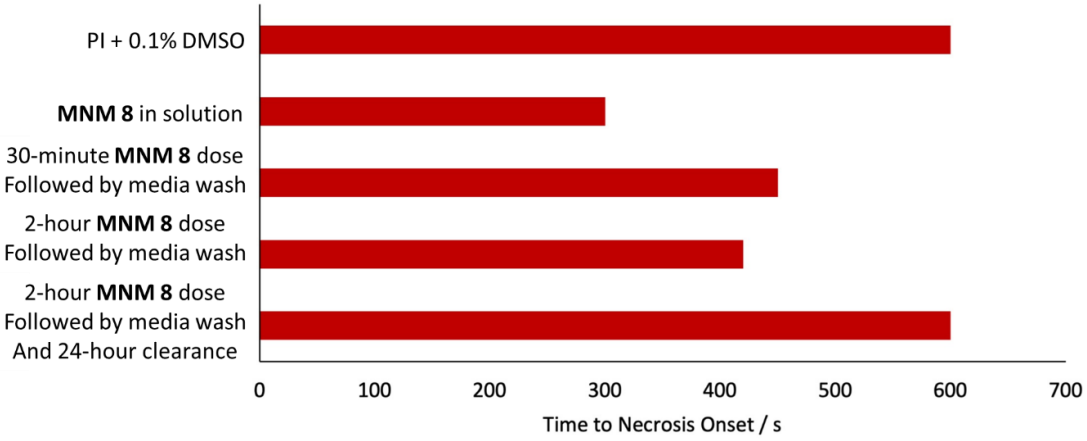

Figure 5.18 Graphical summary of TTN data obtained from 355 nm UV exposure times to first observable PI emission detected within the nucleus of studied cells for **MNM 8** internalisation studies.

Overall, these results for **MNM 8** are incredibly positive and show little difference with the dual arm pegylated **MNM 7**. Implying that only a single functionalised arm is required to enable effective passive crossing of the cell membrane, and that once internalised these MNMs can still be "switched on" by exposing the sample to 355 nm UV laser light. Interestingly, it is seen that the smaller molecular size and weight of the single pegylated compound may enable slightly faster necrosis onset times. Hypothesised to be due to their ability to localise closer together once inside the cell, or membrane, resulting in greater localised mechanical damage and thus faster introduction of PI stain to the nucleus. These exciting results enable further work to continue the possibility of dual functionalised MNMs with one internalising arm and one functionalised with a cell specific recognition peptide. An illustrative example of this is given in

.

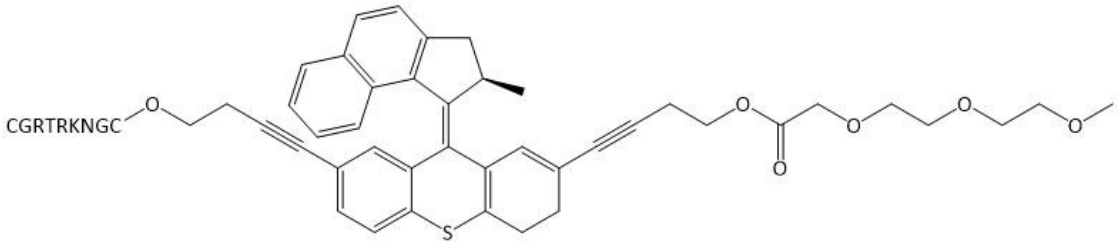

Figure 5.19 Chemical structure of **MNM 8** with additional functionalisation containing a truncated from of Lyp-1 (CGNKRTRGC), a cyclic 9-amino acid long peptide sequence known for targeting breast carcinoma.[41]

5.3 Two-photon 710 nm NIR activation studies of PEG functionalised MNMs

Following on from the extensive troubleshooting, and optimisation, of the new multiphoton laser scanning confocal microscopy set up explored in Chapter 4. The previously examined pegylated MNMs could be thoroughly reinvestigated with 710 nm NIR multiphoton activation. The aims of which being two-fold; firstly, to establish if functionalised MNM can be effetely, and consistently, activated using 2PA and secondly, to work towards future cancer therapeutics combining both the internalisation ability of synthetically modified MNMs alongside the more biologically favourable activation methods awarded by the instrumentational changes of a 2PA set up.

Using an identical systematic approach, to the single-photon work previously displayed, initial investigations of the 2PA of dual pegylated **MNM 7** compare the TTN for samples of NIH 3T3 dosed with the nanomachine in solution and exposed to highly pulsed 710 nm laser light, with both **MNM 1** and the control sample under identical conditions. It should be noted here that for all two-photon work the concentration of added MNM is raised from 0.5 to 1 μM to compensate for the lower probability of a two-photon

excitation event. However, the concentration of DMSO was always ensured to be no greater than 0.1% v/v. The results of these first three experiments are shown in **Figure 5.20**.

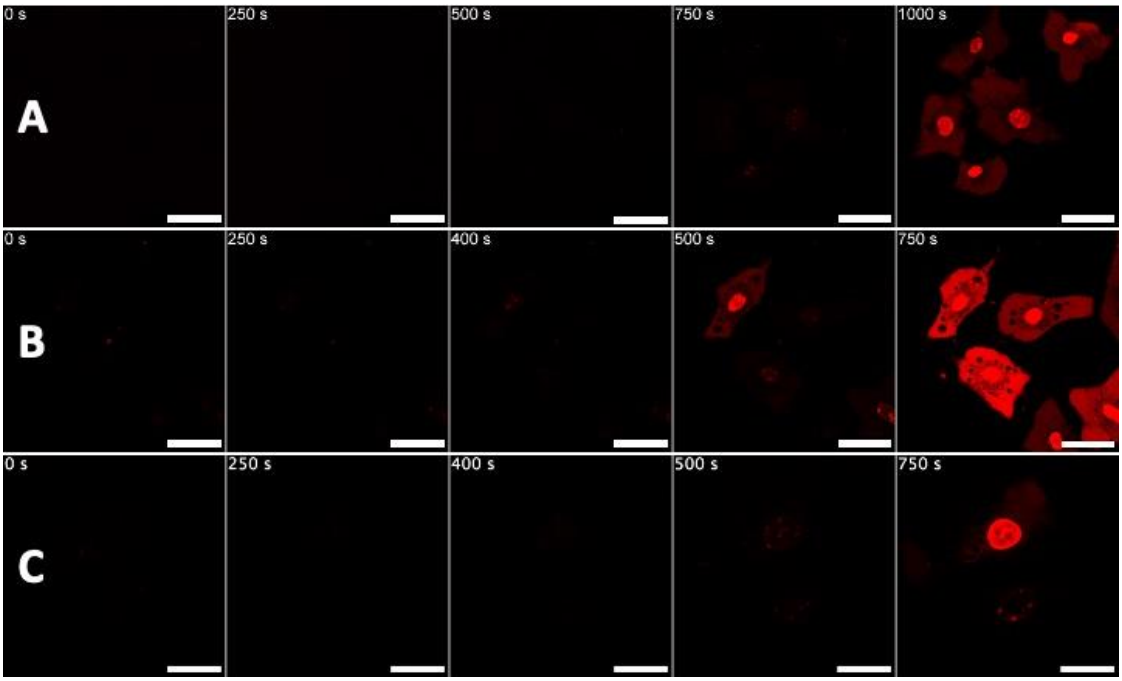

Figure 5.20 Microscopic observation of cell death caused by excitation at 710 nm (NIR-exposure times are shown for each image), quantified by the observation of PI fluorescence within the nucleus. **A** – Control sample: NIH 3T3 cells loaded with 100 nM PI and 0.1% DMSO. **B** – NIH 3T3 cells loaded with 100 nM PI and 1 µM **MNM 1**. C – NIH 3T3 cells loaded with 100 nM PI and 1 µM **MNM 7**. All image sets collected after 30 minutes incubation after dosing procedure. Red channel showing detection of PI fluorescence (λ_{ex} = 543 nm, 0.2 mW; λ_{em} = 600-700 nm). All scale bars set to 25 µm.

These results show remarkable adherence to the previously analysed single-photon activation work. **MNM 7** demonstrates a good ability to accelerate the onset of necrosis when compared to the control sample, showing first frame PI emission within the nucleus at 500 s compared with 750 s - a 33% reduction in TTN. Similar to the observations made during the single-photon UV experiments this acceleration of

necrosis is slightly less than the smaller, unfunctionalized, **MNM 1.** Which was able to cause the first signs of necrosis at 400 s, resulting in a 47% acceleration. This is again able to be rationalised by the smaller molecular weight and size of the unfunctionalized form.

The previous internalisation experiments were also repeated using this new multiphoton activation procedure. The results of which are summarised by the fluorescent microscopy images reported in **Figure 5.21**.

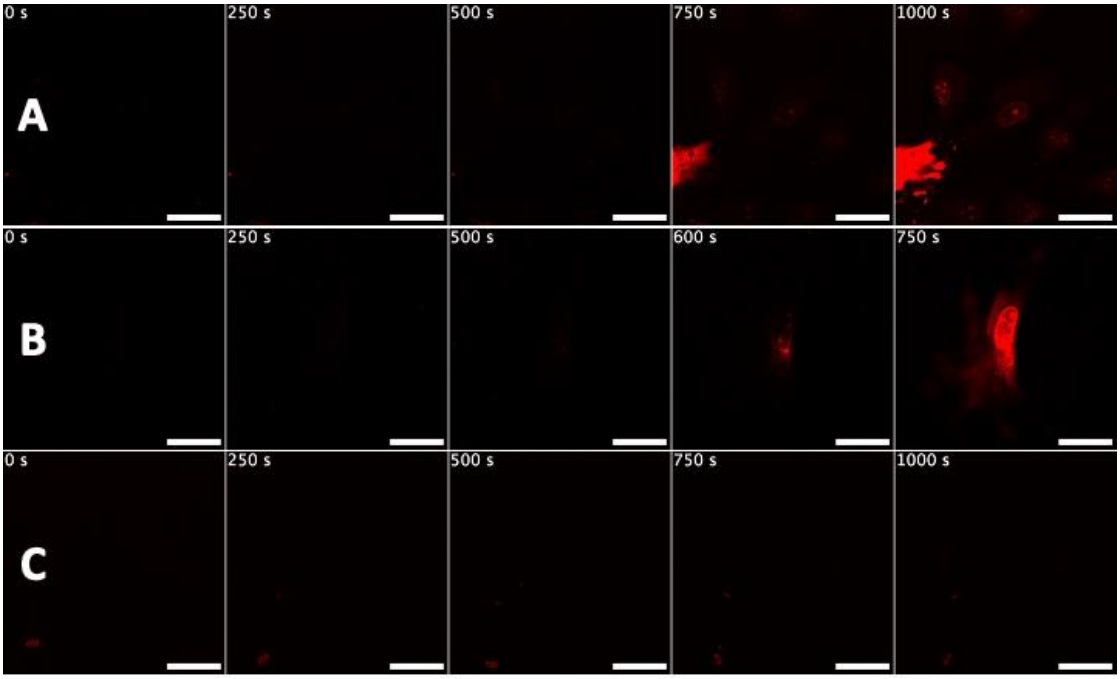

Figure 5.21 Microscopic observation of cell death caused by excitation at 710 nm (NIR-exposure times are shown for each image), quantified by the observation of PI fluorescence within the nucleus. **A** – NIH 3T3 loaded with 1 µM **MNM 7**, followed by 30 minutes incubation and washing with MNM free media, and subsequent staining with 100 nM PI. **B** – NIH 3T3 loaded with 1 µM **MNM 7**, followed by 2-hour incubation and washing with MNM free media, and subsequent staining with 100 nM PI. **C** - NIH 3T3 loaded with 1 µM **MNM 7**, followed by 2-hour incubation, washing with MNM free media, 16-hour clearance, and subsequent staining with 100 nM PI. All image sets collected after 30 minutes incubation after dosing procedure. Red channel showing detection of PI fluorescence (λ_{ex} = 543 nm, 0.2 mW; λ_{em} = 600-700 nm). All scale bars set to 25 µm.

As expected, these procedures saw comparable results with the equivalent single-photon activation work reported earlier in the chapter. Short incubation times of 30 minutes saw small amount of MNM 7 internalisation, resulting in relatively minor

necrosis acceleration, with longer 2-hour incubations causing significantly greater amounts of internalised MNM and shorter TTN. With no measurable negative impact on cell health after being left to clear from the system for one cell division cycle. Interestingly, it appears that early onset necrosis is more easily triggered by 2PA with the relatively small amount of taken up MNM after 30-minutes of incubation when compared with the equivalent single photon experiment. This may suggest that the longer wavelength 710 nm NIR light is better at penetrating the cell sample and activating the dosed MNM from within. As with previous experiments, this measured TTN data is summarised graphically in **Figure 5.22**.

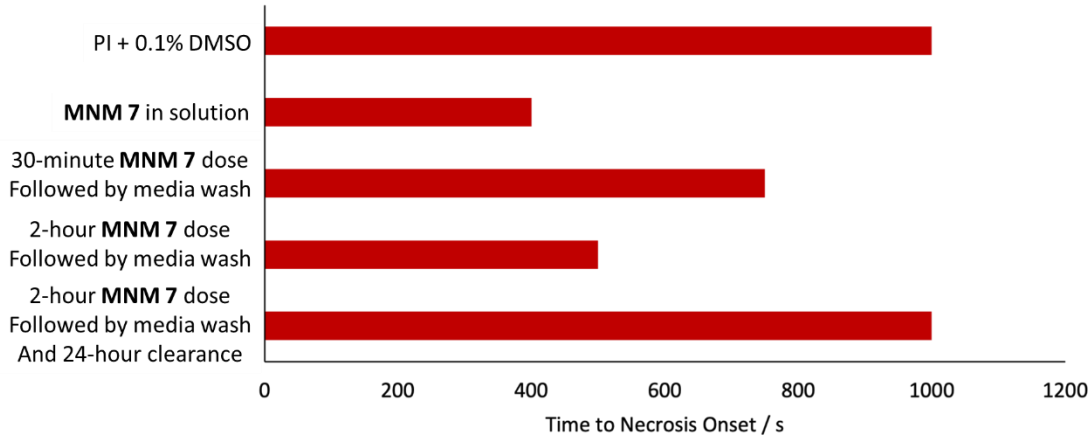

Figure 5.22 Graphical summary of TTN data obtained from 710 nm NIR two-photon exposure times to first observable PI emission detected within the nucleus of studied cells for **MNM 7** internalisation studies.

Having confirmed that PEG functionalised MNMs can not only be non-linearly activated by highly pulsed 710 nm NIR light, but that this process can be initiated from within the cell studied, work now turns to repeating this experimental procedure for the mono-pegylated **MNM 8.** In the same manner as with the single photon UV investigation, the

following images (**Figure 5.23**) again compare this MNM with both its unfunctionalised form as well as a blank control sample.

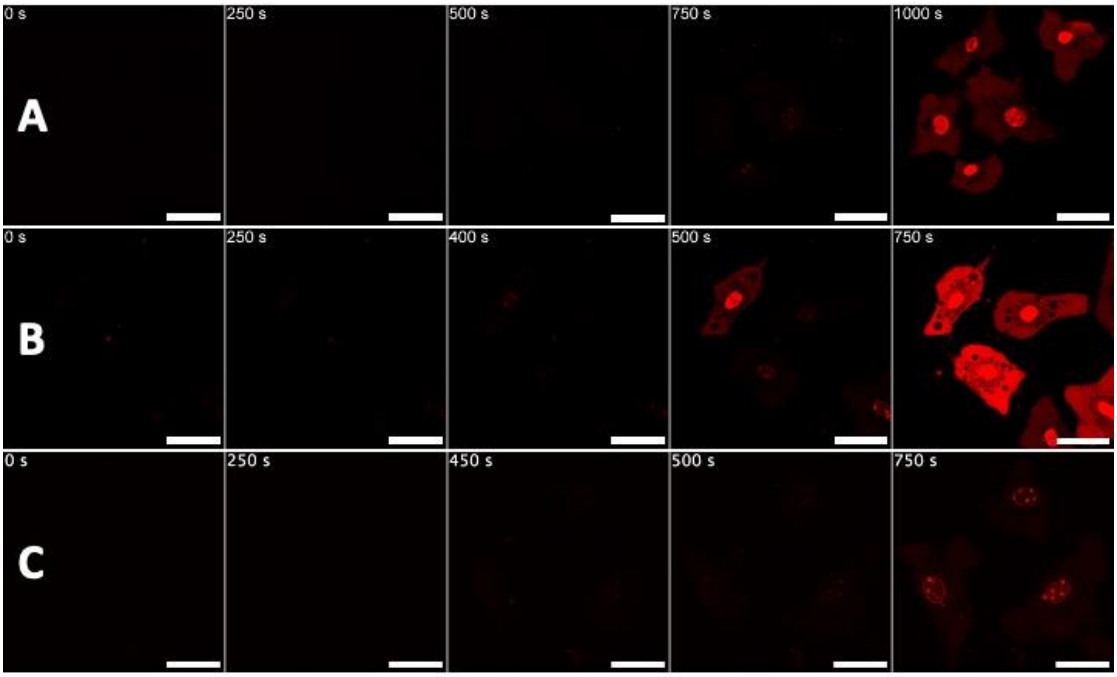

Figure 5.23 Microscopic observation of cell death caused by excitation at 710 nm (NIR-exposure times are shown for each image), quantified by the observation of PI fluorescence within the nucleus. **A** – Control sample: NIH 3T3 cells loaded with 100 nM PI and 0.1% DMSO. **B** – NIH 3T3 cells loaded with 100 nM PI and 1 µM **MNM 1**. C – NIH 3T3 cells loaded with 100 nM PI and 1 µM **MNM 8**. All image sets collected after 30 minutes incubation after dosing procedure. Red channel showing detection of PI fluorescence (λ_{ex} = 543 nm, 0.2 mW; λ_{em} = 600-700 nm). All scale bars set to 25 µm.

Again, great adherence to the chapters hypothesis, and to previous results, is illustrated. In much the same fashion as the single photon work with mono-pegylated **MNM 8**, necrosis is induced at an increased rate when compared to a sample containing no added MNM. Similar to the same 2PA experiment carried out with unfunctionalised **MNM 1**. However, it can also be seen that this acceleration on necrosis onset is slightly slower than the same experiment carried out with MNM 7 (**Figure 5.20 C**). The inverse

of the trend seen for the equivalent single photon work, where the less functionalised MNM was able to induce necrosis at a slightly faster rate than its bulkier counterpart. This may be rationalised by considering the possibility that the mono-pegylated **MNM 8** could have a lower multiphoton cross-section than the dual-pegylated **MNM 7**. The difficulty in measuring 2PE cross-sections of MNMs prevents this being confirmed, as part of this project, but does provide an interesting avenue for further research.

As with previous single- and two-photon experimentation internalisation studies were also completed using 710 nm light to activate **MNM 8**. These resulted are summarised below in **Figure 5.24**.

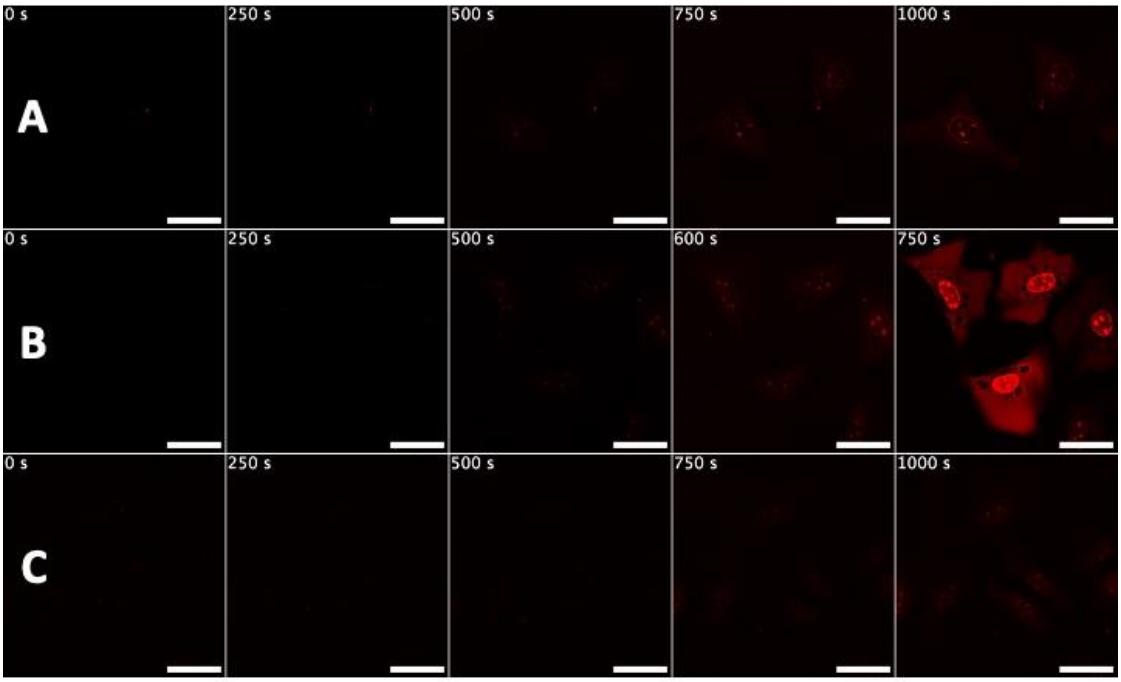

Figure 5.24 Microscopic observation of cell death caused by excitation at 710 nm (NIR-exposure times are shown for each image), quantified by the observation of PI fluorescence within the nucleus. **A** – NIH 3T3 loaded with 1 µM **MNM 8**, followed by 30 minutes incubation and washing with MNM free media, and subsequent staining with 100 nM PI. **B** – NIH 3T3 loaded with 1 µM **MNM 8**, followed by 2-hour incubation and washing with MNM free media, and subsequent staining with 100 nM PI. **C** - NIH 3T3 loaded with 1 µM **MNM 8**, followed by 2-hour incubation, washing with MNM free media, 16-hour clearance, and subsequent staining with 100 nM PI. All image sets collected after 30 minutes incubation after dosing procedure. Red channel showing detection of PI fluorescence (λ_{ex} = 543 nm, 0.2 mW; λ_{em} = 600-700 nm). All scale bars set to 25 µm.

When comparing these experiments (results summarised in **Figure 5.25**) to the results acquired from the 2PA of **MNM 7**, good levels of internalisation are maintained with only one pegylated "arm", compounding the results found when studying single-photon activation. Interestingly, the proposal that **MNM 8** may have a lower 2PCS than **MNM 7**

appears to hold true during these investigations. Great levels of internalisation are seen, with 2-hour incubation times being enough to induce first PI emission at exposure times comparable to experiments where **MNM 8** is free in solution, however the measured TTN is still longer than the corresponding experiments with dual-pegylated MNM 7. Implying that **MNM 8** is not as efficiently activated with 710 nm NIR 2PA.

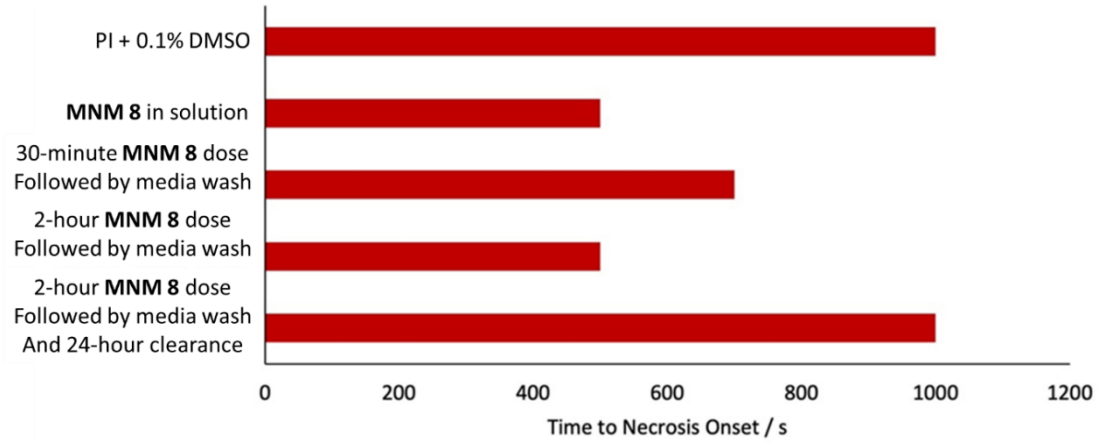

Figure 5.25 Graphical summary of TTN data obtained from 710 nm NIR two-photon exposure times to first observable PI emission detected within the nucleus of studied cells for **MNM 8** internalisation studies.

5.4 Single-photon 355 nm UV activation studies of triphenylphosphine functionalised MNMs

PEG functionalisation is an exciting avenue for MNM research, showing great internalisation properties as well as the ability to be effectively activated with 710 nm NIR 2PA. Showing great potential to further the goal of producing cell specific treatment methods. However, the possibility of these compounds only being localised within the cellular membrane and not fully crossing into the internal space of the sample, reduce the likelihood of being able to induce apoptosis and other cleaner mechanisms of cell death compared to necrosis – the overarching goal of the work presenting in this

chapter. For this reason, TPP+ functionalisation is explored by following a similar experimental procedure in the following section. Utilising a functional group not only shown to passively cross cellular membranes, but also being able to localise at specific area within the cell – in this case the mitochondrial envelope – opens the possibility of a brief activation window within the cell, leading to internal structural damage without affecting the phospholipid bilayer, resulting in possible induction of PCD pathways.

MNM 9 (shown again in **Figure 5.26**) is a "one-armed" TPP+ functionalised nanomachine with a bromide counterion, connected to the MNM core structure *via* a triazole linker. Using this same systematic procedure as seen for all previous single- and two-photon internalisation studies of PEG functionalised MNMs, the first round of investigation focuses on using 355 nm UV excitation to activate the rotary mechanism. To determine if this MNM is able to induce early onset necrosis when the rotor is activated by 355 nm light.

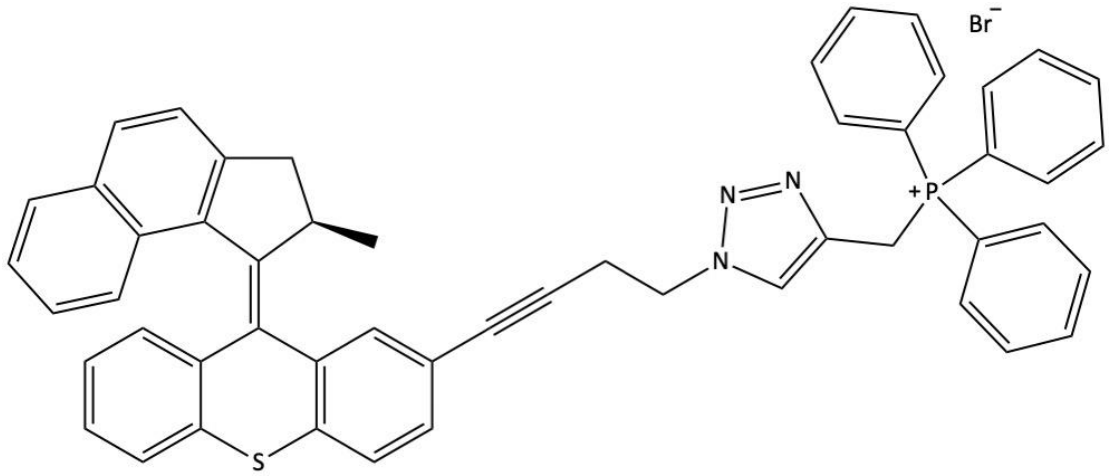

Figure 5.26 Chemical structure of **MNM 9**.

Initially **MNM 9** is held within solution and compared to both its unfunctionalised analogue, **MNM 1**, as well as the control sample dosed with no MNM. These results are summarised by the microscopy images presented in **Figure 5.27**.

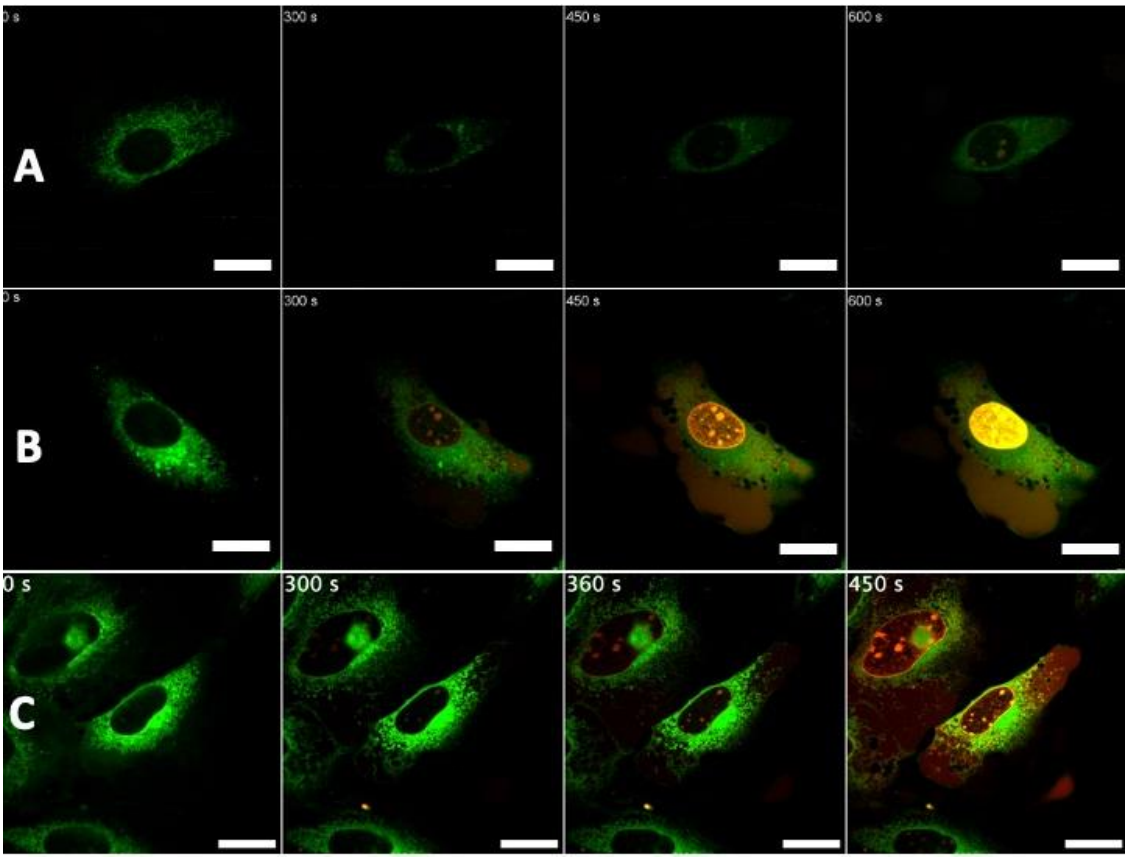

Figure 5.27 Microscopic observation of necrotic cell death caused by excitation at 355 nm (UV-exposure times are shown for each image), quantified by the observation of PI fluorescence within the nucleus. **A** – Control sample: NIH 3T3 cells loaded with 100 nM PI and 0.1% DMSO. **B** – NIH 3T3 cells loaded with 100 nM PI and 0.5 µM **MNM 1**. **C** - NIH 3T3 cells loaded with 100 nM PI and 0.5 µM **MNM 9**. All image sets collected after 30 minutes incubation after dosing procedure. Overlaid channels of PI fluorescence (λ_{ex} = 543 nm, 0.2 mW; λ_{em} = 600-700 nm), and mitochondrial autofluorescence (λ_{ex} = 355 nm, 20 mW, 400 nJ per voxel; λ_{em} = 440-460 nm). All scale bars set to 20 µm.

As expected, **MNM 9** maintains the ability of all other investigated Tour style MNMs to promote the early onset of necrotic cell death when dosed in solution. Showing a great ~50% reduction in TTN with single-photon UV activation of the rotor, when compared to the blank sample, an equivalent acceleration to experiments containing samples

containing **MNM 1**. Interestingly, immediately apparent visual changes in the 355 nm induced mitochondrial autofluorescence are observed when dosed with TPP+ containing nanomachines - illustrated by a direct comparison in **Figure 5.28**.

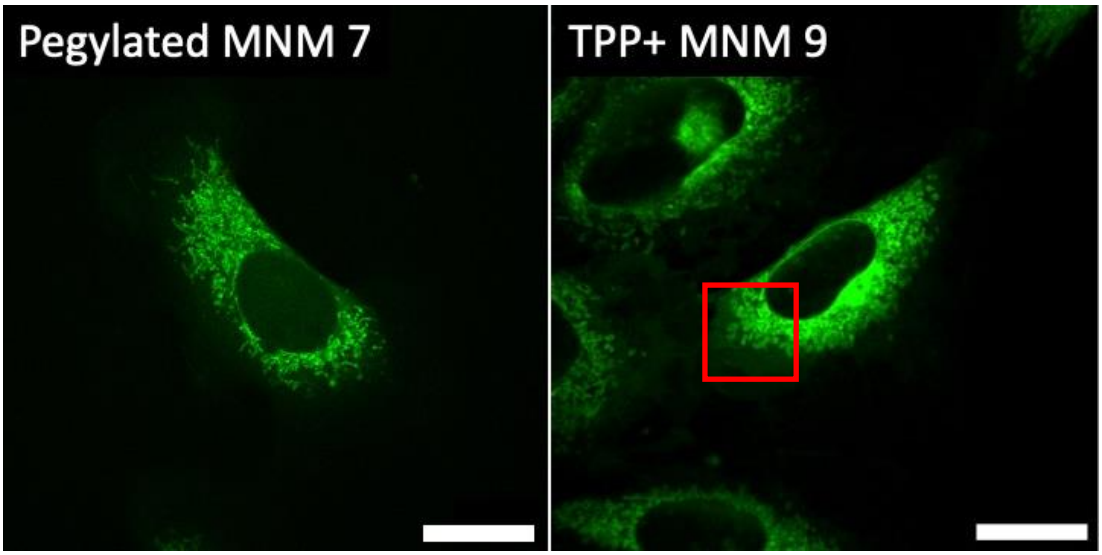

Figure 5.28 Comparison of mitochondrial autofluorescence profile (λ_{ex} = 355 nm, 20 mW, 400 nJ per voxel; λ_{em} = 440-460 nm) for NIH 3T3 cells dosed with 0.5 µM PEG functionalised **MNM 7** (left) and 0.5 µM TPP+ functionalised **MNM 9** (right, red box highlights stark difference in mitochonridal network appearence). Scale bars 20 µm.

When incubated with 0.5 µM of PEG functionalised, internalising, **MNM 7** the mitochondrial network appears relatively unchanged and very similar to that seen for NIH 3T3 samples with no MNM in solution. The network shows uniform brightness across the entire cell, and long string-like structures of mitochondria are nicely order throughout the sample. When dosed with 0.5 µM of the TPP+ functionalised **MNM 9** dramatic alterations are observed, highlighted in red. Instead of the expected string-like network, the mitochondria appear balled into circles, as well as seeming to appear to be held closer to the nucleus of the cell as opposed to being evenly distributed throughout the cytoplasm. This may indicate that the hypothesis of TPP+ functionalised MNMs

being able to localise within the mitochondrial envelope is correct, bolstering the search for an MNM based therapy that can preferentially induce PCD pathways. Crucially, this observed effect on the mitochondria appears to have no adverse effect on the viability of the cells under study. With samples being maintain for several division cycles after **MNM 9** exposure. This fact is reinforced by the following work on the internalisation properties of TPP+ MNMs, with cellular clearance experiments being run for each analogue.

An investigation into the ability of **MNM 9** to cross the cellular membrane, and possibly localise within the mitochondria, is carried out using the same procedures as the previously presented work with PEG functionalised **MNMs 7** and **8**. **Figure 5.29** shows these results for the 30-minute incubation, 2-hour incubation, and clearance experiments.

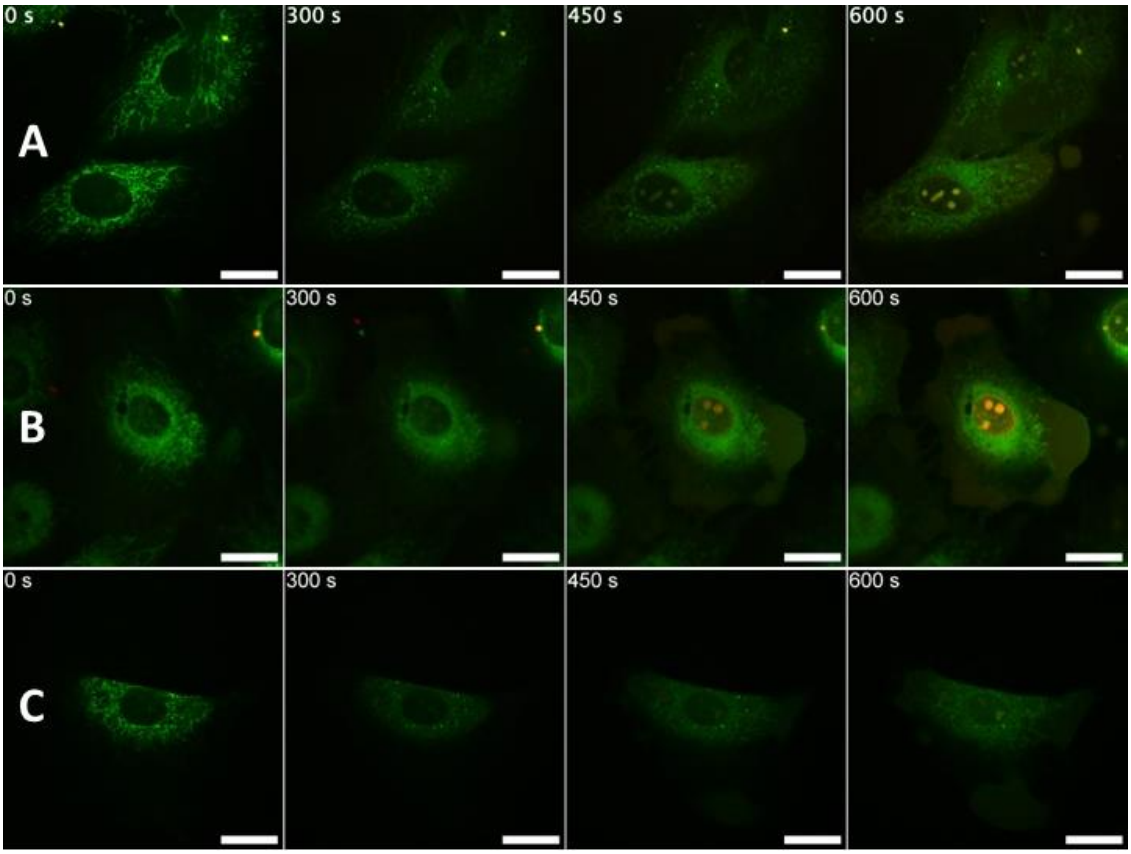

Figure 5.29 Microscopic observation of cell death caused by excitation at 355 nm (UV-exposure times are shown for each image), quantified by the observation of PI fluorescence within the nucleus. **A** – NIH 3T3 loaded with 0.5 µM **MNM 9**, followed by 30 minutes incubation and washing with MNM free media, and subsequent staining with 100 nM PI. **B** – NIH 3T3 loaded with 0.5 µM **MNM 9**, followed by 2-hour incubation and washing with MNM free media, and subsequent staining with 100 nM PI. **C** - NIH 3T3 loaded with 0.5 µM **MNM 9**, followed by 2-hour incubation, washing with MNM free media, 16-hour clearance, and subsequent staining with 100 nM PI. All image sets collected after 30 minutes incubation after staining procedure. Overlaid channels of PI fluorescence (λ_{ex} = 543 nm, 0.2 mW; λ_{em} = 600-700 nm), and mitochondrial autofluorescence (λ_{ex} = 355 nm, 20 mW, 400 nJ per voxel; λ_{em} = 440-460 nm). All scale bars set to 20 µm.

This collection of internalisation studies presents several promising results. It is shown that TPP+ functionalisation can promote internalisation of the functionalised MNM in much the same way as the previously investigated PEG based functionalisations. Necrotic acceleration is observed with incubations times as short as 30 minutes, with TNN reduction approaching the same as that found with **MNM 9** in solution when incubated for 2 hours before commencing the imaging procedure. Importantly, great cellular clearance is shown when left for 24 hours, after 2 hours on incubation with **MNM 9**, coupled with regular media changes with no added MNM. Elevating one of the main concerns with TPP+ functionalisation over the previously established pegylation; that the ability of TPP+ to localise at the mitochondrial membrane would prevent the NIH 3T3 cells from effectively removing the functionalised MNM from the internals of the cell. This does not seem to be a concern as the onset of necrosis appears to return to pre-MNM incubation levels after being left for 24 hours without **MNM 9** in solution.

As for previous MNM internalisation experimental series, **Figure 5.30** is presented to summarise the TTN data shown in the previous live-cell fluorescence microscopy images for easier comparison.

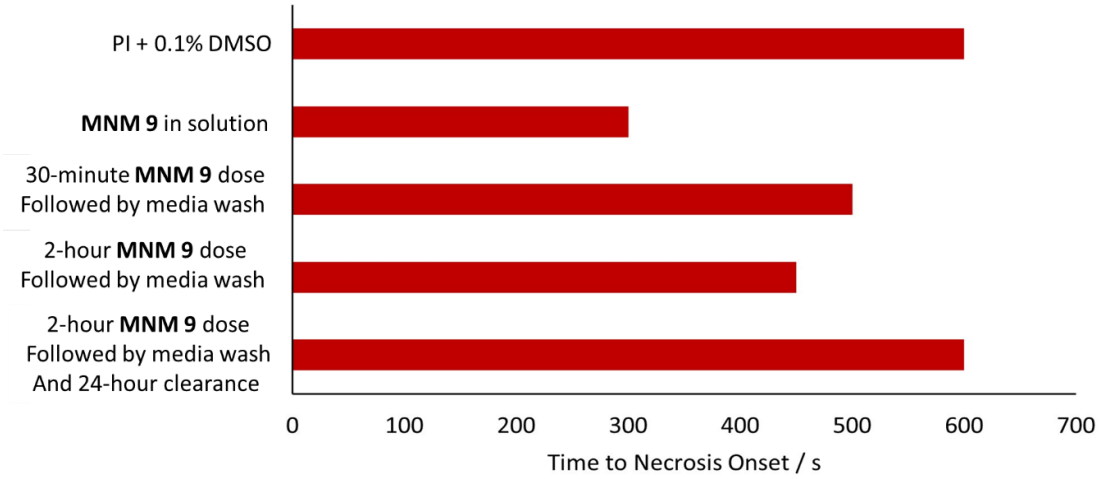

Figure 5.30 Graphical summary of TTN data obtained from 355 nm UV exposure times to first observable PI emission detected within the nucleus of studied cells for **MNM 9** internalisation studies.

MNM 10, shown in **Figure 5.31**, is an alternate analogue of a, "one-armed", TPP+ functionalised, nanomachine. Containing an iodide counterion in place of the previously tested bromide and coupled directly to the carbon chain instead of *via* the previously presented triazole connector.

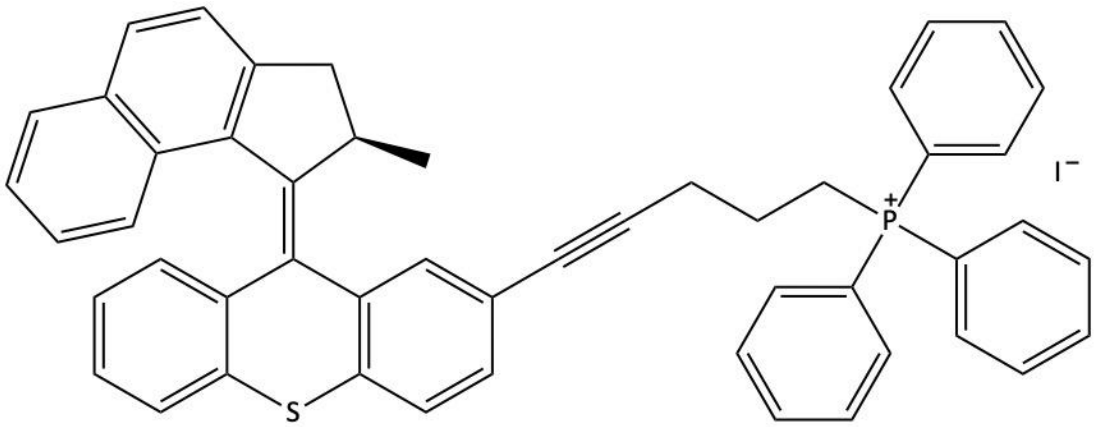

Figure 5.31 Chemical structure of **MNM 10**.

As with all previous investigations, initial live-cell fluorescence microscopy work was carried out with **MNM 10** in solution to be compared to **MNM 1** and the blank 0.1%

DMSO v/v control sample. To verify that this MNM analogue is able to be activated by 355 nm UV laser exposure, and that this rotation is efficient enough to cause sufficient mechanical damage to the cells membrane and promote early onset necrosis. While halides are wildly regarded as relatively non-toxic, with the most pressing concern of Br^- and I^- exposure being the leaching of naturally occurring Cl^- from the body, it was important to assess any difference in cell viability between the two TPP+ analogues.[42] However, it was predicted that little difference would be seen and both **MNM 9** and **10** would be good candidates going forward. **Figure 5.32** once again shows a summary of the microscopy images acquired during this experimentation.

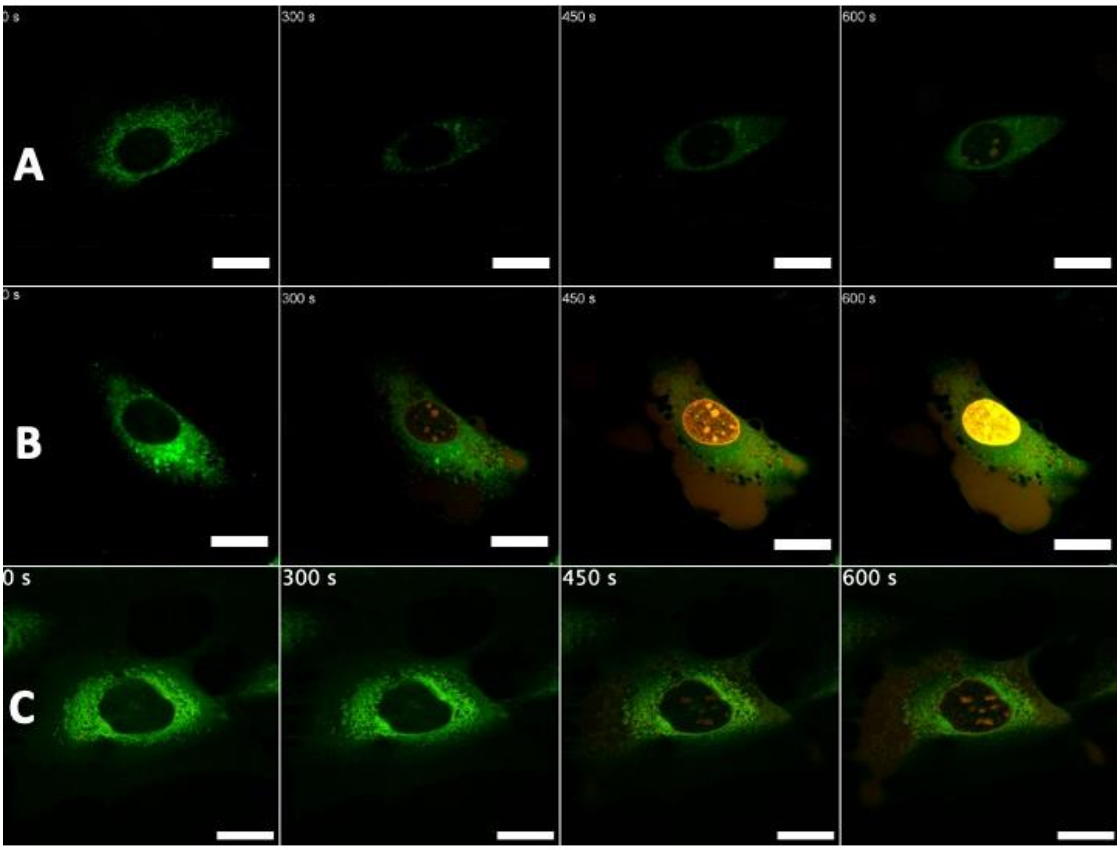

Figure 5.32 Microscopic observation of necrotic cell death caused by excitation at 355 nm (UV-exposure times are shown for each image), quantified by the observation of PI fluorescence within the nucleus. **A** – Control sample: NIH 3T3 cells loaded with 100 nM PI and 0.1% DMSO. **B** – NIH 3T3 cells loaded with 100 nM PI and 0.5 µM **MNM 1**. **C** - NIH 3T3 cells loaded with 100 nM PI and 0.5 µM **MNM 10**. All image sets collected after 30 minutes incubation after dosing procedure. Overlaid channels of PI fluorescence (λ_{ex} = 543 nm, 0.2 mW; λ_{em} = 600-700 nm), and mitochondrial autofluorescence (λ_{ex} = 355 nm, 20 mW, 400 nJ per voxel; λ_{em} = 440-460 nm). All scale bars set to 20 µm.

Interestingly, while the first signs of necrosis are observed at a comparable time to **MNM 1** and all previously investigated MNMs. Less emission, of both channels, is seen within the cell's nucleus. While other necrotic signs, such as PI within the cytoplasm and

blebbing of the cellular membrane, are indistinguishable from other experiments. This may imply that as any internalised MNM is bound to the mitochondria the majority of the internal cellular damage is localised here, and less mechanical stress is placed on the nucleus itself – even after holes are created within the outer membrane. If this is indeed the case, this MNM would make a promising candidate for further evaluation as a means of inducing cleaner PCD pathways. Provided that the internalisation properties are in line with the previously examined TPP+ functionalised **MNM 9**.

It should be noted again that the mitochondrial network exhibited similar structural changes when the sample was dosed with **MNM 10** as seen in previous **MNM 9** investigations. Further confirming the likelihood that these analogues are indeed attracted to the mitochondrial envelope. This comparison is shown in **Figure 5.33**. Like the previous work with MNM 9, no short-term impact on cellular health was observed, and this will be further examined during the following internalisation procedures.

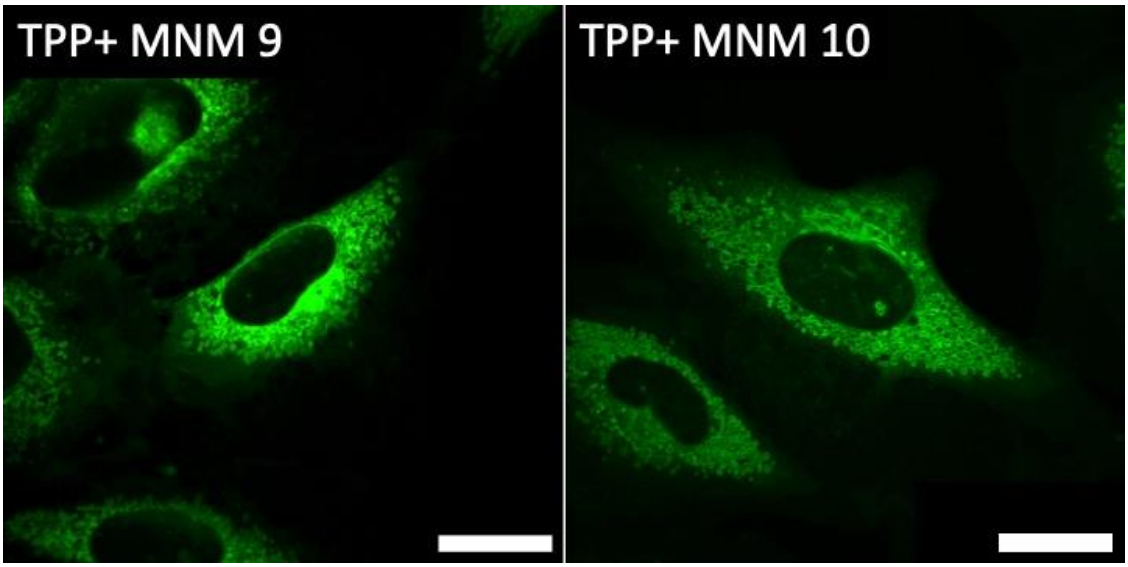

Figure 5.33 Comparison of mitochondrial autofluorescence profile (λ_{ex} = 355 nm, 20 mW, 400 nJ per voxel; λ_{em} = 440-460 nm) for NIH 3T3 cells dosed with 0.5 µM **MNM 9** (left) and 0.5 µM **MNM 10** (right). Scale bars 20 µm.

To ensure **MNM 10** was a viable candidate for further study as an internalising nanomachine capable of both crossing the outer cell membrane and localising at the mitochondria. In the hope that this analogue may aid in the development of an MNM based treatment to trigger apoptosis. The previously well documented series of internalisation procedures were ran with single-photon UV excitation and analysed using live-cell fluorescent microscopy. These results are, once again, summarised in **Figure 5.34**.

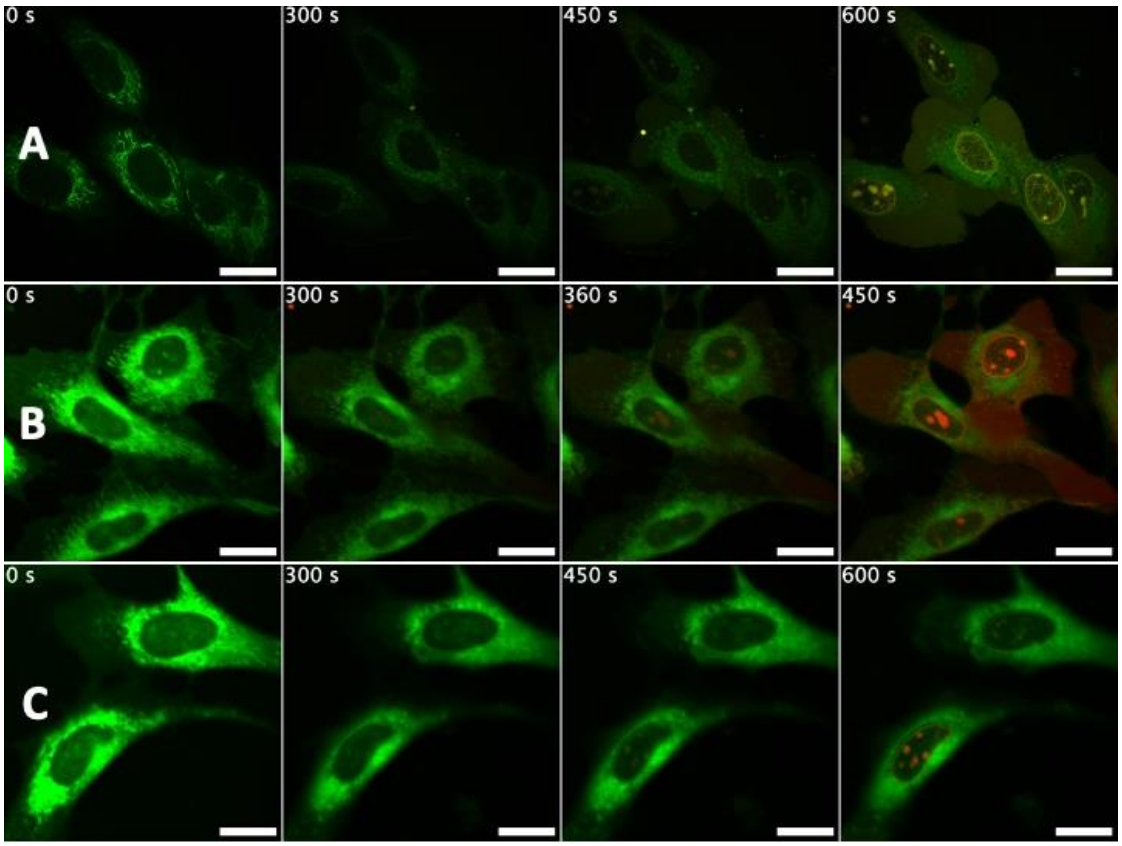

Figure 5.34 Microscopic observation of cell death caused by excitation at 355 nm (UV-exposure times are shown for each image), quantified by the observation of PI fluorescence within the nucleus. **A** – NIH 3T3 loaded with 0.5 µM **MNM 10**, followed by 30 minutes incubation and washing with MNM free media, and subsequent staining with 100 nM PI. **B** – NIH 3T3 loaded with 0.5 µM **MNM 10**, followed by 2-hour incubation and washing with MNM free media, and subsequent staining with 100 nM PI. **C** - NIH 3T3 loaded with 0.5 µM **MNM 10**, followed by 2-hour incubation, washing with MNM free media, 16-hour clearance, and subsequent staining with 100 nM PI. All image sets collected after 30 minutes incubation after staining procedure. Overlaid channels of PI fluorescence (λ_{ex} = 543 nm, 0.2 mW; λ_{em} = 600-700 nm), and mitochondrial autofluorescence (λ_{ex} = 355 nm, 20 mW, 400 nJ per voxel; λ_{em} = 440-460 nm). All scale bars set to 20 µm.

While good internalisation, and promotion of early onset necrosis, is shown for 2-hour incubation periods of **MNM 10** (with all experiments summarised graphically in **Figure 5.35**) - similar to the previously evaluated **MNM 9**. The most important feature to note from these experiments is the slight acceleration of necrosis onset for the 24-hour clearance procedure (**Figure 5.34 C**). While not dramatic, a minor increase in PI brightness seen within the cell after 600 s of 355 nm UV exposure may suggest incomplete clearance of the nanomachine from the system, or a small adverse effect on overall cellular health. However, cellular samples loaded with **MNM 10** were grown for a further three division cycles without any apparent impact on growth rate or morphology and as such any possible impact is deemed to be negligible.

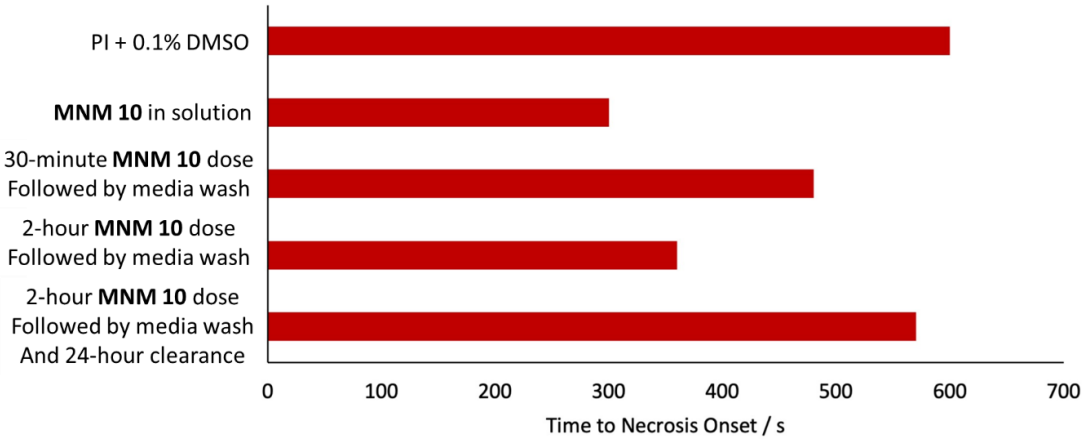

Figure 5.35 Graphical summary of TTN data obtained from 355 nm UV exposure times to first observable PI emission detected within the nucleus of studied cells for **MNM 10** internalisation studies.

Both evaluated TPP+ functionalised MNMs showed great ability to be activated by the linear 355 nm UV process, and disrupt the cell membrane, resulting in early onset necrosis in samples of NIH 3T3 cells. In addition, impressive levels of internalisation were seen with incubation times as short as 2-hours – similar to the previously studied

pegylated **MNMs 7** and **8**. Importantly, morphological changes in the structure of the mitochondrial network appear to bolster the prediction that MNMs addended with TPP+ containing groups are able to localise at the mitochondrial membrane. This may allow for this style of nanomachine to be further evaluated for the ability to induce cleaner route of cell death, when coupled with changes in rotor activation procedure. Before this is explored, further testing of **MNM 10** is carried out, assessing its ability to be activated by 710 nm NIR two-photon excitation.

5.5 Two-photon 710 nm NIR activation studies of triphenylphosphine functionalised MNM 10

Investigations into the two-photon activation of MNMs functionalised with TPP+ containing groups were carried out on **MNM 10**. In part due to the apparent slightly faster internalisation after 30-minute incubation times, but also due to significant practical considerations. Namely, having greater amounts of **MNM 10** in stock compared to the relatively small amount of **MNM 9**, eliminating the need for any addition synthesis. As well as possible biological contamination of previously diluted samples of **MNM 9** leading to non-reliable microscopy results for necrosis onset.

As with previous two-photon investigations initial work was carried out with **MNM 10** in solution, followed by constant exposure to highly pulse 710 nm laser light, with the first signs of necrosis within the nucleus being measured. These results are compared with both **MNM 1**, and a blank run with no loaded MNM, in **Figure 5.36**.

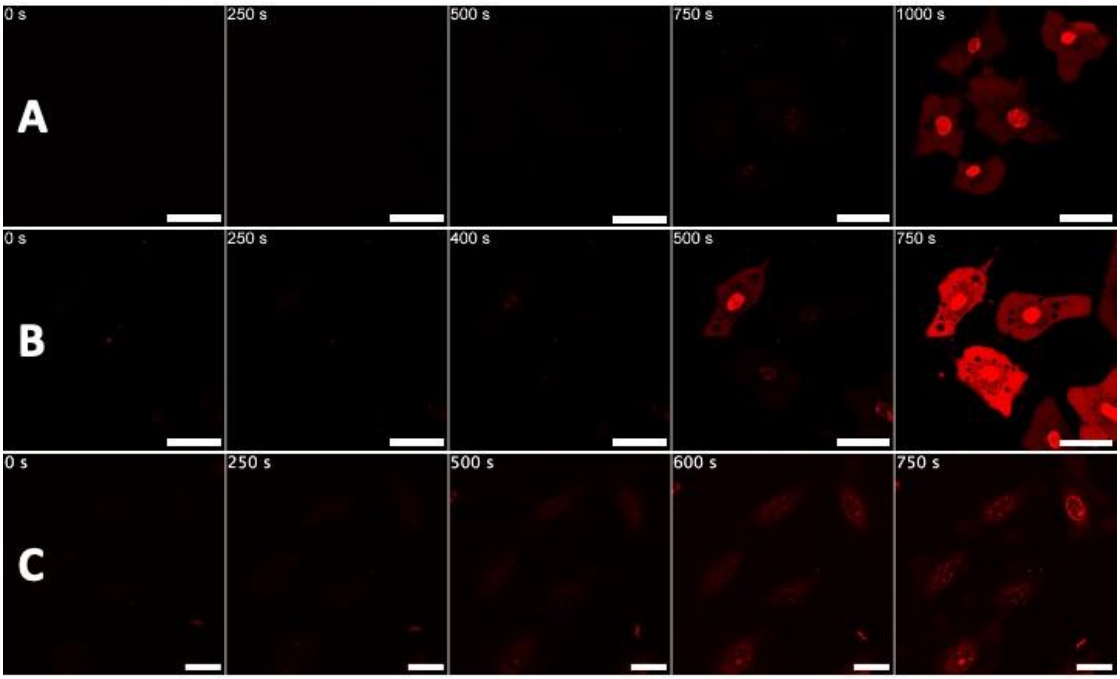

Figure 5.36 Microscopic observation of cell death caused by excitation at 710 nm (NIR-exposure times are shown for each image), quantified by the observation of PI fluorescence within the nucleus. **A** – Control sample: NIH 3T3 cells loaded with 100 nM PI and 0.1% DMSO. **B** – NIH 3T3 cells loaded with 100 nM PI and 1 µM **MNM 1**. C – NIH 3T3 cells loaded with 100 nM PI and 1 µM **MNM 10**. All image sets collected after 30 minutes incubation after dosing procedure. Red channel showing detection of PI fluorescence (λ_{ex} = 543 nm, 0.2 mW; λ_{em} = 600-700 nm). All scale bars set to 25 µm.

In line with the equivalent single photon work, comparable necrotic acceleration (compared to a sample loaded only with 0.1% DMSO v/v) is seen between experiments loaded with TPP+ addended **MNM 10**, and those loaded with unfunctionalised **MNM 1**. Indicating that the addition of the TPP+ moiety has not drastically altered the MNMs 2PCS and efficient rotor activation can still be induced *via* this non-linear process.

Now, work turned towards repeating the internalisation experimental steps, previously seen, to assess if **MNM 10** can still show a good ability to both cross the phospholipid bilayer (and by extension localise in the mitochondrial envelope) and be activated from within the cell by the 710 nm NIR 2PA procedure developed throughout this work. **Figure 5.37** summarises the results collected throughout these experiments.

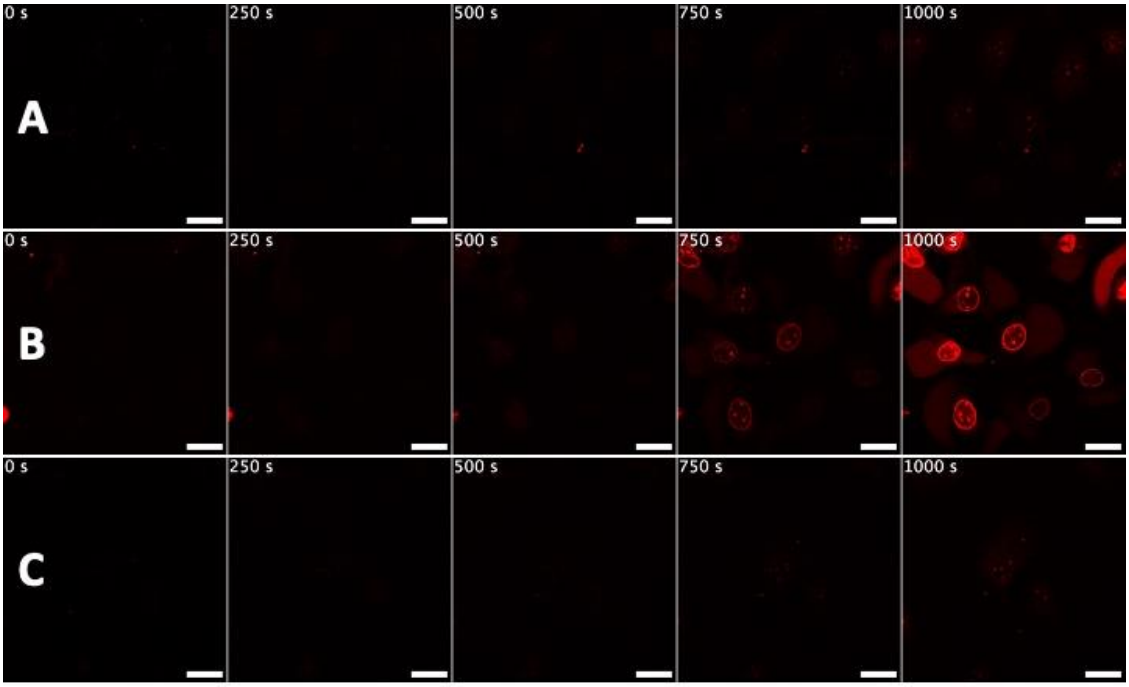

Figure 5.37 Microscopic observation of cell death caused by excitation at 710 nm (NIR-exposure times are shown for each image), quantified by the observation of PI fluorescence within the nucleus. **A** – NIH 3T3 loaded with 1 µM **MNM 10**, followed by 30 minutes incubation and washing with MNM free media, and subsequent staining with 100 nM PI. **B** – NIH 3T3 loaded with 1 µM **MNM 10**, followed by 2-hour incubation and washing with MNM free media, and subsequent staining with 100 nM PI. **C** - NIH 3T3 loaded with 1 µM **MNM 10**, followed by 2-hour incubation, washing with MNM free media, 16-hour clearance, and subsequent staining with 100 nM PI. All image sets collected after 30 minutes incubation after dosing procedure. Red channel showing detection of PI fluorescence (λ_{ex} = 543 nm, 0.2 mW; λ_{em} = 600-700 nm). All scale bars set to 25 µm.

The results obtained follow the same trends observed for all previous work in this chapter. Two-hour incubation times with **MNM 10**, followed by washing with MNM free growth media, and staining with PI allows adequate time for the TPP+ functionalised MNM to passively cross the cellular membrane and be activated with the previously

developed 710 nm NIR multiphoton procedure. Resulting in a great acceleration of necrosis on set in the sample. The results of this series of experimenters are summarised graphically in **Figure 5.38**.

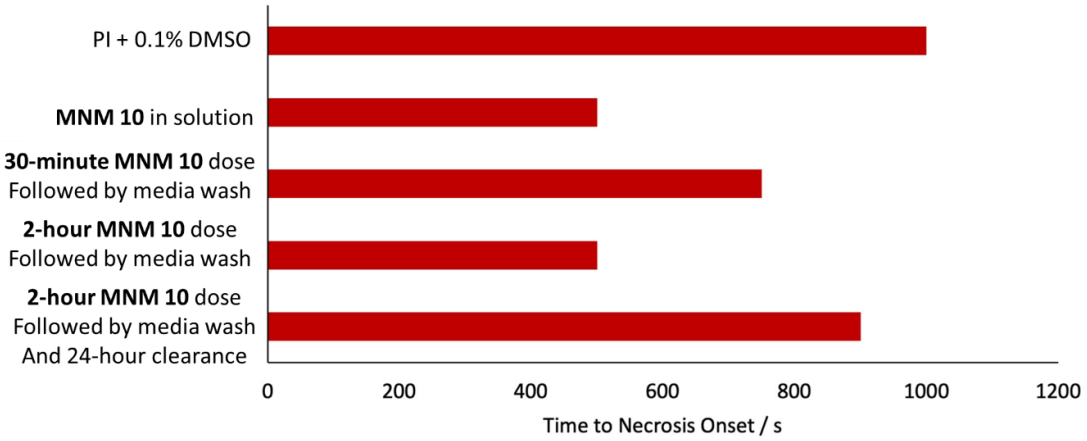

Figure 5.38 Graphical summary of TTN data obtained from 710 nm NIR exposure times to first observable PI emission detected within the nucleus of studied cells for **MNM 10** internalisation studies.

These results illustrate that not only do the multiphoton systems and procedures developed throughout this work (Chapter 4) lead to consistent results for several MNMs containing different functional groups, but also that these techniques can efficiently promote early onset necrotic cell death using internalising MNMs activated with biologically favourable 710 nm NIR light. Helping to pave the way toward our overarching goal of cell specific, next generation, targeted MNM based treatment methods. If the other aim of this chapter – induction of non-necrotic routes towards cell death - can be realised, these techniques may be combined to produce the first NIR activated MNM treatment method that can cause PCD in cellular samples. A massive advancement in the work towards personalised cancer treatments.

5.6 Investigations into the possible promotion of apoptosis using internalising MNM 10

Efforts to work towards triggering apoptosis, and other PCD routes, in samples of MNM loaded NIH 3T3 cells starts first with understanding the minimum UV exposure times required to initiate an irreversible necrotic process. All previous work with both 355 nm UV single photon and 710 nm NIR two-photon activation of the rotor use constant exposure to the light source. Meaning the various MNMs added to the sample for any given experiment are always "switched on". This is a good way to ensure each investigation is providing consistent results, removing laser up time as a variable to consider when balancing the other aspects of the experimental set up. However, it may be the case that the process of necrosis is triggered before the microscopist first observes any PI emission from within the cell and any further activation of the loaded MNMs is unnecessary. If this work is to find a method for preferentially inducing other mechanisms of cell death, the minimum amount of laser "up time" to start the irreversible process towards necrosis must be identified and henceforth never met.

Work was first carried out on blank control samples, loaded only with 0.1% DMSO v/v and 100 nM of PI for necrosis detection, to observe the minimum 355 nm UV exposure time required to trigger necrosis without the presence of any MNM. A series of experiments were run systematically reducing the time of 355 nm UV exposure to the sample and measuring for any indication of necrosis – i.e. any detected fluorescence in the red PI emission channel (λ_{ex} = 543 nm, 0.2 mW; λ_{em} = 600-700 nm) from within the boundaries of the cell's nucleus. The results of this experimental series are shown in **Figure 5.39**.

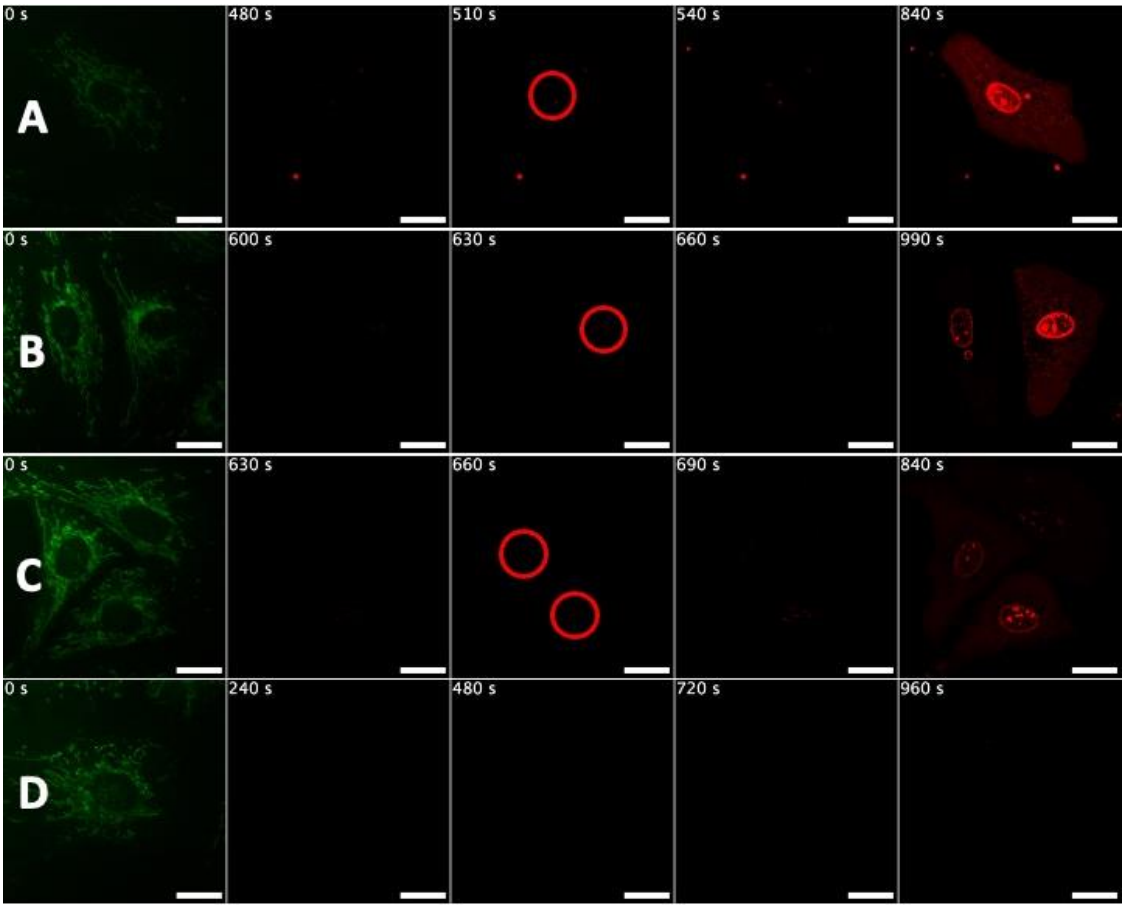

Figure 5.39 Microscopic observation of cell death caused by excitation at 355 nm (Experiment run times are shown for each image), quantified by the observation of PI fluorescence within the nucleus. **A** – Control sample: NIH 3T3 cells loaded with 100 nM PI and 0.1% DMSO. Exposed to 355 nm UV laser light for the entirety of the experiment. **B** – Control sample: NIH 3T3 cells loaded with 100 nM PI and 0.1% DMSO. 355 nm UV laser switched off after **5 minutes** of exposure. **C** - Control sample: NIH 3T3 cells loaded with 100 nM PI and 0.1% DMSO. 355 nm UV laser switched off after **4 minutes** of exposure. **D** - Control sample: NIH 3T3 cells loaded with 100 nM PI and 0.1% DMSO. 355 nm UV laser switched off after **3 minutes** of exposure. All image sets collected after 30 minutes incubation after staining procedure. Overlaid channels of PI fluorescence (λ_{ex} = 543 nm, 0.2 mW; λ_{em} = 600-700 nm), and mitochondrial autofluorescence (λ_{ex} = 355 nm, 20 mW, 400 nJ per voxel; λ_{em} = 440-460 nm). All scale

bars set to 20 µm. Red circles superimposed to illustrate the first observable emission of PI (600-700 nm) within the nucleus of the studied cells.

Initially, comparable results to those seen in previous control samples are found. When constantly exposed to 355 nm UV light, the cells under study show first, very minor, detectable signs of necrosis at 530 s. Leading to the complete necrosis shown at 840 s (**Figure 5.39 A**). When the UV exposure time is limited to five minutes, by switching the laser off during the imaging process, the first detectable signs of necrotic cell death are observed significantly later at 630 s. With a similar result (660 s) seen when UV exposure is ended after 4 minutes of excitation. Upon only 3 minutes of UV laser activation (**Figure 5.39 D**) no indications of necrotic cell death are observed when imaging for up to 16 minutes, implying that this level of UV irradiation is not sufficient to kill the sample.

Following this, a similar investigation was carried out to determine the minimum level of UV exposure required to induce necrotic cell death for samples loaded with unfunctionalised **MNM 1**. It is predicted that a significantly lower UV exposure time will, of course, be needed to induce necrosis in this sample compared to the MNM free control experiment. It is hoped that a sufficiently large window of UV laser up time is available before necrosis is irreversibly triggered, providing a sizeable opportunity to use the previously evaluated internalising MNMs to induce apoptosis. The results of this experimental series are shown in **Figure 5.40**.

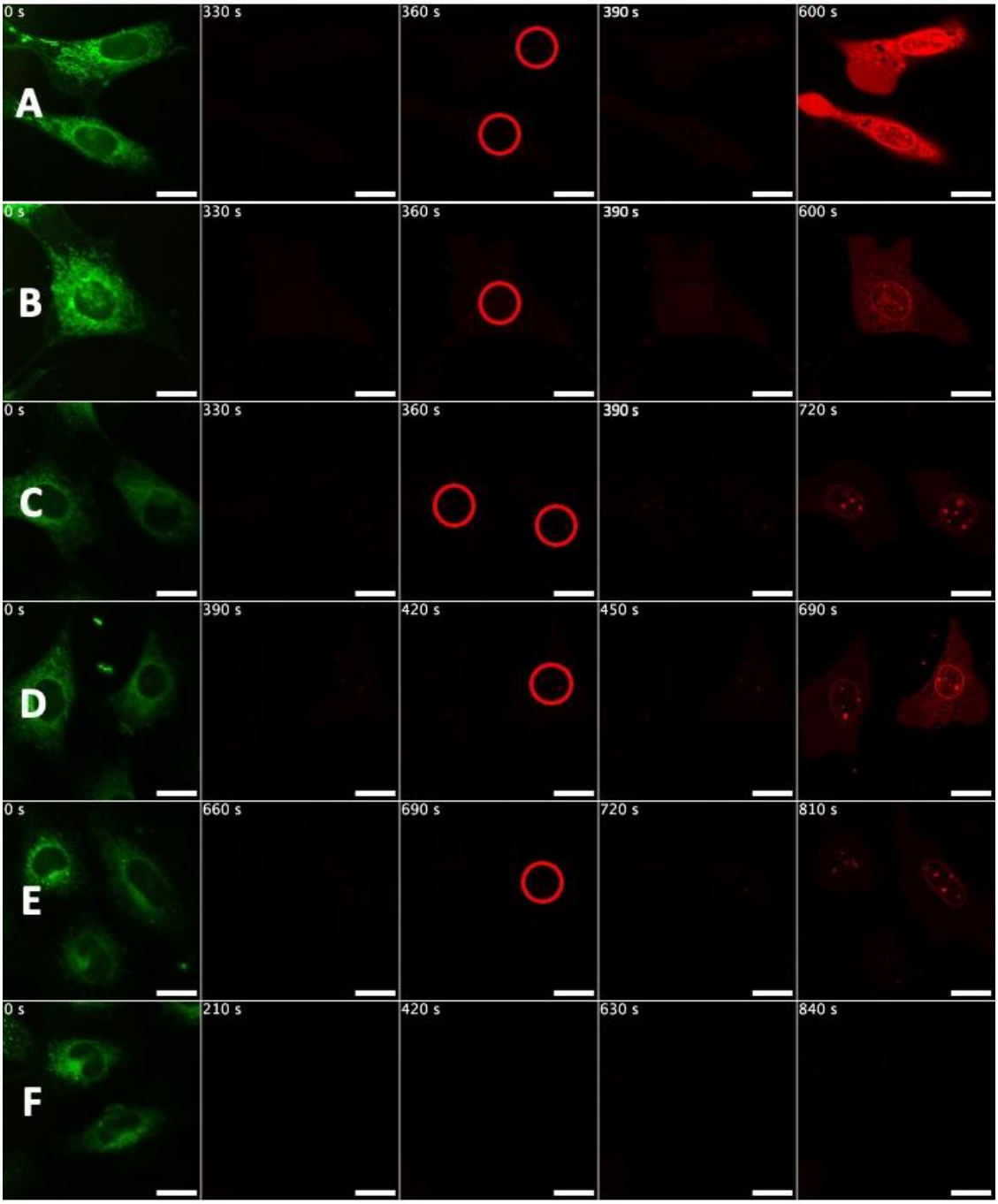

Figure 5.40 Microscopic observation of cell death caused by excitation at 355 nm (Experiment run times are shown for each image), quantified by the observation of PI fluorescence within the nucleus. **A** – NIH 3T3 cells loaded with 0.5 µM **MNM 1**, 100 nM PI and 0.1% DMSO. Exposed to 355 nm UV laser light for the entirety of the experiment. **B** – NIH 3T3 cells loaded with 0.5 µM **MNM 1**, 100 nM PI and 0.1% DMSO. 355 nm UV laser switched off after **5 minutes** of exposure. **C** - NIH 3T3 cells loaded

with 0.5 µM **MNM 1**, 100 nM PI and 0.1% DMSO. 355 nm UV laser switched off after **4 minutes** of exposure. **D** - NIH 3T3 cells loaded with 0.5 µM **MNM 1**, 100 nM PI and 0.1% DMSO. 355 nm UV laser switched off after **3 minutes** of exposure. E - NIH 3T3 cells loaded with 0.5 µM **MNM 1**, 100 nM PI and 0.1% DMSO. 355 nm UV laser switched off after **2 minutes** of exposure. F - NIH 3T3 cells loaded with 0.5 µM **MNM 1**, 100 nM PI and 0.1% DMSO. 355 nm UV laser switched off after **1 minute** of exposure. All image sets collected after 30 minutes incubation after staining procedure. Overlaid channels of PI fluorescence (λ_{ex} = 543 nm, 0.2 mW; λ_{em} = 600-700 nm), and mitochondrial autofluorescence (λ_{ex} = 355 nm, 20 mW, 400 nJ per voxel; λ_{em} = 440-460 nm). All scale bars set to 20 µm. Red circles superimposed to illustrate the first observable emission of PI (600-700 nm) within the nucleus of the studied cells.

As predicted, lower 355 nm UV exposure times are required to induce the onset of necrosis with samples loaded with **MNM 1**. With laser up times as low as 2 minutes still showing complete necrosis after 810 s (**Figure 5.40 E**). One minute of UV exposure appears to be the limit where the dosed MNMs cannot induce enough damage to the cell membrane to cause the onset of necrosis, leading the cell to recover and remain viable. The next stage of this investigation requires using the most promising internalising MNM candidate, determined from the previous work in this chapter. TPP+ functionalised **MNM 10** was selected (for reasons previously explained), incubated with the sample for 2 hours to localise within the mitochondrial membrane of the NIH 3T3 cells, followed by complete removal of any additional MNM in solution from the growth media. The same procedure as the experiments above was then implemented to determine the minimum levels of 355 nm UV exposure required to cause enough mechanical damage to the cell from within to cause necrotic cell death. With the hope

that this information may be iterated upon in the development of new methods to trigger other, more therapeutically favourable, forms of cell death with further experimentation. These results for the induction of necrosis with internalised **MNM 10** are shown in **Figure 5.41**.

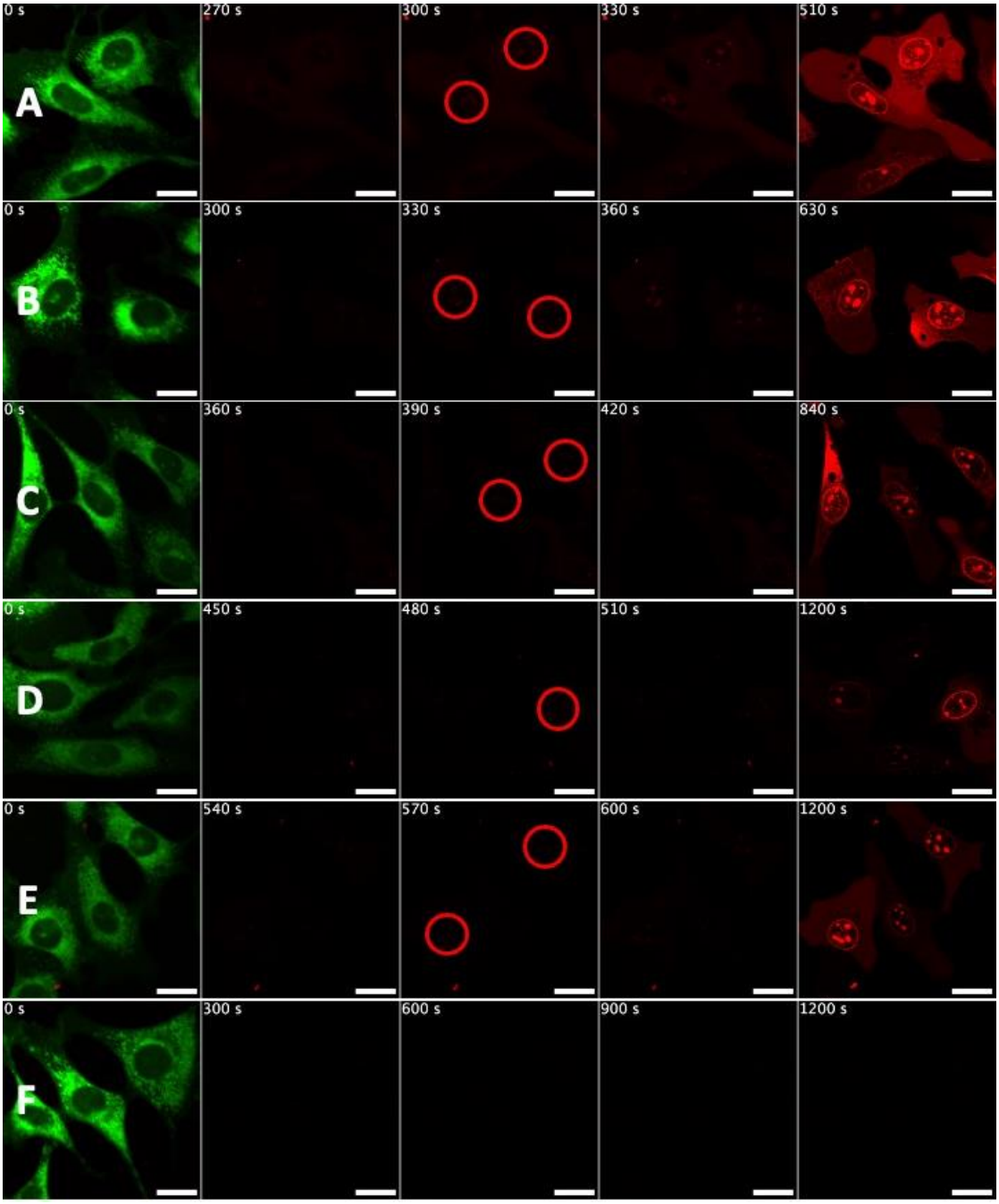

Figure 5.41 Microscopic observation of cell death caused by excitation at 355 nm (Experiment run times are shown for each image), quantified by the observation of PI fluorescence within the nucleus. **A** – NIH 3T3 cells loaded with 0.5 µM **MNM 10** followed by 2-hour incubation and washing with MNM free media, and subsequent staining with 100 nM PI. Exposed to 355 nm UV laser light for the entirety of the experiment. **B** – NIH 3T3 cells loaded with 0.5 µM **MNM 10** followed by 2-hour

incubation and washing with MNM free media, and subsequent staining with 100 nM PI. 355 nm UV laser switched off after **5 minutes** of exposure. **C** - NIH 3T3 cells loaded with 0.5 µM **MNM 10** followed by 2-hour incubation and washing with MNM free media, and subsequent staining with 100 nM PI. 355 nm UV laser switched off after **4 minutes** of exposure. **D** - NIH 3T3 cells loaded with 0.5 µM **MNM 10** followed by 2-hour incubation and washing with MNM free media, and subsequent staining with 100 nM PI. 355 nm UV laser switched off after **3 minutes** of exposure. **E** - NIH 3T3 cells loaded with 0.5 µM **MNM 10** followed by 2-hour incubation and washing with MNM free media, and subsequent staining with 100 nM PI. 355 nm UV laser switched off after **2 minutes** of exposure. **F** - NIH 3T3 cells loaded with 0.5 µM **MNM 10** followed by 2-hour incubation and washing with MNM free media, and subsequent staining with 100 nM PI. 355 nm UV laser switched off after **1 minutes** of exposure All image sets collected after 30 minutes incubation after staining procedure. Overlaid channels of PI fluorescence (λ_{ex} = 543 nm, 0.2 mW; λ_{em} = 600-700 nm), and mitochondrial autofluorescence (λ_{ex} = 355 nm, 20 mW, 400 nJ per voxel; λ_{em} = 440-460 nm). All scale bars set to 20 µm. Red circles superimposed to illustrate the first observable emission of PI (600-700 nm) within the nucleus of the studied cells.

Here, in a similar fashion to the previous experiments with **MNM 1** free in solution, necrosis is induced in the cells under study with UV excitation for as short as one minute. However, late-stage necrosis due complete breakdown of the cellular membrane (shown *via* bright PI emission throughout the internals of the cell, blebbing, and visible holes in the membrane) is observed significantly later than previous investigations. Importantly, it is confirmed that UV exposure times of less than one minute are not adequate to cause necrotic cell death *via* the activation of **MNM 10** from within the cells

mitochondrial network. This provides a window of possible 355 nm UV-induced activation times, 0 – 60 s, where promotion of alternate routes towards cell death may be possible.

To start investigations into this hypothesis, the apoptosis specific detection dye Annexin V Alexa Fluor 488 (AV) is employed. Initial work is carried out on both a MNM free control sample, as well as a sample dosed with unfunctionalised **MNM 1** in solution. To ensure that the inclusion of this stain does not have any measurable impact on the results of the experiment. **Figure 5.42** shows the results for both experiments. It should be noted that the UV-induced mitochondrial autofluorescence is now false coloured blue, while the annexin V conjugate channel is green – PI emission colour is unchanged from previous work.

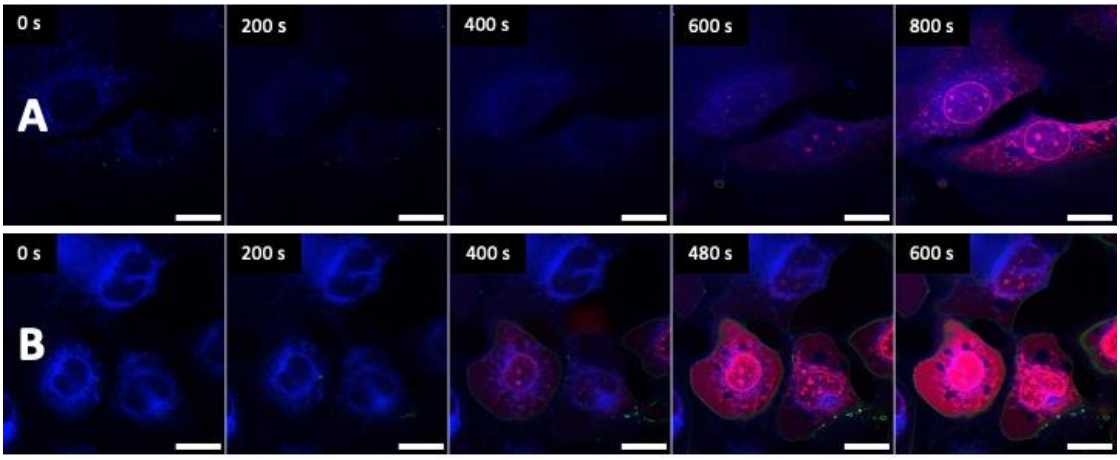

Figure 5.42 Microscopic observation of cell death caused by excitation at 355 nm (UV exposure times are shown for each image), quantified by the observation of PI fluorescence within the nucleus. **A** - Control sample: NIH 3T3 cells loaded with 100 nM PI, 100 nM AV, and 0.1% DMSO. **B** - NIH 3T3 cells loaded with 0.5 µM **MNM 1**, 100 nM PI, 100 nM AV, and 0.1% DMSO. All image sets collected after 30 minutes incubation after staining procedure. Overlaid channels of PI fluorescence (λ_{ex} = 543 nm, 0.2 mW; λ_{em} = 600-700 nm), AV fluorescence (λ_{ex} = 488 nm, 0.2 mW; λ_{em} = 500-550 nm) and mitochondrial autofluorescence (λ_{ex} = 355 nm, 20 mW, 400 nJ per voxel; λ_{em} = 440-460 nm). All scale bars set to 20 µm.

Good agreement is found between these results acquired on samples loaded with 100 nM AV, when compared with previous results collected on samples only containing the required 0.5 µM MNM and 100 nM PI. With the blank sample containing no MNM in solution showing first signs of necrosis onset after 600 seconds of constant 355 nm UV exposure (**Figure 5.42 A**) and the sample loaded with 0.5 µM **MNM 1** exhibiting PI emission within the nucleus after 400 seconds (**Figure 5.42 B**). Both being in line with previous, extensively covered, results. Interestingly, AV emission is detected during these experiments. Illustrating the importance of containing with a necrosis specific detection reagent such as PI. When undergoing necrosis, perforations in the cells outer

membrane are formed, allowing PI to enter the cell and bind to DNA – indicating necrotic cell death. However, this will of course also allow for AV to also enter the internal cellular space, binding to the phosphatidylserine molecules held on the inner surface of the phospholipid bilayer and subsequently exhibiting a 100-fold increase in fluorescence intensity. Thus, an important distinction should be made that it is not only AV detected emission that will indicate apoptosis in the sample but AV emission unaccompanied by red PI emission. Ensuring no holes are present within the membrane, and no necrotic cell death has taken place.

After confirming that the addition of AV to the sample under investigation has little to no measurable impact on the dynamics of the experiment work can be carried out attempting to induce non-necrotic cell death *via* 355 nm UV MNM activation. To this aim, samples of NIH 3T3 incubated for two hours with **MNM 10** followed by washes with MNM free media were stained with both PI and AV. Followed by very brief exposure to the previously used 355 nm UV laser, ensuring excitation of the internalised MNM never exceeded one minute – the minimum timeframe previously shown to start the irreversible onset of necrosis. The acquired live-cell fluorescence microscopy images collected during these experiments are shown in **Figure 5.43**. As with previous experiments involving suspension of UV excitation, the first frame collected is presented with the UV-induced mitochondrial autofluorescence channel and PI emission channels overlaid – with the addition of the AV emission image. Following this only the PI (red) and AV (green) channels are shown. The reasons being two-fold; to ensure any minor emission detected in either dye channel is more easily seen, and due to the removal of the UV laser, at various time points, the 355 nm activated mitochondrial emission is rendered unavailable.

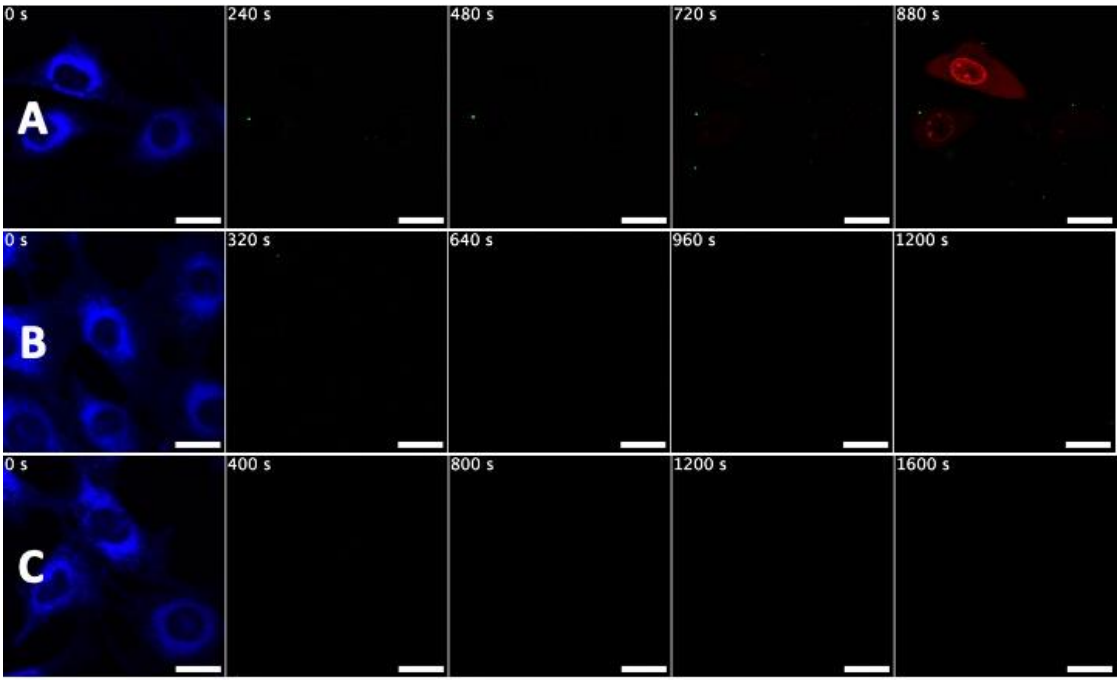

Figure 5.43 Microscopic observation of cell death caused by excitation at 355 nm (experiment run times are shown for each image), quantified by the observation of PI fluorescence within the nucleus. **A** - NIH 3T3 cells loaded with 0.5 µM **MNM 10** followed by 2-hour incubation and washing with MNM free media, and subsequent staining with 100 nM PI, 100 nM AV, and 0.1% DMSO. Exposed to 355 nm UV laser light for **1 minute**. **B** - NIH 3T3 cells loaded with 0.5 µM **MNM 10** followed by 2-hour incubation and washing with MNM free media, and subsequent staining with 100 nM PI, 100 nM AV, and 0.1% DMSO. Exposed to 355 nm UV laser light for **30 seconds**. **C** - NIH 3T3 cells loaded with 0.5 µM **MNM 10** followed by 2-hour incubation and washing with MNM free media, and subsequent staining with 100 nM PI, 100 nM AV, and 0.1% DMSO. Exposed to 355 nm UV laser light for **20 seconds.** All image sets collected after 30 minutes incubation after staining procedure. Overlaid channels of PI fluorescence (λ_{ex} = 543 nm, 0.2 mW; λ_{em} = 600-700 nm), AV fluorescence (λ_{ex} = 488 nm, 0.2 mW;

λ_{em} = 500-550 nm) and mitochondrial autofluorescence (λ_{ex} = 355 nm, 20 mW, 400 nJ per voxel; λ_{em} = 440-460 nm). All scale bars set to 20 μm.

When initially exciting the internalised **MNM 10** with 355 nm UV laser light for one minute (**Figure 5.43 A**) onset of necrotic cell death is still triggered, illustrated by the complete uptake and subsequent emission of PI seen at 880 seconds of observation. Reducing this UV excitation time to 30 seconds, followed by 20 seconds, (**Figure 5.43 B** and **Figure 5.43 C** respectively) while not causing any onset of necrosis, fails to show any AV emission from the outer membrane of the cell. Initially implying that no form of cell death has occurred due to the activation of **MNM 10** from within the cell. However, when studying the transmission images other interesting observations can be made. **Figure 5.44** shows the transmission images for the one-minute UV exposure experiment where necrosis has been clearly observed *via* PI fluorescence. Alongside the 20 second UV exposure results in addition to two further attempts at exciting internalised **MNM 10** for 30 seconds.

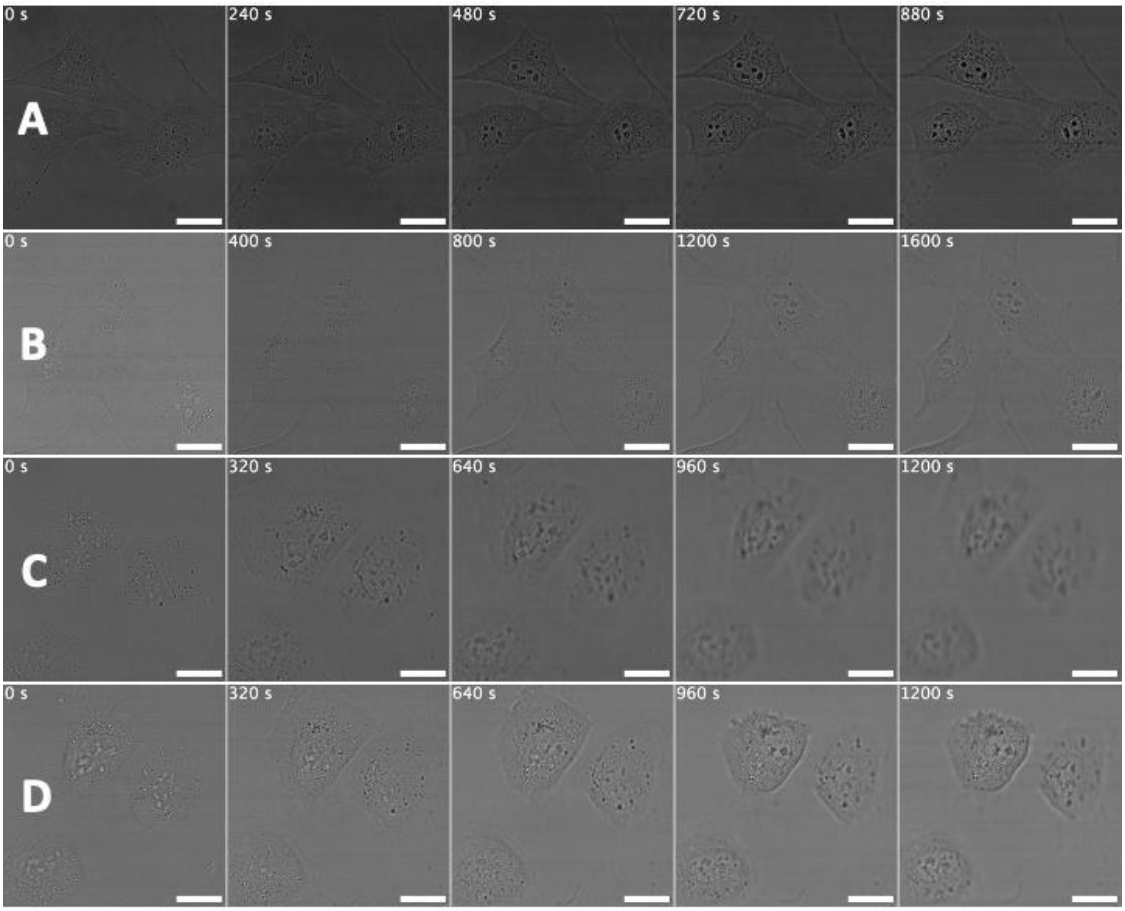

Figure 5.44 Microscopic observation of cell death caused by excitation at 355 nm visualised by morphological changes observed in the transmission image. **A** - NIH 3T3 cells loaded with 0.5 µM **MNM 10** followed by 2-hour incubation and washing with MNM free media, and subsequent staining with 100 nM PI, 100 nM AV, and 0.1% DMSO. Exposed to 355 nm UV laser light for **1 minute**. **B** - NIH 3T3 cells loaded with 0.5 µM **MNM 10** followed by 2-hour incubation and washing with MNM free media, and subsequent staining with 100 nM PI, 100 nM AV, and 0.1% DMSO. Exposed to 355 nm UV laser light for **20 seconds. C and D** -NIH 3T3 cells loaded with 0.5 µM **MNM 10** followed by 2-hour incubation and washing with MNM free media, and subsequent staining with 100 nM PI, 100 nM AV, and 0.1% DMSO. Exposed to 355 nm UV laser

light for **30 seconds**. All image sets collected after 30 minutes incubation after staining procedure. All scale bars set to 20 µm.

When exposed to UV excitation of the MNM's rotor for one-minute, additional confirmation of the previously established necrotic cell death is seen in the transmission image with bulging of the cellular boundaries and blebbing. In contrast, very little change in morphology is seen when internalised **MNM 10** is only activated for 20 seconds – as expected based upon the previous findings of no emission in the florescent channels of either PI or AV. Incredibly interesting results are seen however, for the two experiments with 30 second 355 nm UV laser up time. In these cases, dramatic changes are seen in cell morphology; the cell boundaries clearly shrivel up towards to the centre of the body, accompanied by a significant loss of focus – implying the cell has in fact detached from the slide surface and in now freely moving in solution. Crucially, these observations are coupled with a complete lack of emission with the PI fluorescence channel.

Despite the lack of signal acquired from the AV channel, these morphological observations seem to imply a non-necrotic cell death pathway has been accessed by the activation of the internalised **MNM 10**. The absence of 500-550 nm AV emission could be due to several possible explanations. First, the loss of focus caused by the release of the studied cell from the slide surface and into solution (a common indication of apoptosis and other PCD pathways) may inhibit the detection of any less intense signal. A problem which has already been encountered in this project when setting up a new method for studying 2PA of MNMs - due to the differing focal distances of the laser lines used, making PI hard to detect (**Chapter 4**). Additionally, the timescale of the experiments may not be long enough for the cells studied to shuttle their phosphatidylserine to the outer surface of the membrane. Thus, there is no binding site

for the AV molecules and therefore no detectable emission. While these results are incredibly positive and do seem to indicate the aim of inducing non-necrotic death in NIH 3T3 cells has been realised; additional work may be carried out to conclusively prove this. Namely, flow cytometry could be utilised to study the, possibly apoptotic, cells as they vacate into solution – eliminating the limitation caused by the microscope's focal plane and allowing for longer experiment run times to attempt to detect any proposed AV emission.

5.7 Conclusions and further work

This chapter has presented significant leaps in the development of MNM based cancer therapies. Systematic studies for two families of internalising MNMs, PEG and TPP+ functionalised, have been discussed. Using both the previously established single photon activation of the rotary mechanism by 355 nm UV light, as well as the newly developed and iterated two-photon activation *via* 710 nm NIR wavelengths. In addition to these advances, efforts working towards the promotion of more biologically favourable routes towards cell death have been evaluated. By activating the rotor of internalised, TPP+ functionalised, MNMs bound to the cell's mitochondria with 355 nm UV light for shorter excitation windows than those found to promote the onset of necrosis, evidence was collected of the induction of cleaner PCD routes.

Using the previously established series of internalising experiments (**Chapter 3**) both PEG and TPP+ analogues were evaluated for their ability to passively cross the outer membrane of NIH 3T3 cells. Good levels of passive uptake were seen for both families of MNMs with incubation times as short as two-hours, measured by the acceleration of necrosis onset in samples with no nanomachines left in solution. Observed by the rapid increase in brightness of PI emission from within the nucleus of the cells under study.

While both systems of functionalised MNM (PEG and TPP+) were able to efficiently cross the phospholipid bilayer and be activated from within the cell, evidence was presented that TPP+ functionalised species possessed an additional ability to localise at the mitochondrial membrane. Observed by morphological changes within the 355 nm UV-induced autofluorescence of the cells mitochondrial network. Thought to be caused by electrostatic attraction between the diffuse positive charge across the TPP+ moieties phenyl system and the negative potential of the mitochondrial envelope. This represented a possibility for a further avenue of research, activating these MNMs from within the cell without damaging the outer membrane, leading to possible induction of apoptotic cell death.

Additional exciting progress in the development of this works goal to enable the activation of MNMs with more biologically favourable NIR light *via* a non-linear two-photon process (**Chapter 4**) have also been presented within this chapter. Using the previously discussed experimental and instrumentational procedures, efficient and consistent activation of multiple MNM analogue with two-photon processes was shown to be possible. Importantly, this was seen not just for MNMs in solution but also from within the cell. This may be carried further in the future to iterate upon the work presented in this chapter, in the development of less phototoxic treatment methods.

AV staining of cellular samples with internalised TPP+ functionalised MNMs was carried out to evaluate the possibility of inducing apoptotic cell death *via* MNM based treatment. While these procedures failed to firmly establish any non-necrotic cell death, *via* AV emission, interesting morphological changes were observed in the transmission channel – posing some noteworthy conclusions. When excited with 355 nm UV light for 30 seconds, internalised TPP+ functionalised **MNM 10** consistently exhibited

fundamental apoptotic alterations in cell structure. Namely, cell shrinkage and release into solution from the slide surface. This may indicate that the treated cells have either undergone apoptosis-like PCD without phosphatidylserine shuttling, preventing AV based detection, or are undergoing apoptotic cells death but limitations in the current experimental set up are limiting the ability to detect any AV emission.

While this chapter has effectively iterated on the body of work presented throughout this thesis and presented some incredible advances in MNM based controlled cell destruction, there are many possible avenues to continue this research. Firstly, additional experiments may be set up to continue the evaluation of the induction of non-necrotic routes towards cell death. To draw conclusive evidence on whether non-apoptotic PCD or true apoptosis has been achieved by the developments posed in this chapter. This may require the development of a flow cytometry set up to enable the measurement of AV emission from cells no longer adhered to the growth surface. In addition to this, it may be interesting to combine the results of this chapter's investigations. By using the established experimental methods for introduction of non-necrotic cell death, with the two-photon activation of internalised TPP+ MNMs to establish an introduction of biologically favourable cell death using less phototoxic wavelengths of light. This would represent a great leap in the quest for MNM based cell specific treatment methods.

One important aspect in the development of these photomechanical, MNM based techniques, as new cancer treatment methods is their biodegradability as well as their bioaccumulation in real life systems. While this preliminary in vitro study has not covered this, it is a vital consideration going forward. In **Chapter 2** it was mentioned that the carbon-carbon double bond connecting the stator and rotor halves of the molecules

may be susceptible to oxidation (acting as weak ROS scavengers), this may imply that MNMs may be metabolised into various ketones within the body. A comprehensive study on the possible metabolites and their impact on physiological systems is an important avenue for further work toward developing MNM-based cancer therapeutics.

It should also be considered that the TPP+ MNM analogue utilised in the later stages of this investigation (**MNM 10**) in only functionalised on a single half of the stator, leaving great possibility of further functionalisation. For instance, the stator may also be addended with cell specific recognition peptide sequences to enable the specific targeting of cell types. While the rotor may be functionalised with electron donating groups (**Chapter 3**) such as -OMe to shift the activation wavelength to lower energies. Coupling this with the now extensively tested 2PA procedures poses a great avenue for MNM activation with remarkably high wavelengths. Providing an excellent continuation of the work presented in this thesis.

5.8 References

1 F. F. Davis, A. Abuchowski, T. Van Es, N. C. Palczuk, R. Chen, K. Savoca and K. Wieder, in *Enzyme Engineering*, eds. G. B. Broun, G. Manecke and L. B. Wingard, Springer US, Boston, MA, 1978, pp. 169–173.

2 P. Bailon and W. Berthold, *Pharm. Sci. Technol. Today*, 1998, **1**, 352–356.

3 J. M. Harris and S. Zalipsky, *Poly(ethylene Glycol): Chemistry and Biological Applications*, American Chemical Society, 1997.

4 P. Bailon and C.-Y. Won, *Expert Opin. Drug Deliv.*, 2009, **6**, 1–16.

5 A. A. D'souza and R. Shegokar, *Expert Opin. Drug Deliv.*, 2016, **13**, 1257–1275.

6 W. M. Pardridge, D. Wu and T. Sakane, *Pharm. Res.*, 1998, **15**, 576–582.

7 World Intellectual Property Organization, WO2019016240A1, 2019.

8 World Intellectual Property Organization, WO2011003886A1, 2011.

9 C. A. Kulkarni, B. D. Fink, B. E. Gibbs, P. R. Chheda, M. Wu, W. I. Sivitz and R. J. Kerns, *J. Med. Chem.*, 2021, **64**, 662–676.

10 M. P. Murphy and R. A. J. Smith, *Annu. Rev. Pharmacol. Toxicol.*, 2007, **47**, 629–656.

11 Y. N. Antonenko, A. V. Avetisyan, D. A. Cherepanov, D. A. Knorre, G. A. Korshunova, O. V. Markova, S. M. Ojovan, I. V. Perevoshchikova, A. V. Pustovidko, T. I. Rokitskaya, I. I. Severina, R. A. Simonyan, E. A. Smirnova, A. A. Sobko, N. V. Sumbatyan, F. F. Severin and V. P. Skulachev, *J. Biol. Chem.*, 2011, **286**, 17831–17840.

12 S. R. Jean, M. Ahmed, E. K. Lei, S. P. Wisnovsky and S. O. Kelley, *Acc. Chem. Res.*, 2016, **49**, 1893–1902.

13 M. F. Ross, G. F. Kelso, F. H. Blaikie, A. M. James, H. M. Cochemé, A. Filipovska, T. Da Ros, T. R. Hurd, R. A. J. Smith and M. P. Murphy, *Biochem. Mosc.*, 2005, **70**, 222–230.

14 M. P. Murphy, *Biochim. Biophys. Acta BBA - Bioenerg.*, 2008, **1777**, 1028–1031.

15 G. Cheng, J. Zielonka, O. Ouari, M. Lopez, D. McAllister, K. Boyle, C. S. Barrios, J. J. Weber, B. D. Johnson, M. Hardy, M. B. Dwinell and B. Kalyanaraman, *Cancer Res.*, 2016, **76**, 3904–3915.

16 W. Lei, J. Xie, Y. Hou, G. Jiang, H. Zhang, P. Wang, X. Wang and B. Zhang, *J. Photochem. Photobiol. B*, 2010, **98**, 167–171.

17 K. M. Robinson, M. S. Janes, M. Pehar, J. S. Monette, M. F. Ross, T. M. Hagen, M. P. Murphy and J. S. Beckman, *Proc. Natl. Acad. Sci.*, 2006, **103**, 15038–15043.

18 S. Huang, R. Han, Q. Zhuang, L. Du, H. Jia, Y. Liu and Y. Liu, *Biosens. Bioelectron.*, 2015, **71**, 313–321.

19 C. Reily, T. Mitchell, B. K. Chacko, G. A. Benavides, M. P. Murphy and V. M. Darley-Usmar, *Redox Biol.*, 2013, **1**, 86–93.

20 J. Trnka, M. Elkalaf and M. Anděl, *PLOS ONE*, 2015, **10**, e0121837.

21 A. Glücksmann, *Biol. Rev.*, 1951, **26**, 59–86.

22 J. F. R. Kerr, *J. Pathol.*, 1971, **105**, 13–20.

23 J. F. R. Kerr, A. H. Wyllie and A. R. Currie, *Br. J. Cancer*, 1972, **26**, 239–257.

24 S. Rello, J. C. Stockert, V. Moreno, A. Gámez, M. Pacheco, A. Juarranz, M. Cañete and A. Villanueva, *Apoptosis*, 2005, **10**, 201–208.

25 I. Budihardjo, H. Oliver, M. Lutter, X. Luo and X. Wang, *Annu. Rev. Cell Dev. Biol.*, 1999, **15**, 269–290.

26 L. E. Bröker, F. A. E. Kruyt and G. Giaccone, *Clin. Cancer Res.*, 2005, **11**, 3155–3162.

27 S. Pietkiewicz, J. H. Schmidt and I. N. Lavrik, *J. Immunol. Methods*, 2015, **423**, 99–103.

28 D. V. Krysko, T. Vanden Berghe, K. D'Herde and P. Vandenabeele, *Methods*, 2008, **44**, 205–221.

29 L. Boulos, M. Prévost, B. Barbeau, J. Coallier and R. Desjardins, *J. Microbiol. Methods*, 1999, **37**, 77–86.

30 P. Strzyz, *Nat. Rev. Mol. Cell Biol.*, 2017, **18**, 72–72.

31 S. H. Kaufmann, S.-H. Lee, X. W. Meng, D. A. Loegering, T. J. Kottke, A. J. Henzing, S. Ruchaud, K. Samejima and W. C. Earnshaw, *Methods*, 2008, **44**, 262–272.

32 C. Widmann, in *xPharm: The Comprehensive Pharmacology Reference*, eds. S. J. Enna and D. B. Bylund, Elsevier, New York, 2007, pp. 1–3.

33 J.-P. Aubry, A. Blaecke, S. Lecoanet-Henchoz, P. Jeannin, N. Herbault, G. Caron, V. Moine and J.-Y. Bonnefoy, *Cytometry*, 1999, **37**, 197–204.

34 E. C. de Bruin and J. P. Medema, *Cancer Treat. Rev.*, 2008, **34**, 737–749.

35 R. K. Amaravadi and C. B. Thompson, *Clin. Cancer Res.*, 2007, **13**, 7271–7279.

36 M. Schuster, A. Nechansky and R. Kircheis, *Biotechnol. J.*, 2006, **1**, 138–147.

37 B. A. Carneiro and W. S. El-Deiry, *Nat. Rev. Clin. Oncol.*, 2020, **17**, 395–417.

38 J. P. Waters, J. S. Pober and J. R. Bradley, *J. Pathol.*, 2013, **230**, 241–248.

39 S. Orrenius, P. Nicotera and B. Zhivotovsky, *Toxicol. Sci.*, 2011, **119**, 3–19.

40 H. Rubin, *Proc. Natl. Acad. Sci. U. S. A.*, 2017, **114**, 12237–12242.

41 E. Vivès, J. Schmidt and A. Pèlegrin, *Biochim. Biophys. Acta BBA - Rev. Cancer*, 2008, **1786**, 126–138.

42 A. T. Cameron and M. S. Hollenberg, *J. Gen. Physiol.*, 1922, **4**, 411–422.

Chapter 6: Methods and materials

6.1 General procedures and instrumentation

Commercially available reagents and cell culture supplies were used as received. Absorption spectra were recorded using ATI Unicam UV-Vis spectrometer (Model UV2) using Vision 3.33 software, while all emission and excitation spectra were recorded using ISA Jobin-Yvon Spex Fluorolog-3 luminescence spectrometer alongside DataMax v2.2 software, with all samples held within 1 cm path length quartz cuvettes. NIH 3T3 cell lines were sourced from ATCC (CRL-1658) and have been established and maintained in a category 2 cell culture facility according to established standardized protocol for 12 months and have been periodically monitored for mycoplasma contamination.[1] Cell media and solutions were acquired from Thermo Fisher Scientific. Cell growth flasks and sterile equipment were acquired from Starlab Group. Microscopy channel slides were acquired from Thistle Scientific.

6.2 Cell culture and sample preparation

6.2.1 Cell culture

NIH 3T3 mouse skin fibroblasts were grown as a single monolayer in Gibco™ Dulbecco's Modified Eagle Medium (DMEM) with GlutaMAX™ / F12 supplemented with 10% foetal bovine serum (FBS). Grown in 75 cm^2 plastic culture flasks, with no prior surface treatment. Incubation was carried out at 37 °C and 5% (v/v) CO_2, and in average humidity conditions. Cell harvesting was carried out *via* washing with 10% phosphate buffered saline (PBS) prior to the addition of trypsin solution (0.25%). 5-10 minutes of incubation at 37.5 °C was carried out prior to resuspension in fresh media by repeated aspiration with a sterile plastic pipette.

Cells were defrosted from stocks, kept frozen at -78 °C in freezing media (Gibco™ Dulbecco's Modified Eagle Medium (DMEM) with GlutaMAX™ / F12 supplemented with 10% foetal bovine serum (FBS) with the addition of 10% DMSO), by immediate warming with gloved hand until slightly defrosted to a level where the frozen cellular pellet could move freely in the cryovial. Followed by immediate addition to a pre-warmed to 37 °C 75 cm^2 plastic culture flask. Before incubation overnight, allowing cells to adhere fully.

6.2.2 Microscope slide preparation

Microscopy cells were seeded by addition of 100 µL of concentrated cellular suspension in growth media, acquired by trypsinisation of the stock solutions, on to untreated surface iBibi 500 µL live-cell channel slides, followed by addition of 400 µL fresh growth media into each well and allowed to grow to roughly 50% confluence, at 37 °C in 5% CO_2, 10% humidity. Following cell adherence and division on the slide surface (an average of 48 hours), the growth media was replaced, and cells were treated with the studied nanomachines (0.5 - 1 µM) and Propidium iodide (PI) / Annexin V Alexa Fluor 488 conjugate (AV) stain (100 nM), ensuring DMSO concentration present in the final imaging medium never crossed 0.1% v/v. For live-cell imaging, DMEM GlutaMAX™ / F12 media (10% FBS) lacking phenol red was used from this point onward to prevent unwanted UV-induced fluorescence from the pH indicator. Following incubation, the channels were washed with live-cell imaging media and imaged using a purposely built incubator housing the microscope maintaining 37 °C, 5% CO_2 and 10% humidity.

Two methods were used for MNM incubation and staining procedures for investigating TTN for solutions with MNM in solution, or internalised within the sample: **Standard Method** – The studied MNM were loaded into the channel slides containing 500 µL cell media, by addition of 2.5 µL (for 0.5 µM final concentration – single photon studies) or

5 µL (for 1 µM final concentration – two photon studies) of 1 mM stock solution and left to incubate at 37 °C in 5% CO_2 for 30 minutes, followed by staining with the required fluorescent dyes, 100 nM PI or 100 nM AV, followed by immediate transfer to the microscope incubator housing and subsequent image acquisition. **Internalisation Method** – Studied MNMs were loaded channel slides containing 500 µL cell media, by addition of 2.5 µL (for 0.5 µM final concentration – single photon studies) or 5 µL (for 1 µM final concentration – two photon studies) of 1 mM stock solution and left to incubate for various stated time frames ranging from 30 min to 24 h. Followed by 3x washes with 1 mL fresh MNM-free DMEM GlutaMAX™ / F12 media (10% FBS) lacking phenol red added to one well of the channel slides, tilted and left to run through the channel, and removed from the opposite well. Before subsequent staining with the required fluorescent dyes, 100 nM PI or 100 nM AV, followed by immediate transfer to the microscope incubator housing and image acquisition. Each MNM stock solution was in DMSO with final DMSO concentrations not exceeding 0.1% in the final imaging media solution to avoid unwanted increases in cell membrane permeabilization. It should be noted that all MNM loading experiments were carried out in a light-suppressed environment and the possibility of induced or accelerated uptake due to interaction between the molecular motors and the applied co-stain has been eliminated previously using a series of individual and reversed loading experiments.[2]

6.3 Laser scanning confocal microscopy procedures

6.3.1 Imaging system overview

All live-cell microscopy experiments were performed on a custom built PhMoNa system[3] based on a Leica SP5 II (DMI6000 inverted chassis) LSCM platform containing integrated visible laser lines; 458, 476 ,488, 496, 514 nm Argon and 543, 633 nm HeNe. In addition

to a fibre-coupled 355 nm coherent laser (Nd:YAG third harmonic, 80 mW) for UV activation of the motor, and a femtosecond pulsed coherent chameleon vision ii Ti:Sapphire tuneable (680-1080 nm, 65 mW @ 710 nm, 80 MHz, 100 fs) laser, with additional EOM power control, for NIR rotor activation. The modular PhMoNa technique is based on a laser scanning confocal microscope (LSCM) harnessing spatially modulated illumination intensities, using an in situ-generated raster-scanned standing wave excitation beam optical grid pattern. The threshold algorithm to control brightness automated by the Leica LAX software is calculated by the image specific signal-to-noise ratio. Below is an illustrative diagram (**Figure 6.1**) showing the key features of the microscope set up used.

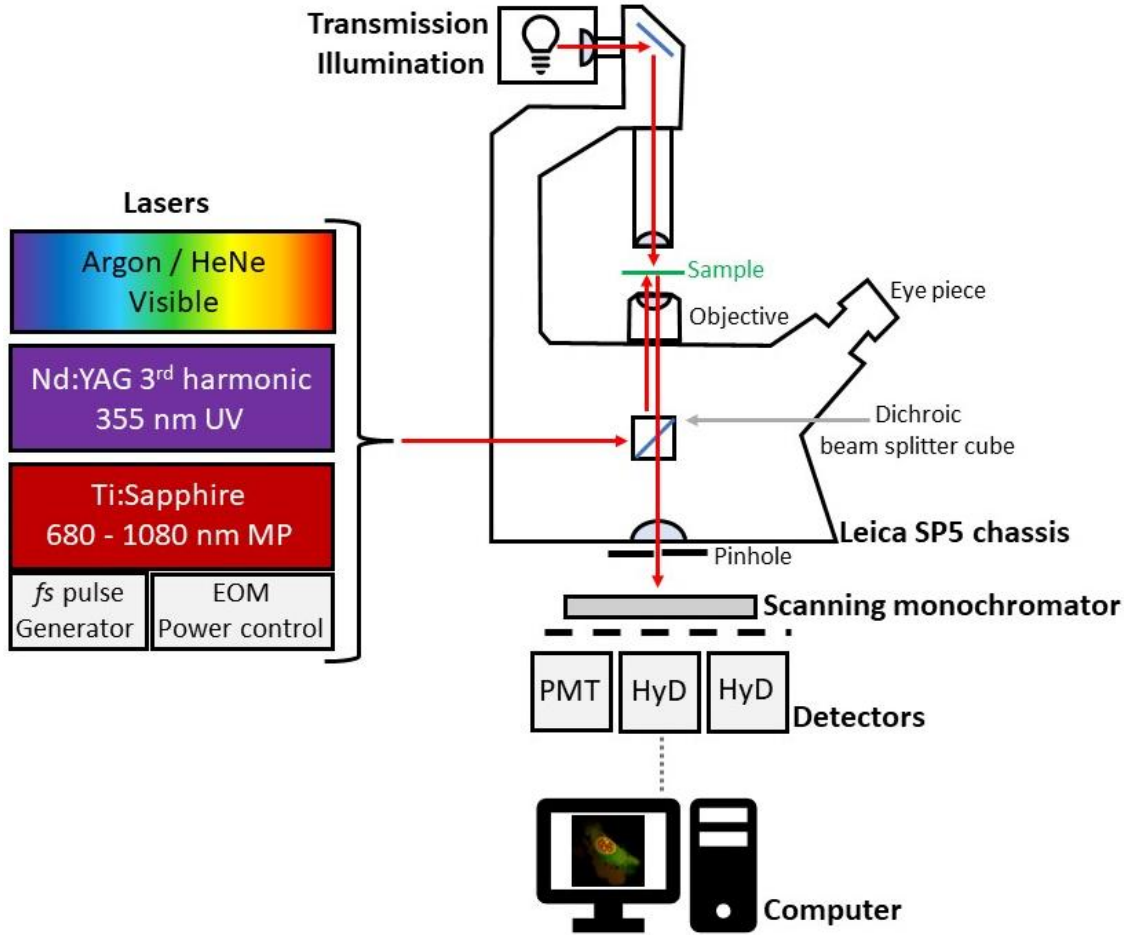

Figure 6.1 Simplified schematic representation of the main hardware components used in the LSCM system used throughout this work.

6.3.2 Single photon 355 nm UV MNM activation imaging procedure

Steady-state fluorescence images were recorded using the PhMoNa enhanced Leica SP5 II LSCM confocal microscope equipped with a HCX PL APO 63×/1.40 NA LambdaBlue Oil immersion objective. Data were collected using 2× digital magnification at 100 Hz/line scan speed (4-line average, bidirectional scanning) at 355 nm (third harmonic NdYAG laser, set at 20 mW, 400 nJ/voxel total dwell time). In order to achieve excitation with maximal probe emission, the microscope was equipped with a triple-channel imaging detector, comprising a conventional PMT system and two HyD hybrid avalanche

photodiode detectors. The frame size was determined at 1024 × 1024 pixel, with ×2 digital magnification to ensure illumination flatness of field and 0.6 airy disc unit determining the applied pinhole diameter rendering on voxel to correspond to 62 × 62 nm2 (frame size 125 × 125 μm^2) with a section thickness set at 188 nm (at 355 nm excitation). HeNe and Argon integrated ion lasers was used to aid parallel transmission image capture of the PI and other loaded stain signals, used to follow the onset of necrosis and other cell death pathways. All imaging parameters are kept constant across experiments; this includes voxel size, laser power, line speed, and averaging sequences, unless otherwise noted within this work.

6.3.3 Two photon 710 nm NIR MNM activation imaging procedure

Multiphoton microscopy live-cell experiments were performed on the same custom built PhMoNa system based on a Leica SP5 II (DMI6000 inverted chassis) LSCM platform operating with a Coherent Chameleon Vision II tuneable (680−1080 nm, 65 mW @ 710 nm, 80 MHz, 100 fs) multiphoton laser for NIR activation of the motor. Using a ×20 0.95 NA oil immersion objective operating at unidirectional 100 Hz scan speed with 2-line accumulation unidirectional 1024 × 1024 pixel FOV for sequential MP nanomachine activation and PI imaging. 2PE activation of the MNMs was achieved using an optimized ×3.5 digital zoom to provide a 120 × 120 µm FOV in order to study 1−3 cells simultaneously and provide sufficient continuous NIR laser scanning with sufficiently long integration time for each pixel, so an adequate photon flux can be delivered to promote nonlinear MNM activation. Scan speeds for NIR activation were set at a unidirectional 100 Hz with the above detailed scan settings. A five-step z-stack, with a 1 µm step size, was enacted to ensure consistent results regardless of cell morphology and compensate for chromatic aberration between the integrated 543 nm HeNe ion and

Coherent Chameleon Vision II tuneable (680−1080 nm, 65 mW @ 710 nm, 80 MHz, 100 fs) multiphoton, lasers.

6.3.4 Post processing

All post image processing was carried out on the open source, plugin prepacked, FIJI (ImageJ 1.52p Java 1.8.0_172 64 Bit).[4] All adjustments to voxel brightness and contrast were kept at constant values within each image set to ensure consistency in the results obtained.

6.4 Synthetic procedures

The synthetic protocols for each on the MNMs utilised throughout this body of work are provided here for the convenience of the reader. However, it should be reiterated that all synthetic work was caried out by our collaborators in Prof. James Tour's lab at Rice university. Further details of the synthesis and characterisation can be found in the relevant published work.

6.4.1 MNM 1

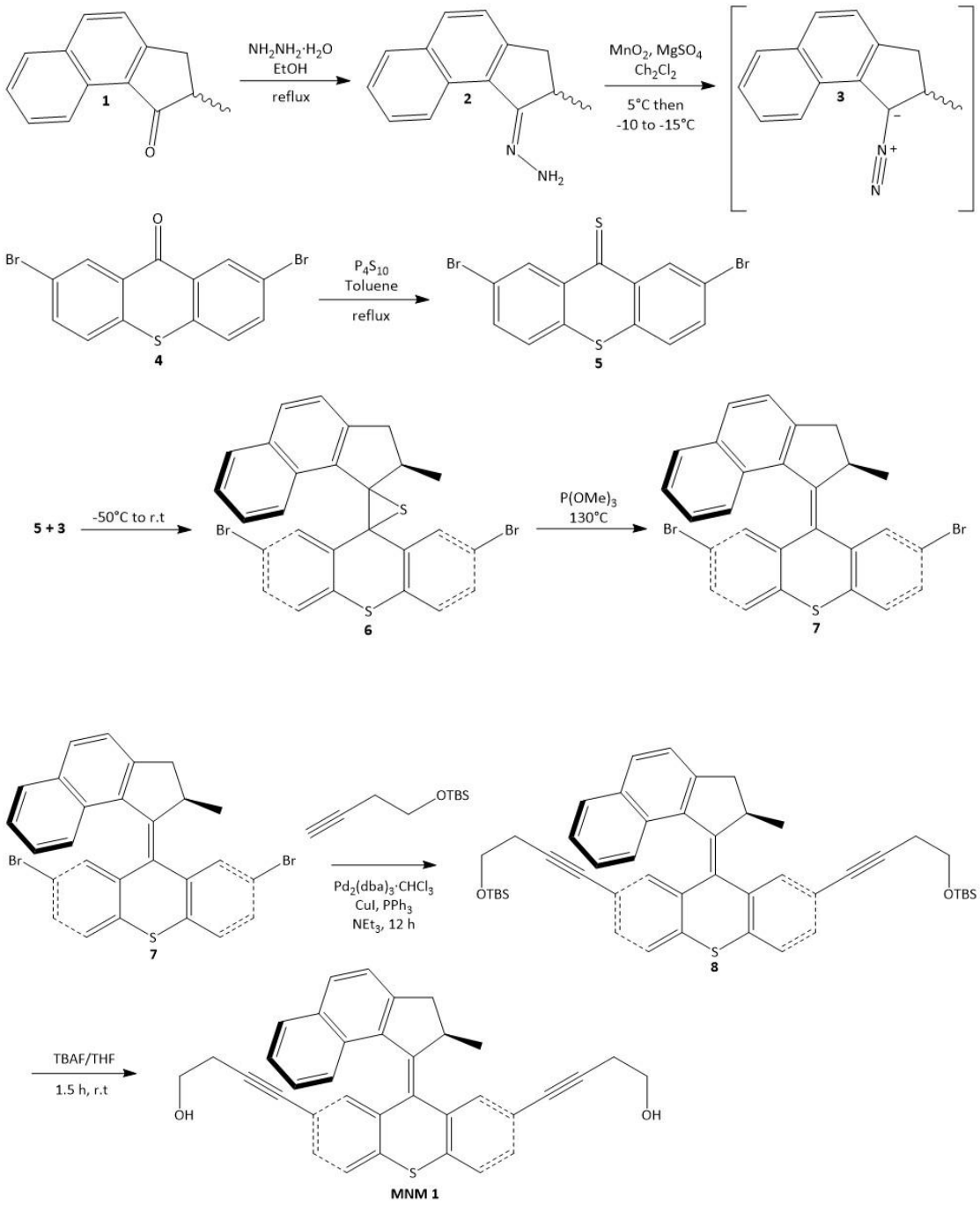

Hydrazone 2. To an oven dried round-bottom flask charged with ketone 1 (1.96 g, 10 mmol) was added EtOH (20 mL) and hydrazine monohydrate (10 mL) through a condenser. The mixture was heated at reflux for 3 d. The cooled reaction mixture was extracted with ether (100 mL) and water (100 mL × 3). The organic layer was dried over

MgSO4 and concentrated under vacuum to afford hydrazone 2 as yellow solid (1.95 g, 93%). Spectroscopic data were identical to those in the literature.[5]

2,7-Dibromo-thioxanthene-9-thione (5). To an oven dried two-neck round-bottom flask charged with thioxanthenone 4 12 (3.25 g, 8.78 mmol) and P_4S_{10} (10 g, 22.5 mmol) was added toluene (250 mL) and the mixture was heated at reflux for 2 d. The mixture was filtered while hot, and the filtrate was collected. The brownish solid that formed upon cooling was filtered, and solid was collected and dried under vacuum (3.2 g, 94 %). Spectroscopic data were identical to those reported in the literature.[5]

Episulfide 6. To an oven dried three-neck round-bottom flask charged with hydrazone 2 (0.99 g, 4.7 mmol) and $MgSO_4$(s) (0.49 g, 50% w/w) was added dichloromethane (25 mL). To this suspension was added quickly MnO_2 (1.62 g, 18.8 mmol, Sigma-Aldrich > 90%) at ca. 5 °C. The reaction flask was immediately immersed and stirred in a cold bath ranging from −15 °C to −10 °C for 1.5 h. After this period, the reaction mixture was cooled to −50 °C and then transferred to a Schlenk filtration tube connected to an oven dried three-neck round-bottom flask. The deep purple filtrate that contained intermediate 3 was collected, and the Schlenk tube was rinsed with pre-cooled dichloromethane (20 mL, −50 °C). To the flask containing the combined filtrate, thione 5 (0.97 g, 2.5 mmol) was added portionwise until no more N_2 evolved. The mixture was stirred for an additional 0.5 h at ambient temperature. The mixture was poured into methanol (80 mL) with vigorous stirring and a white precipitate formed. The solid was filtered, and the filter cake was washed with methanol (30 mL) and dried under vacuum to afford the desired compound 6 (1.19 g, 84%): mp 204 °C (decomp); FTIR (neat) 3078, 3070, 3050, 2974, 2954, 2934, 2898, 2866, 2840, 1616, 1580, 1568, 1556, 1514, 1456, 1436, 1382, 1372, 1252, 1212, 1160, 1132, 1112, 1080, 1052, 1024 cm^{-1} ; ^1H NMR (400 MHz, CDCl3) δ 8.89

(d, J = 8.8 Hz, 1H), 8.00 (d, J = 2.0 Hz, 1H), 7.83 (d, J = 2.0 Hz, 1H), 7.56 (d, J = 8.2 Hz, 1H), 7.54 (d, J = 7.8 Hz, 1H), 7.40–7.34 (m, 2H), 7.29 (d, J = 8.2 Hz, 1H), 7.26–7.20 (m, 1H), 7.18 (d, J = 8.2 Hz, 1H), 6.84 (dd, J1 = 8.2 Hz, J2 = 2.0 Hz, 1H), 6.77 (d, J = 8.2 Hz, 1H), 3.43 (dd, J1 = 6.6 Hz, J2 = 15.4 Hz, 1H), 2.44 (d, J = 15.6 Hz, 1H), 1.57 (qd, J1 = 6.9 Hz, J2 = 6.6 Hz), 1.12 (d, J = 6.9 Hz, 3H); ^{13}C NMR (100 MHz, CDCl3) δ 142.5, 140.9, 136.2, 135.3, 134.4, 134.1, 132.6, 131.8, 130.81, 130.76, 130.1, 129.7, 129.4, 128.2, 127.8, 127.6, 124.5, 124.4, 124.0, 123.4, 120.9, 120.0, 72.2, 60.8, 40.5, 38.1, 21.8. HRMS (APCI) m/z calculated for [M+H]+ $C_{27}H_{19}Br_2S_2$ 564.9295, found 564.9275.[5]

2,7-Dibromo-9-(2-methyl-2,3-dihydro-1H-cyclopenta[a]naphthalen-1-ylidene)-9H-thioxanthene (molecular motor 7). To a 200 mL screw-capped tube charged with episulfide 6 (524 mg, 0.96 mmol) was added trimethyl phosphite (9.6 mL), and the mixture was stirred at 130 °C for 14 h. After the reaction mixture was cooled to room temperature, methanol (30 mL) was added. The precipitate was filtered and washed with methanol (20 mL). The solid was purified by column chromatography on silica gel using hexanes:dichloromethane 9:1 as eluent to afford compound 7 as a pale yellow solid (485 mg, 94%): mp 245–246 °C; FTIR (neat) 3072, 3046, 3032, 3008, 2952, 2920, 2859, 2848, 1616, 1612, 1576, 1568, 1558, 1548, 1540, 1512, 1452, S5 1440, 1394, 1380, 1362, 1346, 1284, 1256, 1204, 1196, 1180, 1152, 1140, 1128, 1084, 1074, 1052 cm^{-1} ; HRMS (APCI) m/z calculated for for [M+H]+ C27H19Br2S 532.9574, found 532.9550. For NMR spectroscopic data, see reference 5.[5]

(4,4'-(9-(2-Methyl-2,3-dihydro-1H-cyclopenta[a]naphthalen-1-ylidene)-9H-thioxanthene-2,7-diyl)bis(but-3-yne-4,1-diyl))bis(oxy)bis(tert-butyldimethylsilane) (molecular motor 8). An oven dried Schlenk tube equipped with a stir bar was charged with motor 7 (750 mg, 1.4 mmol), tris(dibenzylideneacetone)dipalladium(0)-chloroform

adduct (25.6 mg, 0.028 mmol), CuI (5.4 mg, 0.028 mmol), triphenylphosphine (26.3 mg, 0.14 mmol) and 4-(tert-butyldimethylsilyloxy)- but-1-yne (1.44 ml, 7.0 mmol). NEt3 (7 mL) was added and the mixture was stirred at 70 °C overnight. The resulting mixture was partitioned between CH_2Cl_2 (40 mL) and saturated NH_4Cl (aq) (40 mL). The organic layer was dried over anhydrous $MgSO_4$, concentrated, and purified by column chromatography (silica gel; 30% CH2Cl2 in hexanes) to afford 8 as a pale yellow solid (915 mg, 90%): m.p. 207–209 °C; FTIR (neat) 3052, 2954, 2930, 2856, 1588, 1472, 1454, 1388, 1362, 1252, 1218, 1100, 1058, 1006 cm^{-1} ; ^{1}H NMR (500 MHz, CDCl3) δ 7.79 (d, J = 1.7 Hz, 1H), 7.75 (d, J = 8.2 Hz, 1H), 7.70 (d, J = 8.2 Hz, 1H), 7.50 (dd, J1 = 8.0, J2 = 0.4 Hz, 1H), 7.47 (dt, J1 = 8.0, J2 = 0.4 Hz, 1H), 7.44 (d, J = 8.2 Hz, 1H), 7.26 (dd, J1 = 8.1, J2 = 1.8, 1H), 7.19 (ddd, J1 = 8.1, J2 = 5.7, J3 = 2.2 Hz, 1H), 7.03 (dd, J1 = 8.1, J2 = 1.8 Hz, 1H), 6.87 – 6.78 (m, 2H), 6.73 (dd, J1 = 1.8, J2 = 0.5 Hz, 1H), 4.24 (p, J = 6.7 Hz, 1H), 3.86 (t, J = 6.9 Hz, 2H), 3.64 (dd, J1 = 15.4, J2 = 6.2 Hz, 1H), 3.56 (td, J = 7.2, 1.1 Hz, 2H), 2.67 (t, J = 6.9 Hz, 2H), 2.63 (d, J = 15.4 Hz, 1H), 2.34 (t, J = 7.1 Hz, 2H), 0.94 (d, J = 0.4 Hz, 9H), 0.84 (d, J = 0.4 Hz, 9H), 0.78 (d, J = 6.8 Hz, 3H), 0.13 (s, 6H), -0.02 (s, 3H), -0.03 (s, 3H). ^{13}C NMR (125 MHz, CDCl3) δ 147.00, 146.11, 139.96, 137.72, 135.37, 134.85, 134.70, 133.11, 131.55, 130.77, 130.43, 129.38, 129.19, 128.78, 127.91, 127.62, 127.30, 127.16, 125.94, 124.90, 124.41, 123.69, 122.09, 122.04, 88.02, 87.07, 81.35, 80.68, 61.92, 61.76, 39.77, 37.94, 25.96, 25.89, 23.99, 23.68, 19.53, 18.44, 18.32, -5.15, -5.16, -5.27, -5.28. HRMS (APCI) m/z calculated for [M+H]+ C47H57O2SSi2 741.3612, found 741.3584.[6]

4,4'-(9-(2-Methyl-2,3-dihydro-1H-cyclopenta[a]naphthalen-1-ylidene)-9H-thioxanthene-2,7-diyl)dibut-3-yn-1-ol (MNM 1). A 100 mL round-bottomed flask equipped with a stir bar was charged with molecular motor 8 (544 mg, 0.73 mmol). THF (10 mL) and a solution of TBAF (1.83 mL, 1.83 mmol, 1.0 M in THF) were added, and the

mixture was stirred at rt for 1.5 h. The mixture was poured into water (50 mL) and filtered. The solid was collected, washed with water (20 mL ×2) and dried under vacuum to afford desired product MNM 1 as a pale-yellow solid (358 mg, 95%): m.p. 240 °C (decomposition.); FTIR (neat) 3302, 3050, 2954, 2922, 2894, 2838, 1702, 1586, 1516, 1454, 1386, 1338, 1256, 1170, 1042, 1020 cm^{-1} ; ^{1}H NMR (600 MHz, THF-d8) δ 7.87 (d, J = 1.6 Hz, 1H), 7.77 (d, J = 8.2 Hz, 1H), 7.70 (d, J = 8.1 Hz, 1H), 7.53 (d, J = 7.9 Hz, 1H), 7.50 (d, J = 8.0 Hz, 1H), 7.44 (d, J = 8.2 Hz, 1H), 7.26 (dd, J1 = 8.0, J2 = 1.7 Hz, 1H), 7.15 (ddd, J1 = 8.0, J2 = 6.5, J3 = 1.2 Hz, 1H), 7.03 (dd, J1 = 8.1, J2 = 1.8 Hz, 1H), 6.83 (d, J = 8.4 Hz, 1H), 6.80 – 6.75 (m, 1H), 6.68 (d, J = 1.7 Hz, 1H), 4.28 (p, J = 6.8 Hz, 1H), 4.02 (s, 1H), 3.75 – 3.65 (m, 4H), 3.39 (t, J = 7.3 Hz, 2H), 2.64 (d, J = 15.4 Hz, 1H), 2.60 (t, J = 7.0 Hz, 2H), 2.26 (t, J = 7.2 Hz, 2H), 0.76 (d, J = 6.9 Hz, 3H). ^{13}C NMR (150 MHz, THF-d8) δ 148.04, 147.38, 141.26, 138.93, 136.38, 136.04, 135.53, 134.45, 132.35, 131.65, 131.55, 130.52, 130.28, 129.96, S14 128.91, 128.54, 128.50, 128.26, 126.82, 125.81, 125.21, 124.62, 123.68, 123.62, 89.25, 88.25, 81.81, 81.21, 61.79, 61.63, 40.53, 39.11, 24.89, 24.54, 19.79. HRMS (APCI) m/z calculated for [M+H]+ C35H29O2S 513.1883, found 513.1879.

6.4.2 MNMs 2, 3, and 4

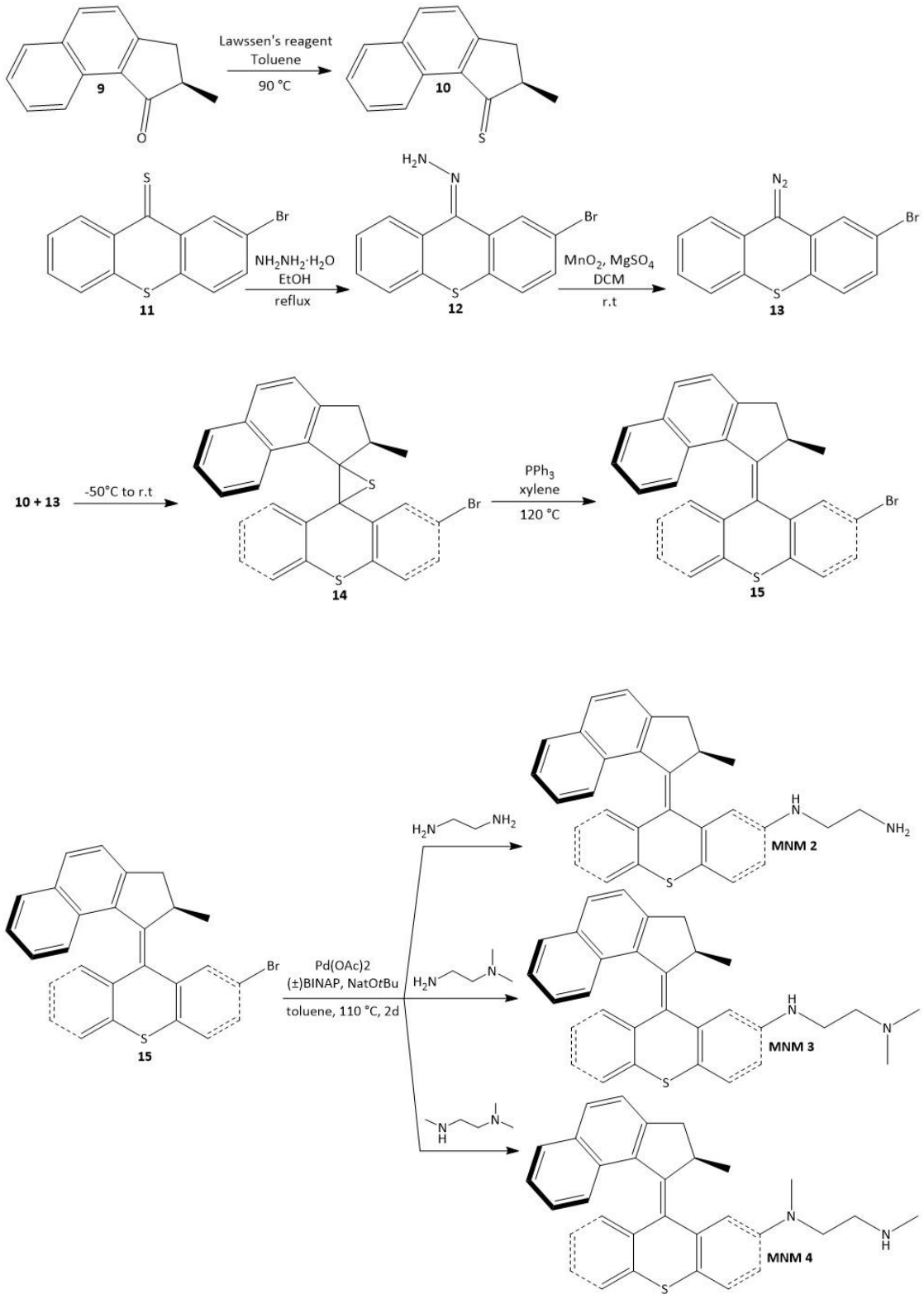

N1-(9-(2-methyl-2,3-dihydro-1H-cyclopenta[a]naphthalen-1-ylidene)-9H-thioxanthen-3-yl)ethane-1,2-diamine (MNM 2). BINAP (7.5 mg, 0.0198 mmol) and

palladium(II) acetate (1.5 mg, 0.0033 mmol) were dissolved in dry toluene (3 mL). This solution was stirred for 30 min at room temperature, where upon it turned from dark red to dark orange. After this period NaOtBu (75 mg, 0.33 mmol) was added, followed by bromo-substituted motor 15 (for detailed synthetic procedure see MNM 5 and 6 synthesis) (30 mg, 0.066mmol) and ethane-1,2-diamine (30 mg, 0.66 mmol). The mixture was stirred at 90 °C for 2 d. Subsequently, the reaction mixture was poured into CH_2Cl_2 (10 mL). After filtration, the solvents were evaporated. The crude product was dissolved in a small amount of CH_2Cl_2 and purified using column chromatography (SiO2; 10% MeOH in DCM) to yield MNM 2 as a brown solid product (20.9 mg, 73%): ^{1}H NMR (500 MHz, Chloroform-d) δ 7.71 – 7.66 (m, 0.5 H), 7.60 (ddd, J = 8.1, 6.9, 3.0 Hz, 2H), 7.50 – 7.41 (m, 1H), 7.32 (d, J = 8.2 Hz, 1H), 7.20 (td, J = 7.6, 1.3 Hz, 0.5 H), 7.11 – 7.05 (m, 1.5 H), 7.05 – 6.99 (m, 1H), 6.87 (td, J = 7.6, 1.4 Hz, 0.5 H), 6.82 – 6.77 (m, 1H), 6.74 (dd, J = 4.8, 2.3 Hz, 1H), 6.68 (ddd, J = 8.4, 6.7, 1.4 Hz, 0.5 H), 6.63 – 6.56 (m, 0.5 H), 6.52 – 6.45 (m, 1H), 6.41 (d, J = 8.4 Hz, 0.5 H), 5.79 (dd, J = 8.4, 2.3 Hz, 0.5 H), 4.17 (qd, J = 6.7, 3.8 Hz, 1H), 3.53 (dt, J = 15.3, 6.5 Hz, 1H), 3.14 – 3.05 (m, 1H), 2.99 (t, J = 5.8 Hz, 1H), 2.85 (t, J = 5.7 Hz, 1H), 2.74 (d, J = 5.8 Hz, 1H), 2.58 – 2.45 (m, 1H), 0.69 (dd, J = 12.3, 6.8 Hz, 3H). ^{13}C NMR (126 MHz, CDCl3) δ 146.57, 146.19, 145.57, 145.49, 144.69, 144.39, 140.95, 138.68, 136.75, 136.49, 135.93, 135.67, 135.42, 135.17, 132.99, 132.95, 129.54, 129.45, 129.04, 128.98, 128.54, 128.52, 128.40, 127.73, 127.67, 127.41, 126.81, 126.38, 126.17, 126.04, 126.00, 125.68, 124.57, 124.51, 124.08, 124.03, 123.81, 123.78, 111.87, 111.84, 110.90, 45.43, 45.24, 40.54, 40.44, 39.85, 37.88, 37.84, 19.54, 19.45.[7]

N1-N1-dimethyl-N2-(9-(2-methyl-2,3-dihydro-1H-cyclopenta[a]naphthalen-1-ylidene)-9Hthioxanthen-3-yl)ethane-1,2-diamine (MNM 3). BINAP (2.5 mg, 0.0066 mmol) and palladium(II) acetate (0.5 mg, 0.0011 mmol) were dissolved in dry toluene (5

mL). This solution was stirred for 30 min at room temperature, where upon it turned from dark red to dark orange. After this period NaOtBu (25 mg, 0.11 mmol) was added, followed by bromo-substituted motor 15 (10 mg, 0.022mmol) and N1 ,N1 ,N2 -trimethylethane-1,2-diamine (20 mg, 0.44 mmol). The mixture was stirred at 90 °C for 2 d. Subsequently, the reaction mixture was poured into CH_2Cl_2 (10 mL). After filtration, the solvents were evaporated. The crude product was dissolved in a small amount of CH_2Cl_2 and purified using column chromatography (SiO2; 10% MeOH in DCM) to yield MNM 3 as a brown solid product (6.3 mg, 61%). For NMR spectroscopic data, see reference 7.[7]

N1,N1-dimethyl-N2-(9-(2-methyl-2,3-dihydro-1H-cyclopenta[a]naphthalen-1-ylidene)-9Hthioxanthen-3-yl)ethane-1,2-diamine (MNM 4). BINAP (5.0 mg, 0.0132 mmol) and palladium(II) acetate (1.0 mg, 0.0022 mmol) were dissolved in dry toluene (3 mL). This solution was stirred for 30 min at room temperature, where upon it turned from dark red to dark orange. After this period NaOtBu (50 mg, 0.22 mmol) was added, followed by bromo-substituted motor 15 (20 mg, 0.044mmol) and N1 ,N2 -dimethylethane-1,2-diamine (20 mg, 0.44 mmol). The mixture was stirred at 90 °C for 2 d. Subsequently, the reaction mixture was poured into CH_2Cl_2 (10 mL). After filtration, the solvents were evaporated. The crude product was dissolved in a small amount of CH_2Cl_2 and purified using column chromatography (SiO2; 10% MeOH in DCM) to yield MNM 4 as a brown solid product (14.6 mg, 72%): ^{1}H NMR (500 MHz, Chloroform-d) δ 7.81 – 7.77 (m, 0.5 H), 7.72 – 7.63 (m, 3H), 7.60 – 7.53 (m, 1H), 7.41 (dd, J = 8.2, 2.9 Hz, 1H), 7.30 (td, J = 7.6, 1.3 Hz, 0.5 H), 7.19 (td, J = 7.5, 1.3 Hz, 0.5 H), 7.15 (ddd, J = 8.0, 6.7, 1.2 Hz, 1H), 7.05 (d, J = 8.5 Hz, 0.5 H), 7.00 – 6.94 (m, 1H), 6.94 (d, J = 2.6 Hz, 0.5 H), 6.89 – 6.85 (m, 0.5 H), 6.84 – 6.78 (m, 1H), 6.76 (ddd, J = 8.7, 4.2, 2.2 Hz, 1H), 6.69 (dd, J = 7.8,

1.4 Hz, 0.5 H), 6.62 – 6.52 (m, 1H), 6.02 (dd, J = 8.6, 2.6 Hz, 0.5 H), 4.28 (t, J = 6.7 Hz, 1H), 3.73 – 3.56 (m, 2H), 3.49 – 3.34 (m, 1H), 3.29 (s, 1 H), 3.00 (s, 1.5 H), 2.92 (t, J = 6.6 Hz, 1H), 2.87 (s, 1.5 H), 2.74 (q, J = 6.3 Hz, 1H), 2.60 (dd, J = 15.4, 6.3 Hz, 1H), 2.52 (s, 1.5 H), 2.45 (s, 1.5 H), 0.79 (dd, J = 15.7, 6.8 Hz, 3H).[13]C NMR (126 MHz, $CDCl_3$) δ 147.59, 147.29, 145.54, 145.45, 144.70, 144.46, 140.89, 138.61, 136.84, 136.57, 135.91, 135.65, 135.42, 135.18, 132.97, 132.91, 129.51, 129.35, 129.02, 128.95, 128.93, 128.52, 128.42, 128.36, 128.33, 127.71, 127.67, 127.64, 127.40, 127.36, 126.86, 126.72, 126.38, 126.14, 125.99, 125.95, 125.66, 124.53, 124.35, 124.00, 123.86, 123.80, 123.74, 111.31, 111.04, 110.97, 110.91, 51.32, 51.13, 48.03, 47.62, 39.83, 39.13, 38.80, 37.87, 37.74, 35.21, 35.14, 19.51, 19.47.[7]

6.4.3 MNMs 5 and 6

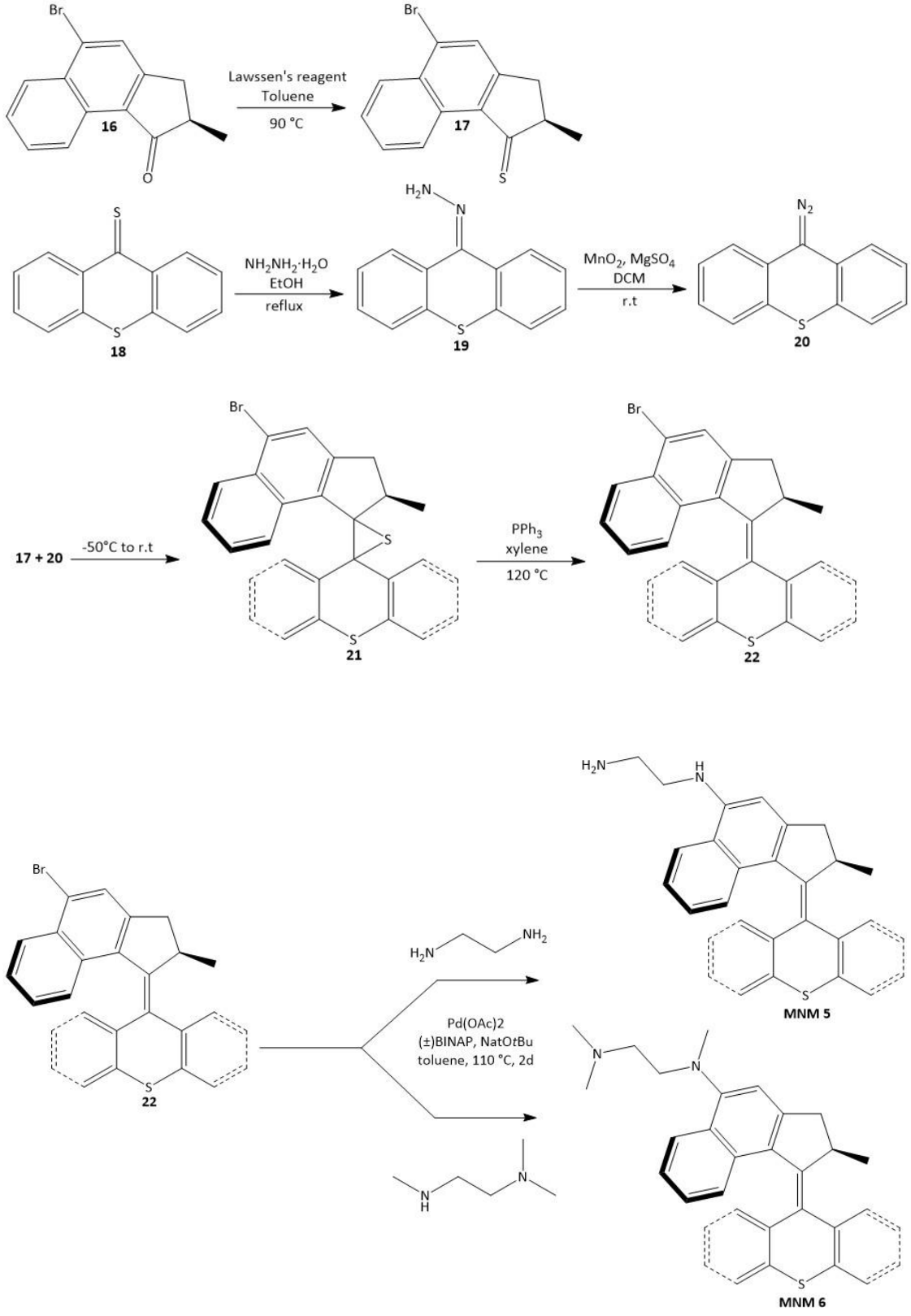

(9H-thioxanthen-9-ylidene)hydrazine (19). An oven-dried round-bottom flask equipped with a stir bar was charged with compound 18 (50 mg, 0.221 mmol) in THF (5.0 ml),

hydrazine monohydrate (1.0 ml) was added, and the mixture was stirred at room temperature for 1 h. The resulting mixture was concentrated in vacuo. The resulting concentrate was used for the next step without further purification.[7]

5-bromo-2-methyl-2,3-dihydrodispiro[cyclopenta[a]naphthalene-1,2'-thiirane-3',9''-thioxanthene] (21). To an oven-dried round-bottom flask charged with hydrazone 19 and $MgSO_4$ (100 mg, 200% w/w) was added THF (5.0 mL). To this suspension was quickly added MnO_2 (500.0 mg, 5.7 mmol, Sigma-Aldrich > 90%) at room temperature. The mixture was stirred for 1 h at the same temperature. The mixture was filtered, and the filtrate was concentrated in vacuo. To the resulting concentrate was added toluene (5.0 mL) and thioketone 17 (34.6 mg, 0.119 mmol). The mixture was heated to 100 °C and stirred for 3 h. After the reaction mixture was cooled to room temperature, the organic phase was dried over anhydrous MgSO4, filtered, and the filtrate was concentrated in vacuo, followed by purification by column chromatography (SiO_2; 10% acetone in DCM) to yield 20 as a bright yellow solid (38.6 mg, 67% for 2 steps): ^{1}H NMR (500 MHz, Chloroform-d) δ 9.12 – 8.96 (m, 1H), 7.99 – 7.93 (m, 1H), 7.92 – 7.83 (m, 1H), 7.75 – 7.63 (m, 1H), 7.52 (s, 1H), 7.45 (ddd, J = 7.6, 1.3, 0.5 Hz, 1H), 7.34 – 7.27 (m, 2H), 7.25 – 7.21 (m, 1H), 7.00 (ddd, J = 7.7, 1.3, 0.4 Hz, 1H), 6.90 (td, J = 7.6, 1.2 Hz, 1H), 6.77 (qd, J = 7.6, 1.4 Hz, 1H), 3.48 (dd, J = 15.3, 6.6 Hz, 1H), 2.38 (d, J = 15.3 Hz, 1H), 1.54, (m, 1 H), 1.07 (d, J = 7.0 Hz, 3H). ^{13}C NMR (126 MHz, Chloroform-d) δ 143.19, 139.17, 136.61, 135.77, 134.61, 132.20, 131.92, 130.68, 130.57, 128.77, 127.87, 126.99, 126.94, 126.82, 126.81, 126.65, 126.55, 125.83, 125.67, 125.25, 124.87, 123.64, 71.51, 62.39, 40.84, 37.94, 21.67.[7]

9-(5-bromo-2-methyl-2,3-dihydro-1H-cyclopenta[a]naphthalen-1-ylidene)-9H-thioxanthene (22). To a 100 mL screw-capped tube charged with episulfide 21 (101 mg,

0.208 mmol) was added triphenylphosphine (108 mg, 0.416 mmol), and the mixture was stirred at 140 °C for 14 h. After the reaction mixture was cooled to room temperature, the resulting mixture was partitioned between DCM (10 mL) and saturated NH_4Cl (aq) (10 mL). The organic layer was dried over anhydrous $MgSO_4$, filtered, and the filtrate concentrated in vacuo. The resulting concentrate was purified by column chromatography (silica gel; 20% DCM in hexanes) to yield 21 as a pale yellow solid (86.4 mg, 89%): ^{1}H NMR (500 MHz, Chloroform-d) δ 8.12 (ddd, J = 8.5, 1.3, 0.7 Hz, 1H), 7.80 (dd, J = 7.8, 1.4 Hz, 1H), 7.78 (s, 1H), 7.65 – 7.61 (m, 1H), 7.59 (ddd, J = 7.8, 1.2, 0.5 Hz, 1H), 7.35 (td, J = 7.6, 1.3 Hz, 1H), 7.30 – 7.27 (m, 1H), 7.26 – 7.22 (m, 1H), 7.01 (ddd, J = 7.8, 7.3, 1.4 Hz, 1H), 6.94 (ddd, J = 8.5, 1.3, 0.7 Hz, 1H), 6.84 (ddd, J = 8.3, 6.7, 1.3 Hz, 1H), 6.71 (ddd, J = 7.7, 1.5, 0.5 Hz, 1H), 6.62 (td, J = 7.5, 1.2 Hz, 1H), 4.39 – 4.27 (m, 1H), 3.66 (dd, J = 15.5, 6.2 Hz, 1H), 2.62 (d, J = 15.5 Hz, 1H), 0.80 (d, J = 6.9 Hz, 3H). ^{13}C NMR (126 MHz, CDCl3) δ 145.93, 145.08, 139.89, 137.60, 135.60, 135.58, 135.42, 130.93, 129.75, 129.22, 128.54, 127.98, 127.78, 127.56, 127.50, 126.86, 126.56, 126.42, 126.39, 126.26, 126.11, 125.54, 125.40, 124.21, 39.49, 37.86, 19.35.[7]

N1,N1-Dimethyl-N2-(2-methyl-1-(9H-thioxanthen-9-ylidene)-2,3-dihydro-1H-cyclopenta[a]naphthalen-5-yl)ethane-1,2-diamine (MNM 5). BINAP (2.5 mg, 0.0066 mmol) and palladium(II) acetate (0.5 mg, 0.0022 mmol) were dissolved in dry toluene (5 mL). This solution was stirred for 30 min at room temperature, where upon it turned from dark red to dark orange. After this period NaOtBu (25 mg, 0.22 mmol) was added, followed by bromo-substituted motor 22 (20 mg, 0.044 mmol) and N1,N1-dimethylethane-1,2-diamine (20 mg, 0.22 mmol). The mixture was stirred at 90 °C for 2 d. Subsequently, the reaction mixture was poured into CH_2Cl_2 (10 mL). After filtration, the solvents were evaporated. The crude product was dissolved in a small amount of

CH_2Cl_2 and purified using column chromatography (SiO2; 10% MeOH in DCM) to yield MNM 5 as a brown solid product (15.0 mg, 74%): ^{1}H NMR (500 MHz, CDCl3) δ 7.80 (dd, J = 7.8, 1.3 Hz, 1H), 7.75 – 7.70 (m, 1H), 7.60 – 7.58 (m, 1H), 7.55 (ddd, J = 7.8, 1.2, 0.5 Hz, 1H), 7.36 – 7.29 (m, 1H), 7.19 (td, J = 7.5, 1.3 Hz, 1H), 7.14 (ddd, J = 8.3, 6.7, 1.3 Hz, 1H), 6.97 (ddd, J = 7.8, 7.3, 1.4 Hz, 1H), 6.88 (ddd, J = 8.5, 1.3, 0.6 Hz, 1H), 6.83 – 6.74 (m, 2H), 6.62 (td, J = 7.5, 1.2 Hz, 1H), 6.53 (s, 1H), 4.24 (p, J = 6.7 Hz, 1H), 3.59 (dd, J = 15.4, 6.3 Hz, 1H), 3.40 – 3.29 (m, 2H), 2.74 (tt, J = 9.4, 4.9 Hz, 2H), 2.56 (d, J = 15.4 Hz, 1H), 2.34 (s, 6H), 0.79 (d, J = 6.8 Hz, 3H). ^{13}C NMR (125 MHz, CDCl3) δ 148.00, 146.75, 145.69, 141.36, 138.77, 135.90, 135.52, 129.64, 128.80, 127.83, 127.67, 127.32, 127.05, 126.23, 126.10, 125.74, 125.49, 125.03, 124.65, 123.90, 122.97, 122.86, 119.85, 101.46, 57.71, 45.19, 40.92, 40.18, 37.51, 19.87.[7]

N1,N1,N2-trimethyl-N2-(2-methyl-1-(9H-thioxanthen-9-ylidene)-2,3-dihydro-1H-cyclopenta[a]naphthalen-5-yl)ethane-1,2-diamine (MNM 6). BINAP (2.5 mg, 0.0066 mmol) and palladium(II) acetate (0.5 mg, 0.0011 mmol) were dissolved in dry toluene (5 mL). This solution was stirred for 30 min at room temperature, where upon it turned from dark red to dark orange. After this period NaOtBu (25 mg, 0.11 mmol) was added, followed by bromo-substituted motor 22 (10 mg, 0.022mmol) and N1,N1,N2-trimethylethane-1,2-diamine (20 mg, 0.44 mmol). The mixture was stirred at 90 °C for 2 d. Subsequently, the reaction mixture was poured into CH_2Cl_2 (10 mL). After filtration, the solvents were evaporated. The crude product was dissolved in a small amount of CH_2Cl_2 and purified using column chromatography (SiO2; 10% MeOH in DCM) to yield MNM 6 as a brown solid product (6.3 mg, 61%): ^{1}H NMR (500 MHz, Chloroform-d) δ 8.04 (dd, J = 8.4, 1.2 Hz, 1H), 7.79 (dd, J = 7.7, 1.4 Hz, 1H), 7.60 (dd, J = 7.8, 1.3 Hz, 1H), 7.57 (ddd, J = 7.8, 1.2, 0.5 Hz, 1H), 7.32 (td, J = 7.5, 1.3 Hz, 1H), 7.22 (dd, J = 7.6, 1.4 Hz, 1H),

7.17 (ddd, J = 8.3, 6.7, 1.3 Hz, 1H), 7.05 (s, 1H), 7.00 (ddd, J = 7.8, 7.3, 1.4 Hz, 1H), 6.87 (dt, J = 8.4, 1.0 Hz, 1H), 6.80 – 6.72 (m, 2H), 6.64 (td, J = 7.5, 1.2 Hz, 1H), 4.36 – 4.20 (m, 1H), 3.62 (dd, J = 15.4, 6.4 Hz, 1H), 3.42 (t, J = 7.0 Hz, 2H), 2.92 (s, 2H), 2.57 (d, J = 15.5 Hz, 1H), 2.46 (s, 6H), 0.78 (d, J = 6.9 Hz, 3H). ^{13}C NMR (126 MHz, CDCl3) δ 146.04, 145.97, 140.57, 138.23, 135.78, 135.46, 130.11, 128.64, 128.54, 128.46, 127.73, 127.70, 127.40, 127.33, 126.85, 126.30, 126.27, 126.17, 126.06, 125.78, 124.63, 123.73, 123.63, 112.90, 56.51, 44.99, 43.49, 39.93, 37.64, 29.70, 19.65.[7]

6.4.4 MNM 7

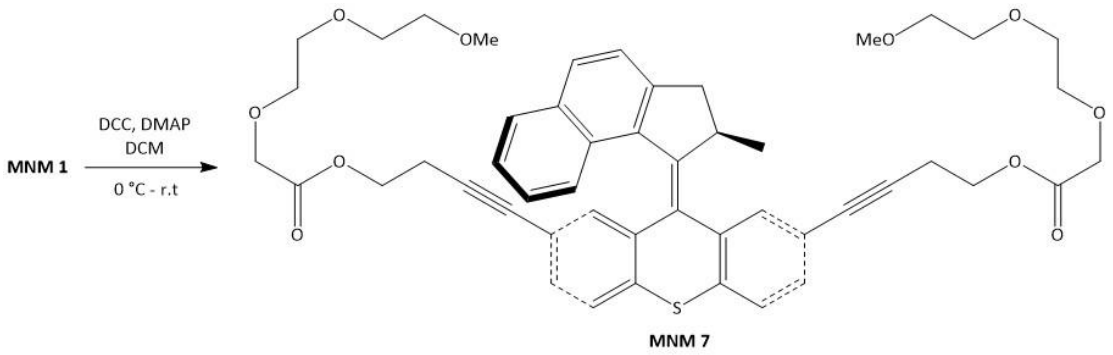

(9-(2-methyl-2,3-dihydro-1H-cyclopenta[a]naphthalen-1-ylidene)-9Hthioxanthene-2,7-diyl)bis(but-3-yne-4,1-diyl)bis(2-(2-(2-methoxyethoxy)ethoxy)acetate) (MNM 7). An oven dried round-bottom flask equipped with a stir bar was charged with MNM 1 (12 mg, 0.022 S29 mmol), 2-(2-(2-methoxyethoxy)ethoxy)acetic acid (0.02 mL, excess), DCC (4.5 mg, 0.022 mml), DMAP (0.3 mg, 0.0022 mmol) and DCM (5 mL) at 0 °C. The suspension was stirred vigorously for 18 h at rt. The resulting yellow solution was partitioned between DCM (20 mL) and water (20 mL). The organic phase was dried over anhydrous $MgSO_4$, filtered and the filtrate was concentrated in vacuo, followed by purification by column chromatography (SiO_2; 20% acetone in DCM) to afford MNM 7 as a bright yellow solid (15.9 mg, 84%): ^{1}H NMR (500 MHz, CDCl3) δ 8.12 (ddd, J = 8.4, 1.4, 0.7 Hz, 1H), 7.77 (d, J = 1.7 Hz, 1H), 7.48 (d, J = 8.0 Hz, 1H), 7.46 (dd, J = 8.0, 0.5 Hz, 1H),

7.23 (dd, J = 8.1, 1.7 Hz, 1H), 7.20 (ddd, J = 8.2, 6.8, 1.2 Hz, 1H), 7.02 (dd, J = 8.0, 1.8 Hz, 1H), 6.83 (ddd, J = 8.3, 6.8, 1.4 Hz, 1H), 6.81 (s, 1H), 6.76 – 6.73 (m, 2H), 6.72 (t, J = 0.9 Hz, 1H), 4.37 (t, J = 7.0 Hz, 2H), 4.22 (s, 2H), 4.18 (q, J = 6.6 Hz, 1H), 4.12 – 4.07 (m, 4H), 4.05 (s, 3H), 3.78 – 3.74 (m, 2H), 3.71 – 3.67 (m, 4H), 3.63 (m, 7H), 3.55 – 3.50 (m, 4H), 3.36 (s, 3H), 3.36 (s, 3H), 2.82 (t, J = 7.0 Hz, 2H), 2.60 (d, J = 15.6 Hz, 1H), 2.49 (t, J = 7.0 Hz, 2H), 0.78 (d, J = 6.8 Hz, 3H). ^{13}C NMR (125 MHz, CDCl3) δ 170.36, 170.22, 157.41, 147.35, 147.25, 140.46, 138.12, 135.95, 135.33, 131.60, 130.86, 129.39, 129.24, 129.03, 127.63, 127.27, 126.70, 125.85, 125.42, 125.12, 124.86, 123.84, 121.85, 121.51, 121.41, 102.00, 85.62, 84.83, 82.07, 81.38, 71.90, 70.99, 70.91, 70.68, 70.63, 70.56, 70.54, 68.64, 68.50, 62.60, 62.42, 59.05, 59.04, 55.63, 40.29, 37.73, 20.05, 19.76, 19.75.[8]

6.4.5 MNM 8

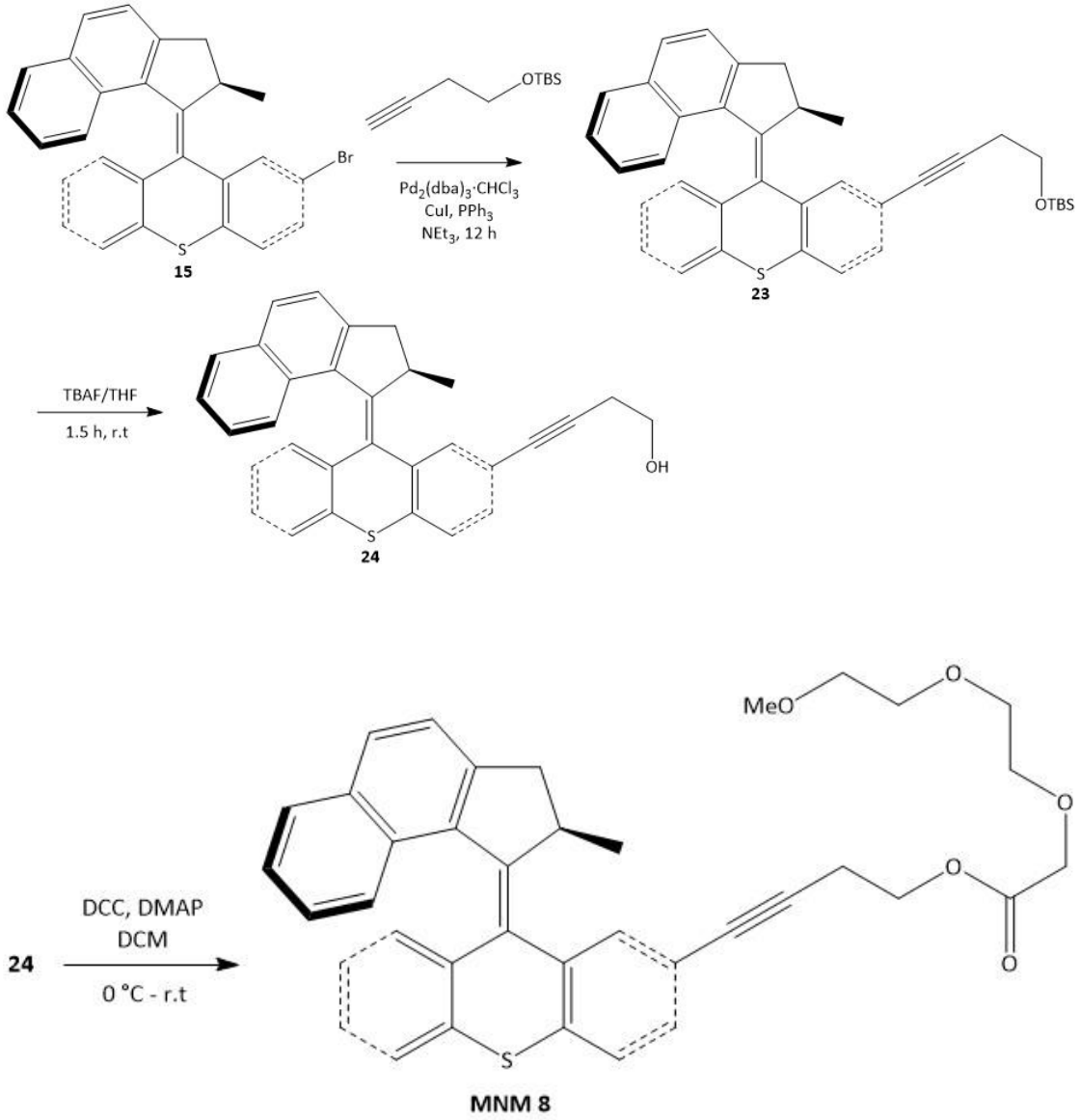

4-(9-(2-methyl-2,3-dihydro-1H-cyclopenta[a]naphthalen-1-ylidene)-9H-thioxanthen-2-yl)but-3-yn-1-yl2-(2-(2-methoxyethoxy)ethoxy)acetate (MNM 8). An oven dried round-bottom flask equipped with a stir bar was charged with 24 (16 mg, 0.029 mmol), 2-(2-(2- methoxyethoxy)ethoxy)acetic acid (0.03 ml, excess), DCC (5.5 mg, 0.029 mml), DMAP (0.5 mg, 0.0029 mmol) and DCM (5 mL) at 0 °C. The suspension was stirred vigorously for 18 h at rt. The resulting yellow solution was partitioned between DCM (20 mL) and water (20 mL). The organic phase was dried over anhydrous $MgSO_4$, filtered and the filtrate was concentrated in vacuo, followed by purification by column

chromatography (SiO2; 20% acetone in DCM) to afford 6 as a bright yellow solid (16.7 mg, 81%). For NMR spectroscopic data, see reference 8.[8]

6.4.6 MNM 9

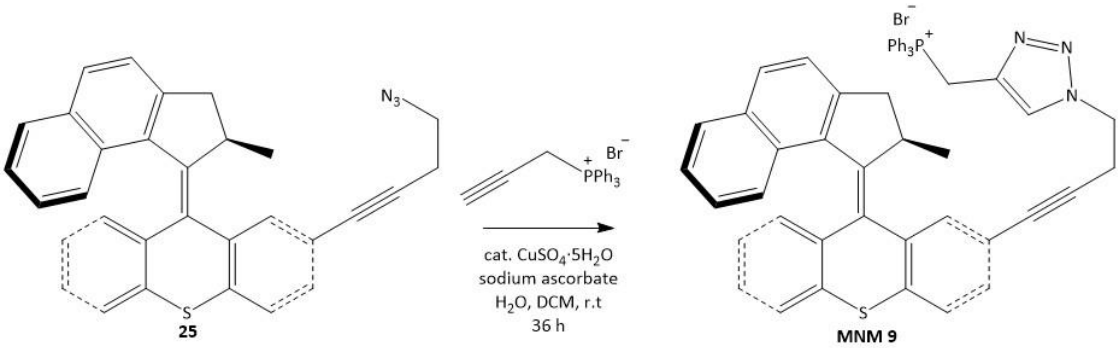

MNM 9. A 2 mL vial charged with motor diazide 25[6] (21.94 mg, 0.039 mmol), Triphenyl(prop-2-yn-1-yl)phosphonium bromide (35 mg, 0.086 mmol), $CuSO_4$. 5H2O(s) (0.97 mg, 0.0039 mmol) and sodium ascorbate (1.62 mg, 0.0117 mmol) was sealed with a rubber septum. A well-degassed mixture of CH_2Cl_2 (0.1 mL) and water (0.1 mL) was added to the vial, and the vial was shaken by a wrist-action shaking machine for 36 h. The mixture was partitioned between CH_2Cl_2 (5 mL) and water (5 mL). The organic phase was dried over anhydrous $MgSO_4$, filtered, and the filtrate was concentrated under vacuum. The crude product was purified by preparative TLC (silica gel, 4% MeOH inCH2Cl2) to afford the desired MNM 9 as an orange solid (45 mg, 85%). For NMR spectroscopic data, see reference 2.[2]

6.4.7 MNM 10

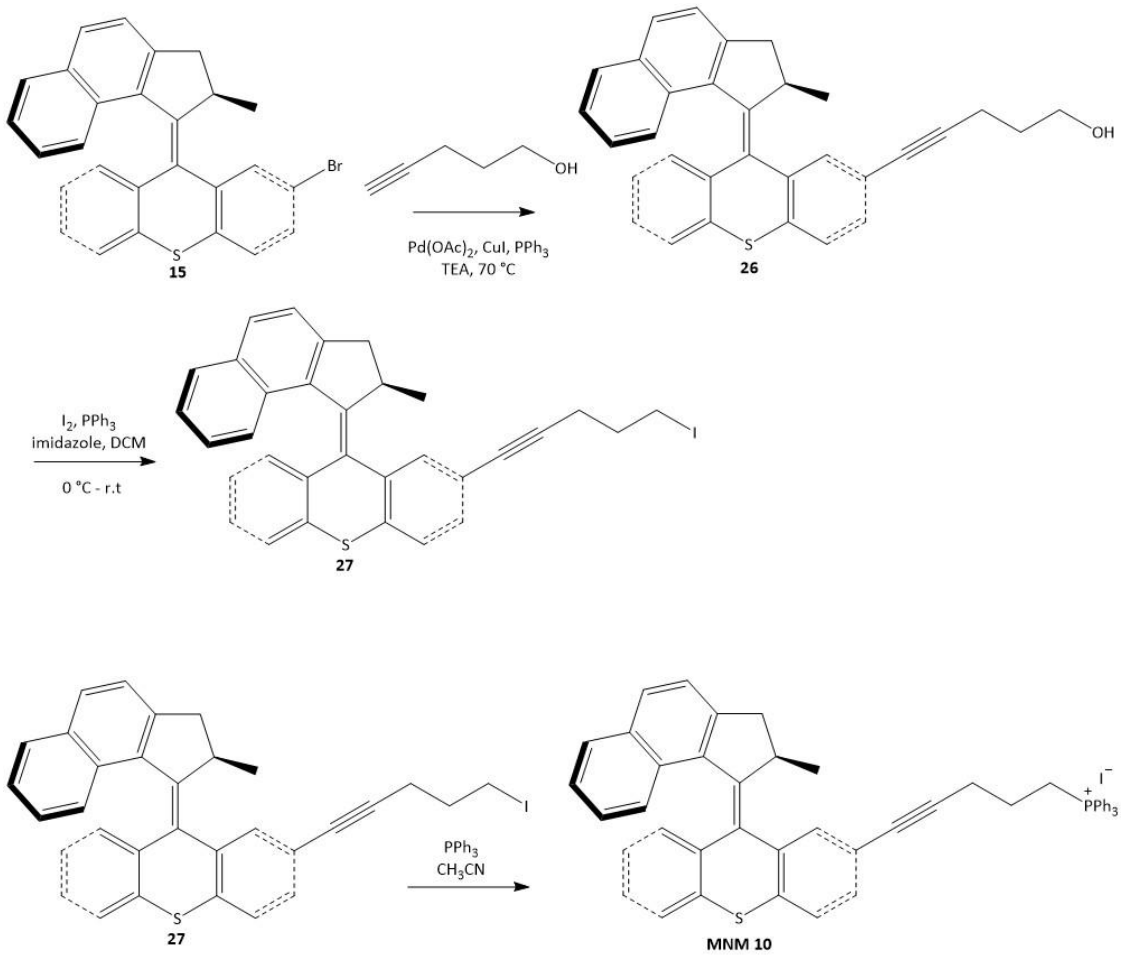

5-(9-(2-methyl-2,3-dihydro-1H-cyclopenta[a]naphthalen-1-ylidene)-9Hthioxanthen-2-yl)pent-4-yn-1-ol (26). An oven dried round-bottom flask equipped with a stir bar was charged with motor 15 (50 mg, 0.11 mmol), palladium(II) acetate (2.5 mg, 0.011 mmol), CuI (2.0 mg, 0.011 mmol), PPh_3 (5.8 mg, 0.022 mmol) and but-4-yn-1- ol (0.03 mL, 0.44 mmol). NEt_3 (3 mL) was added and the mixture was stirred at 70 °C overnight. The resulting mixture was partitioned between DCM (10 mL) and saturated NH_4Cl (aq) (10 mL). The organic layer was dried over anhydrous $MgSO_4$, filtered and the filtrate concentrated in vacuo. The resulting concentrate was purified by column chromatography (silica gel; 30% DCM in hexanes) to afford 26 as a pale yellow solid (39.5 mg, 78%): ^{1}H NMR (500 MHz, CDCl3) δ 7.84-7.67 (m, 3 major isomer protons and 3 minor

isomer protons), 7.62-7.55 (m, 1 major isomer proton and 1 minor isomer proton), 7.53-7.40 (m, 2 major isomer protons and 2 minor isomer protons), 7.33 (m, 1 minor isomer proton), 7.24-7.13 (m, 2 major isomer protons and 2 minor isomer protons), 7.04-6.97 (m, 1 major isomer proton and 1 minor isomer proton), 6.86-6.60 (m, 4 major isomer protons and 3 minor isomer protons), 4.33-4.21 (m, 1 major isomer proton and 1 minor isomer proton), 3.85 (t, J = 6.1 Hz, 2 major isomer protons), 3.73- 3.60 (m, 1 major isomer proton and 1 minor isomer proton), 3.55 (t, J = 6.1 Hz, 2 minor isomer protons), 2.68-2.61 (m, 1 major isomer proton and 1 minor isomer proton), 2.59 (t, J = 7.0 Hz, 2 major isomer protons), 2.24 (t, J = 6.8 Hz, 2 minor isomer protons), 1.95-1.85 (m, 2 major isomer protons), 1.66-1.57 (m, 2 minor isomer protons), 0.793 (d, J = 6.8 Hz, 3 major isomer protons), 0.787 (d, J = 6.8 Hz, 3 minor isomer protons). ^{13}C NMR (125 MHz, CDCl3) δ 146.60, 146.48, 146.04, 145.88, 140.08, 140.02, 137.98, 137.67, 135.68, 135.52, 135.23, 135.15, 135.03, 134.90, 133.08, 132.94, 131.67, 130.64, 130.17, 130.13, 129.07, 129.06, 128.86, 128.80, 128.66, 127.87, 127.86, 127.75, 127.74, 127.73, 127.72, 127.70, 127.44, 127.30, 126.48, 126.39, 126.38, 126.12, 126.12, 126.09, 124.84, 124.75, 124.33, 124.15, 123.79, 123.72, 121.82, 121.75, 89.83, 88.88, 81.00, 80.49, 61.88, 61.54, 39.82, 39.68, 37.88, 37.79, 31.39, 30.99, 19.53, 19.52, 16.12, 15.73.[9]

(5-(9-(2-methyl-2,3-dihydro-1H-cyclopenta[a]naphthalen-1-ylidene)-9Hthioxanthen-2-yl)pent-4-yn-1-yl)triphenylphosphonium iodide (MNM 10). An oven dried round-bottom flask equipped with a stir bar was charged with motor 26 (25 mg, 0.055 mmol), iodine (28 mg, 0.11 mmol) and imidazole (7.5 mg, 0.11 mmol) at 0°C. PPh_3 (28.8 mg, 0.11 mmol) was added slowly at 0°C and the mixture was stirred at room temperature for 30min. Saturated solutions of sodium thiosulfate (10 mL) and sodium bicarbonate (10 mL) were added to the reaction mixture. The organic phase was separated, and the

aqueous phase was extracted with methylene chloride. The combined organic layers were washed with brine, dried over $MgSO_4$, and then concentrated in vacuo. The resulting concentrate was purified by flash column chromatography and the resulting iodide product 27 was used for the next step due to its instability. To a stirred solution of compound 27 in dry acetonitrile (4 mL) at room temperature, PPh_3 (56 mg, 0.22 mmol) was added, and then the mixture was allowed to stir under reflux for 48 h. After TLC analysis indicated the consumption of the starting material, the solvent was subsequently removed under reduced pressure, and the residue was purified by flash chromatography to afford compound 3 as a white solid (19.5 mg, 43% for two steps). For NMR spectroscopic data, see reference 9.[9]

6.5 References

1 L. Young, J. Sung, G. Stacey and J. R. Masters, *Nat. Protoc.*, 2010, **5**, 929–934.

2 V. García-López, F. Chen, L. G. Nilewski, G. Duret, A. Aliyan, A. B. Kolomeisky, J. T. Robinson, G. Wang, R. Pal and J. M. Tour, *Nature*, 2017, **548**, 567–572.

3 R. Pal, *Faraday Discuss.*, 2015, **177**, 507–515.

4 J. Schindelin, I. Arganda-Carreras, E. Frise, V. Kaynig, M. Longair, T. Pietzsch, S. Preibisch, C. Rueden, S. Saalfeld, B. Schmid, J.-Y. Tinevez, D. J. White, V. Hartenstein, K. Eliceiri, P. Tomancak and A. Cardona, *Nat. Methods*, 2012, **9**, 676–682.

5 P.-T. Chiang, J. Mielke, J. Godoy, J. M. Guerrero, L. B. Alemany, C. J. Villagómez, A. Saywell, L. Grill and J. M. Tour, *ACS Nano*, 2012, **6**, 592–597.

6 V. García-López, P.-T. Chiang, F. Chen, G. Ruan, A. A. Martí, A. B. Kolomeisky, G. Wang and J. M. Tour, *Nano Lett.*, 2015, **15**, 8229–8239.

7 A. L. Santos, D. Liu, A. K. Reed, A. M. Wyderka, A. van Venrooy, J. T. Li, V. D. Li, M. Misiura, O. Samoylova, J. L. Beckham, C. Ayala-Orozco, A. B. Kolomeisky, L. B. Alemany, A. Oliver, G. P. Tegos and J. M. Tour, *Sci. Adv.*, 2022, **8**, eabm2055.

8 C. Ayala Orozco, D. Liu, Y. Li, L. B. Alemany, R. Pal, S. Krishnan and J. M. Tour, *ACS Appl. Mater. Interfaces*, 2020, **12**, 410–417.

9 T. Galbadage, D. Liu, L. B. Alemany, R. Pal, J. M. Tour, R. S. Gunasekera and J. D. Cirillo, *ACS Nano*, 2019, **13**, 14377–14387.